Novel imaging techniques for intraoperative assessment of tumour resection margins in breast-conserving surgery

Grootendorst, Maarten Ruben

Awarding institution:
King's College London

Take down policy

If you believe that this document breaches copyright please contact librarypure@kcl.ac.uk providing details, and we will remove access to the work immediately and investigate your claim.

Novel imaging techniques for intraoperative assessment of tumour resection margins in breast-conserving surgery

Maarten Ruben Grootendorst

A thesis submitted to King's College London for the degree of Doctor of Philosophy

Division of Cancer Studies, King's College London

2016

DEDICATION

I dedicate this PhD thesis to my mother and Martha Sixma, two exceptional women in my life who passed away at a very young age due to the consequences of cancer, and whom I miss every day. You will always be an incredible source of inspiration and motivation, and your love and support have been unforgettable and irreplaceable.

Abstract

There is a clear need for more accurate techniques to assess tumour resection margins intraoperatively in breast-conserving surgery (BCS), as to date an average 10 – 30% of patients undergoing BCS require a re-operation to achieve clear margins. This thesis evaluates two novel imaging techniques for intraoperative tumour margin assessment, Terahertz Pulsed Imaging (TPI) and Cerenkov Luminescence Imaging (CLI), that have been developed with a view to reducing re-operation rates in BCS.

Both techniques were evaluated in a first-in-human, single centre study to demonstrate proof-of-principle and feasibility. A TPI handheld probe system (Teraview Ltd., UK) was used to scan breast samples *ex vivo,* and the TPI data was correlated with histopathology to assess diagnostic accuracy. CLI was evaluated intraoperatively by scanning excised BCS specimens from patients that received 2-deoxy-2-(^{18}F)fluoro-D-glucose (^{18}F-FDG) preoperatively using an investigational CLI imaging system (Lightpoint Medical Ltd., UK). An increased Technetium-99m (^{99m}Tc) nanocolloid activity of 150 MBq was used to facilitate sentinel node detection. Radiation doses to theatre staff were measured. CLI images were analysed postoperatively, and margin status correlated with histopathology results.

The TPI handheld probe discriminated invasive breast cancer from benign breast tissue with a high sensitivity (86%) and an encouraging degree of accuracy (75%). Accurate discrimination of cancer from tissue containing a high percentage of fibrous cells proved challenging due to the similarities in the THz pulse between these two types of tissue. Intraoperative ^{18}F-FDG CLI showed to be a feasible and low-risk procedure. Good agreement was found between CLI and histopathology for clear margins of excision. Sentinel nodes could be successfully detected using

the gamma probe and blue dye, and radiation dose to staff was low. Elimination of image artefacts from tissue dissection with the monopolar diathermy device is needed to further refine CLI.

In conclusion, both TPI and ^{18}F-FDG CLI are promising techniques for intraoperative assessment of tumour resection margins in BCS, warranting larger studies to assess the diagnostic accuracy of each technique on different cancer types including DCIS, and the impact on re-operation rates.

Acknowledgements

Source of funding

Table of contents

List of figures

12

List of tables

Abbreviations

^{18}F-FDG	2-deoxy-2-(^{18}F)fluoro-D-glucose
^{99m}Tc	Technetium-99m
AI	Aromatase inhibitor
ALND	Axillary lymph node dissection
APBI	Accelerated partial breast irradiation
AUROC	Area under receiving operating curve
BCS	Breast-conserving surgery
CI	Confidence interval
CLI	Cerenkov luminescence imaging
CNA	Copy number aberration
CPS	Counts per second
DCIS	Ductal carcinoma in situ
DFS	Disease-free survival
DSR	Diffuse reflectance spectroscopy
EBRT	External beam radiotherapy
EMCCD	Electron-multiplying charge coupled device
EPD	Electronic personal dosimeter
ER	Oestrogen receptor
^{18}F	Fluorine-18
FOV	Field of view
FSA	Frozen section analysis
H&E	Haematoxylin and eosin
HER2	Human epidermal growth factor receptor 2
IC	Imprint cytology
IDC	Invasive ductal carcinoma
IDSR	Intraoperative digital specimen radiography
IHC	Immunohistochemistry
ILC	Invasive lobular carcinoma
IOUS	Intraoperative ultrasound
LR	Local recurrence
NIRF	Near-infrared fluorescence
NST	Invasive ductal carcinoma/no special type

OCT	Optical coherence tomography
OS	Overall survival
PCA	Principal component analysis
pCR	Pathologic complete response
PET	Positron emission tomography
PR	Progesterone receptor
RCS	Routine cavity shavings
ROI	Region-of-interest
RS	Raman spectroscopy
SLN	Sentinel lymph node
SLNB	Sentinel lymph node biopsy
SNR	Signal-to-noise ratio
SVM	Support vector machine
TBR	Tumour-to-background ratio
THz	Terahertz
TLD	Thermo-stimulated luminescent dosimeter
TNBC	Triple negative breast cancer
TPI	Terahertz pulsed imaging
TPS	Terahertz pulsed spectroscopy
US	Ultrasound
WLE	Wide local excision

1. Introduction to breast cancer and tumour resection margins in breast-conserving surgery

This chapter provides an overview on the clinical management of breast cancer including breast cancer surgery, the importance of tumour resection margins in breast-conserving surgery (BCS), and the armamentarium of techniques available to assess tumour margins intraoperatively. This thesis evaluates two novel imaging techniques for intraoperative tumour margin assessment, and the scope and aims of each project are outlined at the end of this chapter.

1.1 Breast cancer key facts

Breast cancer is by far the most common cancer among women worldwide, and in 2012 an estimated 1.67 million women were diagnosed with the disease, accounting for 25% of all female cancers (1). In Europe approximately 460,000 women are diagnosed annually, making it the most frequently diagnosed cancer (2). Among men, breast cancer is far less common, accounting for <1% of breast cancer cases.

With the introduction of breast cancer screening in the 1980's, and a greater life expectancy among the world's population, there has been a gradual increase in breast cancer incidence. Currently the estimated lifetime risk to develop breast cancer is 1 in 8 for women in the United Kingdom and the United States (3,4). Despite the fact that early diagnosis and more effective treatment have lowered the mortality rate, with approximately 131,000 deaths per annum, breast cancer remains the most frequent cause of cancer death in women in Europe (2).

1.2 Classification of breast cancer

Breast cancer comprises a heterogeneous disease consisting of several subtypes, each associated with a distinct variability in biological and clinical characteristics. Breast cancer prognosis depends on a variety of factors, including patient age, tumour type, tumour size and grade, lymph node status, lymphovascular invasion and receptor status, and these factors are of key importance when determining the most suitable form of treatment (5). Advances in molecular and genetic profiling have added additional prognosticators, and a brief overview of the latest developments in this field will also be provided in this section.

1.2.1 Types of breast cancer

All breast cancers derive from the terminal ductal lobular unit, and can be roughly classified into non-invasive and invasive cancer. Classification of breast cancer involves histological assessment of morphological based features and immunohistochemical (IHC) analyses. Non-invasive breast cancers, also known as carcinoma *in situ*, are cancers that have not yet broken through the basement membrane, and are thus confined within the ductal lobular units without invading the breast stroma. Ductal carcinoma in situ (DCIS) is the most common form of *in situ* breast cancer, comprising approximately 90% of non-invasive breast cancers, and starts within the duct system (6). DCIS generally is asymptomatic, although some patients may present with a small palpable lump. DCIS is classified into three categories, i.e. low-grade, intermediate-grade and high-grade, the latter being the most aggressive with the highest potential to progress to invasive cancer. If DCIS cells die and pile up, tiny specks of calcium form within the broken cells (called microcalcifications). These calcifications are usually very small and sometimes difficult to identify on imaging, and in combination with its impalpable nature,

DCIS causes additional challenges for accurate preoperative and intraoperative identification.

Over time cancer cells can penetrate through the wall of the ducts and lobules, thereby infiltrating the breast stroma. Invasive carcinomas, in contrast to *in situ* carcinomas, tend to form firm/hard palpable lesions. The most common form of invasive breast cancer, and breast cancer in general, is invasive ductal carcinoma/no special type (NST). NST is found in 40 – 75% of all breast cancer patients (7). Its descriptive is based on the lack of sufficient morphological characteristics to be classified into a specific histological subtype. Invasive lobular carcinoma (ILC) comprises 5 – 15% of invasive breast tumours, and in contrast to NST this type of cancer is well characterised by a proliferation of small cells with a diffuse growth pattern (7). Far less common types of invasive breast cancer include medullary carcinoma (1 – 7%), tubular carcinoma (<2%), mucinous carcinoma (~2%), inflammatory breast cancer (~1%), Paget's disease (<1%), and phylloides tumour (<1%) (7).

1.2.2 Receptor status

Breast cancer cells may express a variety of receptors. Characterisation of receptor status is performed by IHC analyses, and is of importance in selecting appropriate systemic therapies (Section 1.3.4). The three most important receptors in breast cancer are oestrogen (ER), progesterone (PR) and human epidermal growth factor receptor 2 (HER2). ER and PR are hormone receptors, and pathology reporting of ER status is required as per UK national guidelines (8). ER is reported semi-quantitatively with recording of both the proportion and intensity of nuclear cell reactivity. Most histopathology laboratories categorise ER according to Allred score; a score of 3 or more is defined as ER positive (9). The same scoring system

and cut-off is often used to define PR positivity. The Survival, Epidemiology and End Results (SEER) programme which included a total of 155,175 breast cancer patients, found that 63% of women have ER-positive and PR-positive (ER+/PR+) tumours, 13% had ER+/PR- tumours, 3% had ER-/PR+ tumours and 21% had ER-/PR- tumours (10). ER+/PR+ tumours were associated with a lower breast-cancer mortality risk than ER+/ER-, ER-/PR+ and ER-/PR- tumours across the majority of clinical characteristics examined including age, tumour size, stage and grade, and axillary lymph node status. Another study found that patients with ER+ tumours have an improved disease-free survival (DFS) and overall survival (OS) compared to patients with ER- tumours, while PR+ tumours only showed an increase in OS compared to PR- tumours (11).

HER2 is a member of the human epidermal growth factor receptor (EGFR) family, and according to UK guidelines HER2 status should be assessed in invasive breast cancers using IHC as first line and *in situ* hybridisation as second line technique (12). Scores of 0 or 1+ are defined as HER2 negative, and 3+ scores as HER2 positive. Borderline cases with 2+ scores on IHC are generally categorised based on the number of *Her2* gene copies on *in situ* hybridisation; a ratio of 2.00 or more is regarded HER2 positive (13). Approximately 13 – 20% of breast cancer patients are HER2 positive (8). A large retrospective analysis performed by Ross *et al.* based on over 15,000 patients from 47 studies found that in a majority of patients and studies, HER2 positive (HER2+) tumours were associated with poorer prognosis (14).

Triple-negative breast cancers (TNBCs) are defined as tumours lacking expression of ER, PR and HER2. These tumours are found and in approximately 12 – 17% of breast cancer patients (15). Although described as one group, TNBC is a heterogeneous class consisting of different subtypes (16). Several studies have

shown that TNBCs are associated with adverse prognosis in terms of DFS and OS up to 5 years from diagnosis compared to non-TNBCs (16-18). Other characteristics of TNBCs include diagnosis at younger age, higher histological grade, higher rate of nodal positivity, and larger tumour size (18).

1.2.3 Molecular classifications

Although traditional histopathological methods enable classification of breast cancer into different subtypes, identical histological forms may respond differently to therapy. This has led to further investigation into the complex biology and molecular pathways underlying the phenotypic diversity amongst breast carcinomas. The first comprehensive gene expression study using DNA microarrays was performed by Perou *et al.* (19). They identified four intrinsic molecular subtypes: ER+/luminal, HER2+, basal-like, and normal breast-like. A subsequent study revealed that the luminal epithelial group could be further divided into at least two subtypes based on differences in expression of luminal-specific genes: Luminal A and Luminal B (20). A significant variation in clinical outcome was seen between patients belonging to the various groups, including poor prognosis for the basal-like subtype. Prat *et al.* identified another intrinsic subtype known as Claudin-low or mesenchymal-like (21).

Recent work involving gene expression has provided more insight into the mechanisms and genes that drive tumourigenesis, and the complex biology underlying breast cancer heterogeneity (22). A landmark study by Curtis *et al.* revealed that inherited variants and acquired somatic copy number aberrations (CNAs) were associated with altered gene expression in approximately 40% of genes; *cis-* and *trans-*acting CNAs were particularly dominant (23). Based on the

CNAs they identified a total of 10 novel molecular subgroups, each associated with distinct clinical outcomes.

Gene expression profiling also enabled identification of distinct prognostic signatures (24). This has led to the development of diagnostic tests including the MammaPrint and Oncotype DX that aid in predicting clinical outcomes for patients, and help determining which patients may benefit from chemotherapy (25).

Although comprehensive molecular and genetic profiling of breast cancer is still in its infancy, rapid progress is being made and molecular information is already included in the classification of breast cancer in addition to traditional clinical and histopathological information. A true prognostic or predictive value may be a combination of all the above, and future gains in further understanding the biological complexities of breast cancer will hopefully allow developing new targeted therapies that enable more personalised breast cancer treatment.

1.3 Breast cancer management

The management of breast cancer is a multidisciplinary effort involving, amongst others, breast care nurses, surgeons, radiologists, pathologists, medical oncologists, radiotherapists and geneticists. Strategies for breast cancer management are ever evolving, and evidence-based guidelines are continuously being improved. In all centres in the UK, patient management is discussed at multidisciplinary meetings (MDMs) where a multitude of variables including clinical findings, imaging and histopathological results are reviewed. By integrating the clinical management decision from the MDM with the patient's preference, tailored treatments are formulated for each individual patient.

1.3.1 Diagnosis

Methods used by clinicians to diagnose breast cancer are based on 'triple' assessment, consisting of clinical examination, imaging and histopathological assessment. Clinical assessment is performed by obtaining a detailed medical history in combination with physical examination. Symptoms (pain, lump, skin changes, and nipple discharge), duration of complaints, parity, age, drug history (hormonal supplements), and family history are of importance in adequate assessment of the patient's medical history. Physical examination involves systematically feeling for any abnormal lumps in the breast, axilla, and supraclavicular regions.

Mammography and ultrasound (US) imaging are the primary imaging techniques used to diagnose breast cancer. Mammography uses low energy x-rays (usually around 30kVp) to identify changes in the density of breast tissue, architectural distortion and microcalcifications. Besides serving as a diagnostic tool in symptomatic cases, mammography is the mainstay imaging technology for breast cancer screening. The sensitivity and specificity of mammography range from 69 – 90% (26). However, diagnostic accuracy is diminished in women with denser breast tissue, lobular cancer, DCIS without associated microcalcifications and multifocal cancer, thus limiting the usefulness of mammographic imaging in these patients.

US imaging is mostly used in addition to mammography, and has been shown to improve the diagnostic performance compared to mammography alone (27). US examination is particularly useful in aiding the identification of tumours in patients with dense breast tissue on screening mammography (28). The typical sensitivity and specificity of a trained ultrasound operator is around 96% and 65%, respectively (29). However, US imaging of the breast is limited by substantial

inter-operator variability (30), and has a tendency to underestimate the extend of DCIS (31).

Magnetic resonance imaging (MRI) is another important imaging technique for diagnosing breast cancer in a subgroup of patients. By administering an intravenous bolus injection of Gadolinium, areas of increased vascularity are enhanced, thus revealing detailed information about anatomical abnormalities. Studies have shown that MRI is more sensitive in detecting multifocal and multicentric cancers than mammography and US (32-35), especially in invasive lobular carcinoma (36). The reported specificity of MRI, however, is low to moderate ranging between 72 - 75% (37,38). It was initially thought that preoperative MRI might improve surgical care by helping to plan the extent of local resection of the tumour, and potentially reduce re-excision rates in patients undergoing breast-conserving surgery (BCS). Houssami *et al.* showed that MRI encourages more extensive surgery by converting BCS patients to undergo a mastectomy or wider resection of the preserved breast (39). However, due to false-positive findings 1.1% of patients underwent an unnecessary mastectomy, and in 4.4% additional tissue excision could have been averted. Two randomised controlled trials and two large cohort studies found that overall preoperative MRI was not associated with improved margin status or reduction in re-operation rate, although Pengel *et al.* found that MRI resulted in a more complete tumour excision in patients with NST cancers (40-43). In patients with pure DCIS preoperative MRI also does not improve surgical management. A recent meta-analysis by Fancellu *et al.* showed no reduction in positive margins or re-operations in DCIS patients who had preoperative MRI and those who did not (44). The suboptimal specificity and potential for inappropriate surgical management, amongst other factors, resulted in a recommendation by the European Society of Breast Cancer Specialists

(EUSOMA) to only use preoperative MRI in a subgroup of patients with a diagnosis of invasive lobular cancer, high risk patients, patients eligible for partial breast irradiation, and patients with >1 cm discrepancy in tumour size between mammography and US that is expected to impact on treatment decision (45).

Overall the preoperative imaging techniques outlined above provide information on the location and size of the tumour preoperatively, but these techniques have limited intraoperative capabilities. The correlation between tumour size and location on preoperative imaging and histopathological analysis remains suboptimal, thereby creating an element of uncertainty when deciding how much tissue is to be excised intraoperatively. Hence, surgeons can only use this information as a rough guide to define the margins of the tumour.

After imaging techniques have identified a suspicious breast lesion, the cells within that lesion are sampled to confirm the diagnosis. This is done by obtaining a core needle biopsy or fine-needle aspiration biopsy (FNAB), which is usually performed under X-ray or US guidance.

1.3.2 Breast cancer surgery

Most women with breast cancer undergo some type of surgery to remove the primary tumour and lymph nodes in the axilla. The goal of surgical treatment is to achieve locoregional control and to stage the disease to plan adjuvant treatment. Over the last century breast cancer surgery has significantly changed by moving from radical to a more conservative intervention. The main types of surgery to the breast and axilla are described below.

1.3.2.1 Surgery to the breast

During most of the 19th and 20th century breast cancer patients were treated by complete removal of the breast, a procedure known as mastectomy. In the time of Halsted and colleagues, around the start of the 20th century, the radical mastectomy was the gold standard of treatment (46,47). This procedure involved removal of the breast, pectoralis muscles and axillary and supraclavicular lymph nodes, and had severe mutilating effects on patients in terms of functional outcome and cosmesis. Due to an improved understanding of the lymphatic anatomy and its role in the dissemination of tumour cells, and advancements in the development of radiotherapy, less extensive forms of breast surgery were developed (48). This included the modified radical mastectomy (MRM), a procedure similar to the radical mastectomy, but without removal of the pectoralis major muscle. An early study found similar OS rates for MRM compared to radical mastectomy, indicating that less extensive surgery could be equally effective (49). This finding was confirmed in the prospective randomised National Surgical Adjuvant Breast and Bowel Project trial (NSABP B-04) (50). In this study patients were randomised to radical mastectomy or total mastectomy (removal of the breast and pectoral fascia without removal of the pectoral muscles) plus radiotherapy. DFS and OS between both groups were found to be similar; this was true for node-negative patients as well as node-positive patients.

The observation that less radical surgery could provide similar oncological outcomes lead to the revolutionising development of BCS combined with whole-breast radiotherapy for patients with early stage breast cancer, which is now the treatment of choice in this group of patients. The aim of BCS, also called wide local excision (WLE) or lumpectomy, is to remove the primary tumour while conserving as much healthy breast tissue as possible to provide a good cosmetic outcome,

minimise physical trauma and expedite recovery. A randomised controlled trial performed by Fisher *et al.* showed that stage I and II breast cancer patients treated with BCS and postoperative radiotherapy after 5-years had no worse, or in fact even better DFS and OS, compared to patients undergoing total mastectomy (51). The oncological safety of BCS in combination with radiotherapy for both early invasive cancer and DCIS has been confirmed in large randomised controlled studies with follow-up periods of up to 20 years (52-62). The early breast cancer trialists' collaborative group (EBCTCG) performed a meta-analysis using data from 17 randomised controlled trials that started before the year 2000 to assess the recurrence rate and breast cancer death rate from BCS and adjuvant radiotherapy (63). They found a pooled 5-year recurrence rate (locoregional or distant) of 10.6% and 31.1% for node-negative and node-positive patients respectively; the 5-year breast cancer death rate was 4.6% and 19.8%, respectively.

Some of these studies provided preliminary evidence that involved tumour resection margins on postoperative histopathological analysis, i.e. tumour cells close or at the margin of excision, is associated with an increased local recurrence (LR) rate if re-excision of additional tissue is not performed (53,55,61). An in depth description of tumour resection margins and its relation to LR is provided in Section 1.4.

The choice between BCS with radiotherapy or mastectomy depends on several factors, including size and extent of the tumour (relative to the size of the breast), multifocality, multicentricity, the presence of diffuse carcinoma *in situ*, patient preference and the male breast (64). A combination of an increased use of screening mammography, and neoadjuvant chemotherapy and endocrine therapy to downstage the size of the tumour, has significantly increased the number of patients suitable for BCS. Currently approximately two-thirds of newly diagnosed

breast cancer patients in the United Kingdom and the United States undergo BCS as initial treatment (65,66). The current standard management for impalpable breast cancer in patients undergoing BCS is preoperative imaging and tumour localized surgical excision using wire-guided localisation (WGL), radioguided occult-lesion localisation (ROLL) or radioactive-seed localisation (RSL) (67). Palpable breast tumours are excised based on the surgeon's tactile and visible assessment of the breast tissue during surgery. The excised WLE specimen is oriented intraoperatively by placing sutures and/or metal clips and/or ink as per NHSBSP guidelines (8). However, the protocol for specimen orientation varies between different centres (68). In Guy's Hospital the following protocol is used: 1 suture + clip = anterior, 2 sutures + clips = superior, 3 sutures + clips = inferior/nipple. Intraoperative imaging or histopathology may be performed to assess tumour resection margins as discussed in more detail in Section 1.5.

The tumour specimen is then sent for postoperative histopathological analysis to obtain decisive information on tumour size and grade, receptor status, presence of lymphovascular invasion, and tumour margin status (8). An in-depth description of the histopathological procedure for assessing tumour margin status postoperatively is provided in Section 1.4.

Patients with positive histological margins, defined as tumour cells at the inked resection edge on postoperative analysis, have approximately a two-fold greater risk of developing a LR than patients with negative margins (Section 1.4). These patients are recommended to undergo re-excision surgery in order to reduce the risk for LR by obtaining clear resection margins. This involves a second operation in the form of a re-excision (a procedure where a further slice of tissue is excised) or in some cases a mastectomy where there is extensive margin involvement. The re-excised tissue undergoes a similar postoperative histological

examination procedure as the WLE specimen to determine if all the cancer has been excised, and further surgery is required if the initial re-excision fails to obtain clear margins. What constitutes an adequate negative tumour resection margin is currently the subject of intense debate as discussed in more detail in Section 1.4.1 and Section 1.4.2, and therefore the treatment strategy of patients with close margins (i.e. tumour cells within a certain distance from the inked resection edge) varies per country and treatment centre.

Mastectomies are generally performed in patients that are not suitable for BCS, including patients with a large tumour (particularly in women with small breasts), a centrally located tumour, multifocal disease or associated extensive DCIS, or in patients where initial BCS along with one or more re-excisions has not completely removed the cancer. Breast reconstruction can be carried out if clinically indicated and as per patient's preference. The options include immediate versus delayed, and prosthetic versus autologous reconstruction. Each type of mastectomy encompasses the removal of virtually all breast tissue, and therefore positive tumour margins resulting from incomplete removal of the tumour rarely occur.

1.3.2.2 Surgery to the axilla

The lymphatic system of the breast predominantly drains to lymph nodes in the axilla (69), making the axilla one of the main routes for breast cancer metastasis. Axillary lymph node status (positive or negative) and the number of involved lymph nodes are, together with the characteristics of the primary tumour, the most important prognostic indicators in breast cancer, and determine what type of adjuvant treatment is warranted (70). There are two main types of axillary

surgery: axillary lymph node dissection (ALND) and sentinel lymph node biopsy (SLNB).

ALND has been the standard approach for axillary nodal staging, and depending on the anatomic relationship of the nodes to the pectoralis minor muscle, involves dissection of all lymph nodes in axillary level 1, 2 or 3 (64). ALND causes both early and late morbidities for the patient, with complications that include pain, numbness, limited shoulder movement, and breast-cancer related lymphedema (71,72). The latter can affect manual dexterity and cause significant morbidity. Moreover, only 25 – 30% of women with early breast cancer are lymph node positive (71,73), so most women who previously routinely underwent ALND were exposed to the complications of this procedure, with no associated clinical benefit.

In light of this, and the finding that lymphatic spread of breast cancer cells to the axilla appears to follow a regular pattern (74,75), a more conservative approach to stage the axilla in the form of a SLNB was developed (76,77). The sentinel lymph node (SLN) is defined as the node receiving direct lymphatic drainage from the tumour, and therefore is most likely to harbour cancer cells if the primary breast tumour has metastasised. To identify SLNs, a radioactive tracer, blue dye or both are injected locally in the breast, and after accumulation of the tracers, the surgeon uses a gamma probe (a handheld scintillation counter detecting gamma photons) and/or the blue discolouration to locate the SLN. By removing only a limited number of lymph nodes, SLNB significantly reduces the morbidity associated with ALND, while DFS and OS have been shown to be equivalent (78,79). SLNB is now the standard method for staging the axilla in clinically and radiologically node negative breast cancer patients. McMasters *et al.* performed a large clinical study to identify the optimal technique for SLNB, and

found that the combined technique of radioisotope and blue dye was superior to each standalone technique in terms of false-negative rates, with a non-significant difference in detection rate (80). In the United Kingdom the combined technique is recommended as per National Institute for Health and Care Excellence (NICE) guidelines (81).

The excised SLNs (together with the primary tumour) are sent for postoperative histopathological analysis to determine if the SLN is involved, and results are obtained several days after the procedure. In addition to the analysis performed postoperatively, some centres use intraoperative histological, cytological or molecular techniques to assess if the removed SLNs contain tumour cells (82). Based on the postoperative histopathological results, lymph node involvement is staged according to the American Joint Committee on Cancer (AJCC) TNM system (83). Isolated tumour cells (ITCs) are defined as single tumour cells or a cluster of cells <0.2 mm, micrometastases as tumour deposits >0.2 mm and ≤2.0 mm, and macrometastases as tumour deposits >2.0 mm. Patients with ITCs are considered lymph node negative, while those with micrometastases and macrometastases lymph node positive. Previous guidelines would have recommended patients with positive SLNs to undergo further axillary surgery in the form of an ALND (81,84). However, the preferred treatment in SLN positive patients is currently subject of intense debate based on evidence from the Z0011 trial (85) and the AMAROS trial (86). The Z0011 study showed that patients with clinical T1 and T2 tumours and a positive SLN undergoing BCS with whole-breast radiotherapy and systemic therapy do not benefit from additional ALND in terms of DFS and OS. The AMAROS trial demonstrated similar DFS and OS in T1 – T2 invasive breast cancer patients with SLN metastases treated with ALND or axillary radiotherapy without ALND, respectively. Although both studies have some

important limitations which fall outside the scope of this thesis, its results have changed clinical practice, and the option to avoid ALND in a selective group of patients with low to moderate axillary tumour burden should now form part of the discussion between clinician and patient to decide on the optimal treatment strategy (87).

1.3.3 Radiotherapy

Radiotherapy can be administered to the breast and/or lymph nodes in the axilla and supraclavicular fossa. In this section the value of radiotherapy in treating BCS patients will be discussed with a specific focus on its effects in respect to tumour margin status. The clinical and oncological importance of radiotherapy in mastectomy patients and patients with nodal disease will not be described as this falls outside the scope of this thesis.

Several large randomised trials have demonstrated the importance of whole-breast external beam radiotherapy (EBRT) in achieving acceptable oncological outcomes in invasive and *in situ* breast cancer patients undergoing BCS (52,54,59,62). The meta-analysis performed by the EBCTCG group found that the 10-year breast cancer recurrence (locoregional or distant) was roughly 50% lower in invasive breast cancer patients treated with BCS and whole-breast EBRT compared to BCS without radiotherapy, while 15-year breast cancer mortality was reduced by a sixth (63). A recently conducted meta-analysis comparing BCS and whole-breast EBRT to BCS alone in patients with DCIS also found a 50% reduction in LR rate after 10-years (88). Breast cancer mortality did not significantly differ between the two groups.

The EORTC trial investigated the impact of a complementary boost radiation dose to the site of local excision on LR and OS in early stage breast cancer

patients with microscopically negative tumour margins after BCS (89). Although patients receiving a boost had an improved LR, there was no difference in OS while a significantly higher number of patients had severe fibrosis. Boost irradiation is therefore only recommended in invasive breast cancer patients with a high-risk of LR, i.e. patients with high tumour grade, <50 years of age, extensive DCIS, vascular invasion or positive or close margins (87).

A meta-analysis by Houssami *et al.* showed that patients with invasive cancer and microscopically positive margins have a higher risk of LR compared to patients with negative margins, regardless of whether whole-breast EBRT is given (90). Besides, the use of a higher boost (18 – 26 Gy) instead of the standard 10 Gy also does not seem to improve LR or OS (91,92). A recent meta-analysis by Nilsson *et al.* showed that in DCIS patients with positive margins a boost dose could reduce the risk of LR compared to no boost (93). However, the authors emphasise that the level of evidence for this observation was very low due to a lack of randomised controlled trial data. Thus, based on current evidence whole-breast EBRT with or without a boost dose cannot replace the need for re-excision surgery to mitigate the negative oncological outcome of positive margins.

Since early 2000 a more localised type of breast radiotherapy has been developed in the form of accelerated partial breast irradiation (APBI), a technique in which only the original tumour site is targeted. APBI can be delivered using several modalities, including intraoperative radiotherapy (IORT), multicatheter interstitial brachytherapy, intracavitary brachytherapy and EBRT (94). IORT is administered in a single session at the time of surgery, and is designed to provide a large radiation dose to a target tissue, while avoiding irradiation to intrathoracic structures such heart, lung and oesophagus (95). Since the definitive treatment is completed at the time of surgery or shortly afterwards, IORT has the potential to

significantly reduce the number of treatment visits, thereby reducing the substantial burden on women from approximately 6 weeks of conventional postoperative radiotherapy.

To date only two randomised controlled trials have compared whole-breast EBRT with IORT in patients undergoing BCS: the TARGIT-A trial (96) and the ELIOT trial (97). The TARGIT-A trial recruited a total of 3451 early-stage breast cancer patients aged 45 years and older with a diagnosis of invasive ductal carcinoma. Patients in the TARGIT group received a single treatment of radiotherapy at the time of surgery (pre-pathology) or after surgery by re-opening the wound (post-pathology); whole-breast EBRT was given if the postoperative histopathology report showed adverse features (tumour margin <1 mm, extensive *in situ* disease, or unexpected ILC). The 5-year risk for LR was significantly higher in the TARGIT group compared to the EBRT group (3.3% versus 1.3%, p = 0.042). Breast cancer mortality was much the same between groups (2.6% versus 1.9, p = 0.56), while non-breast cancer mortality was significantly lower (1.4% versus 3.5%, p = 0.0086). The latter was mainly attributed to fewer deaths from cardiovascular causes and other cancers. An individual comparison of the pre-pathology TARGIT arm and post-pathology TARGIT arm with the EBRT group still showed a higher LR rate for both forms of IORT treatment, although the difference in the prepathotology arm became non-significant and within the prespecified 2.5% inferiority margin. This highlights the potential importance of delivering IORT at the time of initial surgery to maximise treatment efficacy. The ELIOT trial recruited a total of 1305 patients aged between 48 and 75 years with early-stage breast cancer of ≤2.5 cm in size. IORT was administered intraoperatively as a single dose of radiotherapy with electrons. A significantly higher 5-year LR rate

was found in the IORT arm compared to the EBRT arm (p<0.001); OR did not differ between groups.

The results of the TARGIT-A trial and ELIOT trial outlined above were considered suboptimal in terms of oncological safety. Long-term results from prospective randomised studies of other APBI techniques are yet to be published. The ASTRO and GEC-ESTRO guidelines therefore currently only accept the use of APBI outside of a clinical trial in a specific group of patients with a low risk for LR (98,99)

1.3.4 Systemic therapy

Systematic therapy in the form of chemotherapy, endocrine therapy and biologically targeted therapy has contributed significantly to the reduction in recurrence rate and breast cancer mortality observed over the last two decades (100). Systemic therapies can be a combination of different approaches and can be administered in conjunction to surgery and/or radiotherapy in an adjuvant or neoadjuvant setting. The decision to recommend adjuvant systemic therapy depends on tumour size and grade, number of involved axillary lymph nodes, hormone-receptor status and HER2 expression (64). In the adjuvant setting the main aim of systemic treatment is to control any occult disease, reduce the recurrence rate, and improve long-term survival (101). Neoadjuvant systemic therapy is used in early-stage breast cancer patients to increase the potential for BCS by downstaging the tumour, thus avoiding a mastectomy. It is also used as first line of treatment in patients with unresectable, locally advanced breast cancer to reduce the size of the tumour in order to enable surgery. However, this section focuses only on the established systematic treatments used in early breast cancer patients.

1.3.4.1 Chemotherapy

Adjuvant chemotherapy prolongs DFS and OS in patients with early breast cancer. A meta-analysis by the EBCTCG found that standard CMF (6 cycles of cyclophosphamide, methotrexate and 5-fluorouracil given 4 weekly) and standard 4AC (4 cycles of doxorubicin and cyclophosphamide given intravenous 3-weekly) were equally effective, providing a relative reduction in breast cancer mortality rate of 20 – 25% (102). Regimens with a significantly lower dose per cycle were found to be somewhat less effective, while by adding a taxane to 4AC or by giving a substantially greater dose of non-taxane chemotherapy (CAF and CEF), a further proportional reduction in breast cancer mortality of 15 – 20% could be obtained. The EBCTCG concluded that, on average, the use of polychemotherapy reduces breast cancer mortality by about a third. However, chemotherapeutic agents may cause significant short and long-term side effects including nausea, alopecia, myelosuppression, infertility and cardiotoxicity. Hence, the efficacy of using polychemotherapy regimens needs to be balanced against the effects of the associated toxicity on quality of life and survival (103).

Neoadjuvant chemotherapy (NAC) has been shown to be equally effective as adjuvant chemotherapy for early breast cancer in terms of OS (104). The main advantage of NAC over adjuvant chemotherapy is that it enables more patients to be treated with BCS, avoiding a mastectomy in approximately 25% of patients. An additional advantage is that it facilitates monitoring of tumour response, and in tumours that are not chemosensitive the treatment regimen can be altered, which could save patients from unnecessary toxic-side effects.

1.3.4.2 Endocrine therapy

Endocrine therapy aims to prevent the growth-stimulatory effects of oestrogen signalling in patients with ER+ breast cancer, either by blocking the ER or by reducing the production of oestrogen (64). Tamoxifen acts as an ER antagonist, thereby inhibiting the expression of many oestrogen-regulated genes required for tumour growth (105). Tamoxifen has been the standard treatment in ER+ breast cancer patients based on evidence from early-randomised controlled trials showing a significant prolongation of DFS in ER+ patients treated with tamoxifen (106,107). A meta-analysis performed by the EBCTCG in 2005 showed that 5 years of adjuvant tamoxifen compared to no tamoxifen in ER+ early stage breast cancer decreases breast cancer recurrence and breast cancer mortality by approximately 25% (101). This finding was largely irrespective of the use of chemotherapy, age or tumour characteristics. Although rare, severe toxicities from tamoxifen include an increased risk of endometrial cancer and thromboembolism; more common side effects include hot flushes and gynaecological complications (108).

Aromatase inhibitors (AIs) have emerged as the treatment of choice in postmenopausal ER+ breast cancer patients. AIs reduce the concentration of oestrogen by binding to the aromatase enzyme, thereby preventing the conversion of androgens to oestrogen. This hinders stimulation of ER+ tumour cells, especially in postmenopausal women where oestrogen is predominantly produced by the peripheral tissues. A recent meta-analysis comparing AI-based treatments with tamoxifen in postmenopausal women with ER+ early breast cancer showed that AIs significantly reduce recurrence rate, either as 5-year monotherapy, 2-year treatment followed by 3-years of tamoxifen, or after 2-3 years of tamoxifen (109). The pooled data from the three treatment regimens combined showed that AI-based treatments significantly reduced recurrence rates (30% proportional

reduction) and breast cancer mortality (15% proportional reduction) compared to tamoxifen alone. The use of AIs was associated with fewer endometrial cancers, but more bone fractures. Based on these findings current clinical guidelines recommend that AI-based therapy should be offered to postmenopausal women, especially those at high risk for breast cancer recurrence (110).

1.3.4.3 Biologically targeted therapy

HER2 is overexpressed in approximately 20 – 30% of patients and its overexpression is associated with a worse prognosis (64). Trastuzumab is a humanized monoclonal antibody targeting the extracellular subdomain IV of HER2, thereby reducing tumour growth through several molecular mechanisms (111). Studies have shown that 1-year of adjuvant trastuzumab and chemotherapy significantly improves DFS and OS compared to patients not receiving trastuzumab (112-114). Following these results, 1-year of trastuzumab in addition to adjuvant chemotherapy has become the standard of care for patients with HER2+ early-stage breast cancer. Although clinically beneficial, use of trastuzumab is associated with an increased risk of congestive heart failure (115), and close monitoring of cardiac function before and during the treatment period is therefore necessary (81,87).

In the neoadjuvant setting, studies have evaluated dual anti-HER2+ blockage therapies using trastuzumab in combination with lapatinib. Lapatinib is a small tyrosine kinase inhibitor that binds to the kinase region of EGFR and HER2. Dual blockage with lapatinib showed improved pathologic complete response (pCR) compared to one HER2+ agent (116); early results from the UK EPHOS-B trial even showed pCR in a quarter of patients within 11 days of therapy (117). However, the neoALTTO trial did not find a significant improvement in OS (118).

Dual blockage therapy with lapatinib and trastuzumab in the neoadjuvant setting is therefore based on the currently available evidence is not recommended (110).

1.4 Tumour resection margins

For over 20 years BCS has been the standard of care for treatment of early stage breast cancer patients, and several prospective randomised controlled trials have demonstrated that BCS and whole-breast EBRT is equivalent to mastectomy in terms of survival (Section 1.3.2.1). Obtaining clear resection margins is important in BCS as incomplete resection of the tumour is associated with an increased risk for LR, which could potentially impact on OS as approximately 1 in 4 breast cancer patients that develop a LR die from their disease (63). However, the definition of a clear tumour margin is still subject of debate. Defining the optimal margin width requires a balance between local control and acceptable cosmetic outcome, while minimizing re-excision rates, patient discomfort and treatment costs.

There is global consensus that patients with a positive histological margin after BCS, defined as tumour cells at the inked resection margin on postoperative analysis, should undergo further surgery (re-excision or mastectomy) to reduce the risk for LR associated with positive margins. Houssami *et al.* showed in a recent meta-analysis that for patients with early-stage invasive breast cancer treated with BCS and whole-breast EBRT the odds ratio for LR was 2.44 (95% confidence interval CI 1.97 – 3.03) for a positive margin compared with a negative margin of tumour cells >0 mm from the inked resection edge (90). The increased risk was not mitigated by favourable biology, delivery of systemic therapy (endocrine therapy, chemotherapy, biologic therapy) or radiation boost. A positive resection margin in patients with DCIS who had BCS and radiotherapy is also associated with an increased risk for LR. A meta-analysis by Wang *et al.* and Dunne

et al. found an odds ratio of 2.17 (95% CI 1.69 – 2.86) and 2.78 (95% CI 2.12 – 3.7) compared with negative margins, respectively (119,120).

To date there is no consensus on what constitutes an adequate negative margin, neither for invasive cancer nor for DCIS. The lack of consensus is reflected in the differences observed in the current (inter)national guidelines on tumour resection margins in BCS (Table 1). This controversy arises from a variety of factors. Firstly, the effect of margin width (e.g. 1 mm, 2 mm and 5 mm) on LR has never been studied in a single prospective randomised controlled trial. The available evidence to decide on the optimal margin width instead comes from meta-analyses, retrospective studies or expert opinions. This evidence is often based on data from patients treated before the year 2000, an era when surgical and radiotherapy treatments, and histopathological evaluation, were different from current standards. Obtaining prospective data on the relation between margin distance and LR is practically impossible as this study would require a very large number of patients and stringent quality control in terms of monitoring adjuvant treatment (extent/dose of radiotherapy and systemic therapy) in order to identify the true effect of margin distance on LR rate.

Table 1: Guidelines on negative margin width

Guideline	DCIS[5]	Invasive cancer
NCCN, 2016 (121)	≥1 mm	No tumour on ink
St. Gallen, 2015 (122)[4]	Not specified[1]	No tumour on ink
ABS, 2015 (123)[4]	≥1 mm	≥1 mm
SSO-ASTRO, 2014 (124)	Not specified[2]	No tumour on ink[3]
NICE, 2009 (81)	≥2 mm	Not specified

NCCN: National Comprehensive Cancer Network, ABS: Association of Breast Surgery, SSO-ASTRO: Society of Surgical Oncology – American Society for Radiation Oncology. NICE: National Institute for Health and Care Excellence

1. 80% of panellists felt that margins should be greater for pure DCIS than for invasive cancer, but no recommendation was made on the exact margin width
2. For patients with pure DCIS SSO-ASTRO recommends the guidelines set out by NCCN, i.e. ≥1 mm
3. This guideline does not apply to patients receiving neoadjuvant chemotherapy or APBI, or patients not receiving whole-breast EBRT
4. No details are provided on the type of radiotherapy or systemic therapy to which the guideline applies
5. There are no individual guidelines on margin width for pleomorphic LCIS due to lack of data. The DCIS guidelines therefore also apply to pleomorphic LCIS.

Secondly, the dilemma of margin evaluation is also a result of a lack of standardization in the histopathological assessment of tumour margins, and technical issues related to WLE specimen handling (both surgical and pathological). WLE specimens are generally serial sliced or sliced in a cruciate fashion (a method known as radial block examination); for both methods additional shave margins may be taken (Figure 1). The preferred technique depends amongst other factors on the type of tumour, the tumour size and location, the size of the WLE specimen and the pathologist's preference (8). All methods have in common that the margins assessed under the microscope only represent a fraction of the surface of the WLE specimen, and a calculation by Tucker *et al.* showed that the percentage of the WLE surface area available for microscopic evaluation ranges between <1% and 12% depending on the method used (125). Thus, a negative margin on one single slide is not representative for the margin status of the entire specimen. Besides, studies have shown that the

margin status and number of involved margins differ depending on the margin evaluation method used (126-128).
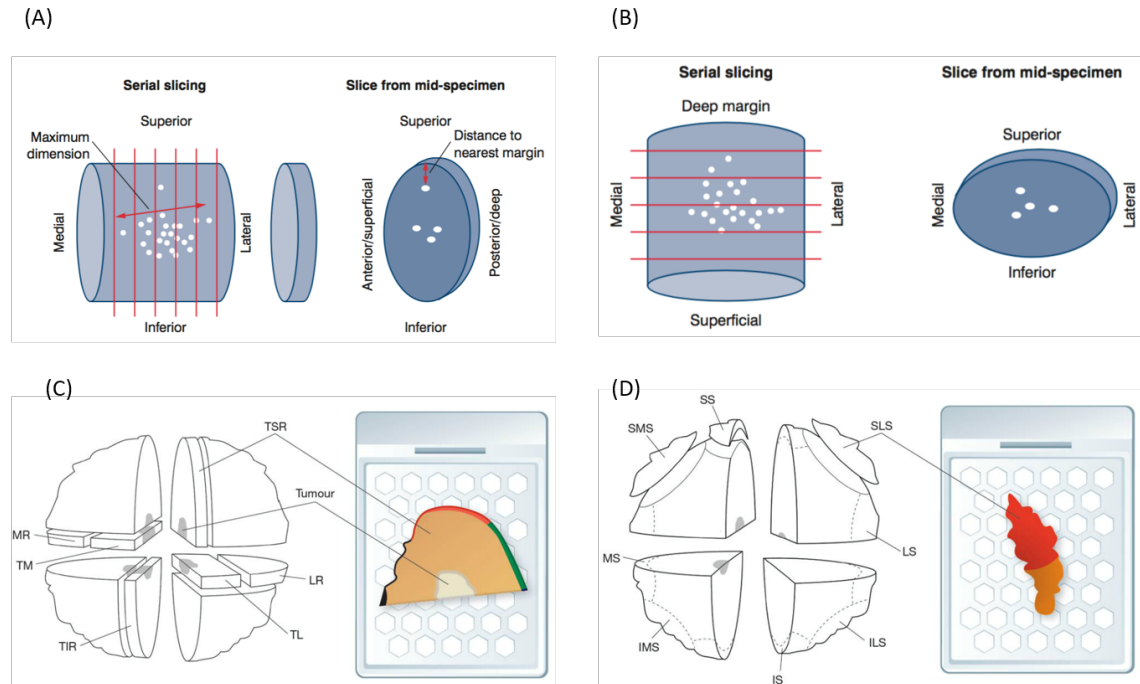
Figure 1: Histopathological techniques for assessing tumour margins of wide local excision specimens. Serial slicing in (A) the medial-lateral plane and (B) the superficial-deep plane. After serial slicing blocks are taken from suspicious areas, and examined for nearest margins and tumour size. (C) Radial block examination. The specimen is sampled as four blocks taken in the medial-lateral and superior-inferior direction, and the margin distance is then measured for each block. TSR = tumour superior radial; LR = lateral radial; TL = tumour lateral; TIR = tumour inferior radial; TM = tumour medial; MR = medial radial (D) Shaved margin examination. This technique is often performed in addition to serial slicing or radial block examination. SS = superior shave; SLS = superolateral shave; LS = lateral shave; ILS = inferolateral shave; IS = inferior shave; IMS = inferomedial shave; MS = medial shave; SMS = superomedial shave. *Image was reproduced from (8) with kind permission from the Royal College of Pathologists.*

Technical specimen handling issues include inaccuracies in microscopic margin evaluation due to a lack of clarity between surgeons and pathologists regarding WLE specimen orientation (129), deformation of the specimen post-excision which decreases the tumour-free margin distance (130,131), and margin assessment errors due to difficulties in correctly identifying the different ink colours used for orientation (132). All of the above factors potentially influence the accuracy of margin evaluation, and limit the ability to identify the optimal margin width from

comparing data on the association between margin distance and LR rates. Lastly, the lack of agreement in optimal margin width is due to differences in interpretation of the available data from the studies published to date. This obvious reason for disagreements in margin definitions is partially a consequence of the aforementioned two points, and the next section provides a clear example of how differences in data interpretation have affected current guidelines on tumour resection margins.

1.4.1 Views on optimal margin width for invasive cancer

A survey amongst breast cancer clinicians in the United Kingdom (133) and the United States (134) showed substantial variations in the definition of a negative margin for invasive cancer, ranging from >0 mm (called 'no tumour on ink', i.e. no tumour cells at the inked resection margin) to >5 mm. The pivotal study in the discussion on the optimal margin width in patients with invasive cancer is the meta-analysis by Houssami *et al.* (90). This study aimed to systematically examine the effect of margin width on LR. A total of 32,263 subjects from 33 studies were included; 31 of these studies were retrospective. Negative margins were grouped as tumour cells at >0 mm, 1 mm, 2 mm and 5 mm respectively, and ORs were calculated with the 1 mm group as referent. No statistical significant difference was found between margin width and LR rate (p = 0.12 for >0 mm versus 1 mm versus 2 mm versus 5 mm, and p = 0.90 for 1 mm, versus 2 mm versus 5 mm, respectively). This finding in combination with the excellent 10-year LR in the NSABP clinical trials that used narrow margin widths (135), and the difficulty for pathologists to reproducibly distinguish margin widths of >0 mm from 1 mm, formed the key arguments for the SSO-ASTRO panel to recommend 'no tumour on ink' as an acceptable margin width (124,136) (Table 1). However, opponents of the

SSO-ASTRO guideline argue that the meta-analysis shows that negative margins have a statistically significant lower risk of LR than close margins (OR = 0.57, p < 0.001), and although not statistically significant there is a trend in reduced LR rate with increased margin distance (OR 1 mm = 1, OR 2 mm = 0.91, OR 5 mm = 0.77, p = 0.9). Instead of evidence to support 'no tumour on ink' they state that the optimal margin width based on the results of the meta-analysis is 1 mm (137). This is in line with a recent study which also supported an optimal margin width of 1 mm for invasive disease (138).

The opponents of the 'no tumour on ink' margin definition also emphasise the weaknesses of the meta-analysis in terms of study design. The main points of critique include that instead of 'no tumour on ink' a margin of 1 mm was used as the referent to assess the relation between margin width and LR, and that the multivariate analysis did not correct for some important covariates associated with an increased risk for LR such as tumour stage and grade, HER2 receptor status, radiation dose and lymphovascular invasion (139). The former means that the data does not support any claims on the oncological safety of 'no tumour on ink'. To adequately investigate the safety of 'no tumour on ink' this would have required choosing a hazard ratio of 1 as the standard for 'no tumour on ink', but Houssami and colleagues state that this was not possible due to the small number of studies employing the 'no tumour on ink' definition and because the statistical modelling was constrained by the variability in negative margin definitions (140). The same paper also notes that whether a margin of 'no ink on tumour' is adequate for ILCs, TNBCs, patients of young age or with an extensive intraductal component could not be examined as this information was not provided in the majority of studies included in the analysis (140). Thus, no recommendations can be made on the optimum margin for patients with these characteristics. Another limitation of

the meta-analysis is that none of the 33 studies included for analysis had central pathology review of margin status. A central pathologist review in the NSABP-06 study only confirmed 'tumour on ink' in 31% of the WLE specimens that were assessed as such by the local histopathologist, indicating that inter-rater variability between pathologists can introduce inaccuracies in assessing the relation between margin width and LR (141).

In the last few years there have not been any papers published advocating the need for margins wider than 1 mm in patients with invasive disease, neither are wider margins recommended by the national, European or American guidelines used to date (Table 1). Thus, although the debate about the adequacy of 'no tumour on ink' and ≥1 mm in terms of oncological outcome is far from over, for now there seems to be agreement that surgical treatment in the form of a re-excision can safely be avoided for margins >1 mm in patients with invasive cancer treated with BCS and radiotherapy.

1.4.2 Views on optimal margin width for DCIS

To date there is also no consensus about what constitutes a negative resection margin in patients with DCIS, and the definition of a negative margin ranges from 'no tumour on ink' to more than a 10 mm free margin. A survey amongst 388 American surgeons with an interest in breast cancer performed in 2009 showed that 22% would accept a margin of 1 mm for DCIS; 52% a margin of 2 mm; 10% a margin of 5mm; and only 4% would accept a margin of 10 mm (142). 'No tumour on ink' was not included in the questionnaire. A recent survey amongst breast units in the United Kingdom found that 5 of the 76 units (6.6%) considered 'no tumour on ink' as an acceptable margin; 17 units (22.6%) accepted a 1 mm margin; 28 units (36.8%) used 2 mm; and in only 1 unit (1.3%) 5 mm was the

acceptable margin (143). Note that in both surveys the majority choose 2 mm as adequate margin; this is different from the ≥1 mm margin width recommended by the most recent NCCN and ABS guidelines (Table 1).

There are some major differences between DCIS and invasive cancer that play an important role in the discussion about an adequate margin of excision, including the clinical features, extent and spatial distribution of DCIS, and the fact that not all patients receive systemic adjuvant therapy and radiotherapy in routine practice. The majority of DCIS presents as clinically impalpable lesions, often with microcalcifications, which may be more extensive than determined preoperatively or intraoperatively (Section 1.3.1). An early study by Holland *et al.* reported that in approximately 30% of patients the mammographic size of DCIS was more than 2 cm smaller than the histological tumour size (144). The same group demonstrated that in approximately 27% of patients occult foci of DCIS can be found more than 2 cm away from the supposed margin (145). A negative margin for DCIS therefore does not mean the absence of residual unresected tumour in the breast; it is rather a surrogate marker for the likelihood and extensiveness of further residual disease. In contrast to patients with invasive cancer, DCIS patients generally do not receive systemic therapy after BCS and not all receive radiotherapy. Data from the National Cancer Data Base showed that in the United States approximately 30% of patients do not receive radiotherapy after BCS (146), while in the United Kingdom this is approximately 50% (147). Since studies have shown that systemic therapy and radiotherapy significantly reduce recurrence rates in breast cancer patients (Section 1.3.3), a wider margin of excision in patients not receiving systemic and/or radiotherapy may be required to reduce the risk for LR from residual unresected DCIS. The aforementioned differences make the definition of an adequate margin for DCIS even more complicated than for invasive disease.

The arguments and scientific evidence for the current guidelines on margin width for DCIS as shown in Table 1 is not well documented. As for invasive cancer there are no prospective studies conducted to assess the relation between margin width and LR. In order to get a better understanding of what could constitute an adequate margin of excision for DCIS patients treated with BCS and radiotherapy, the retrospective studies published data on the relation between LR and margin width are summarised in Table 2. All these studies show a statistically significantly higher LR for positive margins (tumour on ink) compared with margins >0 mm. Moreover, wider margins are associated with a lower number of recurrences. However, there is inconsistency between studies in terms of the optimal margin width. Solin *et al*. showed that margins >2 mm significantly improve local control compared with margins ≤2 mm (148) (Table 2). This is in line with the results from a more recent study (149). A meta-analysis by Dunne *et al*. showed that a 2 mm margin was superior to a margin <2 mm, and although the risk for LR further decreased for margins more than 5 mm, this improvement was not statistically significant (OR = 1.51, p > 0.05) (120). These studies thus seem to favour a margin width of 2 mm or more. However, this is contradicted by a recent study from Van Zee *et al.* (150), indicating that margins >0 mm are as good as larger margins in patients receiving radiotherapy.

Table 2: relation between margin width and recurrence rate in DCIS patients treated with BCS and radiotherapy

Study	Study design	Treatment period	Total no. of patients	Median follow- up period (months)	Total recurrence rate in % (N)	Margin width categories (mm)	Recurrence rate in %[5] (N)	P-value for recurrence rate per margin width
(148)	Multi centre	1973 – 1995	1003	60	10 (100/1003)	Tumour on ink	10.8 (9/83)	-[1]
						≤2	7.0 (11/158)	
						>2	4.0 (24/599)	
(151)	Single centre	1986 – 2000	103	63	13 (13/103)	Tumour on ink	31.3 (5/16)	-[2]
						<1	8.6 (3/35)	
						1 – 5	10.5 (2/19)	
						>5	4.3 (1/23)	
(150)	Single centre	1978 – 2010	1483	75	8.4 (124/1483)	Tumour on ink	10.3 (6/58)	-[3]
						≤2	10.1 (27/268)	
						2 – 10	7.1 (35/492)	
						> 10	8.4 (56/665)	
(152)	Multi centre	1972 – 1998	213	72	17.4 (37/213)	<1	28.8 (21/73)	-[4]
						1 – 10	15.0 (15/100)	
						≥10	2.5 (1/40)	

1. Margins ≥2 mm were associated with a statistically significantly lower local recurrence rate compared to <2 mm margins (p = 0.027) and no tumour on ink (p < 0.001)
2. A non-significant difference was found between no tumour on ink/<1 mm versus 1 – 5 mm margin and >5 mm margin (p = 0.28)
3. A non-significant difference was found between tumour on ink versus no tumour on ink (p = 0.67), ≤2 mm versus >2 mm (p = 0.96), and ≤10 mm versus > 10 mm (p = 0.70)
4. P-values for comparing the three margin width groups was not provided. However, the probability of recurrence within 8 year for <1 mm, 1 – 10 mm, and ≥10 mm was 0.30 ± 0.06, 0.12 ± 0.04, and 0.04 ± 0.04, respectively.
5. Recurrence rate for patients with an unknown margin status are not included in this column

Table 3: relation between margin width and recurrence rate in DCIS patients treated with BCS alone

Study	Study design	Treatment period	Total no. of patients	Median follow- up period (months)	Total recurrence rate in % (N)	Margin width categories (mm)	Recurrence rate in % (N)	P-value for recurrence rate per margin width
(153)[1]	Single centre	1999 – 2009	107	58	4 (4/107)	<10	23.1 (6/24)	<0.01
						≥10	1.5 (1/83)	
(154)	Single centre	1972 – 2004	445	57	18 (79/445)	Tumour on ink	46.9 (15/32)	-
						0.1 – 0.9	34.0 (18/53)	
						1.0 – 1.9	35.0 (7/20)	
						2.0 – 2.0	24.4 (20/82)	
						3.0 – 5.9	20.5 (8/39)	
						6.0 – 9.9	9.1 (2/22)	
						≥10	4.6 (9/197)	
(150)[2]	Single centre	1978 – 2010	1225	75	16 (201/1225)	Tumour on ink	25.0 (10/40)	-
						≤2	25.1 (42/167)	
						2 – 10	16.8 (62/369)	
						> 10	13.4 (87/649)	
(152)	Multi centre	1972 – 1998	256	72	14.8 (38/256)	<1	33.3 (13/39)	-[3]
						1 – 10	18.5 (23/124)	
						≥10	2.2 (2/93)	
(155)	Multi centre	1987 – 2004	222	55	8.6 (19/222)	<1	16.1 (5/31)	-[4]
						1 – 9.9	7.7 (5/65)	
						≥10	7.1 (9/126)	

1. Only patients with DCIS tumour size ≤1 mm were included.
2. No significant correlation between margin width and local recurrence was found for patients receiving radiotherapy (Table 2)
3. P-values for comparing the three margin width groups was not provided. However, the probability of recurrence within 8 year for <1 mm, 1 – 10 mm, and ≥10 mm was 0.58 ± 0.13, 0.20 ± 0.04, and 0.03 ± 0.02, respectively.
4. A trend towards an increased risk of local recurrence in cases <1 mm compared to ≥10 mm was found.

Table 3 shows the results from retrospective studies published on the relation between margin width and recurrence rate in DCIS patients treated with BCS alone. All studies included in the table show a decrease in LR when margin width increases. This finding is in line with the results from a network meta-analysis by Wang *et al.* using data from 7564 patients (119). They showed that margins ≥ 10 mm were associated with a reduced risk of LR compared to a 2 mm margin (OR = 0.43, 95% CI 0.27 to 0.67).

The data in Table 2 and Table 3, and the results from the meta-analysis by Wang *et al.* (119) and Dunne *et al.* (120), indicate that a ≥1 mm margin width for DCIS as recommended by ABS and NCCN may not be adequate for achieving optimal local control, especially for patients not receiving radiotherapy. However, there are multiple factors associated with recurrence in DCIS, including age, tumour size, type and grade, and possible multifocality, and these are important to consider when defining the optimal margin width (156). More importantly, data from clinical studies on the long-term efficacy of specific margin distances, obtained from DCIS patients treated with modern surgery and adjuvant therapy, is of utmost importance for making well-informed recommendations on the margin width required. This will help decide which patients may benefit from a re-operation to obtain wider margins, and in which patients a re-excision can safely be avoided. Regardless of the relation to margin width, the benefits of reduced LR should always be balanced against potential patient benefits and costs benefits associated with re-excision surgery.

1.4.3 Re-operation rates for invasive cancer and DCIS

To date a significant number of patients undergo a re-operation because tumour margins after the initial BCS procedure are deemed inadequate. Table 4 provides

an overview of the re-operation rates obtained from national population-based studies performed in the United States, United Kingdom, Canada and The Netherlands. This table shows that mean re-operation rates for invasive cancer with or without *in situ* disease range between 9.3 – 32.0%. For patients with pure DCIS Van der Heijden *et al.* found a mean re-excision rate of 28.5% (157); this corresponds with the findings from the UK Sloane Project showing a mean re-operation rate of 29% (158). Sole DCIS or DCIS in the presence of invasive disease is generally associated with a higher re-excision rate than invasive disease alone, which is partially due to the clinical and histopathological differences between DCIS and invasive cancer as described in Section 1.4.2. Some studies found a significantly higher rate of re-excision for lobular cancers compared to ductal cancers (157,159), which may be attributed to the diffuse growth pattern of lobular disease, although this difference was not demonstrated in the study by McCahill *et al.* (160).

Among patients that require a re-operation to the affected breast, approximately 40 – 50% in the United Kingdom and The Netherlands choose for a mastectomy (159,161). These patients thus initially opted for breast conservation as the preferred treatment option, but ended up having their breast completely removed. Of the patients that choose re-excision surgery, 7.4 – 12.5% required a second surgical intervention in the form of a re-reexcision or final mastectomy to completely clear their cancer (160-162).

Table 4: Multi centre studies performed after the year 2000 on re-operation rates in BCS

Study	No. of centres	Period	Total no. of patients	Mean re-operation rate in %		
				DCIS	Invasive	Invasive ± DCIS[1]
(157)	96	2008 – 2009	6250	28.5		9.3[2]
(161)	156	2005 – 2008	45793		18.0	29.5
(160)	4	2003 – 2008	2006			22.9[3]
(162)	-	2003 – 2013	87449			30.9[4]
(163)	26	2000 – 2002	489			26.2
(159)	16	2006 – 2007	1923			32.0[5]

1. Invasive cancers with or without ductal carcinoma in situ (DCIS). This group also includes patients with invasive lobular cancer
2. This is not the actual re-operation rate but the percentage of patients with an inadequate surgical margin that would have required re-excision surgery as per national protocol. Invasive lobular cancers had a statistically significant higher number of 'inadequate' margins than invasive ducal carcinomas (p<0.001)
3. No statistically significant difference was found in re-operation rate between patients with invasive ductal carcinoma and invasive lobular carcinoma (p = 0.17)
4. Re-operation rate decreased significantly from 39.5% in 2003 and 2004 to 23.1% in 2011 to 2013 (p < 0.001). Diagnosis of carcinoma *in situ* was associated with an increased risk of re-excision on multivariate analysis (odds ratio 1.57, 95% CI 1.49 – 1.65)
5. Re-operation rate was 36.4% for lobular cancers and 27.9% for ductal cancers. This difference was statistically significant (p = 0.01). Patients with lobular cancers were 54% more likely to undergo re-excision

Re-operations have a significant impact on patients and healthcare systems. They can potentially result in an increased rate of surgical complications (164), compromise cosmetic outcome (165), and increase anxiety and stress for patients and their families. Re-excision surgery also presents a high cost burden on the healthcare system. A recent study in the United States showed that the costs for a re-excision were \$4721 (£3654) per patient (166). These costs are likely to be even higher if the patient ends up having a mastectomy, and need to be multiplied for patients that require two or more re-operations to obtain clear margins.

The studies in Table 4 showed a large variation in re-excision percentages between centres (157,159,160), and individual surgeons (160,162,163). McCahill *et al.* demonstrated that one institution performed a second operation in only 1.7% of patients with negative margins (defined as 'no tumour on ink'), while this was 20.9% at another institution (p<0.001) (160). More importantly, 47.9% of patients had a re-operation for cancer found at 0 – 0.9 mm from the margin, 20.2% had margins 1.0 – 1.9 mm, and in 6.3% of cases margins were 2.0 – 2.9 mm. Another study found that approximately 40.0% of repeat operations was performed for margins <0.1 – 2.0 mm (167). These findings show that a significant number of re-excisions are performed for close but negative margins. This highlights the importance for obtaining consensus on the definition of an adequate excision margin as the current differences cause significant variations in clinical management, thus impacting on patient wellbeing and health economics.

In an attempt to decrease the re-operation rate several methods to facilitate more complete tumour excision at the time of the initial BCS procedure have been proposed. These include the use of routine cavity shavings, oncoplastic BCS techniques and techniques to intraoperatively assess tumour resection margins. Routine shavings and oncoplastic BCS will be briefly discussed in the next two

sections, while an extensive overview of the intraoperative margin assessment techniques and their potential for reducing re-operation rates is provided in Section 1.5

1.4.4 Routine cavity shavings

The main aim of performing routine cavity shavings (RCS) in addition to conventional BCS is to sample extra tissue from the four radial margins, with or without the anterior and posterior margin, to decrease the positive margin and re-operation rate. Routine shavings are different from selective shavings; the latter is standard practice in BCS as surgeons excise margins where the tumour is deemed to be close based on intraoperative imaging or gross evaluation. RCS has been introduced in the 1990s, but so far no meta-analysis or systematic review has been published on the oncological and/or cosmetic outcomes of this technique.

Table 5 shows the results from 2 important randomised controlled studies performed after 2000 comparing the positive margin rate of conventional BCS with RCS. These studies show that RCS can significantly reduce positive margin rates. Single centre, retrospective studies have reported similar findings (168-170). These results show the potential benefit of RCS in centres with a high rate of incomplete tumour excision with standard BCS. However, RCS is likely to be of limited value to institutions with a positive margin rate and/or re-excision rate of 20% or less with conventional BCS.

An important potential limitation of RCS is a reduced cosmetic outcome due to excision of a higher volume of breast tissue. Several studies have compared excision volumes between standard BCS and RCS, with contradictory results. Guidroz *et al.* (171) and Jones *et al.* (172) showed no significant difference in excision volume, while Chagpar *et al.* (173) and Huston *et al.* (170) found that the

total volume of tissue excised was significantly larger in the RCS group. The excised tissue volumes between these studies differed markedly for both the BCS and RCS group, highlighting the variation amongst surgeons and centres in surgical practice, and the need for randomised controlled multi centre studies and meta-analyses to robustly assess the impact of RCS on excision volume and cosmetic outcome.

Chagpar *et al.* recently performed a cost-analysis to assess the potential cost benefits of RCS compared to standard BCS (174). They found that although RCS significantly reduced re-excision rates (27.6% for BCS versus 10.9% for RCS, p < 0.01), direct hospital costs were higher due to increased operating room time ($1137 versus $1315, p = 0.03) and pathology costs from processing and analysing additional tissue slides ($795 versus $1195, p<0.01). Overall there was no significant difference in total costs between BCS and RCS ($11,219 versus $10,476, p = 0.40). This finding in combination with the limited improvement in re-operation rate in centres with a rate of 20% or less, questions the real benefit of RCS for patients and healthcare systems, especially now oncoplastic techniques are being used more often as described in the next section.

Table 5: Randomised controlled trials comparing positive margin rate of conventional BCS and BCS plus routine cavity shavings

Study	Study design	Period	Definition of negative margin	Total no. of patients	No. of patients with DCIS only	Positive margin rate BCS in % (N/N_{TOTAL})	Positive margin rate RCS in %[1] (N/N_{TOTAL})	P-value
(173)	Randomised controlled trial, single centre	2011 – 2013	Invasive: >0 mm DCIS: ≥1 mm	235	45	33.6 (39/116)	19.3 (23/119)	0.01
(172)	Randomised controlled trial, single centre	2009 – 2012	Invasive: >1 mm DCIS: >2 mm	75[2]	13	45.2 (14/31)	15.6 (7/45)	<0.01

1. RCS = routine cavity shavings
2. One patient had bilateral cancer. For both breasts BCS was performed, so the total number of breast specimens was 76

1.4.5 Oncoplastic breast-conserving surgery techniques

Oncoplastic BCS techniques have emerged over recent years as a further refinement of standard BCS. This type of surgery enables surgeons to excise a larger tissue volume with wider surgical margins, while minimizing potential deformities and maximizing cosmetic outcome by immediate reconstruction of the conserved breast at the time of initial surgery. Multiple oncoplastic BCS techniques have been introduced; the most appropriate technique depends amongst other factors on the volume of tissue to be excised and the location of the tumour (175).

De La Cruz *et al.* performed the largest comprehensive literature review to date on the oncologic outcomes of oncoplastic BCS (176). They included 55 studies and evaluated data from over 6000 patients. Studies with over 5-year follow-up showed excellent mean LR, DFS and OS rates of 6.0% (range 0 – 14.6%), 85.4% (range 59.6 – 100%) and 93.4% (range 82.9 – 100%), respectively. Although results varied amongst the studies included in the review, the vast majority of studies showed recurrence and survival rates comparable to patients undergoing conventional BCS. Oncological safety has also been confirmed in another review on oncoplastic BCS (177).

In the studies included by De La Cruz *et al.* mean positive margin rate and re-excision rate was low; 10.8% (range 0 – 39.7%) and 6.0% (range 0 – 26.7%), respectively (176). Positive margin rates were not significantly different for the different margin definitions used in the included studies (p = 0.162). A meta-analysis comparing standard BCS with oncoplastic BCS found significantly lower positive margin rates (21% versus 12%, p<0.001) and re-excision rates (14.6% versus 4%, p<0.001) for the oncoplastic technique (178). Importantly, cosmetic outcome has shown to be as good or better than with standard BCS (178,179).

Overall these studies indicate that oncoplastic breast conservation in patients with early-stage invasive breast cancer is a safe treatment option that potentially provides a low positive margin and re-excision rate, and good cosmetic outcome without compromising recurrence or survival. Large randomised controlled trials are needed to further evaluate the clinical and health-economical benefits of oncoplastic BCS versus conventional BCS.

1.5 Techniques for intraoperative assessment of tumour margins

Despite the limitations described in Section 1.4, the 'gold standard' for assessing tumour margin status to date is postoperative histopathological analysis. The results from histopathology typically become available within 5-7 working days after the initial BCS procedure, thus requiring patients with inadequate margin clearance to undergo a delayed second operation to obtain clear margins. Regardless of the type of surgical technique used, i.e. BCS alone, BCS plus routine cavity shavings, or oncoplastic BCS, accurate assessment of tumour resection margins intraoperatively would enable surgeons to excise additional breast tissue in the scenario of close margins at the time of initial surgery, thus potentially preventing the need for a re-operation.

There are several important criteria that should be considered when developing or evaluating intraoperative margin assessment technologies. Firstly, the time required to assess tumour resection margins should be within a time-window that is acceptable for providing surgical guidance during the BCS procedure. Ideally information on margin status is provided real-time, but in general 20 – 30 minutes is considered to be within acceptable limits. An important factor in determining the acceptable length of the procedure is the impact on re-excision rates; longer examination times may be feasible but only if it does not

affect quality of care and significantly reduces overall treatment costs. Secondly, high diagnostic performance in terms of accuracy, sensitivity and specificity is paramount. Of key importance in this is the ability to detect DCIS accurately, as this is one of the main causes of inadequate surgical excision in BCS to date. There are several factors that potentially affect diagnostic accuracy, including lateral resolution (the ability to distinguish two individual points in a plane parallel to the field of view), axial resolution (the ability to distinguish two individual points in a plane perpendicular to the field of view), and tissue sampling area. Intraoperative margin assessment techniques should have millimetric resolution to identify small tumour foci in (focally) positive margins, and to accurately detect tumour cells within a few millimetres of the tissue's surface. The tissue sampling area, i.e. the surface area of the tissue that can be assessed in one single measurement, is preferably large to prevent potential user errors and to facilitate rapid assessment of WLE specimens and/or surgical cavities. Thirdly, the technique needs to be safe for patients and clinical staff. This requirement is of special concern for techniques employing radioactivity including Cerenkov Luminescence imaging (CLI) (Chapter 3). Fourthly, the overall costs of the technology need to be relatively low to provide potential cost savings for the health care provider and the payer. Again, this ultimately depends on the impact of the technique on re-operation rate and quality of care. Lastly, wide clinical adoption requires the intraoperative margin assessment technique to be pragmatic and implementable in existing clinical workflows. Effort should be made to minimize the labour intensiveness of the technology, while avoiding complex logistics to maximize ease-of-use. Criteria that are of secondary importance are the applicability of the technology to other solid cancers that would benefit from intraoperative tumour margin assessment (e.g. prostate, colorectal and head and neck cancer), the ability to intraoperatively

assess lymph node status, and the dimensions of the equipment. Small sized equipment that can be used inside an operating theatre or in an adjacent room is preferred to enable short lines of communication between the surgical team and the operator of the equipment.

To date there are a number of techniques available to assess tumour resection margins intraoperatively, either in current clinical use, or in the research phase, and all these techniques aim to reduce re-operation rates. The next two sections provide a thorough overview of each individual technique and its pros and cons in light of the criteria mentioned above.

1.5.1.1 Clinically established techniques

The established techniques to assess tumour resection margins intraoperatively can be divided into imaging techniques providing information at a macroscopic level, and histopathological techniques that assess margins microscopically. Imaging techniques include intraoperative digital specimen radiography (IDSR) and intraoperative ultrasound guided resection (IOUS), while intraoperative histopathological techniques entail frozen section analysis (FSA) and imprint cytology (IC). Several reviews have been published describing these techniques (180-182). Very recently, St John *et al.* published a meta-analysis on the diagnostic performance of the established techniques for intraoperative margin assessment (183). The primary outcome measure of the study was diagnostic accuracy of each technique compared with gold-standard histopathology. Pooled sensitivity and specificity were calculated, as well as pooled positive and negative likelihood ratios, and diagnostic odd ratios. Secondary outcome measures included positive margin rate and re-operation rate. The results from this meta-analysis are shown

in Table 6. Results from additional papers not included in the meta-analysis are also shown.

Intraoperative digital specimen radiography

IDSR is used to acquire two-dimensional images from excised WLE specimens in the operating theatre. Prior to imaging, metal surgical clips are applied to the specimen to enable anatomical orientation on the x-ray image. Image acquisition takes less than 5 seconds per image, and by rotating the specimen in between images multiple views can be obtained to assess the adequacy of excision. The meta-analysis from St John *et al.* included 9 IDSR studies containing data from 715 patients (183). Six studies were retrospective and 3 studies were prospective. Pooled sensitivity was 53% (95% CI 45 – 61%); pooled specificity was 84% (95% CI 77 – 89%) (Table 6). Pooled positive and negative likelihood ratio was 3.3 (95% CI 2.1 – 5.0) and 0.56 (95% CI 0.46 – 0.69), respectively. Heterogeneity between studies was low and not significant (I^2 0%, Cochran Q 0.188), indicating that there was consistency between studies in terms of study design and diagnostic accuracy of IDSR. Positive margin rate and re-excision rates in the studies included in the analysis ranged between 7.0 – 42.0% and 5.0 – 37.1%, respectively. Bathla *et al.* and Kaufmann *et al.* demonstrated that use of IDSR resulted in an absolute reduction in positive margin rate of 22.6% and 8.0%, respectively (184,185). Despite its potential for reducing re-operation rates, an important limitation of IDSR is that *in situ* cancers are only detected if microcalcifications are present, which is one of the explanations for the suboptimal sensitivity in Table 6. Other limitations include the potential to overestimate the margin distance due to underestimation of the tumour size on the radiography image, unreliable specimen orientation if surgical marker clips are missing or positioned wrongly, and

inaccurate margin assessment in specimens with irregular margins due to spiculated lesions and opacities (186). These limitations all impact on the diagnostic performance of IDSR.

Intraoperative ultrasound guided resection

IOUS is a method of excising a tumour under direct visualisation, thus providing the surgeon with real-time information of the tumour extent. Prior to excision the US probe is directed over the lesion to define every margin of excision, and immediately post-excision *ex vivo* US examination of the WLE specimen is performed to confirm the tumour has been completely excised with a sufficient margin. IOUS can also be used to assess the post-excision surgical cavity.

In the 4 studies included in the meta-analysis of St John *et al.,* pooled sensitivity, specificity, positive likelihood ratio and negative likelihood ratio were 59% (95% CI 36 – 79%), 81% (95% CI 66 – 91%), 3.2 (95% CI 2.0 – 5.2) and 0.5 (95% CI 0.32 – 0.80), respectively (183) (Table 6). These results are comparable to IDSR. However, due to the small number of studies and the significant heterogeneity between studies (I^2 96%, Cochran Q 41.3), which amongst other factors was a result of inconsistencies in diagnostic accuracy between studies, caution should be taken when interpreting these findings. Studies reporting on positive margin and re-excision rate show values ranging between 3.1 – 34.4 and 2.0 – 20.8%, respectively (183) (Table 6). The highest rates were found in patients with pure DCIS, indicating the challenge of accurate identification of microcalcifications on sonography (187). A meta-analysis by Ahmed *et al.* comparing IOUS-guided surgery with WGL surgery in patients with non-palpable breast cancer demonstrated a statistically significantly lower positive margin rate for IOUS, while no difference in resection volume was found (188)**.** An advantage

of IOUS over other localisation techniques used for non-palpable breast cancer, i.e. WGL, ROLL and RSL, is that the need for preoperative localisation can be avoided. This prevents potential scheduling issues on the day of surgery between the radiology department and/or nuclear medicine department, and the surgery unit (67). IOUS-guided surgery has been shown not to extend tumour excision time compared to palpation-guided excision (14 min versus 15 min, p = 0.38), indicating that the technique is time-efficient (189). Besides, a recent study comparing IOUS and palpation-guided BCS found an improved cosmetic outcome and patient satisfaction for the IOUS group (190). Although these results clearly indicate the potential of IOUS for significantly improving quality of care in BCS, especially since US probes are widely available in centres worldwide, widespread implementation of this technique has been limited by the inability of surgeons to acquire formal training by a senior breast radiologist that is required for obtaining accreditation in breast ultrasonography (67). This is partially due to the lack of breast ultrasonography courses offered by the national societies of breast surgery, but the initial resistance from the radiology community to train surgeons in the adequate use of this technique is also likely to play a role. Sufficient training is essential as successful application of IOUS has a learning curve (191), and the inconsistencies in diagnostic accuracy between studies included in the meta-analysis of St John *et al.* could be due to differences in diagnostic performance between operators. Another limitation includes the relatively low resolution of US, challenging accurate detection of small (non-palpable) tumours, which could result in unnecessary excision of close margins due to false-positive findings (67).

Frozen Section Analysis

FSA for intraoperative margin assessment is used in several solid cancer types, including colorectal, gastric, prostate and breast cancer, and this technique has not undergone significant changes since its introduction in the 1990s. In breast cancer, the excised WLE specimen is oriented with sutures and/or surgical clips as per local protocol, the margins are inked, and the specimen is then thinly sliced and inspected. Sections from suspected tissue areas (e.g. macroscopically suspect lesion, palpable lesion or microcalcifications seen on preoperative mammography) are then frozen, cut, stained and analysed microscopically to evaluate the closest margin of resection. The microscopic margin status on FSA is then reported back to the surgeon, and any re-excised margins may also be submitted for FSA.

St John *et al.* assessed the diagnostic accuracy of FSA using data from 9 studies. Pooled sensitivity and specificity were 86% (95% CI 78 – 91%) and 96% (95% CI 92 – 98%), respectively (183) (Table 6). Pooled positive likelihood ratio and negative likelihood ratio were 21.6 (95% CI 10.4 – 44.8) and 0.15 (95% CI 0.09 – 0.23), respectively. Thus, diagnostic performance of FSA seems substantially better than IDSR or IOUS, but one should note that heterogeneity between the 9 included studies was high (I^2 97%, Cochran Q 58.24). An earlier systematic review comparing conventional postoperative histopathology, FSA and IC also found a high diagnostic performance for FSA; pooled mean and standard deviation for sensitivity and specificity was 83 ± 13% (range 58.1 – 100%) and 95 ± 8% (range 77.8 – 100%), respectively (192) (Table 6). The authors of the systematic review also calculated pooled mean and standard deviation for re-excision rate. This was 10 ± 6% (range 0 – 41.6%) for FSA; significantly lower compared to the 35 ± 3% reported for conventional histopathology (p<0.0001). Two single centre studies showed higher false-negative findings in patients with DCIS, small non-palpable

tumours and post-neoadjuvant therapy, indicating that diagnostic performance may be lower in this group of patients (193,194). As with conventional postoperative histopathology, FSA only assesses a small amount of tissue from the WLE specimen, thus potentially missing involved tumour margins in tissue that is not analysed microscopically. Moreover, FSA requires a relatively large part of the specimen, which may compromise postoperative histopathological evaluation. Besides, FSA requires significant human resources and the expertise of an on-site histopathologist, which is not always readily available. Another important concern when using FSA is the time required to perform the procedure; Esbona *et al.* reported a mean duration of 27 minutes with a maximum of 53 minutes in a study that did total circumference sampling of the WLE specimen (192). This could increase surgery time, ultimately reducing the number of operations that can be performed per day, and may affect quality of care as more and longer anaesthesia is required. Osborn *et al.* performed a cost-effectiveness analysis and found that FSA is only cost-effective for institutions with a re-excision rate of more than 36% (195). Due to these limitations FSA is not used widely; a recent study by Harness *et al.* amongst SSO-ASTRO panellists showed that only 5% of the panel members used FSA in their institution (134).

Imprint cytology

IC has been proposed as a simple and more rapid alternative to FSA. The excised WLE specimen is oriented and pressed onto specifically coated glass slides to make an imprint of all 6 tumour resection margins. The principle is based on the difference in cellular surface characteristics; malignant cells show less cohesion and are therefore more likely to adhere to the slides than benign cells. Slides are then air-dried, stained, and analysed microscopically by a cytopathologist. By

analysing a larger tissue surface area, sampling errors inherent to FSA are less likely to occur. Moreover, IC preserves the WLE specimen and its tumour-tissue relationships, thus minimising the risk of compromising postoperative histopathology. However, with IC only superficial tumour cells are detected, and information on the margin width (i.e. distance from tumour cells to the specimen edge) and focality (i.e. quantity of cancerous cells approaching the cut edge) cannot be obtained.

St John *et al.* included 1129 patients from 11 IC studies in their meta-analysis (183). They found a diagnostic accuracy comparable to FSA. Pooled sensitivity, specificity, positive likelihood ratio and negative likelihood ratio of 91% (95% IC 71 – 97%), 95% (95% IC 90 – 98%), 18.9 (95% CI 9.2 – 38.9) and 0.10 (95% CI 0.03 – 0.34), respectively (Table 6). These results were slightly better than the findings reported in an earlier systematic review by Esbona *et al.* (192) (Table 6); they found a pooled mean and standard deviation for sensitivity and specificity of 72 ± 38% (range 8.3 – 99%) and 97 ± 3% (range 92 – 100%), respectively. There was no statistically significant difference in sensitivity and specificity between IC and FSA (p = 0.53 and p = 0.58, respectively), but IC took considerably less time (mean 13 min versus 27 min). Pooled mean re-excision rate was 11 ± 4% (range 0 – 33%); significantly lower than the 35 ± 3% for standard postoperative histopathology (p = 0.001). In both the study by St John *et al.* (183) and Esbona *et al.* (192) large variations were found for sensitivity, indicating that substantial differences in diagnostic performance between institutions and operators may be present. Cox *et al.* demonstrated the applicability of IC for patients with pure DCIS; a positive margin rate of only 6.8% was observed in the 104 patients included in the study (196). A small study by Valdes *et al.* in 12 patients with invasive lobular carcinoma found a high number of false-negatives,

resulting in a sensitivity and specificity of 8.3% and 98.3% respectively (197). The authors explain that due to individual tumour cells embedded in fibrous stroma, and numerous microscopic satellite foci often observed in lobular cancers, false-negative findings are more likely, thus questioning the value of IC in invasive lobular disease. Important pitfalls of the technique include errors in interpretation based on specimen surface irregularity, cauterization, dryness, or over-interpretation of atypical cells (198,199). Besides, successful implementation of the technique requires cytopathology training and certification. Current work focuses on developing automated analysis tools for interpreting IC slides, which could potentially reduce the workload of the cytopathologist and the costs associated with IC (199). However, whether this will help increase the small number of centres that currently use IC for margin assessment in breast cancer, 2% based on an SSO-ASTRO audience poll by Harness *et al.,* remains to be seen (134).

Table 6: Diagnostic performance of clinically established techniques for intraoperative tumour margin assessment

Technique	Study	Study design	No. of patients[1]	No. of patients with pure DCIS	Sens (%)	Spec (%)	Positive margin rate in % (% absolute reduction)	Re-excision rate in % (% absolute reduction)	Limitations
Specimen radiography	(183)	Meta-analysis	715	-[3]	53.0	84.0	-	-	Detection of *in situ* disease;
	(185)	Cohort, prospective, single centre	121	29	36.0	71.0	20.0 (8.0)	-	Underestimation of tumour size/overestimation of margin distance; Accurate image interpretation challenging
Imprint cytology	(183)	Meta-analysis	1129	-	91.0	95.0	-	-	Labour intensive;
	(192)	Systematic review	2296	-[4]	72.0	97.0	-	11.0	Interpretation of IC slides prone to errors; No information on margin width and/or focality
Ultrasound	(183)	Meta-analysis	482	-	59.0	81.0	-	-	Diagnostic accuracy operator dependent;
	(189)	Randomised controlled trial, multi centre	134	0	-	-	3.1 (14.3)	2.0	Limited training opportunities;
	(200)[2]	Case-control, retrospective, single centre	155	155	-	-	34.4	20.8 (9.7)	Suboptimal resolution especially for systems with centre frequency below 10MHz

Technique	Study	Study design	No. of patients	No. of patients with pure DCIS	Sens (%)	Spec (%)	Positive margin rate in % (% absolute reduction)	Re-excision rate in % (% absolute reduction)	Limitations
Frozen section analysis	(183)	Meta-analysis	1979	-	86.0	96.0	-	-	Lengthy (~30 min);
	(192)	Systematic review	3675	-5	83.0	95.0	-	10.0	Labour intensive; Small percentage of total WLE specimen analysed

1. In studies that only reported the number of specimens it was assumed that each patient only had one specimen scanned
2. Only patients with pure DCIS were included
3. The meta-analysis from St John *et al.* included studies that contained patients with invasive disease with or without DCIS, as well as pure DCIS. A breakdown of the diagnostic accuracy per tumour type is not provided
4. Exact number of DCIS patients is not specified but in 4 out of the 8 studies DCIS was present in the dataset
5. Exact number of DCIS patients is not specified but in 11 out of the 15 studies DCIS was present in the dataset

1.5.1.2 Novel investigational techniques

To address the limitations of the established techniques available for intraoperative assessment of tumour margins, several novel techniques have been developed in the last two decades. These include the MarginProbe, diffuse reflectance spectroscopy (DRS), optical coherence tomography (OCT), Raman spectroscopy (RS), near-infrared fluorescence imaging (NIRF) and the intelligent knife (iKnife). An explanation of each technique and the results published to date in breast cancer is provided below. Other techniques that may be promising for assessing tumour margins in the near future include photoacoustic imaging and the ClearEdge. These techniques are still in an earlier stage of development and therefore will only be discussed briefly. Note that apart from the MarginProbe all published results on investigational techniques for intraoperative margin assessment come from observational studies; no reports have been published yet on the use of these techniques to guide surgical excision and assess the impact on positive margin and re-excision rate (Table 7).

MarginProbe

The MarginProbe (Dune Medical, Caesarea, Israel) uses radiofrequency spectroscopy to detect minute differences in electromagnetic properties between benign and malignant breast tissue. The device consists of a console and a detachable, single-use, sterile handheld probe with an effective measurement area of 7mm and a detection depth of about 1 mm (201). The small sampling area makes the MarginProbe prone to user errors as focally positive margins may be missed. Each measurement takes approximately 1 to 5 seconds to complete, and results are displayed on the display of the console as a 'positive' or 'negative' read-out. Most studies report that a maximum of 8 measurements per margin were

performed; total imaging time is therefore less than 5 minutes. In 2012 the device received Federal Drug Administration approval as a diagnostic tool to aid tumour margin evaluation in BCS.

Two randomised controlled trials and three prospective cohort studies have evaluated the performance of the MarginProbe, with mixed results. Sensitivity and specificity for detecting breast cancer ranged from 70.0 – 75.2% and 46.4 – 70.0% (Table 7). Pappo *et al.* reported that the diagnostic accuracy was affected by tissue heterogeneity; lower sensitivities and specificities were found for tissue containing less than 50% of a single tissue type, indicating that the device is less sensitive for detecting small tumour foci (202). They also found a lower detection rate for pure DCIS compared to invasive cancer (63% versus 70%, respectively).

The two randomised controlled trials by Schnabel *et al.* (203) and Allweis *et al.* (204) both showed a reduction in re-excision rate in the MarginProbe arm compared to the control arm (19.8% versus 25.8% and 5.6% versus 12.7%, respectively), although in the trial by Allweis *et al.* this difference was not statistically significant (p = 0.098). The MarginProbe may also facilitate more complete tumour excision in patients with non-palpable DCIS; Thill *et al.* found a re-excision rate of 18.0% when the MarginProbe was used compared to a historical re-excision rate of 38.8% (205). However, the real benefits of the MarginProbe in this patient population remains to be determined, as large randomised studies have not yet been performed for patients with pure DCIS. Another potential downside related to the use of the MarginProbe is an increase in tissue volume excised as shown in both randomised controlled trials (204,206). This may impact on cosmetic outcome and overall patient satisfaction.

Diffuse reflectance spectroscopy

DRS as a tool for margin assessment in BCS was first described in 2000 by Biglio *et al.* (207)*.* By illuminating tissue with light in the visible or near-infrared (NIR) wavelength range, diffuse reflectance spectra can be obtained that provide information on the intrinsic light absorption and scattering properties of breast tissue (208). In the visible – NIR range the primary absorbers in the breast include β-carotene, oxygenated and deoxygenated haemoglobin, while the primary scatterers are cells and nuclei. Since changes in human tissue associated with malignant transformation include alterations in cellular composition and morphology, vascularization, and metabolic rate, diffuse reflectance spectra can be used as an intrinsic contrast to differentiate malignant from benign tissue. Depending on the wavelength and tissue optical properties DRS has a sensing depth of 0.5 – 8.0 mm (209).

Table 7 shows that sensitivity and specificity ranges between 67 – 85% and 67 – 96%, respectively. The highest sensitivity and specificity of 85% and 96% reported by Keller *et al.* was obtained by combining DRS with autofluorescence imaging, indicating that a multimodal imaging approach may provide superior results (210). Apart from Laughney *et al.* all studies in Table 7 used a fiberoptic DRS probe to acquire reflectance spectra from tumour margins. An important limitation of these probes is their small sampling area, which affects the acquisition time and increases the likelihood for sampling errors as with conventional histopathology. Brown *et al.* reported that the time required to scan a single resection margin was 20 – 25 minutes, which is far too long for use in a surgical setting (211). In an effort to increase the sampling area, and consequently decrease acquisition times, planar fibreless DRS systems have been developed (209,212). These systems enable non-contact tissue imaging with a substantially

larger field of view (FOV). Laughney *et al.* were able to image an area of approximately 14x20 cm with an acquisition matrix of 696x520 pixels to give a pixel resolution of 201x366 microns (209). However, as with all optical imaging technologies, the detected spatial resolution is limited by the physics of light transport in tissue, so the practical resolution is lower. While these developments enable shorter acquisition times, improvements in data processing for near-real time diagnostic feedback are required to facilitate implementation of DRS into an intraoperative setting. Another factor that may challenge *in vivo* DRS is alteration of the reflectance spectra from absorption of (visible) light by blood and coloured dyes, including the blue dye used in patients undergoing SLNB. Future studies in which DRS is used to guide surgical decision-making will determine the true potential of DRS for reducing positive margin and re-excision rate.

Optical coherence tomography

OCT has emerged as a high-resolution optical diagnostic imaging modality that is being used in ophthalmology, gastroenterology, cardiology, gynaecology, neurology and dermatology (213). More recently, OCT has been investigated as a technique to assess breast tumour margins. OCT is the optical equivalent to ultrasound, but instead of acoustic waves it is based on the reflection of light from a NIR light source. By measuring the reflected light, cross-sectional tomographic images of the tissue microstructure can be obtained with a micron-scale resolution similar to histopathology, and a penetration depth between 200 μm and 2 mm depending on the tissue composition (214). The contrast observed on OCT images reflects the spatial variations in index of refraction within the tissue, and the ability to differentiate between benign and malignant breast tissue is amongst other factors due to the increase in nuclear-to-cytoplasm ratio and the increase in

cellular and nuclear density associated with oncogenesis (214). As with DRS, OCT does not require physical disruption, processing, sectioning or staining of the tissue, nor is there a need for an exogenous contrast agent.

Studies performed to date show a sensitivity of 60.0 – 100% and specificity of 69.0 – 92.1% (Table 7). Zysk *et al.* (215) and Erickson-Bhatt *et al.* (216) both used a handheld OCT imaging probe, while Nguyen *et al.* employed an OCT system that did not require tissue contact (214). Variants of conventional OCT systems based on optical coherence microelastography (217) and polarization-sensitive OCT (218) are currently being developed, aiming to further improve the contrast between benign and malignant breast tissue. Important strengths of OCT over some other technologies is the ability for *in vivo* assessment of the resection bed (216), and its potential for intraoperative lymph node assessment (219). Wide-field OCT systems may be able to overcome the current limitation of a small sampling area, but reports published to date have not yet evaluated the diagnostic performance of such systems (220). Moreover, due to the high volume of images acquired with OCT, advances in automated tissue type classification are needed to speed up image interpretation and reduce labour-intensity (221). Future interventional studies should not only assess the impact of OCT on oncological outcomes, but also the effect on cosmesis as OCT may increase the volume of tissue excised due to false-positive findings (215).

Raman spectroscopy

Raman scattering is the inelastic scattering of photons upon interaction with molecules. The change in photon energy level as a result of inelastic scattering depends on the vibrational energy of the molecule involved, and thus Raman spectra contain information on a molecular level that can be used to detect

changes in cells and tissues (222).   Inelastic scattering is relatively rare, i.e. approximately 1 in 10 million scatter events are inelastic, and RS is therefore much less efficient than other optical techniques including DRS and OCT that predominantly depend on elastic scattering. Hence, obtaining a sufficient signal-to-noise ratio in a time-window that is acceptable for intraoperative use is challenging, and RS may require strict control of the light environment (for example by using a light tight box) to reduce 'noise' from ambient light sources (223). Similar to TPI as explained in Chapter 2, the use of RS for tissue diagnosis requires developing a classification model based on a 'training' dataset. These models use mathematic algorithms to identify unique fingerprints in the Raman spectra, and are then applied to data from prospective measurements to predict the type of tissue. In order for RS to provide optimal diagnostic accuracy in a wide patient population, the training dataset should contain data from as many patients and tumour types as possible. The same is true for TPI. Acquiring such a large-scale dataset is a time-consuming and potentially costly endeavour due to the heterogenetic nature of breast cancer. In a study by Haka *et al.,* Raman spectra from specimens containing pure DCIS were excluded from analysis as this pathology was not included in the training dataset used for diagnostic algorithm development (223).

Deng *et al.* recently published a meta-analysis on the diagnostic performance of RS for discriminating benign from malignant breast tissue (224) (Table 7)**.** A total of 7 studies were included; all these studies were done in an *ex vivo* setting by applying RS to excised tissue specimens. 4 studies used fresh tissue specimens, while 3 studies used frozen-thawed tissue. All studies compared RS to gold standard histopathology. Pooled sensitivity was 92% (95% CI 86 – 96%); pooled specificity was 97% (95% CI 93 – 98%). Subgroup analysis showed that the

diagnostic performance of RS was higher in studies that acquired more than 200 Raman spectra for tissue classification compared with studies using less than 200 spectra, indicating that longer acquisition times per measurement may be required for optimal discriminative power. Interestingly, studies using frozen tissue had a significantly higher sensitivity and specificity than studies using fresh tissue, which is likely due to changes in optical properties as a result of freezing (225). Based on these findings one might question the value of using frozen-thawed specimens to evaluate technologies intended for intraoperative use on fresh non-processed specimens.

Proof-of-principle for using RS to scan the post-excision surgical cavity has been provided by Haka *et al.* (226). Although their dataset only contained 1 spectrum from a histologically positive margin, the overall accuracy of the diagnostic algorithm was 93.3%, thus showing the potential for *in vivo* RS. RS has also been successfully used for *ex vivo* assessment of axillary lymph node status (227). In order for RS to provide near real-time diagnostic information, ongoing developments focus on ways to decrease image acquisition times. An interesting development is the use of multi-model imaging by integrating fluorescence and Raman spectroscopy. This approach is currently being evaluated in a pre-clinical setting (228,229). Other groups are exploring the use of exogenous nanoparticles to increase RS signal intensity (222), but such contrast agents require stringent regulatory approval before being used in a clinical setting, and thus provide a less attractive option for fast translation of RS from bench to bedside.

Near-infrared fluorescence imaging

In NIRF a fluorophore is administered systemically or locally in the tumour, after which the target area is irradiated by an external laser that emits light in the NIR

wavelength range (700 – 900 nm). Upon excitation, the fluorophore will release photons of a higher NIR wavelength, which are captured by an NIRF camera system and digitally converted into an image of the tumour site in real time. Several excellent reviews have been published recently describing NIRF for image-guided surgery, including its use for NIRF-guided SLNB (230-232).

The last years have seen great advances in the development of NIRF camera systems and NIRF probes (232,233). Probes can broadly be divided into non-targeted probes, targeted probes which target enzymes and receptors that are upregulated in cancer cells, and targeted probes that exploit the catalytic activity of a target to generate an imaging signal. The latter two are of most interest for NIRF-guided resection, as these tracers have the potential to provide the surgeon with tumour-specific molecular information on the location and extent of the lesion. However, progression to the clinic has so far been limited primarily because the development of clinical-grade contrast agents is expensive and time-intensive with regards to risk regulatory aspects, and substantial delays have often been encountered because of IP issues or fear of litigation (234,235). As a result of this, there are to date no tumour-targeted fluorescent tracers that have Food and Drug Administration (FDA) or European Medical Agency (EMA) approval (236), and all the published studies to date on NIRF for image-guided surgery in breast cancer have been pre-clinical (231,232). Phase I/II clinical studies in breast cancer are now also underway, assessing the safety and feasibility of a protease-activated tracer (NCT02391194), and tracers targeting VEGF (NCT01508572), c-MET (EudraCT number 2014-003554-13), and cathepsins (NCT01626066 and NCT02438358). Results from the cathepsin-targeted tracer, LUM015, were recently presented at the Annual Meeting of the American Association for Cancer Research (237). LUM015 did not demonstrate any adverse pharmacological

activity, and was selectively taken up in tumours, resulting in a mean tumour to normal fluorescence ratio of 5.4. The increased tumour fluorescence was significantly higher than normal tissue fluorescence (p<0.0001). Results from the other clinical studies are eagerly awaited to obtain further insight in the feasibility of NIRF imaging as a tool to improve the accuracy of tumour excision in patients undergoing BCS.

iKnife

The iKnive detects cancer by using rapid evaporative ionisation mass spectroscopy (REIMS) to analyse the smoke from evaporating tissue during surgical resection. This system consists of a commercially available electrosurgical pencil that has been slightly modified to transfer the aerosol to a distant mass spectrometer, which provides audio-visual information on tissue diagnosis within 0.7 – 2.5 seconds. As with DRS, RS and TPI, tissue classification with the iKnive requires training of a classification algorithm to recognise the features in the mass spectra that can then be used to differentiate benign from malignant tissue. This demands a large-scale database with data from a wide variety of tumour sub-types to account for potential differences in spectra due to tissue heterogeneity.

In 2013 Balog *et al.* published results on the diagnostic performance of the iKnive to discriminate malignant from benign tissue (238) (Table 7). The breast training dataset contained data from a total of 16 patients; 10 invasive lobular carcinomas, 4 invasive ductal carcinomas and 2 adenomas. Classification was performed on only 2 breast cancer patients, both with invasive lobular carcinomas, and showed a sensitivity and specificity of 100%. Differentiation of malignant from benign breast tissue was predominantly based on differences in the composition of membrane phospholipids. More recently a conference abstract was published,

showing a sensitivity and specificity of 93.0% and 91.9% respectively on a dataset containing spectra from 89 excised breast specimens from 66 patients (239) (Table 7). Their dataset did not contain DCIS, so the ability of the iKnife to accurately detect DCIS is yet to be determined. Practical limitations of the technology include the limited speed of surgical resection (~1mm/s) to obtain sufficient mass spectroscopic information, and the need to cauterise tissue in order to establish the tissue diagnosis.

Other techniques

Photoacoustic imaging combines optical imaging with US. Tissue is illuminated with a short-pulsed light beam, and absorption of the optical photons causes tissue to expand, which generates a characteristic sound wave that is detected by an US transducer to form an image. This image represents a spatial map of optical absorption from endogenous absorbers (e.g. haemoglobin, melanin and water), or exogenous contrast agents such as dyes or nanoparticles (240). Pre-clinical studies have shown the ability of photoacoustic imaging to accurately image tumours and assess the completeness of tumour resection (241-243), but clinical results have not yet emerged in literature.

The ClearEdge is a battery operated hand-held device equipped with a sterile single-use probe that images an area of 13x13 mm. The device discriminates benign from malignant breast tissue using bio-impedance spectroscopy. A recent paper assessed the diagnostic performance of this device on 335 margins from 58 patients (244) (Table 7). Sensitivity and specificity was 87.3% and 75.6%, respectively. In the 49 patients where margin excision was guided by the readings of the device, re-operation rate was 8%, compared to a re-

excision rate of 37% if the device would not have been used. These results are promising, and data from larger studies is eagerly awaited.

Table 7: Diagnostic performance of investigational techniques for intraoperative tumour margin assessment

Technique	Study	Study design	No. of patients	No. of patients with pure DCIS	Sensitivity (%)	Specificity (%)	Limitations
MarginProbe	(203)	Randomised controlled trial, multi centre	596	161	75.2	46.4	
	(204)	Randomised controlled trial, multi centre	293	20	-[1]	-[1]	Suboptimal sensitivity and specificity; Accurate detection of DCIS challenging; Potential for increased excision volume; Small sampling area
	(202)	Cohort, prospective, multi centre	76	16	70.0	70.0	
	(245)	Cohort, prospective, multi centre	57		71.0	68.0	
Diffuse reflectance spectroscopy	(246)	Cohort, prospective, single centre	48	3	79.0	67.0	
	(210)	Cohort, prospective, single centre	28	-	85.0	96.0	

Technique	Study	Study design	No. of patients	No. of patients with pure DCIS	Sensitivity (%)	Specificity (%)	Limitations
Continued	(211)	Cohort, prospective, single centre	70	9	74.0	86.0	
	(209)	Cohort, prospective, single centre	47	1	79.0	93.0	Long acquisition times (>20 min); Small sampling area of handheld DRS probes;
	(207)	Cohort, prospective, single centre	31	-	67.0	79.0	Artefacts from blood and coloured dyes if present on tissue surface
Optical coherence tomography	(215)	Cohort, prospective, multi centre	47	15	60.0[2]	69.0[2]	Image analysis time-consuming and labour-intensive;
	(214)	Cohort, prospective, single centre	37	15	100	82.0	Small sampling area;
	(216)[3]	Cohort, prospective, single centre	35	23	91.7	92.1	Artefacts from blood and coloured dyes if present on tissue surface
Raman spectroscopy	(224)	Meta-analysis	699	-[4]	92.0	97.0	Weak-signal intensity; Control of light environment may be required

Technique	Study	Study design	No. of patients	No. of patients with pure DCIS	Sensitivity (%)	Specificity (%)	Limitations
iKnife	(238)	Cohort, prospective, single centre	2	0	100	100	
	(239)	Cohort, prospective, single centre	66	0	93.0	91.9	Requires physical disruption of tissue; No data on performance in DCIS
ClearEdge	(244)	Cohort, prospective, single centre	58	-	87.3	75.6	[5]

1. Study did not report sensitivity and specificity, but did show a non-significant reduction in re-excision rate between the device arm and control arm, respectively (5.6% versus 12.7%, p = 0.098)
2. In the table the average sensitivity and specificity are displayed. Depending on the margin definition, sensitivity and specificity ranged between 55 – 65% and 68 – 70%, respectively
3. This study also used OCT for scanning the post-excision surgical cavity, but sensitivity and specificity were only provided for *ex vivo* WLE specimen assessment
4. Of the 7 studies included in the meta-analysis 2 studies obtained Raman spectra from DCIS. Diagnostic performance is reported in one study, showing an accuracy of 94% for DCIS
5. Data from more studies is required to be able to thoroughly evaluate the pros and cons of this technology for assessing tumour margins

1.6 Summary

Over the last century breast cancer surgery has significantly changed by moving from radical to conservative. In early-stage breast cancer, the primary treatment option for the majority of women is BCS by WLE of the tumour. BCS aims to completely excise the lesion with a sufficient margin of healthy tissue, and in combination with radiotherapy, BCS provides similar oncological outcomes than mastectomy. What constitutes an adequate tumour resection margin is subject of intense debate, but to date approximately 10 – 30% of BCS patients undergo a re-operation because tumour margins are deemed insufficient. Re-operations potentially have several negative consequences including delay in commencement of adjuvant therapy, worse cosmesis, and increased patient anxiety and health care costs.

Surgical techniques in the form of routine cavity shavings or oncoplastic BCS may be performed in an attempt to reduce re-excision rates, but success of such approaches are limited due to inherent microscopic nature of breast cancer, making the use of palpation and visual inspection to accurately assess the extent of the tumour and margins of excision challenging. Several imaging and histopathological techniques to assess tumour resection margins intraoperatively are currently available for clinical use, but these techniques have failed to penetrate routine practice due to limitations in terms of diagnostic accuracy, reporting times, logistics or technical demands. A variety of novel intraoperative margin assessment techniques have emerged in recent years, which are currently being evaluated in a clinical trial setting. Results on the speed, cost-effectiveness, and usability of these techniques have not yet been published, and information on the impact on re-excision rate is limited. Thus, the potential value of these

techniques for improving quality of care in BCS and reducing health care costs is

yet unknown.

1.7 Aim

This thesis aims to evaluate two novel, innovative imaging techniques to intraoperatively assess tumour resection margins in BCS:

1. Terahertz Pulsed Imaging (TPI)
2. Cerenkov Luminescence Imaging (CLI)

To use TPI for scanning tumour resection margins on excised WLE specimens Teraview Ltd. (Cambridge, UK) has developed a TPI handheld probe system. A first-in-human, single centre study was performed to evaluate the ability of this device to discriminate benign from malignant breast tissue *ex vivo* (Section 2.3).

To use CLI for assessing tumour resection margins on excised WLE specimens Lightpoint Medical Ltd. (Chesham, UK) has developed an intraoperative CLI imaging device. A first-in-human, single centre clinical trial was performed to evaluate the feasibility, safety, and performance of intraoperative ^{18}F-FDG CLI to assess tumour margin status in breast cancer patients undergoing BCS with SLNB or with ALND (Section 3.4).

2. Terahertz pulsed imaging to assess tumour resection margins in breast-conserving surgery

This chapter describes terahertz pulsed imaging (TPI) and its application for imaging cancer, with a specific focus on the feasibility of TPI for margin assessment in breast cancer. The first part of this chapter provides an introduction to terahertz (THz) radiation, THz imaging systems, and the interaction of THz radiation with biological tissue. This is followed by an overview of the published literature on the use of THz in cancer imaging to date, and the studies undertaken in breast cancer. The last part of this chapter focuses on the first-in-human *ex vivo* study I have conducted to evaluate the ability of a handheld TPI device to discriminate benign from malignant breast tissue.

2.1 Introduction to terahertz radiation and terahertz pulsed imaging

THz radiation covers the frequency range from 0.1-10 THz on the electromagnetic spectrum (1 THz = 10^{12} Hz), corresponding to a wavelength of 3 mm - 30 μm. The THz spectrum was previously known as the 'THz gap', due to a lack of efficient THz sources and detectors. This changed in 1975 with the advent of the Auston Switch; an optically-gated photoconductive emitter to generate and detect THz radiation (247). Furthermore, the development of stable, turnkey ultrafast lasers in the 1980s helped accelerate progress in the development of THz technology (248). Since then, THz technology has advanced rapidly. Optimised THz generators and detectors have evolved, and affordable THz systems are now commercially available. As a result of this, THz has become a new area for research in physics, biology, materials science and medicine. Between 1994 and 2013, the number of

THz related journal publications has almost grown exponentially, and THz related biomedical research is being conducted by several groups worldwide (249).

2.1.1 Terahertz systems

The plethora of THz applications has resulted in the development of a wide variety of THz systems. Among others, the laser source used, the technique for generation and detection of THz electromagnetic (EM) waves, the image geometry, and the consideration of using spectroscopy or imaging are all components that can be modified in terahertz systems depending on the type of application and user requirements.

Continuous wave versus pulsed wave

Depending on the laser source, THz radiation can be generated as a continuous wave (CW) or as a pulsed wave. The former typically generates radiation of a single fixed frequency, and is therefore generally restricted to applications where only features at specific frequencies are of interest (250). Pulsed wave systems generate broadband THz radiation up to several THz, with the possibility of coherent detection. Such a system is used in this project. Coherent detection comprises the recording of the amplitude and phase of THz waves in the time domain, which can be used to obtain more details of the target such as spectral and depth information (251). This broadens the applicability of pulsed wave systems, but due to the higher costs of a pulsed laser source these systems are generally more expensive.

Generation and detection of THz radiation

The most common setup used in pulsed wave THz systems comprises a femtosecond (1 fs = 10^{-15} sec) laser and a photoconductive emitter and detector (250). The emitter consists of a semiconductor crystal and two planar electrodes (Figure 2). The incidence of the laser pulse on the photoconductive emitter releases electron-hole pairs. Applying an electric field across the two electrodes then accelerates these charge-carriers. As a result of accelerating the electron-hole pairs, electromagnetic THz waves are produced which then radiate into free space. The spectral range of the generated THz waves depend on various conditions, including the shape and power of the input laser pulse, the voltage, and the characteristics of the crystal used in the photoconductive emitter (252).
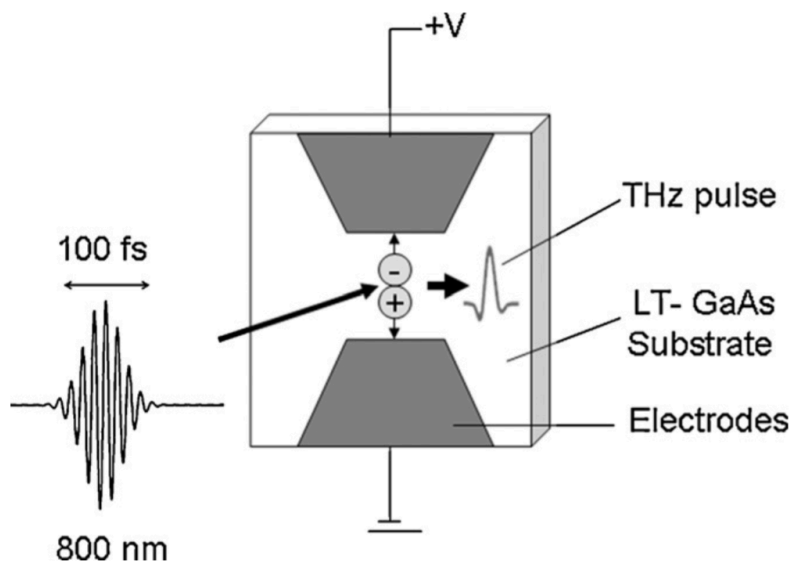
Figure 2: Terahertz photoconductive emitter. In this example a 100 femtosecond (fs) 800 nm laser pulse is incident on a semiconductor crystal made of low temperature gallium arsenide (LT-GaAs), resulting in the emission of THz pulses. *Image was reproduced from (253) with kind permission from Elsevier.*

Detection of THz radiation essentially works in reverse order to THz emission. THz electromagnetic waves incident on the photoconductive receiver accelerate the electron-hole pairs produced by the incident femtosecond laser beam. The amplitude of the resultant electric field is then measured. By measuring the

amplitude at a number of discrete time points, an entire THz pulse profile can be reconstructed in the selected time domain range (254), and analysis of the THz pulse can provide unique information about the sample of interest.

System geometries

THz systems can operate in two geometries: reflection and transmission. In the former THz radiation reflected off the sample is detected, while in the latter THz radiation that is transmitted through the sample is detected. Due to the strong attenuation in biological tissue as will be further explained in Section 2.1.3, THz imaging in transmission geometry is limited to very thin samples (typically less than a few millimetres) in order to acquire data with a sufficient signal-to-noise ratio (255). Obtaining thin samples is challenging because fresh tissue is soft and highly deformable. Besides, thin samples are more susceptible to drying, which could affect the properties of the tissue in the THz frequency range. Conversely, samples used for imaging in reflection geometry are preferably a few millimetres thick to prevent interference of THz pulses reflected from non-tissue structures located underneath the tissue sample (253). These factors should carefully be considered when deciding on the preferred imaging geometry. For the purpose of using THz imaging to distinguish malignant from benign breast tissue in an *ex vivo* setting, a reflection-based imaging system is required, as excised breast specimens are much thicker than a few millimetres.

Terahertz pulsed spectroscopy and Terahertz pulsed imaging

THz pulsed spectroscopy (TPS) is primarily performed to determine the optical properties, i.e. absorption coefficient and refractive index, of a sample in the THz frequency domain. TPS was first described in 1995 by Hu *et al.* (256). In TPS, a

Fourier transform is applied to the time domain data, thereby obtaining information in the frequency domain. By performing an analysis on the frequency domain data as described in detail by Fitzgerald *et al.* (254) and Ashworth *et al.* (257), the complex refractive index can be extracted, from which the frequency dependent real refractive index and real absorption coefficient can be derived.

Terahertz pulsed imaging (TPI) can be viewed as an extension of TPS, whereby THz pulses from a sample are detected over one (x) or two (x, y) spatial dimensions to create an image (258). In 2-dimensional imaging each spatial coordinate (x, y) acquires THz pulses, and these pulses can be analysed in both the time and frequency domain to obtain unique biological information on the sample. It is also possible to look within a sample, as THz waves are reflected at an interface of two structures with a different refractive index. THz waves from deeper located structures will be reflected at a slightly later time point, and thus the depth of each structure can be estimated by analysing the time it requires before a THz wave is detected. This 'time-of-flight' technique enables obtaining TPI images that provide a 3D-view of a layered structure (259).

2.1.2 Terahertz contrast mechanisms in biological tissue

The contrast observed in TPI of biological tissue is indirectly a result of differences in the absorption coefficient and refractive index within the tissue sample. Although the underlying mechanism behind the change in optical properties of tissue in the THz frequency range is not fully understood, it is known that water plays an important role. In water, and other polar liquids, the hydrogen bonds between molecules (intermolecular) and within a single molecule (intramolecular) strongly vibrate in the THz frequency range (260). As a result of this strong vibrational sensitivity, THz radiation is highly absorbed by water. Since water

molecules are the main component in biological structures and within cells, the high sensitivity of THz to water provides an intrinsic contrast mechanism that can be exploited for biomedical applications. Cancers, including breast cancer, are known to have higher water content when compared with benign tissue, thus making THz imaging an especially promising modality in cancer diagnostics (261-266). The increased water content in cancers is amongst other factors thought to be a result of impeded diffusion due to increased cellularity, neovascularisation, necrosis and inflammation (261,263). However, water content is not the sole source of contrast in THz imaging of cancers as shown by studies on dehydrated, wax-embedded tissue samples (267-269). It has been suggested that the observed contrast in the absence of water is due to differences in proteins and lipid content present in certain cancers, or from other cellular or structural changes (263,270,271). Current work focuses on obtaining a better understanding of the contrast mechanisms that contribute to the differences observed in THz imaging between benign and malignant tissue. An improved understanding of these mechanisms could enable identification of changes in the composition and physiology of biological tissue based on the characteristics of the THz pulse (272).

2.1.3 Penetration depth and spatial resolution

The high absorption of THz by water limits the penetration of the radiation in biological tissue. The penetration depth is dependent on the frequency of the THz radiation, the absorption coefficient of the tissue, and the signal-to-noise ratio of the imaging system. MacPherson *et al*. found that for a signal-to-noise ratio of 1000 at 1 THz, the penetration depth in skin and adipose tissue was 0.5 mm and 3 mm, respectively (255). The deeper penetration of THz radiation in adipose tissue is due to lower water content compared to skin tissue, which results in a lower

absorption coefficient in the THz frequency range. Overall, it is important to note that higher frequencies penetrate less deeply into tissue than lower frequencies. The handheld TPI probe used in the breast study (Section 2.3.2.1) has a bandwidth of 0.1 – 1.8 THz. In adipose tissue, of which the breast predominantly consists, it can therefore be assumed that the penetration depth will be a few millimetres maximum. Hence, this device is specifically suited for imaging tumour cells within a few millimetres of the resection border, and is not applicable to imaging deeper located structures.

Image resolution is also an important aspect when using TPI for biomedical imaging. Resolution can be divided into lateral resolution and axial resolution. The former is defined as the distance at which two points are distinguishable in the direction perpendicular to the direction of the THz pulse, while the latter is the distance between two distinguishable points in the direction parallel to the direction of the THz pulse. Lateral resolution is calculated by using the Rayleigh-based equation (273):

$$Lateral\ resolution = \frac{1.22\ \lambda}{2\ n \sin \theta} = \frac{0.61\ \lambda}{NA}$$

where λ is the wavelength, n the refractive index of the sample, θ the angle at which the reflected THz pulse enters the system, and NA the numerical aperture. For radiation with a frequency of 1.8 THz and 0.1 THz, and a system with an optimal optical arrangement in which NA is 1, the lateral resolution is 135 μm and 1.83 mm, respectively. Axial resolution depends on the system's bandwidth (BW) and the refractive index of the sample (n), and can be calculated by using the following equation (255):

$$Axial\ resolution = \frac{c}{2nBW}$$

where c is the speed of light in air (approximately 3 x 10^8 m s^{-1}). The bandwidth of the handheld TPI probe system is 1.7 THz (0.1 – 1.8 THz). Assuming a refractive index of 1.6, 2.0 and 2.2 at 1 THz for adipose, fibrous and tumour tissue respectively (274), the axial resolution of the system ranges between 0.04 – 0.06 mm (40 – 60 μm). It should be noted that the lateral and axial resolution calculated above present the theoretical limits, and depend amongst other factors on the system configurations (including the number of pixels and pixel size), fluctuations in the laser source and the quality of the measurement itself. The practical resolution of TPI systems will be lower, but unfortunately no data is available on the lateral and axial resolution of the TPI handheld probe system used in the breast study (Section 2.3.2.1).

As explained in this section, lateral resolution, axial resolution and penetration depth are all frequency dependent. Higher frequency THz radiation provides a better image resolution, while decreasing the penetration depth. The 0.1 – 1.8 THz frequency range of the TPI handheld probe is a good trade-off between high imaging resolution and a sufficient penetration depth that meets the positive margin definition of <1 mm as per current ABS consensus (Table 1).

2.1.4 Biological effects of terahertz radiation

Due to the recent surge in the use of TPI for biomedical applications, and the expected increase in the near future, there has been vast scientific interest in the effects of THz radiation on biological tissue (275). The energy level of THz radiation with a wavelength of 1 THz is roughly 4.14 meV, which is much less than the keV and MeV energies that are typical for X-ray beams (276). Moreover, this is far below the typical energy (several eVs) required to remove electrons from biological molecules, and thus THz is a non-ionising type of radiation (277).

Because of its lower energy, THz radiation interacts differently with living cells than high-energy ionizing radiation from for example ultraviolet light, X-rays and gamma rays. The current understanding of the biological effects of THz radiation is, however, still limited (277). Most studies have found that THz radiation did not cause DNA damage (278-282), although one study did find changes indicative of DNA damage in human skin tissue exposed to THz radiation (283). Changes in gene expression after exposure to THz radiation have also been reported (284-289). Some of these studies report upregulation of inflammation genes and gene instability that could lead to an increased cancer risk (287,289), although others found that these changes were not carcinogenic; it has even been suggested that THz radiation could provide new therapeutic treatments for certain skin diseases (285,286). The risk for damaging effects to occur is amongst other factors dependent on the tissue type, study design (*in vitro, ex vivo, in vivo*) and exposure conditions including the energy density, duration and frequency of the THz radiation (277). Since these factors were very different in all the above studies, it is difficult to draw any conclusions on the effects of THz radiation on biological tissues. Besides, no studies have been published to date on the effects on breast tissue, so the safety of THz in breast cancer remains unknown. Hence, further work is needed to establish the THz exposure conditions that induce damaging effects in biological tissue in general, and breast tissue in particular.

2.2 Terahertz for cancer imaging

As described above the sensitivity of THz radiation to changes in water content and tissue composition, in combination with its submillimeter imaging resolution and low energy levels, make THz a potential application for imaging cancers. Most of the work on the use of THz for imaging malignancies has focused on skin, colon

and breast cancer. A description of the results published to date in these types of cancer can be found in the sections below. The studies discussed specifically focus on fresh tissue specimens as opposed to processed specimens, i.e. formalin fixed, paraffin embedded or freeze dried tissue, as processing of human tissue alters its water content and structure, which in turn affects the tissue's response to THz radiation. This prevents accurate comparison of results from studies on processed samples with studies using fresh unprocessed samples, including the TPI handheld probe breast study discussed in Section 2.3.

In addition to its use in imaging skin, colon and breast cancer, studies have also shown that THz technology can successfully be applied for *ex vivo* imaging of oral (290,291), gastric (292,293), and brain cancer specimens (294), as well as metastatic lymph nodes in patients with cervical cancer (295). These small pilot studies have all used processed specimens rather than fresh specimens, and a detailed description of these findings is therefore not provided.

2.2.1 Skin cancer

Skin cancer is the most common form of cancer globally and can be divided into non-melanocytic and melanocytic types (296). Skin cancers are often treated by surgical excision, where the aim is to excise the tumour with a margin of a few millimetres of healthy tissue (296). Ideally Moh's micrographic surgery is used; a technique where the tumour is excised in layers, and each layer is assessed histologically during surgery to obtain information on the tumour margin distance. Although Moh's surgery has a success rate of approximately 95% (297), it is time-consuming and labour intensive, and a non-invasive method to accurately diagnose skin cancer and facilitate delineation of tumour margins would be a major benefit to patients and healthcare systems (298).

The use of TPI to non-invasively diagnose basal cell carcinoma (BCC), which accounts for approximately 80% of all non-melanomatous skin cancers, was first described in 2003 by Woodward *et al.* (299). They scanned 21 excised skin samples *ex vivo* with a 0.1 – 2.7 THz broadband imaging device in reflection geometry. The raw THz waveforms were filtered to remove high and low frequency noise, and divided by a reference waveform, to obtain processed waveforms (called impulse functions). THz images were generated based on the minimum peak value (Emin) of the impulse function of each pixel, and a significant difference between the Emin of BCC and normal skin tissue was found. This enabled distinguishing benign from malignant skin tissue on TPI (Figure 3).
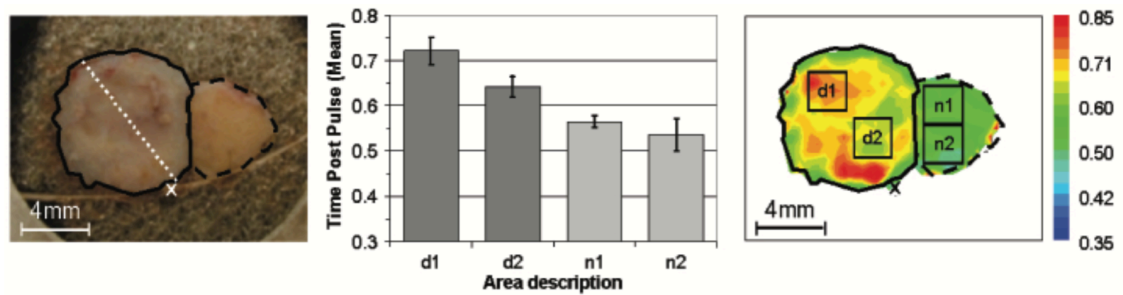
Figure 3: *Ex vivo* TPI of skin tissue containing basal cell carcinoma. Left: photographic image of BCC (solid boundaries) and benign skin tissue (dashed boundary). Centre: Histograms showing the Emin values and standard deviations for BCC areas d1 and d2, and benign tissue areas n1 and n2. Right: TPI image with clear contrast between BCC and benign tissue that enables identification of tumour margins. *Image was reproduced from (299) with kind permission from Elsevier.*

In 2004, Wallace *et al.* confirmed the ability of TPI to image BCC *ex vivo* in reflection mode, and also showed that TPI could be used *in vivo* to identify the extent of BCC and delineate the margins of excision using a portable TPI system (TPI Scan, TeraView Ltd., UK) (300). Scanning a 2 cm^2 area took roughly 4 minutes and, although not real-time, showed that images could be acquired within a time-period suitable to guide surgical excision.

TPS measurements of fresh tissue with a THz spectrometer (TPI Spectra1000, TeraView Ltd., UK) revealed that BCC has a higher absorption coefficient and refractive index than benign skin tissue, which was attributed to the higher water content found in BCC (301). These findings thus offer an explanation for the observed contrast in TPI of BCC.

A CW THz imaging system as a lower-cost alternative for the pulsed imaging systems described above has also been successfully used in *ex vivo* imaging of fresh BCC specimens (302). The same research group also showed that besides water, tryptophan could be a potential intrinsic biomarker for THz imaging of skin cancer, as this component of the human skin proved to be sensitive to THz radiation in the 1.84 THz range (271).

A combination of optical and CW THz imaging has also been described for imaging non-melanocytic skin cancer (303). Six BCC and three squamous cell carcinoma samples were scanned *ex vivo*. THz proved useful in indicating the approximate location of the tumour, while the optical images provided the morphological detail needed to demarcate the boundaries of the tumour. This indicates that for optimal delineation of non-melanocytic skin cancers (and potentially other cancers as well), a combination of imaging modalities may be preferred.

It is currently not yet known whether THz imaging can be used to image melanocytic skin cancers, nor is there information on the ability of THz to differentiate between types of skin cancer, so further studies to investigate other skin lesions are warranted (253).

2.2.2 Colon cancer

Colon cancer screening aims to detect pre-cancerous dysplastic polyps and cancerous lesions at an early stage as the prognosis of colon cancer improves profoundly if the disease is detected and treated early (304). Subjects with abnormal screening results undergo a colonoscopy during which suspicious areas are biopsied to establish a diagnosis. However, identifying malignant lesions on endoscopic imaging can be challenging, especially because dysplastic tissue (and some inflammatory diseases) can be hard to distinguish from malignant disease. Implementation of THz imaging in an endoscopic system could therefore aid in more accurate detection of colon cancer.

The use of THz technology to image colon cancer was first described in 2011 (305). Typically around 30 minutes post excision, cancerous, dysplastic and healthy colon tissue was scanned from a total of 30 patients, using a reflection THz imaging system (TPIimaga1000, TeraView Ltd., UK). It was found that the absorption coefficient and refractive index were higher for neoplastic tissue (cancer and dysplasia) than for benign tissue. Staining of the pathology slides revealed differences in angiogenesis of blood vessels and lymphatic vessels between normal colon tissue, dysplastic tissue and cancer, indicating that the observed contrast may be due to differences in water content as well as structural differences. A total of 17 parameters in the time and frequency domain were calculated from the impulse functions, with the aim of constructing an automated model for the classification of healthy, dysplastic and cancerous colon tissue. Initial results based on logistic regression analysis showed a sensitivity and specificity of 82% and 77% for distinguishing healthy from dysplastic and cancerous tissue, respectively. Sensitivity and specificity for discriminating healthy from dysplastic tissue alone was 89% and 71%, respectively. Interestingly, the parameter values

from samples consisting of the same tissue type, but obtained from different patients, showed variations. The authors suggest that adjusting for these patient-to-patient variations (also called inter-patient variability), by using the healthy tissue measurements of each individual patient as a reference to calibrate the system, could improve the contrast between healthy, dysplastic and cancerous colon tissue, thus improving the discriminative power.

Eadie *et al.* used the 17 parameters from the same *ex vivo* colon tissue dataset and applied additional analyses to evaluate whether the diagnostic accuracy, i.e. sensitivity and specificity, could be improved (306). Both principal component analysis (PCA) and decision trees were applied to the 17 parameters to reduce the number of inputs, and thereby model complexity, while preventing overfitting of the data. By reducing the number of data inputs, data reduction methods also improve the efficiency of the algorithm compared to using the full dataset, which enables near real-time classification required to use THz in an intraoperative setting. Neural networks and support vector machine (SVM) algorithms were used to provide tissue classifications based on cross-validation. By using such intelligent analysis methods, diagnostic accuracy improved remarkably. Depending on which data reduction and classification method was used, sensitivity and specificity for classifying healthy from both dysplastic and cancerous tissue exceeded 92% and 87% respectively, while for healthy and dysplastic tissue values higher than 96% and 87% were reported. By applying these methods to the data obtained from three new patients who were not included in the initial dataset, they were able to show that the technique could be generalized to further patients, and that patient specific calibration of the system as suggested by Reid *et al.* may not be needed. However, classification in one of the three patients was less accurate, indicating that inter-patient variations may still

cause problems, and that a larger dataset is required to draw conclusions about the feasibility of a 'one-size fits all' approach.

In order to use THz imaging to aid *in vivo* discrimination of benign and cancerous colon tissue during colonoscopy, implementation of the technology within a clinical endoscope is paramount. Several groups have worked on developing THz endoscopic imaging systems (307-310). So far, Doradla *et al.* are the only ones who tested the performance of their device on human cancer tissue (310). A total of six formalin fixed specimens (three cancerous and three benign) were imaged *ex vivo* with a prototype single-channel CW THz endoscopic system in reflection mode. An increased reflection was found in malignant tissue compared to healthy tissue, which was attributed to greater scattering form structural changes in the diseased tissue including an increased vasculature. Although these results appear to be a promising step towards the use of THz technology to image organs previously inaccessible, *in vivo* studies are needed to assess the real benefit of THz in aiding detection of cancerous colon lesions.

2.2.3 Breast cancer

Breast tissue in patients with breast cancer can be sub-divided into fibrous, adipose and tumour tissue. Various research groups have studied the ability of THz technology to discriminate between benign breast tissue and tumour tissue, with the aim of eventually using THz imaging for intraoperative tumour margin evaluation to reduce re-excision rates in BCS. This section provides a non-exhaustive overview of the results published to date.

The application of THz technology to breast cancer was first proposed by Fitzgerald *et al.* in 2004 (311). Freshly excised breast samples were scanned using a portable TPI imager (TPI Scan, TeraView Ltd., UK). This device operates in

reflection geometry and emits broadband radiation of 0.1 – 3.0 THz. Impulse functions were obtained by processing the raw THz waveforms, and two parameters in the time domain were calculated and used to construct the THz image: the minimum value *Emin,* and the ratio between the minimum value and the maximum value *Emin/Emax*. By using these parameters they were able to demonstrate the ability of TPI to image both invasive ductal carcinomas and DCIS.

Based on the results of this pilot study, a more comprehensive study was conducted using the same imaging device (312). A total of 22 excised breast samples from 22 women were scanned. All samples were fresh at the time of measurement, except two DCIS samples that had been fixed in formalin before scanning. Samples were scanned for less than 5 minutes and, similar to the previous study, THz images were constructed by using the parameters *Emin* and *Emin/Emax*. The THz images were evaluated by comparing the size and shape of the tumour on histopathology with the size and shape of the tumour region on TPI (Figure 4). In all 22 samples, there was excellent correlation between histological tumour size and tumour size on TPI (correlation coefficient > 0.82 for both parameters). A good correlation between tumour shape on histopathology and TPI was also found; a median correlation of 0.71 and 0.69 for *Emin* and *Emin/Emax*, respectively. This study confirmed the ability of TPI to distinguish invasive ductal carcinoma from benign breast tissue, and also showed the potential for identifying invasive lobular carcinoma and pure DCIS.
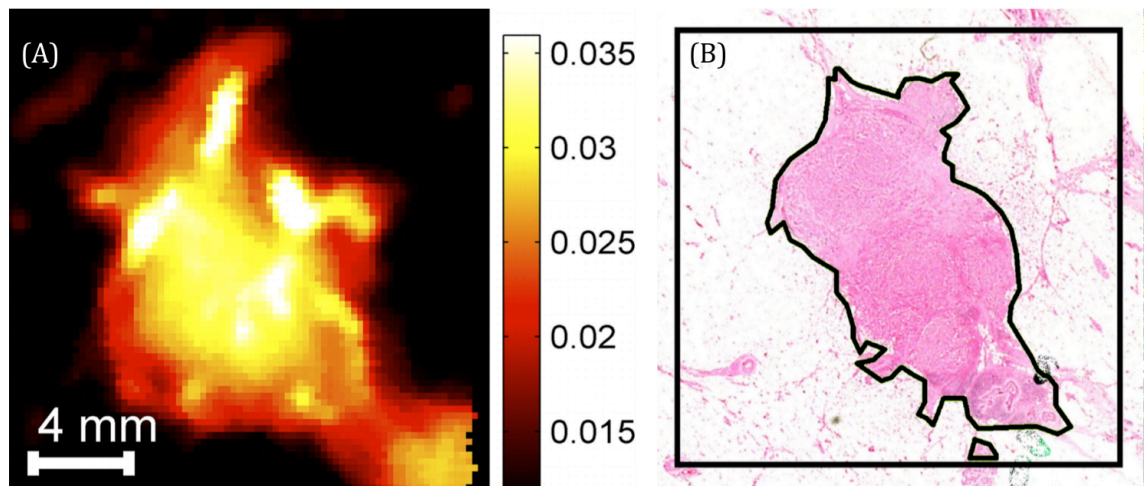
Figure 4: TPI image using the parameter *Emin* (A) and histopathology image (B) of invasive ductal carcinoma. The tumour size and shape on TPI correlate well with histopathology (outlined in black). *Image was reproduced from (312) with kind permission from the Radiological Society of North America (RSNA).*

To better understand the origin of contrast observed between benign and malignant breast tissue on TPI, Ashworth *et al*. used TPS to measure the optical properties of fibrous adipose and tumour tissue (274). A total of 105 breast tissue samples from 20 patients were measured with a 0.1 – 4.0 THz spectrometer (TPIspectra1000, TeraView Ltd., UK) in transmission geometry within 24 hours of excision. To ensure that the moisture content of the specimens remained constant, the samples were kept in a refrigerated, humidified environment before scanning. After scanning, the samples were submitted to a breast histopathologist who for each sample reported the percentage content of adipose, fibrous and tumour tissue. Samples were considered suitable for the study if more than 50% of the sample consisted of one of these three tissue types and could therefore be grouped accordingly into 'benign adipose', 'benign fibrous', or 'cancer'. Based on histopathology, a total of 74 samples with a 'homogeneous' tissue content (i.e. containing >50% of one tissue type) were included for analysis. A clear difference was found in the refractive index between the three tissue types in the frequency range 0 – 2.0 THz (Figure 5A). Tumour had the highest refractive index, followed

by fibrous and adipose tissue. The greatest difference between the three tissue types was found at 0.32 THz. The difference in absorption coefficient was less profound (Figure 5B). Adipose tissue had a markedly lower absorption coefficient, but the coefficients of fibrous stroma and cancer showed overlap for most of the frequency range.
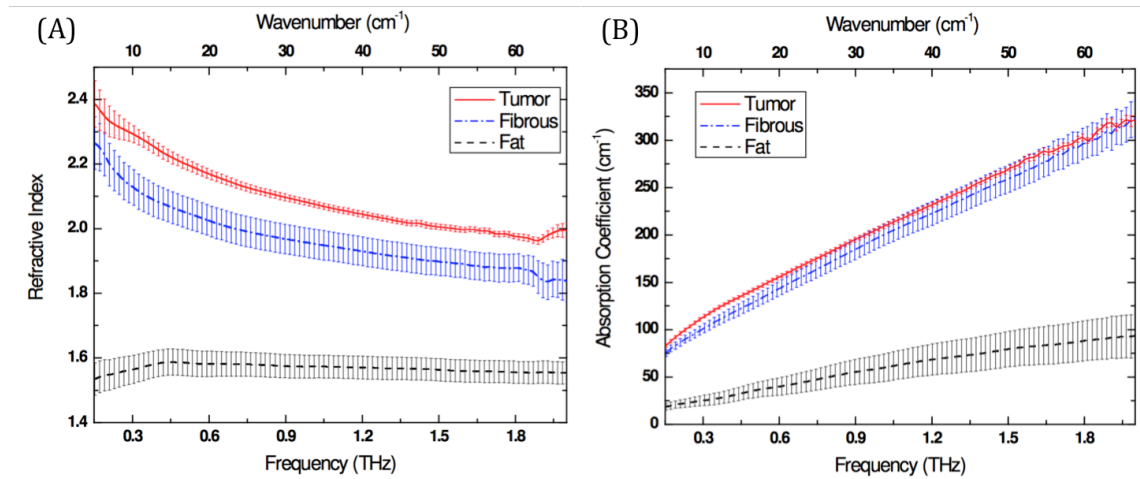
Figure 5: Optical properties of adipose, fibrous and cancerous breast tissue measured by TPS. (A) Refractive index (B) Absorption coefficient. Error bars represent 95% confidence intervals (CI). The types of breast cancer included in the 'tumour' group are not reported by the authors. *Image was reproduced from (274) with kind permission from the Optical Society of America (OSA).*

Based on the spectroscopy data, simulations were performed to predict the impulse functions of all 3 tissue types when TPI in reflection would be performed. As expected from the clear differences in absorption coefficient and refractive index, the impulse function from adipose tissue was very different compared to fibrous and cancer tissue (Figure 6). The latter two tissue types showed very subtle differences, indicating that accurate discrimination between benign fibrous and malignant breast tissue using TPI might be challenging. The shape of the simulated impulse functions is different from the impulse functions obtained with the TPI handheld probe (Figure 11). This is due to differences in processing of the

raw THz pulses. Details on the processing steps used to obtain the simulated impulse functions in Figure 6 can be found in (313).
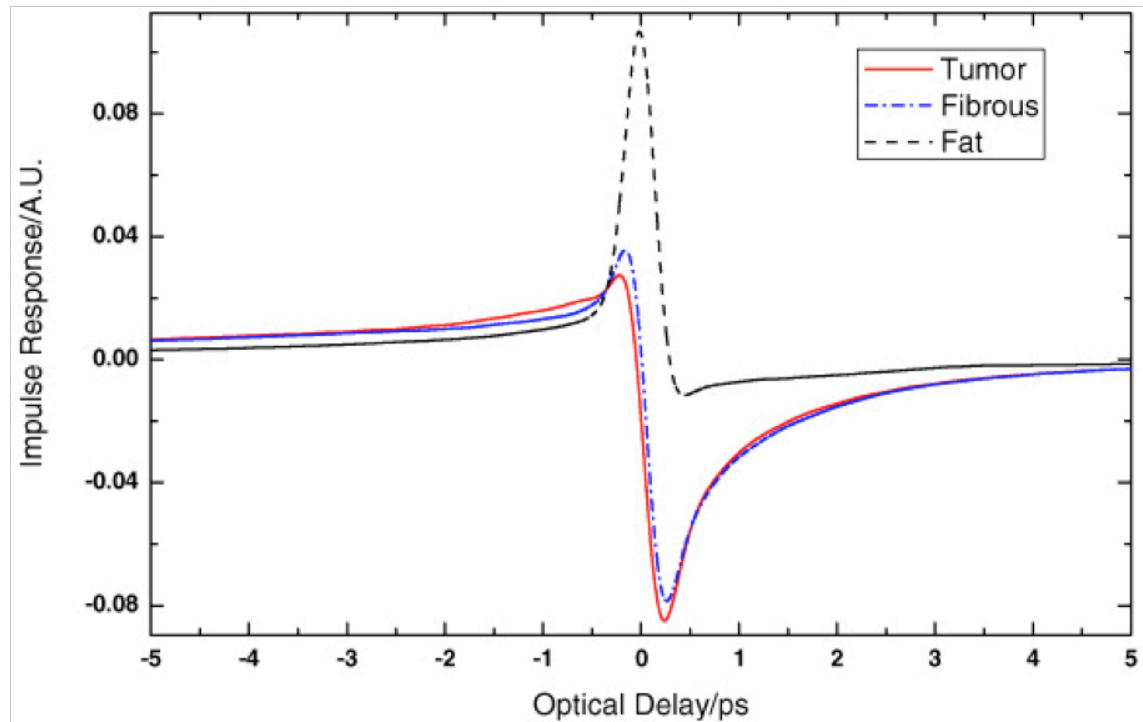
Figure 6: Simulated TPI impulse functions from fibrous, adipose and cancerous breast tissue. The shape of the impulse function from fibrous and tumour show small differences; most of these differences are present around the maximum and minimum amplitude. The signal from adipose tissue is clearly distinct. *Image was reproduced from (274) with kind permission from the Optical Society of America (OSA).*

Following on from their work published in 2006 (312), Fitzgerald *et al*. extended the TPI breast tissue dataset to include a total of 51 breast samples from 51 patients (314). By correlating the TPI image to the histopathology image, regions of interest were selected from areas of fibrous, adipose and cancerous tissue. Only the fibrous and tumour THz pulses were included for analysis to specifically assess the ability of TPI to distinguish these two types of tissue. No information is provided on the type of tumours included in the dataset. Different data analyses methods were used with the aim to identify the method providing the best performance in terms of accuracy. A total of 10 parameters in the time and frequency domain were calculated from the impulse function. In addition to these

'heuristic' parameters, data reduction using PCA was applied to the full impulse function as well as to all ten parameters. Tissue classification was performed using SVM. They found accuracies exceeding 90%; PCA applied to all 10 parameters gave the highest accuracy of 91.9%. These results show that despite the similarities in THz pulses, the TPI Scan system (TeraView Ltd., UK) can accurately discriminate fibrous from cancerous breast tissue. However, the TPI Scan system is not suitable for intraoperative assessment of WLE specimens; the device uses a sample holder to image samples with a maximum size of 20 x 20 mm, which requires larger tissue specimens to be sliced to obtain samples that fit the dimensions of the holder. Thus, in order to use the TPI Scan for intraoperative margin assessment it would require sectioning multiple areas from all six margins of the intact WLE specimens. This is not appropriate in the routine setting in the operating theatre, as excess manipulation of tissue close to or at the resection margin could affect margin assessment on gold-standard postoperative histopathology, thus potentially compromising patient care. Hence, using TPI for assessing tumour margins ideally requires a device that could be used to scan excised WLE specimens of any size intraoperatively without the need to manipulate or incise the intact specimen. Based on these requirements Teraview Ltd. (Cambridge, UK) developed a handheld TPI probe system. A detailed description of this device can be found in Section 2.3.2.1.

A small study was performed to test whether the prototype version of the handheld TPI probe system showed promise in discriminating benign from malignant breast tissue (315). Breast tissue samples, obtained from sectioning freshly excised mastectomy specimens or WLE specimens, were measured *ex vivo* for 20 seconds. Prior to measuring, a disposable, protective sheath was wrapped around the imaging probe to prevent contamination from biological tissue. THz

pulses were emitted and detected over a length of 7 mm with a scan speed of 4 Hz, i.e. in 1 second an area of 7 mm was scanned 4 times. For each sample the histopathologist reported the percentage of each tissue type as adipose, fibrous, or tumour, and 'homogeneous' samples containing >75% of one 'pure' tissue type were used for analysis. Four parameters from the reflected impulse function were calculated for the three tissue types and subsequently compared (Figure 7). Similar to the results obtained with the TPI Scan, adipose tissue showed clear differences compared to fibrous and tumour tissue, respectively. However, no differences were found between fibrous tissue and cancer for *Power at 0.119 THz* and *Max Amplitude*, and only minute differences were seen for *Pulse Integral* and *Full Width Half Maximum (FWHM)*. Large 95% confidence intervals (CI) were present in *Pulse Integral* and *Power at 0.119 THz.* Although the authors do not discuss reasons for the observed ranges, potential explanations for the observed variations could be inter-patient variability or inconsistencies in the THz pulses produced by the TPI system (Section 2.3.3.4). The performance of the device was not assessed in terms of accuracy, sensitivity and specificity, but the lack of contrast between fibrous tissue and tumour for all four parameters indicates that misclassifications between these two types of tissues are likely to occur.

The tissue samples that were scanned with the prototype TPI handheld probe in the study of Ashworth *et al*. are not an accurate representation of the tissue composition found at the resection border of patients with 'close' or 'positive' margins as the tumour samples used for analysis consisted of >75% tumour cells. Involved margins are often identified microscopically as a small number of tumour cells immersed in a 'background' of fibrous and/or adipose tissue (316). These small tumour islands are thus very likely to only cause a subtle change to the incident THz pulse; the information in the THz pulse will be

predominantly from the benign tissue background. Thus, accurate discrimination of tumour samples with a lower tumour cell percentage, which is a better representation of the composition found clinically, will be even more challenging.
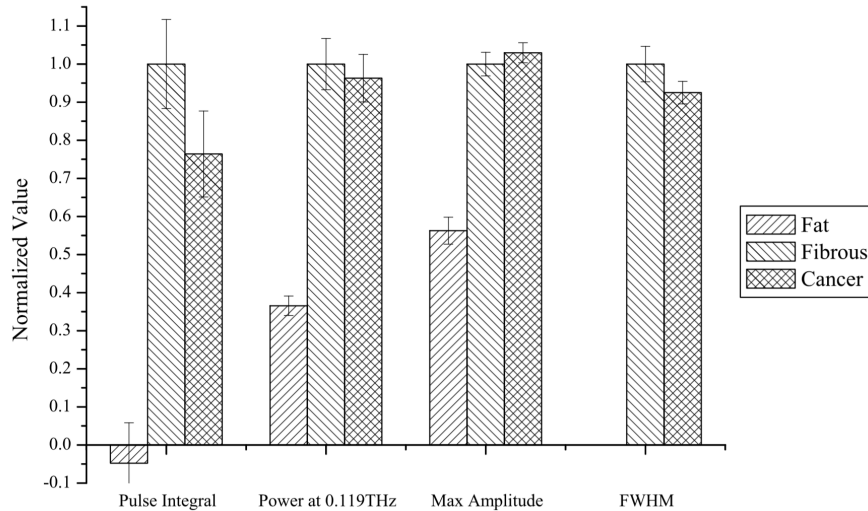
Figure 7: Average parameter values for adipose, fibrous and tumour tissue scanned with the prototype TPI handheld probe system. The values are normalised to fibrous tissue. The error bars represent 95% CI. *Image was reproduced from (315) with kind permission from Institute of Electrical and Electronics Engineers (IEEE).*

2.2.4 Summary

In the last three decades THz technology has rapidly advanced and, to date, THz imaging systems are used in a variety of biomedical applications. THz radiation is sensitive to changes in water content and, combined with its sensitivity to molecular and structural changes, this is thought to be the underlying contrast mechanism to distinguish benign and malignant tissue on TPI. This unique sensitivity, in combination with the submillimeter imaging resolution and low energy levels, makes TPI of particular interest for cancer imaging.

TPI has been successfully used for *ex vivo* imaging of oral, gastric, skin, colon and breast cancer. Studies in breast cancer have found that the main challenge is accurate discrimination of benign fibrous from malignant tissue, whilst adipose tissue can be more easily identified. All these studies used static THz

systems that could only image small tissue samples (<2 cm) obtained from non-diagnostic breast tissue. In addition, the homogeneous tissue samples analysed in these studies are not truly representative of the tissue composition found in patients with 'close' or 'positive' tumour resection margins, and the ability of TPI to detect tumour at a margin, where a mixture of benign and tumour tissue is more commonly seen, is therefore yet to be determined.

To facilitate the use of TPI to scan tumour resection margins on excised WLE specimens, Teraview Ltd. has developed a TPI handheld probe system. The next section describes the first-in-human study conducted to evaluate the ability of this probe to discriminate benign from malignant breast tissue using samples that better resemble the tissue composition found at the edge of WLE specimens.

2.3 First-in-human clinical study to evaluate the ability of a terahertz pulsed imaging handheld probe to discriminate benign from malignant breast tissue *ex vivo*

2.3.1 Aim

A first-in-human, single centre study was performed to evaluate the ability of a handheld TPI probe to discriminate benign from malignant breast tissue in an *ex vivo* setting.

The aims of the study were:

1. To obtain a dataset that is representative of the tissue composition found at the resection border of WLE specimens;

2. To evaluate the performance of the TPI handheld probe system in terms of accuracy, sensitivity, specificity and predictive values using two data analysis and classification methods.

2.3.2 Materials and Methods

2.3.2.1 TPI handheld probe system

In this study, version 2.0 of the TPI handheld probe system is used (Teraview Ltd. Cambridge, UK) (Figure 8). This system consists of a main unit that contains a femtosecond laser (Menlo Systems GmbH, Martinsreid, Germany) that produces 780 nm laser pulses at a rate of 100 MHz. The pulses are guided down optical fibres, contained within a metallic cable called the "umbilical cord", to the handheld imaging probe.
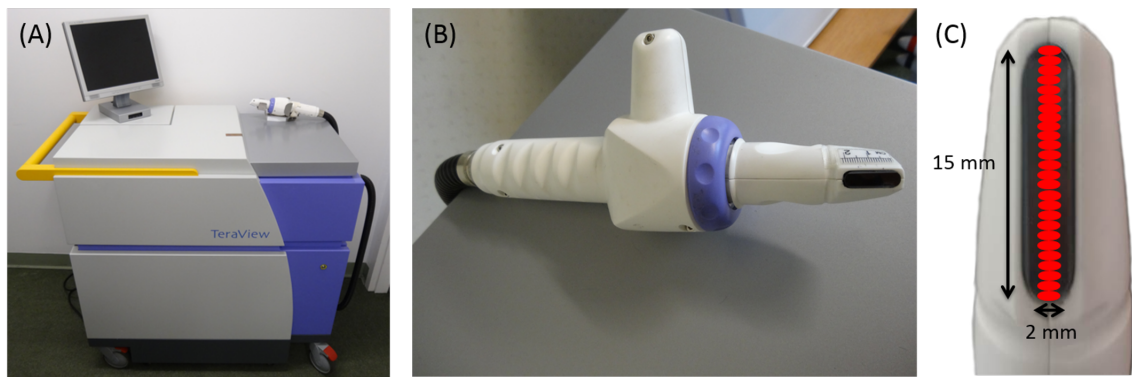
Figure 8: TPI handheld probe system. (A) Main unit with computer monitor, handheld imaging probe and black umbilical cord (visible on the right). (B) Close up of the handheld imaging probe. (C) Close up of the head of the imaging probe showing the black quartz window. The probe scans an area of 15 x 2 mm, and acquires data from 26 pixels (red dots).

Within the imaging probe laser pulses are incident on a photoconductive emitter and detector (Figure 9). This results in the production and detection of THz pulses of bandwidth 0.1 – 1.8 THz. An oscillating mirror guides the THz pulses onto a quartz window present at the tip of the probe. By controlled rotation of this mirror, an area of 15 x 2 mm is scanned with a frequency of 4 Hz. The 15 mm axis contains a total of 26 pixels, thus providing a pixel resolution of approximately 0.6 mm. During scanning each pixel acquires THz pulses over time to form a TPI image (Figure 11).
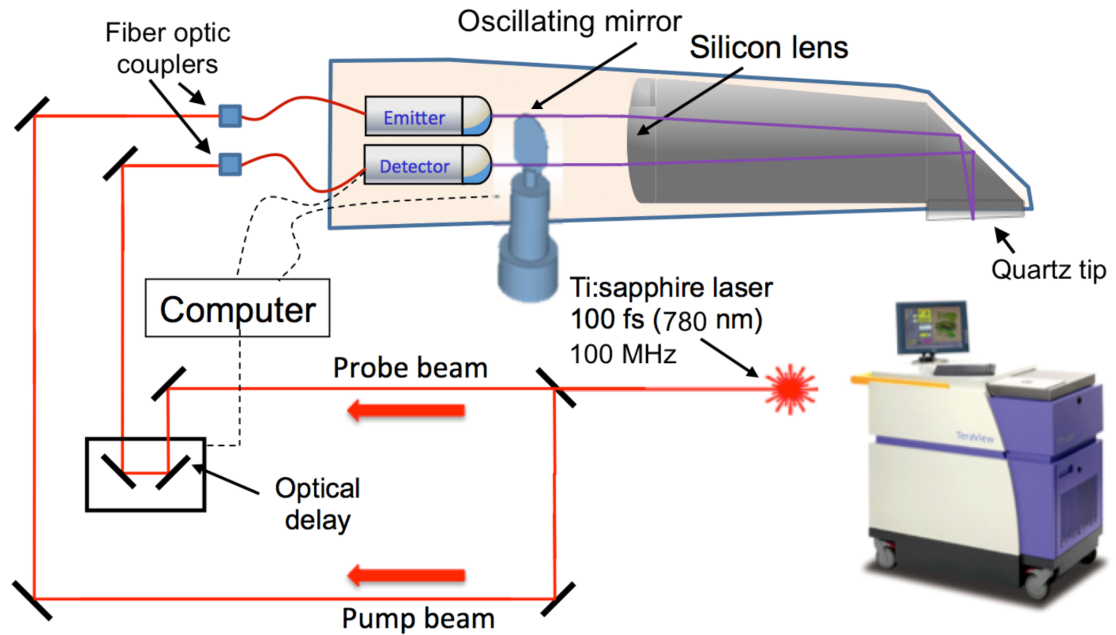
Figure 9: Schematic illustration of the TPI handheld probe system. The emitted laser pulses are split into a "pump beam" and a "probe beam". The pump beam is guided through the optical fibres in the umbilical cord, and subsequently incident on the photoconductive emitter to produce THz pulses. The probe beam is guided onto the photoconductive detector to detect the THz pulses reflected from the tissue sample. By altering the path length of the probe beam, the time of arrival at the detector in respect to the incident THz pulse can be changed, thus sampling the THz pulse in the time domain.

2.3.2.2 Tissue preparation and TPI data acquisition

Between August 2013 and August 2014, breast tissue from patients who underwent BCS or mastectomy at Guy's Hospital in London were scanned with the TPI handheld probe after written informed consent was obtained (REC 12-EE-0493). Excised BCS or mastectomy specimens were taken from the operating theatre to the adjacent King's Health Partners Cancer Biobank, where the specimens were inked and sliced by an Advanced Practitioner as per standard protocol. Subject to the amount of tissue that was required for diagnostic purposes, tissue samples were obtained with an average length, width and thickness of 10 mm, 5 mm and 2 mm, respectively.

Prior to scanning the tissue samples, a Tegaderm layer (3M Tegaderm Film, 3M, Berkshire, UK) was applied to the probe's quartz window, and the remainder of the probe was wrapped in a disposable protective sheath to prevent contamination from tissue. A 60 second water measurement was performed to assess the signal intensity and shape of the THz pulses emitted by the TPI handheld probe on each day of measurement.

Tissue samples were placed in a standard histology cassette (Unisette™, Simport, Beloeil, Canada) that tightly fitted the head of the imaging probe to enable consistent and controlled THz measurements (Figure 10). All tissue samples were scanned within 60 minutes post excision. Each sample was measured for 20 seconds consecutively by positioning the probe on the sample. Upon completion of each measurement a photograph of the sample in the cassette was taken, to facilitate accurate correlation of the TPI data with the final histology slide.

After the sample was scanned, the layer of Tegaderm was removed from the probe's quartz window and a 60 second air measurement was performed that was used as a reference for data processing (Section 2.3.2.3). For orientation purposes the top and the right surface of the tissue sample were then inked red and black respectively, after which the histology cassette containing the sample was closed, and placed in formalin for 24-48 hours, processed and paraffin wax embedded. Three to 4 micron sections were then cut and stained with haematoxylin and eosin (H&E). The histology slides were digitalised, and subsequently viewed and analysed using a histopathology slide viewer software (NDP.view2, Hamamatsu, UK).
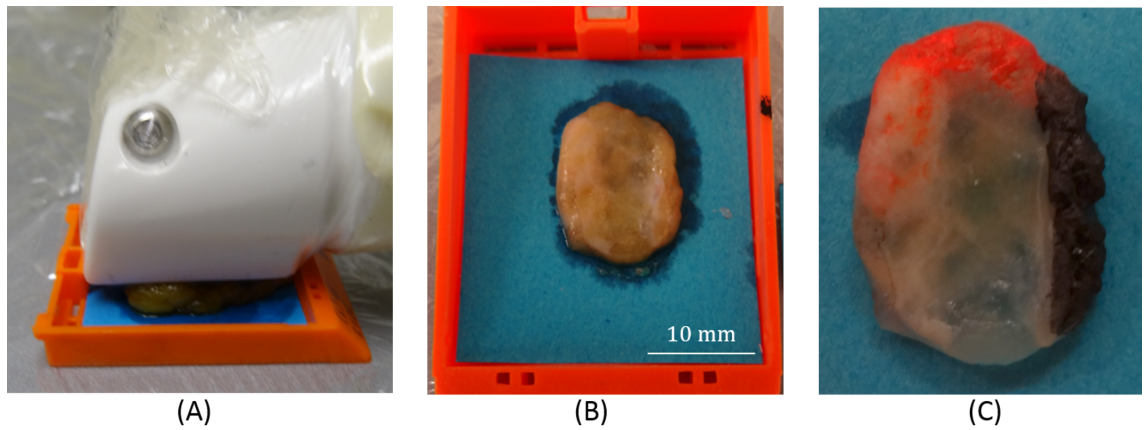
Figure 10: TPI measurement of tissue sample. (A) TPI handheld probe measurement of tissue sample positioned in histology cassette. Note that the head of the imaging probe tightly fits in the cassette, which facilitates applying a consistent pressure throughout the measurement, while preventing displacement of the probe. (B) Photograph of the tissue sample obtained after the sample was scanned. The imprint of the probe on the sample is clearly visible. This photograph was used to facilitate accurate correlation of TPI with histopathology. (C) Photograph of tissue sample after it was inked. Inking was performed to enable spatial orienation of the sample when analysed microscopically by the pathologist.

2.3.2.3 THz data processing

During data acquisition with the TPI handheld probe, each pixel acquired raw THz pulses throughout the duration of the measurement. These pulses were deconvolved to extract meaningful information for discriminating benign from malignant breast tissue. This was done by converting the raw THz pulses to the frequency domain using a Fast Fourier Transform function. A double Gaussian filter was applied to suppress the high and low frequency noise components. Waveforms were then divided by an "air without Tegaderm" reference that was acquired at the end of each measurement day. Referenced waveforms were converted back to the time domain, and aligned to compensate for small offsets in the phase of the detected pulses due to changes in the optical path length that occur when optical fibres in the umbilical cord slightly deform when the probe is moved during scanning (251). All these processing steps were performed using customised software written in Python (an open source programming language);

the software was developed in close collaboration with Teraview Ltd. (Cambridge, UK). The deconvolved pulses – called impulse functions - of each pixel were then imported into MATLAB (Mathworks, USA), and averaged over time, resulting in one impulse function for each pixel.

2.3.2.4 Correlation of TPI data with histopathology

Accurate correlation between the TPI image and the histopathology slide of each sample is paramount for evaluating the ability of the TPI handheld probe to discriminate benign from malignant breast tissue. Correlation was performed by mapping the TPI 15 x 2 mm scan area onto the digitalised pathology slide (Figure 11). To ensure accurate correlation, the following protocol was established. The imprint of the probe, visible on the photographs taken from each sample, was used to determine how the probe was positioned on the sample during measurement. The clear contrast between the air-tissue interface and adipose-fibrous/tumour interface on TPI, which is especially pronounced at time points t = 7.97 ps, t = 8.93 ps, and t = 9.67 ps, was used to determine the location and number of pixels that contained tissue information (Figure 11). By correlating the TPI information to the air-tissue interface and tissue composition on the histopathology slide, the 15 x 2 mm scan area was mapped onto the digital histopathology image in the viewer software (Figure 11). If the number of tissue-containing pixels on TPI and histopathology differed by more than three, the sample was excluded from further analysis, as accurate correlation could not be assured.
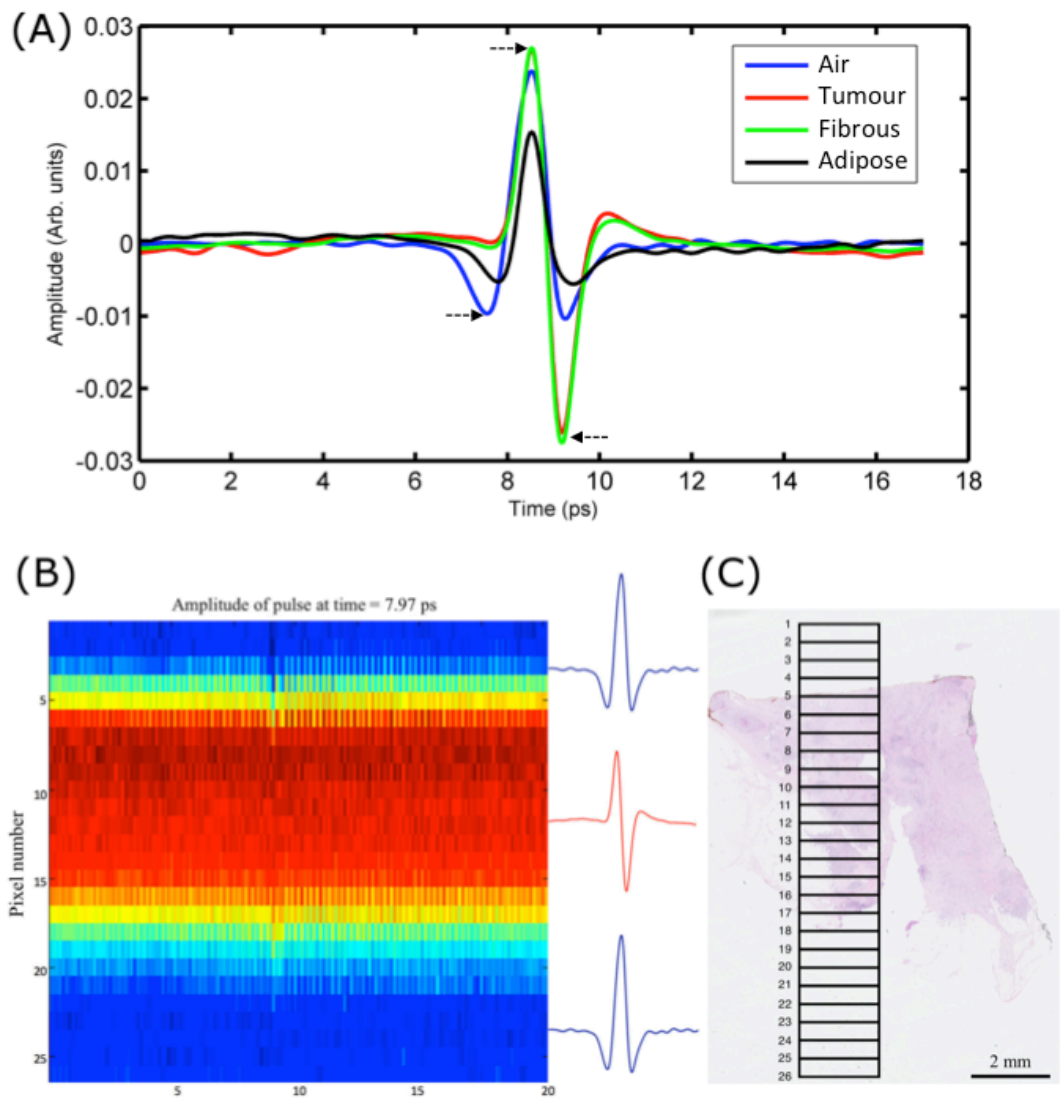
Figure 11: Correlating TPI with histopathology. (A) Typical impulse function from breast tissue containing a high percentage of tumour, fibrous, and adipose cells, and air, respectively. Clear differences are seen between the impulse functions from air and from tissue, and between adipose and tumour/fibrous samples, especially at time points t = 7.97 ps, t = 8.93 ps, and t = 9.67 ps (black arrows). (B) TPI image from sample based on the amplitude of the impulse function at t = 7.97ps. A clear contrast can be seen at the air-tissue interface at pixel 5 and pixel 17. Note the 'edge effect' at these interfaces, causing a distortion in the impulse functions of these pixels. (C) Digital histopathology slide of the same tissue sample. By using the photograph of the sample in combination with the air-tissue interface visible in the TPI image, the TPI 15 x 2 mm scan area can be accurately mapped onto the histopathology slide (black rectangle). The pixels are displayed as intermittent horizontal lines at 0.6 mm distance in the scan window. Pixel 5 – 17 contain invasive ductal carcinoma/no special type (NST); the percentage of tumour cells in each pixel area ranges between 5 – 10%. The tissue immediately surrounding the tumour cells (called background) is composed of fibrous tissue, whilst fatty adipose tissue is seen inferiorly.

2.3.2.5 Histopathological analysis and selection of TPI data

The digital histopathology slide of each sample was analysed in the viewer software by a Consultant breast histopathologist (S.E.P.). For each pixel, the histopathologist assessed the tissue types (tumour, fibrous, or adipose), and the percentage content of each tissue type present in the pixel area. Tissue percentages were reported in 5% intervals. In samples where the tumour type could not be reliably assessed (for example due to paucity of cells or crushing), the histopathologist used the clinical histopathology report to decide on the type of tumour present in the sample.

For a subset of samples an intra-rater variability analysis was performed to assess the ability of the histopathologist to consistently score the tissue samples used for this study. More specifically, the analysis aimed to determine how often a pixel would be assigned to a different tissue percentage subgroup when a second histopathological evaluation was performed. For this analysis, a total of 92 pixels from 7 tumour samples and 125 pixels from 7 benign samples were re-evaluated by the same histopathologist eight weeks after the first analysis. To prevent potential bias from *a prior* knowledge, the histopathologist was blinded to the results of the first analysis and not informed that a re-evaluation was performed. Weighted kappa coefficients were calculated to assess the agreement in subgroup classification between evaluation 1 and 2 (*kappa 2* function of the 'irr' package v0.84, R statistical software v3.2.2). A kappa coefficient (κ) greater than 0.80 was considered excellent agreement (317). A Wilcoxon signed-rank test was performed to assess whether evaluation 1 was statistically significantly different from evaluation 2. The level of significance was defined as $p < 0.05$.

The information on the tissue composition of each pixel, obtained from histopathology, was used to select region-of-interests (ROIs) in the TPI images. To avoid selecting distorted impulse functions that could occur due to "edge effects" present at the air-tissue interface (314) (Figure 11), ROIs needed to be one pixel away from the edge of the sample. To account for potential inaccuracies in the correlation between TPI and histopathology, which could result in selecting TPI data with a different tissue percentage or wrong tissue type, the pixel above and below the selected ROI needed to be of the same tissue type as the pixels in the ROI, and the percentage content of the respective tissue type could only differ by a maximum of 10%. Multiple ROIs could be selected within one tissue sample as long as these criteria were met.

Following ROI selection, pixels were grouped according to tissue type and tissue percentage (Table 9). Pixels containing tumour tissue, and pixels containing pure fibrous tissue or a mixture of fibrous and adipose tissue, were divided into groups of 20% (i.e. 1 – 20%, 21 – 40%, 41 – 60%, 61 – 80%, and 81 – 100%). Pure adipose pixels were grouped separately in a "100% adipose" group, as previous work has shown clear differences between the impulse function from adipose tissue and fibrous and tumour tissue, respectively (315).

2.3.2.6 TPI data analysis and classification

Classification of each of the selected impulse functions as malignant or benign was performed using two data analysis and classification methods: (1) heuristic parameters in combination with support vector machine (SVM) classification and (2) Gaussian wavelet deconvolution with Bayesian classification.

2.3.2.6.1 Parameters and SVM classifier

Each pixel from the handheld probe acquired data in the time domain, or through Fourier transform, in the spectral (frequency) domain. Characterization of the type of tissue can be done by calculating parameters from the acquired time domain pulses and frequency pulses, respectively. The ability of this so-called "heuristic approach" to discriminate benign from malignant breast tissue was assessed by classifying all pulses in the database using a SVM algorithm. This analysis was performed in MATLAB (Matlab 2013A, Mathworks Inc., USA) using a software script specifically developed for this project in close collaboration with collaborators from the University of Western Australia.

Several parameters were calculated that captured different parts of the pulse shape, including amplitudes, integrals, linear fits and quadratic fits. Many of these parameters can have a large range of time points and frequency points, further called indices, for which they can be calculated. From all parameters, a total of 733 different indices were evaluated. A receiver operating characteristic (ROC) analysis was performed to identify the optimal time or frequency index for each parameter (318). This analysis works by classifying the impulse function of each pixel from each sample as either malignant or benign, depending on whether the value of each parameter is below or above a specifically set threshold value. The predicted classification is then compared to the true histopathological classification to calculate sensitivity (the number of tumour pulses correctly classified as tumour) and specificity (the number of benign pulses correctly classified as benign). By plotting the sensitivity against 1-specificiy for various threshold values, a ROC curve is obtained. The area under the ROC curve (AUROC) is a measure of the predictive power (i.e. performance) of each parameter. The AUROC value ranges from 0-1; an ideal parameter has an AUROC of 1, whereas a

random guess would have an AUROC of 0.5. In this way, the best performing time indices for each time domain and frequency domain parameter could be identified. Figure 12 shows the AUROC values for the amplitude of the impulse function over a range of time indices.
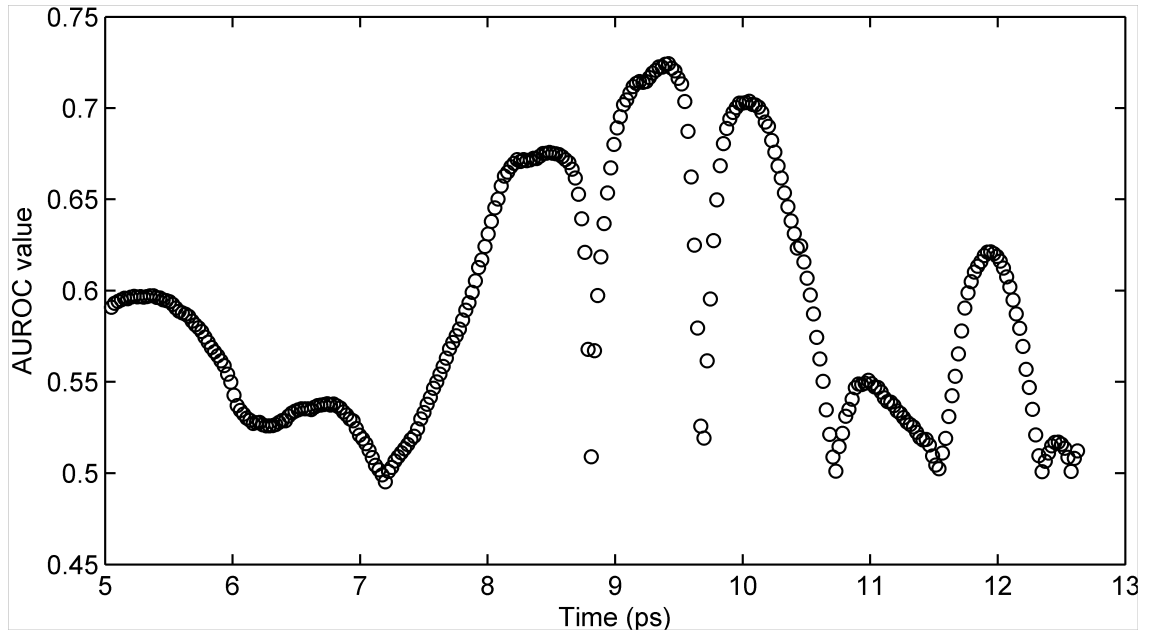
Figure 12: AUROC analysis to evaluate the discriminative power of the amplitude parameter for time indices 5.0 – 12.6 ps. The highest AUROC values of 0.72 and 0.70 were found at t = 9.42 ps and t = 10.05 ps respectively, and these two parameters were therefore selected for tissue classification with SVM.

The AUROC analysis was performed for three different subgroups of the dataset. Firstly, AUROC values were calculated using all tumour and all fibrous data. Pure adipose data was excluded from this analysis, as previous work has shown that adipose tissue can be easily identified due to the clear differences in the impulse function (315), and the emphasis in this work therefore was to find parameters that were strong in discriminating fibrous tissue from tumour. Parameters with an AUROC value ≥ 0.7 were selected. Secondly, to identify additional parameters that performed specifically well for the most challenging situation of discriminating tumour from pure fibrous tissue, AUROC values were

calculated using all tumour data and 100% fibrous data, and parameters with the highest AUROC value were selected. Lastly, to confirm that the selected parameters were also strong in discriminating tumour from pure adipose data, AUROC values were calculated using all tumour and 100% adipose data.

Correlation between parameters could potentially cause overfitting of the data, which affects the classification performance, as the noise in the data is captured as opposed to the real tissue signal, while reducing efficiency of the classification algorithm by increasing the dimensionality of the data (319). Thus, including correlated parameters in the analysis could result in a less robust and less reliable outcome, whilst increasing computational time. The selected parameters were therefore assessed for correlation by calculating the linear correlation coefficient r for all possible pairs of parameters. Parameters were considered correlated and excluded from analysis when $-0.7 < r > 0.7$.

Uncorrelated parameters were used in a SVM classification algorithm to predict the type of tissue for all impulse functions in the dataset. In SVM, a training data set is used in which each of the data points are marked to belong to one of two binary categories, i.e. tumour or benign. These data points are represented in a multidimensional space; the number of dimensions depends on the amount of parameters used for analysis. SVM then constructs a boundary to separate the data points of both categories. New data points obtained from a so called "validation dataset" are mapped into that same space, and based on which side of the boundary they fall on, each point is classified as tumour or benign, respectively.

Since 'close' or 'positive' margins of excision in BCS are often identified histologically as small number of tumour cells immersed in a benign tissue background of fibrous and adipose tissue, at the edge of a WLE specimen, it is a prerequisite that the TPI handheld probe is highly sensitive for detecting cancer.

To maximize the sensitivity of the probe to identify cancer, training of the SVM classifier was performed by marking pixels as tumour, if the pathologist had identified any amount of cancer cells in that pixel area. Fibrous and adipose pixels solely consisted of benign tissue. SVM classification was performed for each parameter individually, as well as for combinations of two, three or four parameters respectively, to identify the parameter(s) that provided the best classification result in terms of accuracy.

2.3.2.6.2 Gaussian wavelets and Bayesian classifier

Tissue classification was also performed using Gaussian wavelet deconvolution in combination with a Bayesian classifier. Gaussian wavelet deconvolution is a form of signal processing that uses different orders of Gaussian derivatives to expand the information in the signal, while reducing the noise (320). In contrast to heuristic parameters, Gaussian wavelet deconvolution can be applied to the full THz impulse function. This method was considered a suitable approach because of the similarities between the signal features of a Gaussian function and its derivatives (Figure 13), and the TPI impulse functions from breast tissue (Figure 11). Successful application of wavelet techniques to analyse THz data has also been demonstrated by other groups (321,322). For our analysis, Gaussian derivatives of order 0 (normal Gaussian function), 1, 2, 3 and 4 were applied to the impulse function of each pixel. Higher order Gaussian derivatives were not used to avoid potential overfitting.

The Gaussian deconvolved data were then fed into a Bayesian classification algorithm (319). In contrast to binary classification performed with SVM, the Bayesian algorithm can classify data-points into more than two classes; in our study all impulse functions in the dataset were classified as adipose, fibrous or

cancerous, respectively. Adipose and fibrous tissue were then grouped together as 'benign' in order to calculate the performance parameters described in Section 2.3.2.6.3. Similar to SVM, pixels were marked as tumour when containing any amount of cancer cells.
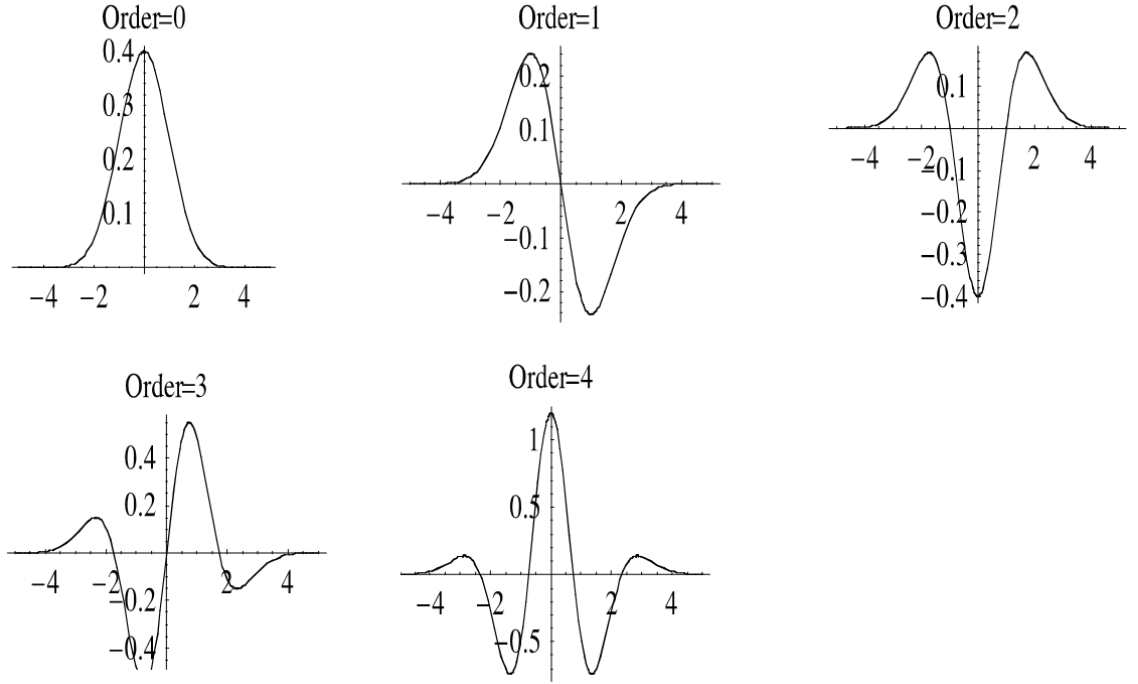
Figure 13: Gaussian derivatives of order = 0, 1, 2, 3, and 4, respectively

2.3.2.6.3 Classification of TPI data

Due to the relative small size of the dataset, training and validation of the SVM classifier and Bayesian classifier were performed using leave-one-out-cross-validation (LLOCV). In LOOCV, all pixels from one sample are left out, and the pixels from the remaining samples are used to train the classification algorithm. The trained algorithm is then applied to the pixels of the sample that was left out. This process is repeated for all the samples in the dataset to obtain classification results for all pixels. By comparing the predicted tissue type of each pixel to the true histological tissue type, accuracy, sensitivity, specificity, positive predictive value and negative predictive value were calculated using the equations in Table 8.

Accuracy is considered the most clinically relevant parameter for evaluating the performance of the TPI handheld probe as it takes both sensitivity and specificity into account, thus providing information on the overall ability of the probe to accurately detect both tumour and benign tissue.

Table 8: Equations used to calculate the performance of the classifiers. TP = true positive, FN = false negative, FP = false positive, TN = true negative, PPV = positive predictive value, NPV = negative predictive value, Acc = accuracy. All these performance parameters are multiplied by 100 (x100) to obtain percentages.

Predicted tissue type	**True histological tissue type**		
	Tumour	*Benign*	
Tumour	TP	FP	PPV = TP/(TP + FP)
Benign	FN	TN	NPV = TN/(TN + FN)
	Sens = TP/(TP + FN)	Spec = TN/(TN + FP)	Acc = (TP + TN)/ (TP + TN + FP + FN)

2.3.2.7 TPI handheld probe system stability

Water is considered a homogeneous liquid with well-known THz characteristics. Data acquired from water measurements therefore provides insight in the stability of the TPI handheld probe, as any fluctuations in the shape and intensity of the detected THz pulses are induced by the system itself. To assess the signal stability, parameter values were calculated from a total of 3 water measurements acquired on different measurement days.

2.3.3 Results

2.3.3.1 Tissue sample characteristics and histopathology intra-rater reliability

In total, 126 samples from 106 patients were scanned; 46 samples from 32 patients met the strict criteria established to ensure accurate correlation of TPI with histology, i.e. a photograph was available of the sample in the histology cassette, the number of tissue containing pixels on TPI and histopathology differed by 3 or less, and ROIs could be selected in areas with a tissue content varying less than 10%. These samples were included for analysis. Of these, 20 samples contained tumour; 16 invasive ductal carcinoma/no special type (NST), 2 NST admixed with DCIS, 2 invasive lobular carcinoma (ILC). Twenty-two samples contained pure fibrous tissue or a mixture of fibrous and adipose tissue, and 4 samples contained pure adipose tissue.

The total number of pixels for analysis was 257; 115 tumour pixels, 116 fibrous pixels and 26 pure adipose pixels (Table 9). The mean number of pixels selected per sample was 5 (range 1 – 17). The tumour pixels predominantly consisted of NST (N = 92) and ILC (N = 19). Most of the tumour pixels contained a low to moderate percentage of tumour cells ranging between 1 – 60% (N = 98). Almost all tumour cells had a background of pure fibrous tissue; only 5 had a background containing a mix of fibrous and adipose. Most of the fibrous pixels had a high percentage of fibrous cells ranging between 81 – 100% (N = 91). Only 26 of the 257 pixels consisted of pure adipose tissue.

The intra-rater reliability analysis showed excellent agreement in cell density subgroup classification between histopathological evaluation 1 and evaluation 2 (κ = 0.89) (p = NS). This confirmed that the established subgroups reliably reflected the tissue composition of the samples, and thus could be used to

evaluate the performance of the TPI handheld probe system for different tissue groups.

Table 9: Pixel characteristics TPI analysis dataset.

Tissue percentage groups (%)	Tumour					Fibrous		Adipose*
	NST	NST + DCIS	ILC	No. of pixels	BG	No. of pixels	BG	No. of pixels
81 – 100	3	1		4	F	91	A	26
61 – 80	11	2		13	F	2	A	
41 – 60	22		6	28	F	7	A	
21 – 40	33	1	12	46	F: 43 F/A: 3	3	A	
1 – 20	23		1	24	F: 22 F/A: 2	13	A	
No. of pixels	92	4	19	115		116		26

NST = invasive ductal carcinoma/no special type; DCIS = ductal carcinoma in situ; ILC = invasive lobular carcinoma; BG = background tissue. In our dataset the background consisted of fibrous tissue (F), adipose tissue (A), or a mixture of fibrous and adipose tissue (F/A).
*: these pixels contained 100% adipose tissue

2.3.3.2 Parameters and SVM classification

A total of 11 parameters were selected based on the AUROC analysis: 10 time domain parameters and 1 frequency parameter (Table 10). A visual representation of these parameters is shown in Appendix Figure 27. Most of the time domain parameters capture the area around the minimum amplitude of the pulse, and the return to baseline after the minimum. P1 – P7 were selected based on their overall ability of discriminating tumour from pure fibrous tissue and mixed fibrous and adipose tissue, while P8 – P11 were specifically selected to enhance the TPI probe's ability to discriminate tumour from pure fibrous tissue (Table 10). All 11 parameters showed strong discriminative power to distinguish tumour from pure adipose tissue (mean AUROC = 0.97, range 0.84 – 1.0).

Table 10: Overview of selected time domain and frequency domain parameters and their AUROC values.

Parameter	Definition	AUROC value (cell density group)[1]
P1	Quadratic fit 9.85 – 10.48 ps	0.76 (All T and F)
P2	Linear fit 9.42 – 9.67 ps	0.73 (All T and F)
P3	Amplitude at t = 9.42 ps	0.72 (All T and F)
P4	Integral 9.14 – 9.65 ps	0.72 (All T and F)
P5	Peak to peak (Emax minus Emin)	0.71 (All T and F)
P6	Emin (minimum amplitude)	0.70 (All T and F)
P7	Amplitude at t = 10.05 ps	0.70 (All T and F)
P8	Quadratic fit 8.26 – 8.79 ps	0.74 (1 – 20% T, 100% F)
P9	Integral 7.47 – 9.62 ps	0.83 (41 – 60% T, 100% F)
P10	Emax (maximum amplitude)	0.73 (81 – 100% T, 100% F)
P11	Power in spectrum at frequency = 1.11 THz	0.82 (61 – 80% T, 100% F)

1. T = tumour, F = pure fibrous tissue or a mixture of fibrous and adipose tissue, 100% F = pure fibrous tissue only

Table 11: Performance of heuristic parameters with SVM classification, and wavelet deconvolution with Bayesian classification. SVM classification results are shown for individual parameters and parameter combinations that performed best in terms of accuracy. The best individual parameter and parameter combination is underlined.

Parameters	Accuracy (%)	Sensitivity (%)	Specificity (%)	PPV[1] (%)	NPV[2] (%)
P1	_73_	_87_	_62_	_65_	_85_
P2	72	81	64	65	81
P3	70	77	65	64	78
P4	72	77	69	67	78
P5	72	92	56	63	90
P6	69	86	56	61	83
P7	69	87	54	61	84
P8	68	90	49	59	86
P9	56	69	46	51	64
P10	68	93	48	59	89
P11	56	56	57	51	61
P1 and P6	_75_	_86_	_66_	_67_	_85_
P1, P6 and P11	71	72	70	66	76
P1, P6, P9 and P11	67	56	75	65	68
Gaussian wavelets	69	87	54	60	84

1. Positive predictive value
2. Negative predictive value

The SVM classification results of the individual parameters, and the combination of parameters that performed best in terms of accuracy, can be found in Table 11. The performance of all parameter combinations can be found in Appendix Table 19, Appendix Table 20 and Appendix Table 21, respectively. Overall the combination of P1 and P6 provided the best performance with an accuracy, sensitivity, specificity, positive predictive value and negative predictive value of 75%, 86%, 66%, 67% and 85%, respectively. These values were obtained as a result of 16 of the 115 tumour pixels being misclassified as benign; 48 of the 142 benign pixels were misclassified as tumour. Of the misclassified tumour pixels, 10 pixels contained NST from a total of 7 samples. Six contained ILC; 5 of those were from a single sample. All misclassified tumour pixels had a tumour content ≤60%. Of the 48 misclassified benign pixels, 46 were fibrous pixels containing 81 – 100% fibrous cells; only 2 of the 1 – 80% fibrous pixels were misclassified as tumour, and

all 26 pure adipose pixels were correctly identified as benign. The two-dimensional parametric plot of P1 and P6 showed no clear differences between tumour and high percentage fibrous tissue (Figure 14A); this provides an explanation for why most of the SVM classification errors occurred in these two tissue groups (Figure 14B). Pixels with a high adipose content (1 – 80% fibrous pixels and pure adipose pixels) were generally clearly different from pixels containing a high percentage of fibrous tissue (81 – 100%) and cancer (Figure 14A). The accuracy, sensitivity, specificity, positive predictive value and negative predictive value for discriminating 1 – 80% fibrous and pure adipose tissue from tumour (i.e. excluding the predominantly fibrous group with 81 – 100% purity) was 87%, 86%, 96%, 98%, 75%, respectively.
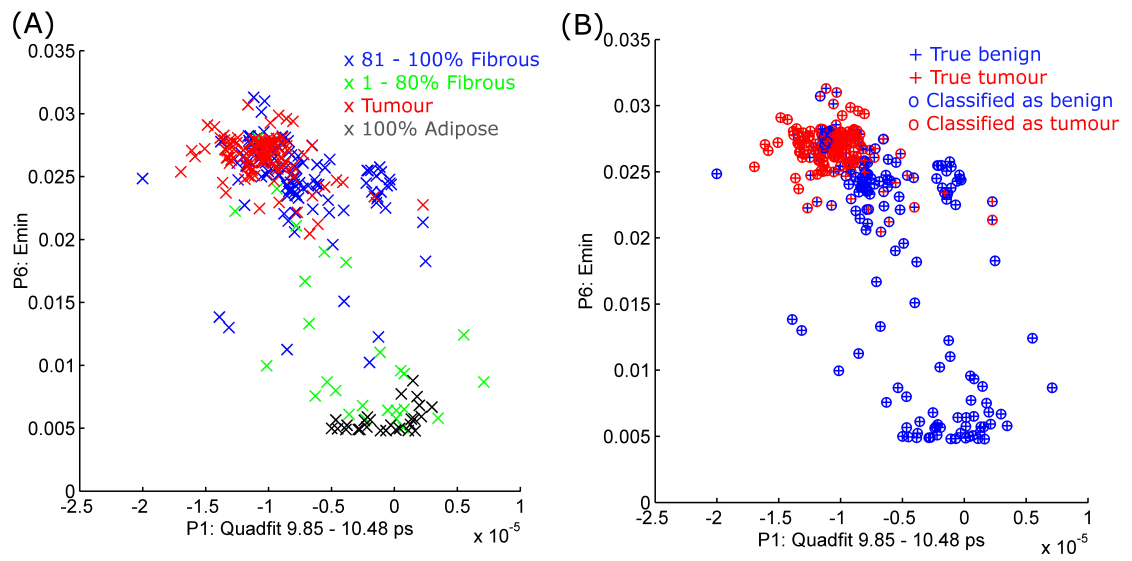
Figure 14: Two-dimensional parametric plot (A) and SVM classification results (B) for the combination of parameters P1 and P6 that performed best in terms of accuracy.

2.3.3.3 Gaussian wavelets and Bayesian classification

The accuracy, sensitivity, specificity, positive predictive value and negative predictive value of Gaussian wavelet deconvolution and Bayesian classification was 69%, 87%, 54%, 60%, 84%, respectively (Table 11). Of the 115 tumour pixels,

15 were misclassified as benign. Nine contained NST from a total of 4 samples. Six pixels contained ILC; 5 of those were from a single sample. All misclassified pixels contained ≤60% tumour cells.

Sixty-six of the 142 benign pixels were wrongly classified as tumour; 64 of these were 81 – 100% fibrous pixels, only two 1 – 80% fibrous pixels were misclassified. All pure adipose pixels were correctly classified. The accuracy, sensitivity, specificity, positive predictive value and negative predictive value of the handheld probe for discriminating 1 – 80% fibrous and pure adipose from tumour was 88%, 87%, 96%, 98% and 77%, respectively.

2.3.3.4 TPI handheld probe system stability

Figure 15 shows that there are clear differences in the THz pulses between measurement days. These differences are present in both the signal intensity (P11) and signal shape (P1 – P10). The 26 pixels of a single measurement also show differences, albeit less profound than the differences between measurement days. Variations within the 60-second measurement period were also observed as indicated by the large 95% CI of each individual pixel.
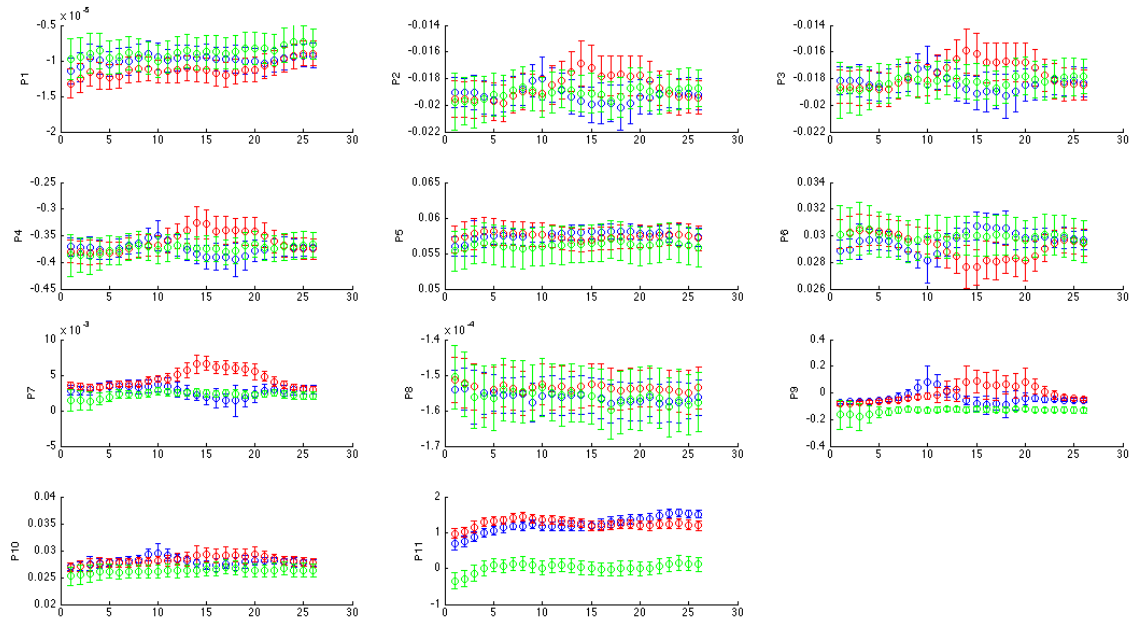
Figure 15: THz pulses from TPI handheld probe on 3 different measurement days shown in red, blue, and green, respectively. Parameter values and 95% CI are shown for all 11 parameters. The differences observed between measurement days and between pixels from a single measurement illustrate the challenges of the system in terms of signal stability.

2.3.4 Discussion

This first-in-human study has evaluated the performance of a TPI handheld probe system to discriminate breast cancer from benign breast tissue in an *ex vivo* setting. A total of 257 pixels acquired from scanning 46 breast tissue samples were included for analysis. The tumour samples predominantly contained low-to-moderate tumour cell percentages, resembling the tissue composition found at the resection border of WLE specimens from patients with positive margins. Two data analysis and classification methods were assessed: (1) parameters in combination with SVM classification and (2) Gaussian wavelet deconvolution with Bayesian classification. On the full dataset the former provided the best performance in terms of accuracy (75%). Both methods had excellent sensitivity (86% and 87%, respectively) and thus show promise for the identification of tumour at the margins of WLE specimens, allowing immediate further excision of appropriate

margins and reducing subsequent second operations/re-excision rates if the TPI handheld probe had been used intraoperatively. Specificity was 66% and 54% for SVM and Bayesian respectively; for both methods the lower specificity was due to pixels with 81 – 100% fibrous tissue that were wrongly classified as tumour. The accuracy, sensitivity and specificity increased to 88%, 87%, and 96% respectively, when discriminating samples with 1 – 80% fibrous and pure adipose tissue from tumour.

The reported pooled sensitivity and specificity of the established techniques to intraoperatively assess tumour margins during BCS are 53% (95% CI 45 – 61%) and 84% (95% CI 77 – 89%) for specimen radiography, 59% (95% CI 36 – 79%) and 81% (95% CI 66 – 91%) for ultrasound imaging, 86% (95% CI 78 – 91%) and 96% (95% CI 92 – 98%) for frozen section analysis, and 91% (95% IC 71 – 97%) and 95% (95% IC 90 – 98%) for imprint cytology, respectively (183) (Table 6). Thus, based on the results of the present study, the TPI handheld probe appears to perform similarly or better in terms of sensitivity, while the performance in terms of specificity is lower. Compared to specimen radiography and ultrasound, which are also imaging technologies, TPI has the potential advantage that image interpretation is not needed as the device can provide a binary read-out (tumour or no tumour). This may overcome the need for training that is required for obtaining ultrasound accreditation (Section 1.5.1.1). Potential advantages over the histopathological techniques frozen section analysis and imprint cytology are the fact that TPI is non-invasive (i.e. no physical tissue disruption is needed for assessing margin status), does not require an on-site cytologist or histopathologist, and allows for assessing a larger tissue surface.

There are currently a number of emerging imaging techniques that focus on enhancing intraoperative margin assessment. These include techniques based on

radiofrequency spectroscopy (MarginProbe), bio-impedance spectroscopy (ClearEdge), rapid evaporative ionisation mass spectroscopy (iKnive), and optical imaging techniques that utilize the visible or near-infrared part of the electromagnetic spectrum (diffuse reflectance spectroscopy, optical coherence tomography, near-infrared fluorescence imaging and Raman spectroscopy) (Section 1.5.1.2). Results published to date have shown a sensitivity and specificity of 70 – 75% and 46 – 70% for the MarginProbe, 87% and 76% for ClearEdge, 67 – 85% and 67 – 96% for diffuse reflectance spectroscopy, 60 – 100% and 69 – 92% for optical coherence tomography, 92% (95% CI 86 – 96%) and 97% (95% CI 93 – 98%) for Raman spectroscopy, and 93 – 100% and 91.9 – 100% for the iKnive (Table 7). Although the performance of the handheld probe in this first-in-human study is somewhat lower than some of these other emerging techniques, TPI uses a different region of the electromagnetic spectrum and thus provides complementary information. It is possible that combinations of technologies could significantly improve the overall accuracy of identifying involved margins.

Several papers have reported on the ability of TPI to discriminate freshly excised benign from malignant breast tissue (312,314,315,323). Ashworth *et al.* performed a small pilot study using a prototype version of the TPI handheld system (315); all other studies were conducted with systems not suited for intraoperative imaging of WLE specimens. Similar to the present results, they found that THz impulse functions from fibrous tissue and breast cancer had strong similarities, while impulse functions from adipose tissue had clearly different features. However, none of the TPI studies in breast cancer published to date have used a dataset representative of the tissue composition found at the resection border of patients with positive margins, as all tumour samples included for analysis contained >50% tumour cells. Thus, the results in our study are the first

that can be used to derive insight in the potential benefits of TPI in enabling more accurate and complete tumour resection in BCS.

The accuracy, sensitivity and specificity of the TPI probe for discriminating tumour from mixed fibrous and adipose tissue, and pure adipose tissue, was 87%, 86%, and 96% for SVM, and 88%, 87% and 96% for Bayesian, respectively. Discrimination of these tissue types is most relevant clinically, as the incidence of breast cancer is highest in older women, who are likely to have fatty or mixed fibrous and fatty breasts compared to younger women who may have more dense breasts primarily composed of fibrous tissue (324).

While the results of this feasibility study are promising, several limitations were noted. Firstly, there were marked differences in the THz pulses emitted by the TPI handheld probe system on different measurement days (Figure 15). By normalising the parameter value of tissue to the parameter value of water measured on the same day, one could adjust for this source of variation. This could improve the contrast between tumour and benign breast tissue, which ultimately could allow for more accurate tissue classification. Secondly, the 0.6 mm pixel distance used for correlating TPI and histopathology was based on a linear movement of the THz pulse beam across the 15 x 2 mm scan area. However, in practice the THz beam moves faster in the centre of the scan area and slows down upon reaching the top and bottom boundary, resulting in a larger distance between pixels located in the centre compared to the edges. This introduces a degree of inaccuracy, which was not accounted for in this study. Lastly, the current dataset does not contain THz pulses from cases of pure DCIS. These samples could not be assessed, as DCIS is generally non-palpable and particularly problematic to sample in the fresh state without impairment of gold-standard, formalin fixed, paraffin wax embedded histological assessment. However, DCIS is often the cause of the

clinical recommendation for re-operations in BCS; in some reports DCIS is found close or at the margin in up to 70% of patients (325). It is therefore of key importance to assess the sensitivity of the TPI handheld probe for detecting DCIS. A single centre study at Guy's Hospital will be conducted in which both classification methods, i.e. parameters in combination with SVM classification and wavelet deconvolution with Bayesian classification, will be applied prospectively on data acquired from fresh breast tissue scanned at the King's Health Partners Cancer Biobank. By acquiring TPI data from the cut surface of incised mastectomy specimens and from intact and incised WLE specimens, cases of DCIS as well as of invasive carcinoma will be included, without detrimental effect on patient management. TPI classification results of both classification methods will be compared to the histopathological results from the scanned tissue areas to assess diagnostic accuracy. By performing a DCIS subgroup analysis insight should be obtained on the ability of TPI to accurately detect DCIS. Depending on the performance on this prospective dataset, a subsequent study will be conducted in which the surgeon will use the system intraoperatively for real-time margin assessment. This study will evaluate the impact of the TPI handheld probe on re-excision rate and volume of excision as well as confirming accuracy of the technique.

In conclusion, the results of this first-in-human study show that the TPI handheld probe can discriminate invasive breast cancer from benign breast tissue with a high sensitivity and an encouraging degree of accuracy. The main challenge for TPI is accurate discrimination of cancer from tissue containing a high percentage of fibrous stroma, due to the similarities in the THz pulse between these two types of tissue. Based on the results of this feasibility study, another

single centre, *ex vivo* study will be conducted to further assess the performance of

the TPI handheld probe for detecting invasive disease as well as DCIS.

3. Cerenkov luminescence imaging for intraoperative tumour margin assessment in breast-conserving surgery

This chapter describes CLI and the application of CLI in image-guided cancer surgery, with a specific focus on assessing tumour resection margins in BCS. The first part of this chapter outlines the characteristics of Cerenkov radiation and CLI, and the results published to date on the use of CLI for image-guided surgery. The remaining part of this chapter focuses on the results of two-lead in studies and a first-in-human clinical study I have conducted to evaluate the feasibility of 2-deoxy-2-(^{18}F)fluoro-D-glucose (^{18}F-FDG) CLI for tumour margin assessment in BCS.

3.1 Introduction to Cerenkov luminescence and Cerenkov luminescence imaging

CLI is a novel imaging modality that was first used to image cancer *in vivo* in 2009 (326). CLI combines molecular and optical imaging by detecting Cerenkov photons emitted by positron emission tomography (PET) imaging agents. Cerenkov photons are emitted by a charged particle (positron or electron) when travelling through a dielectric medium at a velocity greater than the velocity of light in that medium.

The Cerenkov phenomenon seems to have been first observed by Marie Curie in the late 19th century. In her biography she describes observing a pale blue glow from the radium containing bottles in her laboratory. The first person to systematically describe Cerenkov radiation was Pavel Cerenkov, and together with Il'ja Mikhailovic Frank and Igor Yevgenyevich Tamm who developed the

theoretical framework, they won the Nobel Prize in Physics in 1958 for their contribution to the discovery of the Cerenkov effect. To a layperson's mind, Cerenkov radiation is the blue glow in the cooling water basins that surround nuclear reactors.

After its discovery in 2009, CLI has gained significant scientific interest in the field of biomedical imaging. A search of Embase and Medline performed on 28 December 2015 using the keywords 'Cerenkov Luminescence Imaging' provided a total of 103 and 59 articles, respectively. Several review papers have outlined the various applications of CLI including its use in Cerenkov luminescence imaging dosimetry (CLID), radionuclide therapy monitoring, tumour response monitoring and photoactivation therapy (327-331). An in-depth explanation of the complex physics underlying Cerenkov radiation and CLI has also been reported (332,333); a simplified explanation with an emphasis on the features that are relevant to image-guided surgery is provided in the following sections.

3.1.1 The basics of Cerenkov radiation

Cerenkov radiation is produced when a charged particle travels through a dielectric medium, i.e. a medium that can be polarised by an electric field, with a speed faster than the speed of light in that medium (334). When propagating, the charged particle (a positively charged positron or negatively charged electron) induces a local polarization by displacing the positive and negative charges of the atoms in the medium (Figure 16).
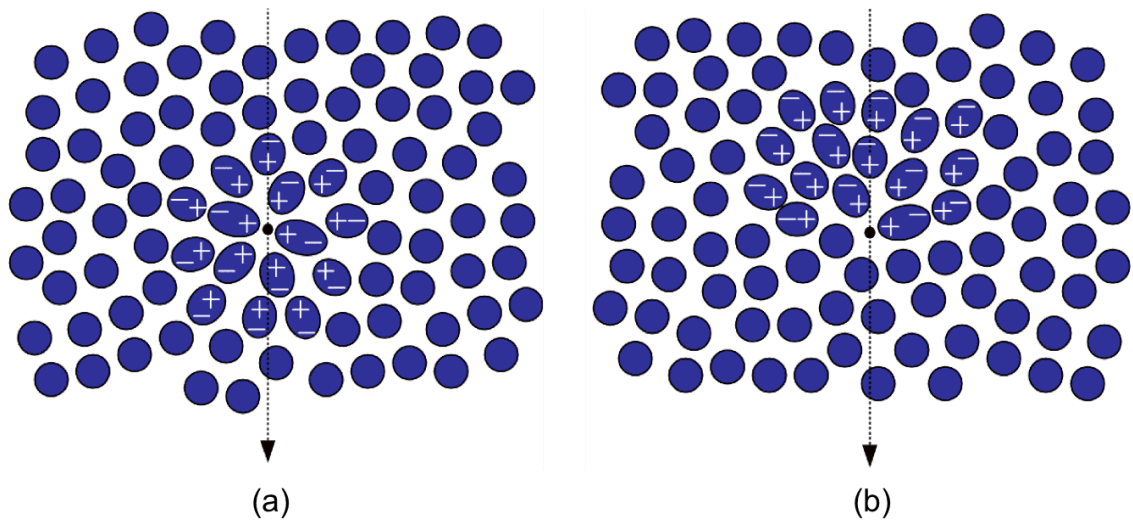
Figure 16: A charged particle, in this case an electron, passing through a dielectric medium with a) particle speed lower than speed of light in medium b) particle speed larger than speed of light in medium.

In a situation where the particle's velocity does not exceed the speed of light in that medium, the polarisation field surrounding the particle is perfectly symmetrical, and there is no electric field at larger distances. The net result is that no Cerenkov radiation is emitted. When the particle's speed exceeds the speed of light however, the polarisation becomes asymmetrical along the track of the particle, resulting in a dipole electric field at larger distances from the particle. As the particle passes the electrons of the atoms return to their ground state, thereby emitting the transferred energy as optical photons that are known as Cerenkov radiation. Thus, Cerenkov radiation is produced as secondary emission; it is not the charged particle generating light but the medium as a reaction to the particle.

For Cerenkov radiation to be emitted, the charged particle needs to exceed a certain energy threshold. This threshold is expressed by $v \geq c/\eta$, where v is the charged particle's velocity, c is the speed of light in vacuum, and η is the refraction index of the medium. From this expression becomes clear that the Cerenkov threshold is related to the refractive index of the medium. By using the relationship between the velocity of the particle and its energy as described by

equation 2 and 3 in Gill *et al.*, it is found that in water with a refractive index of 1.33 the threshold is 0.264 MeV (335). In soft tissues the refractive index typically ranges from 1.36 – 1.40, resulting in a threshold for the production of Cerenkov radiation of approximately 0.219 – 0.250 MeV. These thresholds are lower than the beta particle energies from radionuclides used in PET, and these radionuclides thus emit Cerenkov radiation in both water and tissue (336). As the charged particle travels through the medium it loses energy due to interactive processes with its surroundings including absorption and scattering, and eventually its energy falls below the threshold and Cerenkov light is no longer produced. For the much heavier alpha particles the Cerenkov threshold in water and tissue is 1926 MeV and 1673 MeV, respectively (337). Although none of the energies from existing alpha-emitting radionuclides come near this threshold (typical alpha particle energies range between 3 and 7 MeV), studies have shown emission of Cerenkov photons by alpha-emitters (337-339). There are two explanations for this observation, depending on the type of radionuclide: either photons arise from the short-lived beta-emitting daughter radionuclides of some alpha emitters (e.g. Actinium-225), or they are produced by electrons that arise from Compton scattered high-energy gamma photons. Regardless of the mechanism Cerenkov radiation from alpha emitters is thus produced indirectly by secondary beta particles. The pure gamma-emitter Technetium-99m (^{99m}Tc) is also able to produce optical photons as shown by several groups (340-342). Although the mechanism of this optical emission is not yet fully understood, it is assumed to be from OH radicals that are excited by the low energy Compton electrons (340) or from gamma excitation of the luminophores that are present in ^{99m}Tc based tracers (e.g. the amino acids in ^{99m}Tc-macroaggregates albumin) (342). This form of luminescence is known as radio luminescence and differs from Cerenkov radiation;

it has a different wavelength spectrum and its signal intensity is lower in tissue (343). The latter may provide additional challenges for its use in image-guided interventions, and the remainder of this section will therefore solely focus on Cerenkov radiation.

The number of Cerenkov photons N emitted per distance travelled x can calculated by using equation 1, which is derived from the Frank-Tamm equation (335):

$$\frac{dN}{dx} = 2\pi\alpha \left(1 - \frac{1}{\beta^2\eta^2}\right) \int_{\lambda_1}^{\lambda_2} \frac{1}{\lambda^2} d\lambda$$

Here is α the fine structure constant (1/137), β is the ratio between particle's velocity and the speed of light in vacuum (v/c), and the integral is over the interval λ_1 to λ_2. From this equation it follows that the intensity of the Cerenkov radiation depends on a particle's velocity, and thus its energy. Fluorine-18 (^{18}F), the most commonly used radionuclide in PET imaging, has an average and maximum β-energy of 250 keV and 633 keV, respectively. As a result, only 47% of the decays produce a positron that exceeds the energy threshold for production of Cerenkov radiation in water (332). Yttrium-90 (^{90}Y), a radionuclide often used in radiation therapy, has a much higher average and maximum β-energy of 934 keV and 2.28 MeV respectively, and 90% of its produced electrons are above the Cerenkov threshold in water. Gill *et al.* recently studied 47 radionuclides widely used in Nuclear Medicine, and used Monte Carlo simulations to quantify the expected Cerenkov light yield (photons/decay) for each radionuclide in tissue (η=1.4) (335). They found that ^{18}F emits 2.58 photons per decay in tissue; approximately 23 times less than the 58.5 photons per decay emitted by ^{90}Y. The light yield from some commonly used radionuclides in order from high to low are shown in Table 12. Although it is important to realise that the reported light yields do not take into

account the wavelength dependent absorption and wavelength dependent scattering that would occur in human tissue – this would reduce the number of detectable photons – it is clear that the signal intensity of CLI can be improved significantly by using higher-energetic isotopes. However, even with the use of such isotopes the Cerenkov light yield from a single radioactive decay process is low in comparison to, for example, the light yield from a single fluorescent molecule. Fluorescein and Indocyanine green (ICG), fluorophores used in fluorescence image-guided surgery, emit roughly 3 orders of magnitude more photons (344). This low light yield requires strict control of the light environment to obtain a sufficient signal-to-background ratio (SBR) when using CLI in an intraoperative setting as explained below.

Another characteristic of Cerenkov light is its broad emission spectrum that ranges from approximately 400 – 900 nm (326). The light intensity is inversely proportional to the square of the wavelength ($1/\lambda^2$). This is why Cerenkov radiation is strongest towards the blue end of the visible spectrum, and hence why Cerenkov radiation appears blue.

The fundamental resolution of Cerenkov radiation is determined by the distance over which a β-particle emits light. It was found that for ^{90}Y and ^{18}F this distance is approximately 2 mm and 0.3 mm, respectively (332). This shows that lower-energetic tracers have a better physical resolution limit, but the downside is a lower light yield and thus sensitivity.

Table 12: Relevant characteristics of Cerenkov radiation and CLI for image-guided cancer surgery.

Cerenkov radiation definition	Optical radiation emitted by charged particles when travelling through a dielectric medium with a speed larger than the speed of light in that medium
Threshold energy for Cerenkov radiation emission (335)	Water (η=1.33): 0.264 MeV Biological tissue (η=1.36 – 1.40): 0.219 – 0.250 MeV
Cerenkov radiation is emitted by	β^+, β^-, and α-emitting radionuclides
Cerenkov intensity from radionuclides most commonly used in clinic in order from high to low (335)	$^{90}Y > {}^{68}Ga > {}^{15}O > {}^{124}I > {}^{11}C > {}^{89}Zr > {}^{18}F > {}^{131}I > {}^{64}Cu$
Cerenkov radiation spectrum (326)	400 - 900 nm
Fundamental resolution (332)	0.3 - 2.00 mm
Camera requirements for Cerenkov radiation detection	High-sensitivity optical cameras with single-photon detection capability
Typical penetration depth in tissue	<1 cm (depending on tissue composition and radionuclide)
Typical CLI acquisition times	1 – 5 min
Types of images acquired with CLI	Photographic image: anatomical information Functional image: information on the uptake and location of the radiopharmaceutical
Advantages of CLI for image-guided cancer surgery	Ability to use clinically approved tumour-targeted radiopharmaceuticals Potential for multi-modality imaging with the same tracer: preoperative imaging with gamma-camera, PET or SPECT, intraoperative imaging using CLI +/- beta-probe or gamma-probe Small form factor of CLI equipment allowing implementation of CLI technology in intraoperative specimen chamber, flexible endoscope and rigid laparoscope External excitation source not required: less tissue autofluorescence
Challenges of CLI for image-guided cancer surgery	Faint signal Light-tight imaging conditions required Radiation dose to patient and staff Strict regulations for use of radiotracers Complex logistics that requires close multi-disciplinary team work

3.1.2 Characteristics of Cerenkov luminescence imaging from an image-guided surgery perspective

CLI images can be acquired by detecting the Cerenkov light from PET tracers using ultra-high sensitivity optical cameras such as electron-multiplying charge coupled device (EMCDD) cameras. The CLI image can be analysed semi-quantitatively in photon radiance. CLI and PET are directly correlated due to both techniques measuring the photons produced by positron-emitting radiopharmaceuticals; PET measures the annihilation photons and CLI measures the Cerenkov photons. Several studies have shown a strong correlation between CLI and PET for different radiopharmaceuticals *in vitro, ex vivo* an*d in vivo*, thus demonstrating the feasibility of CLI for molecular imaging of living subjects. An overview of the published literature on the correlation between CLI and PET is provided in Table 13. This table also includes results on the correlation between CLI and radiotracer activity.

There are several reasons why CLI has sparked so much interest in the field of biomedical imaging, and why it is a promising technology to guide surgical resection. Firstly, CLI images can be acquired with clinically approved tumour-targeted radiopharmaceuticals that have been used for over two decades in molecular medical imaging (336). This provides great potential for rapid translation of CLI into clinical practice. Especially the possibility to use the most commonly used PET radiopharmaceutical ^{18}F-FDG, facilitates wide clinical adoption of CLI, as this is a versatile tracer that can be used in several solid cancers, including melanoma, lung, colorectal, head and neck, breast and oesophageal cancer (345).

Table 13: Literature overview on the correlation of CLI and PET.

CLI parameter	PET parameter	Correlation between CLI and PET	Radiopharmaceutical	In vivo, in vitro, ex vivo	Ref
Radiance	%ID/g	R^2=0.93, 0.95, 0.93, 0.89	^{18}F-FDG	*In vivo*	(346)
Radiance	%ID/g	R^2=0.97	^{18}F-FDG	*In vivo*	(336)
Radiance	Activity	R^2=0.95	^{18}F-FDG	*In vivo*	(347)
Radiance	Activity	R^2=0.98	^{18}F-FDG	*In vivo*	(348)
Radiance	Activity conc.	R=0.51	^{18}F-FDG	*In vivo*	(349)
Radiance	%ID/cm^3	R^2=0.83	^{18}F-FDG	*In vivo*	(350)
Radiance	%ID	R^2=0.82	^{18}F-FDG	*In vivo*	(350)
Radiant vol.	Glycolytic vol.	R^2=0.99	^{18}F-FDG	*In vivo*	(350)
Radiance	Activity	R^2=0.99	^{18}F	*In vitro*	(351)
Radiance	Activity	R^2=0.97	^{18}F-FDG	*In vitro*	(352)
Radiance	Activity conc.	R^2=0.99	^{18}F-FDG	*In vitro*	(349)
Radiance	Activity	R^2=0.97	^{18}F-FDG	*Ex vivo*	(347)
Intensity	Activity conc.	R^2=0.98	^{68}Ga	*In vitro*	(353)
Intensity	Activity conc.	R^2=0.99	^{68}Ga	*In vivo*	(353)
Radiance	%ID/g	R=0.89	^{89}Zr-trastuzumab	*In vivo*	(354)
Radiance	%ID/g	R=0.98	^{89}Zr-J591	*In vitro*	(338)
Radiance	Activity conc.	R=0.98	^{89}Zr-J591	*In vitro*	(338)
Radiance	%ID/g	R^2=0.85	^{89}Zr-rituximab	*In vivo*	(355)
Radiance	Activity	R^2=0.98	Na-^{131}I	*In vitro*	(356)
Radiance	Activity	R^2=0.99	^{131}I-NGR	*In vitro*	(357)
Radiance	%IA/g	R^2=0.94, 0.98	^{90}Y-DOTA-AR	*In vivo*	(358)
Radiance	%IA/g	R^2=0.91, 0.99	^{90}Y-DOTA-AR	*Ex vivo*	(358)

The ability to use clinically approved tumour-specific tracers is an important advantage over conventional optical imaging techniques such as targeted near-infrared fluorescence imaging, as to date there are no tumour-specific fluorescent tracers that have been approved by the Food and Drug Administration (FDA) or European Medical Agency (EMA) (236). Targeted fluorescence imaging faces a significant commercial hurdle for clinical adoption because the process of obtaining regulatory and reimbursement approval is costly and lengthy (234), while the revenue of imaging agents is often low compared to therapeutic agents, which makes it a significantly less interesting investment for industry (235,359) (Section 1.5.1.2).

In addition to the already approved PET tracers a significant number of new tracers are being developed for market approval including ^{18}F-FES, ^{68}Ga-PSMA, ^{68}Ga-DOTATOC, ^{18}F-NaF, ^{18}F-Choline, and ^{18}F-FDOPA (360,361).

The ability to use the same tracer for both CLI and PET or SPECT enables dual-modality molecular imaging. PET and SPECT provide preoperative information on the location and extent of the tumour, while CLI can be used as an intraoperative adjunct to aid lesion identification and guide surgical resection. The use of the same tracer ensures visualisation of the same structures and facilitates a more accurate comparison between modalities. Depending on the patient pathway and half-life of the tracer, preoperative and intraoperative imaging could be performed using only one tracer injection, or by re-injecting the tracer. By capturing a white-light image with a standard camera at the time of CLI image acquisition, the functional information from the CLI image can be combined with the anatomical and structural information from the photograph, thereby providing the surgeon with information on the nature, location and extent of the cancerous tissue.

Beta-emitting radiopharmaceuticals can also be detected by a beta-probe or gamma-probe (362-364), so these tools could potentially be used in addition to CLI-guided surgery to overcome the limited penetration depth of CLI as a result of absorption and scattering.

The optical imaging systems required to acquire CLI images can be small in dimension or use fibreoptics or laparoscopic capabilities. Unlike a PET system this provides the ability to use CLI in an operating theatre or in endoscopy equipment, and examples of such applications are provided in Section 3.2.

CLI faces a number of challenges for routine clinical adoption. As mentioned earlier Cerenkov luminescence is very faint due to the small number of optical Cerenkov photons emitted by charged particles. In biological applications the signal intensity is further reduced by strong tissue attenuation from chromophores like (oxy)haemoglobin and light scattering, which is more pronounced in the 400 – 650nm range (365,366). Consequently the acquisition time required to obtain high-resolution images with a sufficient signal-to-noise ratio (SNR) is longer than with conventional optical imaging. Typical imaging times in pre-clinical and clinical CLI studies range from 1 to 5 minutes (Table 14). When imaging with handheld devices (e.g. endoscopes) it is essential that during image acquisition the device is not moved as this causes blurring of the image resulting in a reduced image quality. In an *in vivo* environment this may prove especially difficult due to abdominal activity and breathing artefacts, and motion-correction algorithms may be needed to correct for this.

The weak light intensity also requires a light-tight environment, as any leakage of ambient light will overwhelm the CLI signal. Since Cerenkov radiation is strongest in the visible wavelengths it cannot be spectrally separated from the

much brighter ambient lights currently used in operating theatres. Control of the light environment is therefore currently achieved by imaging in a light-tight specimen chamber or room with light-sealed doors, or in anatomical areas that provide natural darkness (e.g. gastrointestinal tract).

An often mentioned limitation of optical imaging in general is the limited light penetration depth and thereby the inability to image deep located tissue. This was nicely illustrated by Chin *et al*., who calculated the reduction in signal intensity from one ^{18}F-isotope and one ICG molecule in 1mm of tissue, and found a reduction in signal intensity of 77% and 39%, respectively (344). Because Cerenkov light is 'blue-weighted' and tissue absorption and scattering are significantly increased for these wavelengths, CLI is mainly applicable for imaging superficially located tissue, and specifically suited for imaging tumour cells within a few millimetre from the resection border.

Due to the half-life dependency of radiotracers, the window in which CLI imaging needs to be performed to obtain a sufficient SNR and image quality is limited. Well-designed logistics and close collaboration between nuclear medicine, radiology and surgical departments are therefore a prerequisite for the successful implementation of CLI in current clinical and surgical workstreams.

A challenge for CLI-guided surgery in particular is the radiation exposure to patients and theatre staff from using radiopharmaceuticals. For patients the effective dose from a 300MBq ^{18}F-FDG injection is approximately 6mSv; this is comparable to the radiation dose for a typical chest CT scan (367) and much lower than the 20-2500 mSv radiation exposure from diagnostic and interventional fluoroscopy procedures (368). Staff members that work in close proximity of the patient during surgery are also exposed to radiation. The received radiation dose is dependent on the time between injection and the start of the interventional

procedure, the proximity to the patient, and the duration of the procedure. Various groups have published staff radiation doses from ^{18}F-FDG-guided cancer surgery procedures (369-371), and have shown that the radiation dose received per procedure is generally low. For example, for a 105 minute procedure starting approximately 1 hour after injection of 370MBq ^{18}F-FDG, the exposure to the surgeon was 42 μSv (369). However, depending on the national annual occupational dose limit (50mSv in the United States and 20mSv in the United Kingdom and most other countries) and type of procedure, the number of procedures an individual can perform per year without exceeding the permissible limits for professional workers may be restricted. Regardless of these limits, there are strict requirements for the use of radioactivity in clinical practice. For example, routine staff monitoring is a requisite for each institution that conducts radiotracer guided procedures, strict regulations need to be followed with regards to clinical waste disposal and handling of radioactive specimens, and staff need to attend radiation safety training prior to participation in any procedure involving radiation (372). These requirements could hinder adoption of radioguided surgical technologies, especially in small district hospitals that do not have access to nuclear medicine or radiation safety departments.

An overview of the aforementioned characteristics of Cerenkov radiation and CLI in light of image-guided surgical applications can be found in Table 12.

Table 14: Overview of published studies on CLI-guided surgery.

Pre-clinical or clinical	Indication	Tumour type	Tracer	Dose	CLI device	Acquisition time	Ref
Pre-clinical	CLI-guided tumour resection	HER2+ breast cancer	[89]Zr-DFO-trastuzumab	4 MBq	Ivis optical imager	2 – 5 min	(354)
Pre-clinical	CLI-guided tumour resection	Glioblastoma	[68]Ga-3PRGD2	3.7 MBq	Ivis optical imager	1 – 5 min	(373)
Pre-clinical	Cerenkov luminescence endoscopy	Brain glioma	^{18}F-FDG	37 MBq	Custom-build flexible fibre endoscope light-tight box	5 min	(374)
Pre-clinical	Cerenkov luminescence endoscopy	Glioblastoma	^{90}Y-PRGD2, ^{18}F-FP-PRGD2	8.1 MBq, 33 MBq	Custom-build flexible fibre endoscope light-tight box	6 min	(375)
Pre-clinical	Cerenkov luminescence endoscopy	Colon cancer	^{18}F-FDG	24 MBq	Clinically approved rigid laparoscope coupled to emCCD camera in light-tight box	5 min	(376)
Clinical	Cerenkov luminescence endoscopy	Rectal cancer	^{18}F-FDG	9.25 MBq/kg	Clinically approved flexible fibre endoscope coupled to emCCD camera	5 min	(348)
Pre-clinical	CLI-guided lymph node mapping	N/A	^{68}Ga-SPIONs[1]	5 – 10 MBq	CCD camera positioned in light-tight box	2 -10 min	(377)
Pre-clinical	CLI-guided lymph node mapping	N/A	^{18}F-FDG	1.2 MBq	Ivis optical imager	2 min	(378)

1. SPIONs: Superparamagnetic iron oxide particles

3.2 Applications of Cerenkov luminescence imaging for image-guided surgery

Various research groups have been successful in using CLI for image-guided surgical interventions, despite the limitations mentioned in the previous section. The section below provides an overview of the results published to date, including two clinical applications of CLI that are not directly related to image-guided surgery.

The majority of the work published to date on the use of CLI to guide surgical excision is pre-clinical, although one clinical study was also published recently (Table 14). These studies show the ability to perform CLI-guided surgical excision of tumours using a variety of radiopharmaceuticals (clinically approved as well tracers used for research purposes only) and different CLI embodiments, including standard Ivis optical imaging systems, custom-build flexible fibre endoscope systems, and clinically approved rigid laparoscope and flexible endoscope systems coupled to emCCD cameras. An example that nicely illustrates CLI-guided tumour excision is shown in Figure 17.

An important advantage of using CLI in an endoscopic setting is that these make use of anatomical dark chambers, so that there is no interference from external light sources. Besides, this technology can also be implemented in other types of endoscopes such as a bronchoscope or hysteroscope, and future applications of CLI could for example focus on lung cancer, endometrial cancer and metastatic lymph nodes in the abdomen, pelvis and thorax. .

CLI has also been successfully used for lymph node identification and image-guided lymph node excision using ^{18}F-FDG and ^{68}Ga-labelled superparamagnetic iron oxide particles (SPIONs) (Table 14).
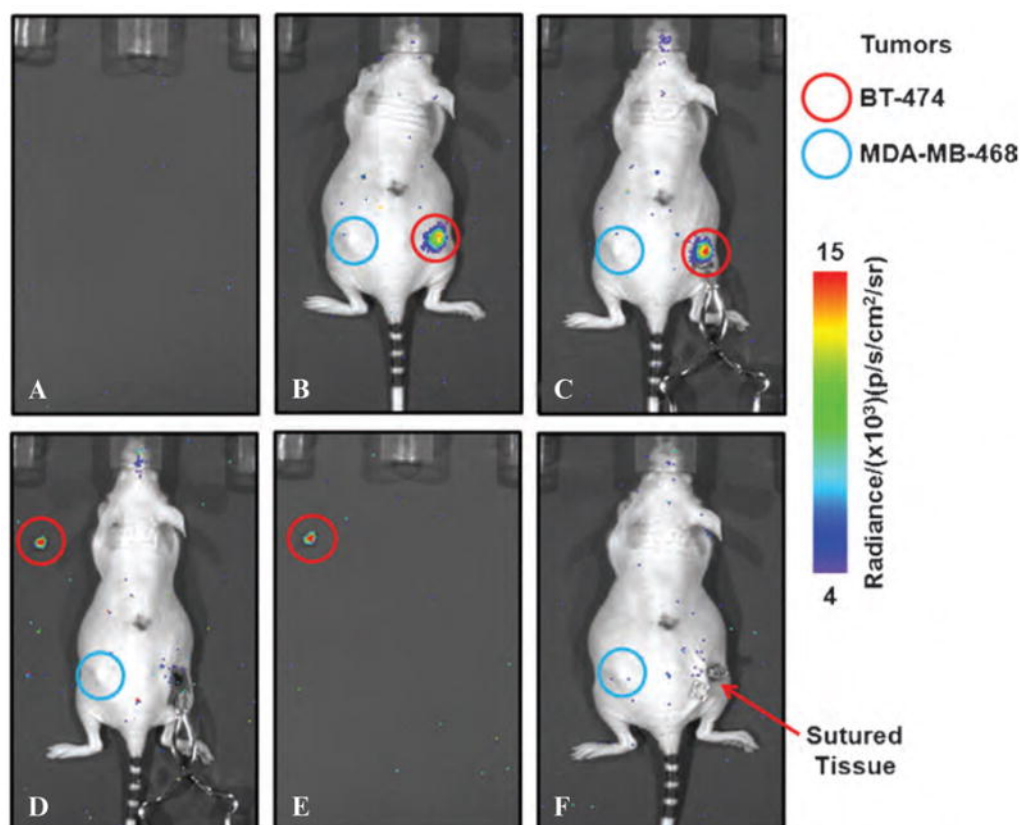
Figure 17: ^{89}Zr-DFO-trastuzumab CLI guided tumour excision. A) Empty background image acquired prior to surgery. B) Image acquired pre-incision and C) post-incision when the tumour was exposed after the skin was removed. D) Image of the post excision surgical cavity and the excised tumour (left top corner). No CLI signal is left at the excision site, thus indicating complete removal of the tumour. E) Image of excised tumour alone F) Image acquired straight after the surgical wound was closed with sutures. *Image was reproduced from (354) with kind permission from SAGE Publications.*

Two other interesting clinical applications of CLI, although not directly related to image-guided surgery, were also published recently. Spinelli *et al.* imaged the thyroid gland of a patient treated for hyperthyroidism who received 550MBq of Iodine-131 (^{131}I) (379). By using an emCCD camera positioned in a light-tight room, tracer uptake in the thyroid could be visualised with a 2-minute exposure time. This application is of clinical interest as imaging the uptake of beta-emitting radiopharmaceuticals could provide a rapid and inexpensive alternative for monitoring radiation doses given to superficial organs.

Thorek *et al.* evaluated CLI for non-invasive detection of nodal disease in a preoperative clinical setting (349). Patients with lymphoma, leukaemia and

metastatic lymphadenopathy scheduled to undergo standard clinical ^{18}F-FDG PET were included. CLI imaging was performed immediately after the PET-scan in a dark room with a single-photon sensitive camera positioned on a standard photography tripod. The preliminary results from four patients (2 lymphoma, 1 lung cancer and 1 breast cancer) showed that metastatic lymph nodes in the neck or axilla had a statistically significant higher Cerenkov signal than negative nodes (p = 0.02), and this finding strongly correlated with the results from PET. Figure 18 shows an example of a positive and negative axillary lymph node on preoperative CLI and PET, respectively.
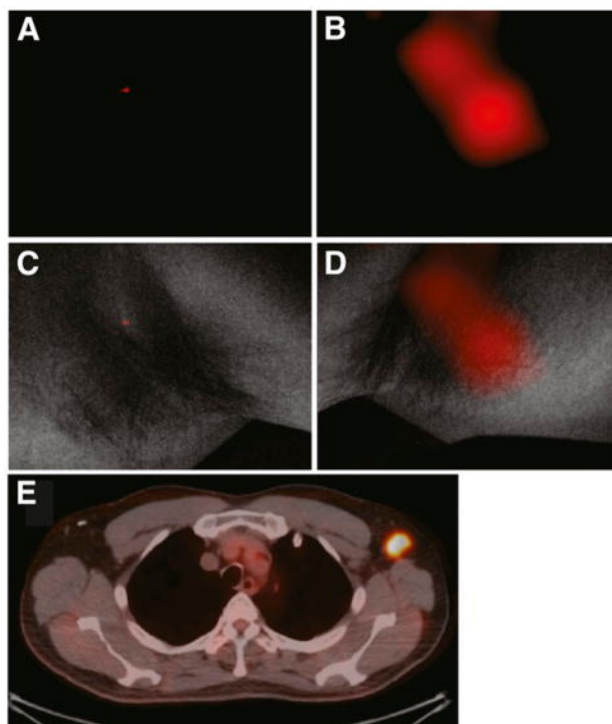
Figure 18: CLI and PET/CT image of a patient with a positive and negative node in the left and right axilla, respectively. CLI image and grey-scale photographic image overlaid with Cerenkov signal of negative node (A and C) and positive node (B and D). The CLI signal from the positive lymph node colocalized with the increased signal on PET/CT. *This research was originally published in (349) by the Society of Nuclear Medicine and Molecular Imaging (SNMMI), Inc.*

A patient population that can benefit from accurate preoperative identification of nodal disease are breast cancer patients with involved lymph nodes. If positive lymph nodes are identified preoperatively on CLI their treatment could convert

from SLNB to immediate ALND, thus preventing the patient from undergoing an unnecessary surgical procedure. Alternatively, these patients may undergo neoadjuvant chemotherapy followed by SLNB +/- ALND. Completion of this study (ClinicalTrials.gov Identifier NCT01664936) will provide insight in the real value of CL imaging in aiding medical and surgical decision-making preoperatively.

3.2.1 Summary

CLI is a fast-emerging optical imaging technology that has rapidly progressed from bench to bedside. This rapid development has been facilitated by the ability to use clinically approved tumour-targeted PET tracers including ^{18}F-FDG. Its high-resolution, wide applicability across a range of solid cancers, and small size imaging equipment makes CLI a suitable technique for image-guided surgery in general, and intraoperative margin assessment in particular due to the millimetric penetration depth of Cerenkov luminescence. The last section of this chapter describes the first-in-human study conducted to evaluate the feasibility of intraoperative ^{18}F-FDG CLI for margin assessment in patients undergoing BCS. Prior to commencement of this first-in-human study two lead-in studies were performed to assess the ^{18}F cross-talk and to determine the activity of ^{99m}Tc-nanocolloid required to successfully perform standard of care SLNB in patients undergoing ^{18}F-FDG CLI-guided surgery. These lead-in studies are described in the next section.

3.3 Lead-in studies to assess gamma probe cross-talk from ^{18}F and to determine the ^{99m}Tc dose required to successfully perform standard of care sentinel lymph node biopsy in patients undergoing ^{18}F-FDG CLI guided surgery

One of the main routes for breast cancer metastasis is via the lymphatic system towards lymph nodes, predominantly to lymph nodes located in the axilla (Section 1.3.2.2). SLNB is the standard method of staging the axillary lymph nodes in clinically and radiologically node negative breast cancer patients. The SLN is defined as the node receiving direct lymphatic drainage from the tumour, and therefore considered to have the highest chance of harbouring cancer cells if the primary breast tumour metastasizes. If the SLN is free of cancer cells, the other lymph nodes in the axilla are also considered to be free and further axillary treatment can be omitted. SLNB is often performed at the same time as BCS, and standard practice at Guy's Hospital is based on the combined technique of blue dye and the radioisotope ^{99m}Tc. Both tracers are injected locally in the breast, and after the tracers are accumulated in the SLN, the surgeon uses a gamma probe (handheld scintillation counter) and/or the discolouration from the blue dye to locate the SLN.

The presence of ^{18}F-FDG in subjects undergoing ^{18}F-FDG CLI-guided surgery (Section 3.4) will result in a greater than normal background signal being detected by the handheld gamma probe due to the down-scatter of 511keV ^{18}F gamma photons into the ^{99m}Tc energy window. This cross-talk background could potentially hinder detection of low-activity SLNs in patients undergoing SLNB at the time of BCS.

3.3.1 Aim

Two lead-in studies were conducted prior to commencement of the intraoperative ^{18}F-FDG CLI study to assess the ^{18}F cross-talk and to determine the ^{99m}Tc dose required to successfully perform standard of care SLNB in patients undergoing ^{18}F-FDG CLI guided surgery.

3.3.2 Materials and Methods

3.3.2.1 Lead-in study I: SLNB simulations using the GAPS simulator

To determine the effects of the cross-talk background on the detectability of radioactive lymph nodes, a simulation study was performed using the computerized gamma probe simulator (GAPS) (Figure 19) (380). The GAPS system has previously been used in the UK national breast SLNB training program 'NEW START', and provides simulations of the radioactivity distribution and gamma probe response that allows accurate objective assessment of the surgeon's ability to localise SLNs on the surface of a manikin of the female breast and axilla.
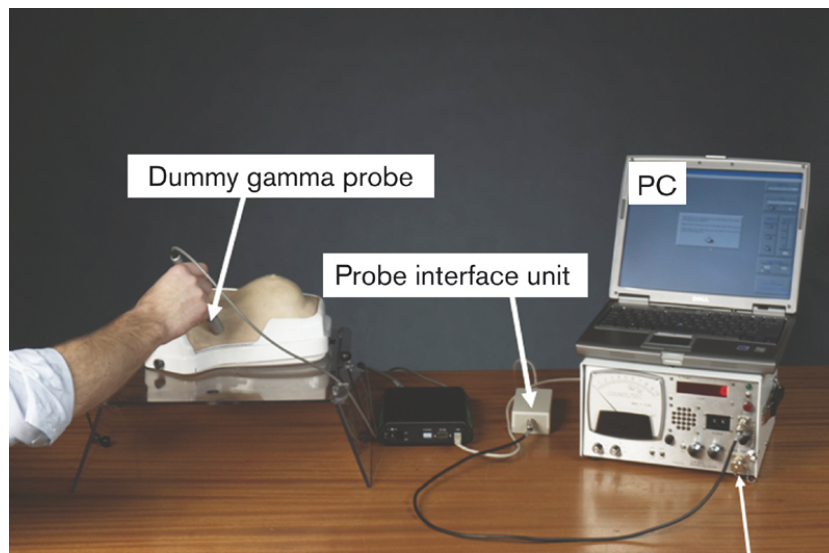
Figure 19: Computerized gamma probe simulator (GAPS). The PC is connected to the dummy gamma probe via the interface unit, which allows tracking the position of the gamma probe in relation to the virtual lymph node. During the SLNB simulations the PC screen was turned away from the surgeons so they were blinded to their localisation results. *Image was reproduced from (380) with kind permission from Wolters Kluwer Health.*

The measurements were performed by two breast surgeons (AP and AK), with extensive experience of performing SLNB procedures. After one test case to familiarize the surgeons with the GAPS system, each surgeon was presented with 3 simulated SLNB cases individually. In each case the injection site, two SLNs and a spatially uniform ^{18}F background signal with Poisson distributed noise were simulated. The simulated SLN count rates ranged between 56 and 373 counts per second (cps), and were based on a 150MBq ^{99m}Tc injection, a SLN tracer uptake ranging from 0.06% to 0.4% of the administered dose, an average SLN depth (30mm from the axillary skin surface) (381), and a time between tracer injection and SLN detection of 3 hours, which is common for 1-day SLNB protocols. The dose of 150MBq ^{99m}Tc is markedly higher than the standard dose of 20MBq used for 1-day SLNB procedures at Guy's Hospital. This increased dose was chosen to ensure a significant rise in SLN count rate, thus facilitating SLN detection in a ^{18}F background, whilst keeping within a dose range that is well established (382). The range in SLN % tracer uptake covers the lower spectrum of tracer uptake reported in literature (383), thus assessing the surgeon's performance in the clinically most challenging situation of identifying SLNs with a low count rate. The ^{18}F background signal was set to a mean of 560 cps, corresponding to an ^{18}F-FDG dose of 5MBq/kg, which is the dose CLI study patients received (Section 3.4). Calibration measurements of count rates from ^{99m}Tc and ^{18}F sources with the same gamma probe system and high-energy collimator as in the CLI study, the Europrobe 3 (Eurorad S.A., France), were used to set the count rates simulated by the GAPS system. The SNR, defined as the ratio of the node count rate to the background count rate, varied from 0.67 and 0.10 in the simulations.

The surgeons performed surface scans with the GAPS gamma probe to localize as many nodes as they could, and indicated when they thought they had

localized a SLN. SLN detection was only considered successful if the surgeon indicated that they had located a node, and if the position pointed at by the probe was within 10mm of the virtual node.

3.3.2.2 Lead-in study II: gamma probe measurements in ^{18}F-FDG PET patients

Following on from the SLNB simulations, gamma probe measurements of the axilla were performed to confirm that the simulated ^{18}F background signal corresponded to the gamma probe cross-talk found *in vivo*.

After research ethics committee approval and written informed consent was obtained, a total of 20 female patients scheduled for a diagnostic ^{18}F-FDG PET scan were included at the PET Centre at St Thomas's Hospital (ISRCTN29552671). Approximately 60 minutes after receiving an intravenous injection of ^{18}F-FDG, but prior to PET imaging, the Europrobe 3 gamma probe with a high energy collimator was used to perform 10 second measurements of the lowest and highest count rates in the left and right axilla, respectively. The measurements of both axillae were performed shortly after each other (within 5 minutes) so that effects of radioactive decay between measurements were negligible. The background count rate was also measured, and the 10s count rates were averaged to give cps. The gamma probe system and configurations used to perform the ^{18}F-FDG axillary cross-talk measurements were the same as in the CLI study (Section 3.4). The axilla was defined as the triangle between the pectoralis major, the latissimus dorsi and the edge of the breast. By placing the probe perpendicular to the skin, the entire axilla was scanned. Patient and injection characteristics such as height, weight and injected activity were recorded. An independent samples t-test was performed to compare the highest signal in the right axilla and left axilla respectively, and a p-value of <0.05 was considered statistically significant.

3.3.3 Results

3.3.3.1 Lead-in study I: SLNB simulations using the GAPS simulator

The SLN detection results per surgeon can be found in Table 15. The majority of the SLNs were accurately detected. Nodes with 0.4% (373 cps), 0.3% (280 cps) and 0.1% (93 cps) of injected activity were found by both surgeons, representing successful localization of nodes even with a SNR as low as 0.17. Both surgeons could not detect the SLN with the lowest simulated uptake (0.06% uptake, 56 cps). The mean spatial accuracy for detected nodes was 2.6mm and 4.0mm for surgeon 1 and surgeon 2, respectively.

Table 15: SLN detection results from SLNB simulations using the GAPS simulator.

Surgeon	Case	^{18}F BG[1] (cps)	SLN 1 (cps)	SLN 1 detected?	Localization error SLN 1 (mm)	SLN 2 (cps)	SLN 2 detected?	Localization error SLN 2 (mm)
1	1	560	373	Y	2.50	93	Y	6.40
	2	560	280	Y	1.40	93	Y	2.43
	3	560	280	Y	0.50	56	N	-
2	1	560	373	Y	1.27	93	Y	3.99
	2	560	280	Y	3.00	93	Y	9.70
	3	560	280	Y	2.00	56	N	-

1. BG: background signal

3.3.3.2 Lead-in study II: Gamma probe measurements in ^{18}F-FDG PET patients

The patient and ^{18}F-FDG injection characteristics can be found in Table 16. The mean and standard deviation of the lowest and highest gamma probe signal in the right axilla was 310 ± 77 cps (range 133 – 488) and 372 ± 85 cps (range 233 – 616), respectively. The mean and standard deviation of the lowest and highest gamma probe signal in the left axilla was 299 ± 80 cps (range 161 – 553) and 359 ± 74 cps (range 236 – 582), respectively. The highest count rate, which is clinically

most relevant as it causes the greatest interference when detecting SLNs, did not differ between left and right axilla (p = 0.596), thus indicating that the cross-talk is similar in both axillae.

Table 16: Patient and ^{18}F-FDG injection characteristics from the gamma probe cross-talk study in PET patients.

Characteristic	Mean (range)
Age (years)	61.5 (40-81)
Height (cm)	161 (145-178)
Weight (kg)	69.3 (45-101)
Blood glucose level (mmol/L)	5.7 (4.3-16.4)
Injected Activity (MBq)	343.8 (307.5-387.0)
Time between injection and first measurement (min)	59.7 (49-79)
Background count rate (cps)	12.5 (6.7-24.8)

3.3.4 Discussion

The SLNB simulations and gamma probe cross-talk measurements in ^{18}F-FDG PET patients showed that by using an increased administered activity of 150MBq ^{99m}Tc-nanocolloid, a gamma probe collimator suitable for 511 keV energy photons and blue dye, surgeons would be able to successfully detect SLNs in a 5MBq/kg ^{18}F-FDG background.

The mean gamma probe signal found in the left and right axilla in ^{18}F-FDG PET patients was lower than the 560cps (5MBq/kg) used in the SLNB simulations. The lower values probably reflect the renal excretion and non-uniform uptake *in vivo*; the 560 cps used in the simulations were obtained from gamma probe calibration measurements with ^{18}F distributed in a water volume. The spatial accuracy with which the two surgeons in this study located the SLNs (2.6 mm and 4.0 mm, respectively) corresponded to the mean localisation accuracy of 3.8 mm found for the 94 surgeons participating in the NEW START SLNB training program

(380). Performance may have improved if the surgeon's would have performed a larger number of cases. Overall the investigators were confident after conducting both lead-in studies that SLNB could be performed safely and successfully in patients undergoing ^{18}F-FDG CLI guided surgery, and patient recruitment to the CLI study commenced.

3.4 Intraoperative assessment of tumour resection margins in breast-conserving surgery using ^{18}F-FDG Cerenkov luminescence imaging – a first-in-human clinical study

3.4.1 Aim

A first-in-human, single centre clinical trial was performed to evaluate the feasibility, safety, and performance of intraoperative ^{18}F-FDG CLI to assess tumour margin status in breast cancer patients undergoing BCS with SLNB or with ALND.

3.4.2 Materials and methods

3.4.2.1 Patient recruitment and patient preparation on the day of surgery

Research Ethics Committee approval was obtained prior to patient recruitment (REC Ref: 14/WM/0050) (ClinicalTrials.gov identifier NCT02037269). Between June 2014 and February 2016, patients with histologically confirmed invasive breast cancer on core biopsy with or without associated DCIS, due to undergo primary BCS with curative intent and SLNB or ALND, were recruited at Guy's Hospital in London after written informed consent was obtained. We excluded patients who were younger than 30 years of age, who had surgery or radiotherapy in the operated breast in the past two years, who had received neoadjuvant systemic therapy for their current cancer, who were pregnant or lactating, who had a blood glucose level of ≥ 12 mmol/l on the day of surgery or who had known hypersensitivity to ^{18}F-FDG. Females of childbearing age needed to have a negative pregnancy test (by Beta HCG qualitative analysis), a history of a surgical sterilisation, or a history of no menses in the past twelve months.

On the day of surgery patients scheduled to undergo SLNB received a periareolar intradermal injection of 150 MBq ^{99m}Tc-albumin-nanocolloid (Nanocoll™, GE Healthcare, UK) in a volume of 0.1-0.15 ml. The increased ^{99m}Tc activity of 150 MBq was calculated based on the results from the lead-in cross-talk studies described in Section 3.3. Patients were then injected intravenously with 5 MBq/kg ^{18}F-FDG (up to a maximum of 300 MBq) and typically 45-60 min post-^{18}F-FDG injection, were taken to the operating theatre for their surgery.

3.4.2.2 Surgery and intraoperative specimen radiography

Following induction of anaesthesia, patients due to undergo SLNB were injected in a periareolar subdermal position with a sterile solution of 2ml Patent Blue V and 3ml of normal saline. To minimize radiation exposure to theatre staff from ^{18}F-FDG by reducing the time spend in close proximity of the patient, a standard breast operating set was pre-arranged on a sterile tray. Surgery to the breast was then carried out ahead of SLNB or ALND in an effort to minimize signal intensity reduction from radiotracer decay in the time between ^{18}F-FDG injection and CLI imaging. The WLE specimen was excised using both monopolar diathermy (Valleylab Force FX™ electrosurgical generator with HCP-01 Skintact surgical pencil) and scissors or scalpel. The excised specimen was orientated with sutures and metal surgical clips (1 suture/clips = anterior margin, 2 sutures/clips = superior margin and 3 sutures/clips = nipple margin) as per local protocol.

Immediately post excision, all WLE specimens were x-rayed intraoperatively using a Faxitron digital specimen radiography system (Faxitron Bioptics, USA). The anterior and posterior margins of the specimen were positioned in the imaging plane to enable assessment of the four radial margins. The image was assessed intraoperatively and excision of cavity shave margins was

performed if the tumour was believed to be close to the edge of the specimen on radiography.

Following excision of the WLE specimen, SLNB or ALND was performed. For SLNB a Europrobe 3 gamma probe with a high-energy collimator was used (Eurorad SA, France). SLNs were defined as nodes that were radioactive, blue, or palpable (384). The number of excised SLNs, the *ex vivo* SLN gamma probe signal (counts per second – cps), and the presence of blue nodal discoloration were recorded. Upon completion of the procedure the gamma probe background signal in the axilla was measured.

3.4.2.3 Intraoperative CLI of WLE specimens and lymph nodes

Following specimen radiography, CLI imaging of the WLE specimen was performed using a prototype intraoperative CLI imaging device (Lightpoint Medical Ltd, UK) (Figure 20). This system consists of a custom-built light-tight dark box containing two optical pathways: one for CLI imaging and one for white-light imaging for anatomic reference. The CLI imaging pathway includes an ultra-fast f/.95 lens and a reflex mirror to fold the optical pathway into an EMCCD camera. The FOV of the CLI camera is 8×8 cm and the acquisition matrix is 512×512 to give a pixel resolution of 156.25 microns. The EMCCD is thermoelectrically-cooled to -80°C and is radiation-shielded with lead to prevent annihilation photons from scintillating in the EMCCD chip, i.e. "gamma strikes". The white-light imaging pathway provides a photographic reference image using a standard CMOS camera.
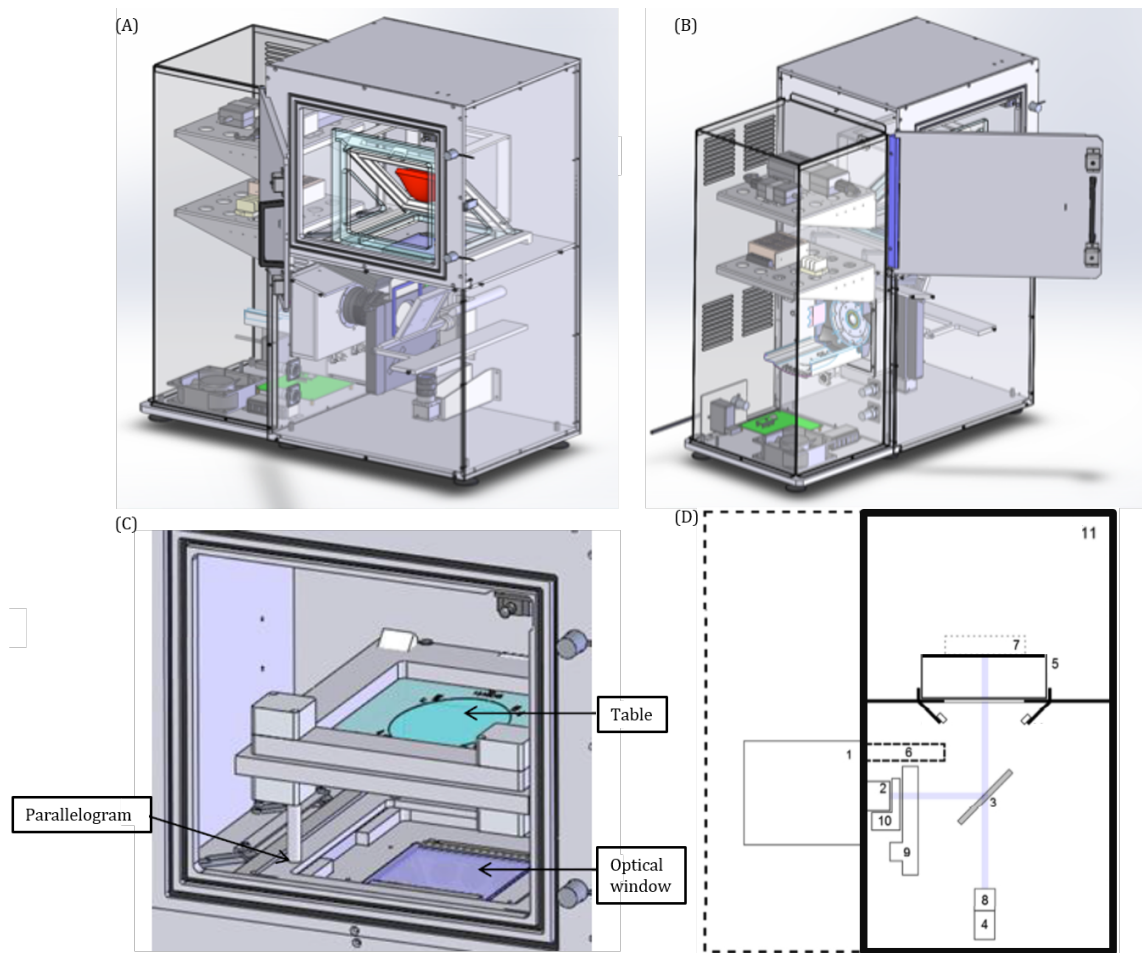
Figure 20: Prototype intraoperative CLI imaging device. (A and B) Computer aided design rendering. The red object indicates the location of the tissue specimen. (C) Specimen chamber. The specimen table is placed on a parallelogram to facilitate accurate positioning of the specimen in the centre of the FOV. (D) Schematic diagram. Component labels: 1) EMCCD camera, 2) f/.95 lens, 3) Hinged reflex mirror, 4) CMOS reference camera, 5) Specimen table, 6) Lead radiation shielding for EMCCD camera, 7) Focal zone, 8) Fixed lens for reference camera, 9) Filter wheel, 10) LED RGB light array, 11) Specimen chamber. The purple line shows the optical paths for the EMCCD camera and the reference camera as determined by the angle of the reflex mirror.

The WLE specimen was positioned on a specimen table consisting of a black metal framework with a transparent sheet of cling film spanned between its four corners (Figure 20C). The margin of interest was positioned in the FOV by using the surgical sutures to guide orientation, and subsequently imaged.

Following intact WLE specimen imaging, the surface of the specimen was immediately inked intraoperatively in order to preserve its orientation for histopathological analysis. Six distinct ink colours (Davidson®, Bradley Products

Inc., US) were applied to the 6 margins. The inked specimen was then incised through the posterior margin to visualize the primary tumour and tumour margins. Following incision, the incised WLE specimen was imaged. In one patient sequential image acquisition over a 50-minute time-period was performed to determine the half-life ($t_{1/2}$) of the radiance observed in the tumour.

The first 10 patients were included in the optimization dataset and the remaining 12 patients in the analysis dataset. In the first 10 patients the image acquisition protocol was optimized by testing different image acquisition times (100, 300, 400 sec) and pixel binning settings (2x2, 4x4, 8x8). A 300-sec acquisition time and 8x8 pixel binning was found to provide sufficient sensitivity for tumour detection and good spatial resolution (1.25 mm) within a time-window feasible for intraoperative use, and these settings were used in the remaining 12 patients included in the analysis dataset. The EMCCD imaging parameters were fixed at 300x EM gain, 3.3 μs vertical pixel shift period, 1 MHz horizontal shift frequency, and +1 clocking voltage.

SLNs or palpable lymph nodes in ALND specimens were also imaged intraoperatively with CLI using the same imaging settings. Excessive adipose tissue surrounding the nodes was resected prior to imaging.

Upon completion of WLE CLI, the radioactivity content of the WLE specimen was estimated using a radiation (scintillation) monitor (Type 41/44A, Series 300 mini-monitor, ThermoScientific, USA) or handheld radiation spectrometer (Raymon10 GR1, Kromek PLC) in order to help interpret the signal intensity on CLI. Measurements were performed at several positions around the specimen, and postoperatively the cps (type 41) and spectra (Kromek) were processed and decay-corrected to the time of CLI imaging to obtain radioactivity estimates. Prior to use in the CLI study both devices were calibrated.

After imaging was completed, all specimens were placed in a sufficient volume of 10% buffered formalin to ensure optimum fixation, and sent for histopathological analysis the next day as per standard of care.

3.4.2.4 Radiation safety monitoring

The occupational radiation hazards of using ^{99m}Tc-nanocolloid in the context of SLNB procedures are fairly well known (385), but there is less information about the risks posed by surgical techniques using ^{18}F-FDG. To ensure compliance with United Kingdom legislation regarding ionising radiation (386-388) when performing ^{18}F-FDG CLI in BCS using the dual radiotracers ^{99m}Tc-nanocolloid and ^{18}F-FDG, several radiation safety measures were put in place. Prior to starting the CLI study all staff received training sessions to become familiar with the radiation control procedures and occupational risks, and to learn how to minimise exposure by reducing unnecessary time in close contact with the patient without compromising patient care. At the start of each surgical procedure staff members were issued with electronic personal radiation dose (EPD) monitors (PDM-112 and PDM-122, Hitachi-Aloka Medical Ltd., Japan) for the body (Luxel+, Landauer, UK), and thermo-stimulated luminescent (TLD) ring dosimeters for the extremities (Landauer, UK). The detection limit TLD ring dosimeter was 100 μSv. Body dosimeters were worn in the anterior top pocket of the clothing and the extremity dosimeters were worn with the TLD facing inwards towards the palmer side of the hand. All staff took typical surgical precautions to avoid body fluid contamination, with surgical gowns and sterile gloves providing a barrier to radioactive body fluid contamination. Contamination monitoring of staff, rooms, equipment and waste was carried out after each procedure using a radiation monitor (Type 41/44A, Series 300 mini-monitor, ThermoScientific, USA). As ^{99m}Tc is the isotope with the

longest half-life (6.02 hours) the waste storage requirements for CLI procedures are similar to standard SLNB procedures. Surgical items and clinical waste contaminated with radioactivity were segregated and stored between 1-7 days after the procedure to allow for natural decay of the radioactivity. The time taken for the various stages of the procedure, i.e. from induction of anaesthesia to recovery, were recorded for each procedure.

3.4.2.5 Histopathology

Histopathological analysis of WLE specimens and lymph nodes was performed as per United Kingdom National guidelines (8). The WLE specimen was serially sliced at 2 mm intervals or sliced in a cruciate fashion. Representative sections of the tumour and all 6 relevant margins were selected by the pathologist, processed, paraffin wax embedded and 3 to 4 micron sections were cut and stained with H&E. In the last patient a large-format pathology block was obtained from the full-face tissue surface that was visible on the incised WLE specimen image to enable point-to-point correlation of CLI and histopathology.

Microscopic margin distance measurements of all 6 margins were performed by a specialist experienced breast pathologist (S.E.P.). Microscopic invasive tumour size and whole tumour size (including DCIS extending from the main invasive mass) were also measured. Positive margins were defined as invasive cancer or DCIS <1 mm from the specimen surface. Clear margins were defined as invasive cancer or DCIS ≥1 mm distant. The histological margin distances were reported in increments of 1 mm, but margins more than 5 mm were reported as >5 mm.

Lymph nodes measuring 5 mm or less in maximum dimension were typically sliced in 2 halves; nodes greater than 5 mm in maximum diameter were

sliced thinly at 2-mm intervals. All sections were processed and H&E stained. Nodes were reported as normal or containing macrometastasis (≥2 mm), micrometastasis (>0.2 mm, <2 mm), and isolated tumour cells (≤0.2 mm).

The pathologist was blinded to the interpretation of the CLI images so that interpretation of margin distance, tumour size and lymph nodes would not be biased.

3.4.2.6 Image analysis

All CLI and radiography images were analysed postoperatively in order to provide a controlled and standardized analysis environment. Measurements of the mean radiance (photons/s/cm^2/sr) were performed by drawing ROIs on the unprocessed CLI images using Mirada imaging software (Mirada XD3, Mirada Medical, Oxford, UK). ROIs were selected in areas showing increased signal intensity ('tumour') and no increased signal ('tissue background'). Tumour-to-background ratios (TBRs) were calculated. Gamma strikes were excluded from ROI analysis. The tumour radiance from the sequential incised WLE images was fit to a monoexponential, to determine the radiance half-life ($t_{1/2}$) by $t_{1/2} = \frac{\ln(2)}{\tau}$, where τ is decay constant.

Assessment of margin status on CLI was performed on the incised WLE specimen images. The analysis was done independently by two experienced breast surgeons (AP and AK), and performed prior to analysis of the radiography images to prevent potential confirmation bias from *a priori* knowledge of the radiological margin status. Prior to analysis, CLI images were processed by applying a median filter (filter size range 5 – 10, filter threshold range 10 – 15) and Gaussian filter (filter width: 1, filter threshold: 0.5). A stronger Gaussian filter (filter width: 4 or 5) was applied to images with a low TBR to increase the visibility of the tumour. The

preoperative diagnostic information that would typically be available to the surgeon was provided including patient age, clinical tumour size, screen detected (Y/N), mammographic tumour size, ultrasound tumour size, and histological tumour type, grade and receptor status on core biopsy. Per patient, a colour image containing information on specimen orientation was shown together with a grey-scale image and Cerenkov image. All images were displayed on a standard computer monitor (23", 1920 x 1080 pixels, 250 cd/m^2 luminance). The grey-scale image was overlaid with the Cerenkov signal to provide a fused image containing both functional and anatomical information. The leveling was set using the software's default leveling, and manually adjusted based on the surgeon's clinical judgment. Both surgeons then independently reported whether an elevated radiance from the tumour could be identified on CLI; in patients displaying an elevated tumour radiance the margin distance of the margins visible in the image was measured using the ruler function in the imaging software. The total time required to complete margin assessment was approximately 2 min per patient. As an exploratory outcome measure, tumour size was also measured. Upon completion of the measurements surgeons were asked whether, given the CLI image, they would have performed a cavity shaving had the image been available at the time of surgery, assuming there was more tissue to excise. Surgeons also scored image quality on a 5-point Likert scale: 1 = very poor – image not interpretable, 2 = poor but interpretable, 3 = fair, 4 = good, 5 = very good.

Following CLI image analysis, specimen radiography image analysis was performed on a Coronis 3MP screen (20.8", 1536 x 2048 pixels, 500 cd/m^2 luminance) using standard GE PACS imaging software. Surgeons were presented with the same preoperative diagnostic information, but the images were shown in a different order to avoid potential sequential bias. The number of surgical marker

clips was noted, and the reliability of specimen orientation assessed. If the orientation was considered reliable, the margin distance and tumour size on radiography was measured. Whether an additional cavity shaving would have been performed based on the radiography image was also noted.

The final histopathology results of the surgically excised tissue were not available at the time of CLI and radiography image analysis, and could therefore not bias the surgeon's assessment.

3.4.2.7 Statistics

Weighted Kappa coefficients were calculated to assess the agreement in margin distance between CLI and definitive histopathology, and to assess the inter-rater agreement between surgeons ('irr' package, version 3.2.2, R statistical software). A kappa coefficient (κ) greater than 0.75 was considered good agreement (317). Agreement between histological tumour size and tumour size on CLI and radiography respectively was assessed by calculating the mean difference in tumour size ± std and intraclass correlation coefficients (ICC) (SPSS® version 23.0; IBM, Chicago).

3.4.3 Results

3.4.3.1 Intraoperative imaging of WLE specimens

A total of 22 patients were included in the study. The CLI results and postoperative histopathology results from the 12 patients included in the analysis dataset are shown in Table 17. The mean administered ^{18}F-FDG activity was 295 ± 18 MBq (range 259 – 325). The mean time between ^{18}F-FDG injection and WLE excision was 86 ± 26 min (range 50 – 146), and the mean time between ^{18}F-FDG injection and commencement of CLI image acquisition was 118 ± 26 min (range 88 – 180).

Tumour margin assessment on CLI was performed on incised WLE specimen images to allow for visualization of the tumor extent and to avoid image artifacts created by the monopolar diathermy. Ten of the 12 patients in the analysis dataset had elevated tumour radiance on CLI (Table 17). Mean tumour radiance and TBR in these 10 patients was 560 ± 160 photons/s/cm^2/sr (range 308 – 871) and 2.41 ± 0.54 (range 1.63 – 3.22), respectively. The half-life of the tumour radiance was 115.5 min, which is consistent with the 109.8-minute half-life of ^{18}F (Figure 21). This correspondence supports that the detected tumour radiance is Cerenkov luminescence from ^{18}F-FDG. In the 10 patients with an elevated tumour radiance, mean radioactivity in the WLE specimen at the time of CLI imaging was 90 ± 48 kBq. The radioactivity in the 2 patients without an elevated radiance was 14 kBq and 19 kBq, respectively.

Table 17: CLI and postoperative histopathology results for each patient in the analysis dataset.

Patient	Tumour type[1]	Histologic grade invasive (1 – 3)	ER/HER2 status of invasive cancer (Pos/Neg)	Mean tumour radiance (photons/s/cm2/sr)	TBR[2]	Margin distance CLI surgeon 1, 2 (mm)	Margin distance histopath (mm)	Tumour size CLI surgeon 1, 2 (mm)	Invasive tumour size histopath[5] (mm)	Whole tumour size histopath[5] (mm)
1	NST+DCIS	2	Pos/Neg	-[3]	-	-	-	-	13	13
2	NST+DCIS	3	Neg/Pos	453.59	2.34	6, 6	>5	*[4]	22	22
3	NST	3	Neg/Neg	871.16	3.22	2, 2 / 28, 30	3 / >5	20, 18	20	20
4	NST+DCIS	3	Neg/Neg	-[3]	-	-	-	-	14	14
5	NST+DCIS	3	Pos/Neg	405.76	2.03	2, 3	5	18, 18	20	20
6	ILC	2	Pos/Neg	544.04	2.44	9, 9	>5	20, 19	22	22
7	NST	3	Pos/Neg	667.47	2.72	10, 11	>5	*[4]	25	25
8	NST+DCIS	2	Pos/Neg	308.30	1.63	6, 8 / 16, 15	>5 / >5	19,19	15	35
9	NST+DCIS	3	Pos/Neg	593.93	3.08	14, 13 / 6, 7	>5 / >5	14, 15	18	19
10	NST+DCIS	3	Pos/Neg	648.29	2.46	8, 8	>5	22, 22	19	29
11	NST+DCIS	2	Pos/Neg	466.03	2.54	15, 14 / 9, 9	>5 / >5	13, 11	13	13
12	NST+DCIS	3	Pos/Neg	637.08	1.63	9, 9 / 30, 31 / 22, 22	>5 / >5 / >5	12, 10	14	14

1. NST: invasive ductal carcinoma/no special type, DCIS: ductal carcinoma in situ, NST+DCIS: NST admixed with DCIS, ILC: invasive lobular carcinoma
2. TBR: tumour-to-background ratio
3. No elevated tumour radiance on CLI
4. The tumour was not sufficiently exposed after incision and therefore tumour size in medial-lateral or superior-inferior direction could not be measured
5. In the 8 patients where the tumour size could be measured on CLI, the histopathological tumour size displayed in the table is the tumour size measured in the same direction as the tumour size measurement on CLI, i.e. in the medial-lateral or superior-inferior direction. In patient 3, 11 and 12 the largest histological invasive and whole tumour size (i.e. extent of DCIS and invasive cancer) was measured in a different direction, and was 32 mm, 33 mm and 25 mm, respectively.
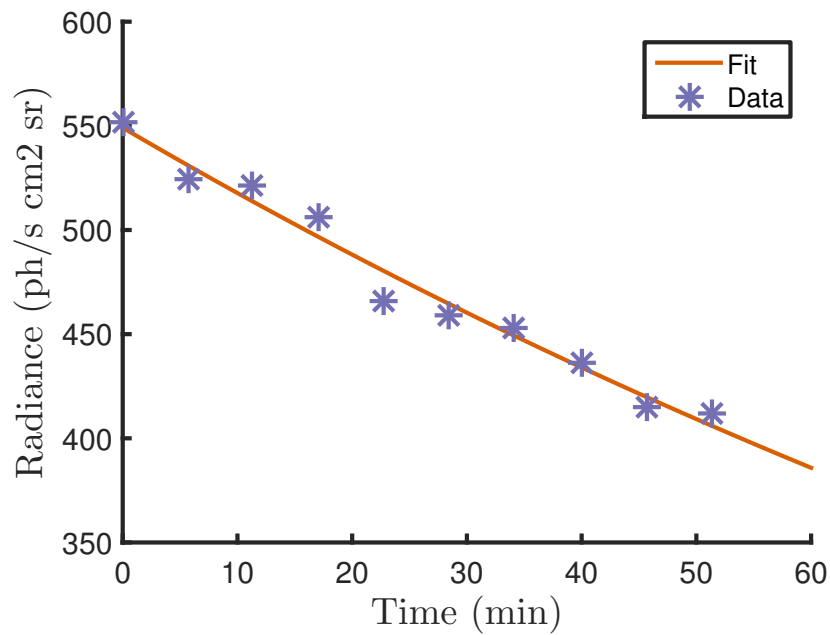
Figure 21: Decay of tumour radiance on 10 consecutive CLI images from an incised WLE specimen. The data points are fitted with a monoexponential function f (x)= $548.55e^{-0.006x}$, which gives $t_{1/2}$ is 115.5 min

In the 10 patients with elevated tumour radiance, a total of 60 margins could be assessed histologically, 26 margins were evaluable on specimen radiography, and 15 margins were assessable on CLI. Of the 45 histological margins that were not evaluable on CLI, 40 were not in the field-of-view of the CLI image, and 5 could not be assessed due to migration of the specimen orientation ink onto the margin edge, preventing optical margin interrogation. Eighteen of the 60 histological margins were not assessable on specimen radiography due to the inability to reliably orientate the specimen on the radiography image, and 16 margins were not in the image field-of-view.

The margin distance from the 15 margins measured on CLI and histopathology is shown in Table 17. Two margins measured between 1 and 5 mm on CLI and histopathology (Figure 22) (Figure 23); the remaining 13 margins were >5 mm by both modalities. There was good agreement between the histological margin distance and the margin distance on CLI as measured by both surgeon 1

and surgeon 2, respectively (κ surgeon 1 = 0.76, κ surgeon 2 = 0.86). The agreement in margin distance between surgeons was also good (κ = 0.91).

Five margins could be assessed on both CLI and specimen radiography, and all were >5 mm on both modalities, as well as histologically. An example of a CLI, radiography and histopathology image from a patient with >5 mm resection margin width is shown in Figure 24.

Two patients (17%) had a positive margin on postoperative histopathological analysis; both were medial margins, with DCIS <1 mm distant. These margins were not visible in the CLI image as specimen incision had only exposed the superior, inferior and posterior margins; the medial margin could therefore not be assessed.
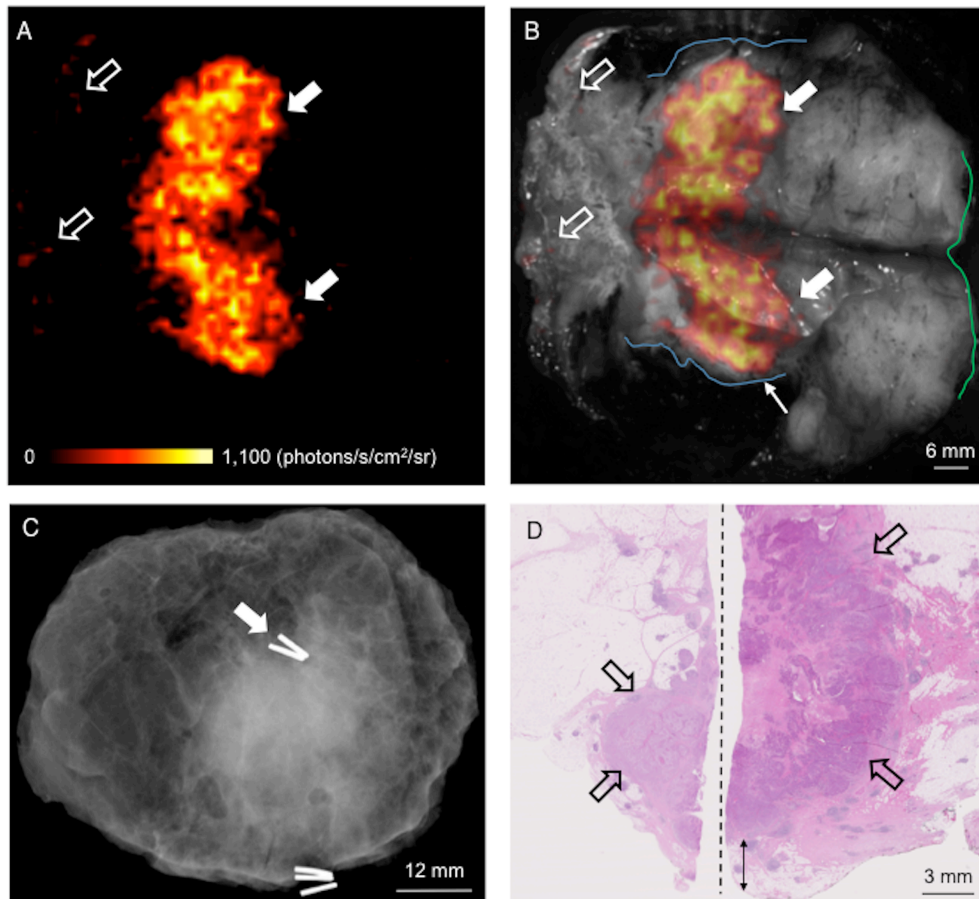
Figure 22: WLE specimen from a patient with a grade 3, ER-/HER2-, invasive ductal carcinoma/no special type (NST). (A) Cerenkov image; (B) Grey-scale photographic image overlaid with Cerenkov signal. An increased signal from the tumour is visible (white arrows); mean radiance is 871 ± 131 photons/s/cm2/sr, mean TBR is 3.22. Both surgeons measured the posterior margin (outlined in blue and location of measurement shown with small white arrow) as 2 mm, and indicated that a cavity shaving would have been performed if they had access to the CLI image during surgery. The medial margin (outlined in green) measured >5 mm by both surgeons. Pathology ink prevented assessing the lateral margin; a phosphorescent signal is visible (open arrows). Tumour size in the medial-lateral direction measures 20 mm and 18 mm for surgeons 1 and 2, respectively. (C) Specimen radiography image with two surgical clips marking the superior margin and three clips marking the medial/nipple margin. The absence of one surgical clip to mark the anterior margin, and the odd position of the superior margin clips, prevented margin distance and tumour size measurements because reliable orientation could not be assured. (D) Combined histopathology image from two adjacent pathology slides on which the posterior margin (bottom of image) and part of the primary tumour are visible (open arrows). The dashed vertical line indicates the intersection between the two sections. The distance from the posterior margin measured 3 mm microscopically (double arrow). The medial margin, located outside the right side of the image, is > 5 mm. The medial-lateral histological invasive tumour size measures 20 mm.
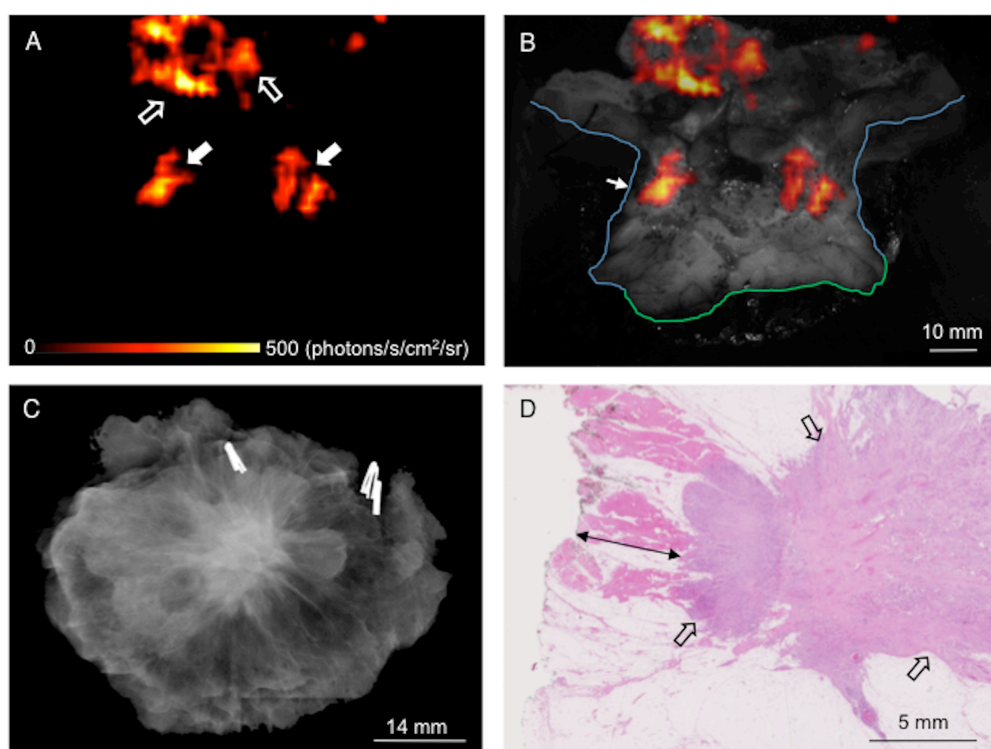
Figure 23: WLE specimen from a patient with a grade 3, ER+/HER2-, NST admixed with high grade DCIS. (A) Cerenkov image; (B) Grey-scale photographic image overlaid with Cerenkov signal. An increased signal from the tumour is visible (white arrows); mean radiance is 406 ± 51 photons/s/cm^2/sr, mean TBR is 2.03. The posterior margin (outlined in blue) is 2 mm or 3 mm on CLI as measured by surgeons 1 and surgeon 2, respectively; both surgeons would have performed a cavity shaving if the image had been available intraoperatively. The medial margin (outlined in green) is >5 mm. Tumour size in the medial-lateral direction measures 18 mm according to both surgeons. (C) Specimen radiography image. Two surgical clips mark the superior margin; three surgical clips mark the medial/nipple margin. All 4 radial margins were >5 mm and both surgeons indicated they would not have performed a cavity shaving. Medial-lateral tumour size was 18 mm and 21 mm according to surgeons 1 and 2, respectively. (D) Histopathology image showing the posterior margin (left side of image) and part of the tumour (open arrows). The posterior margin was 5 mm distant histologically (double arrow). The medial margin (not visible in image) was > 5 mm distant. The invasive and whole tumour size both measured 20 mm histologically.
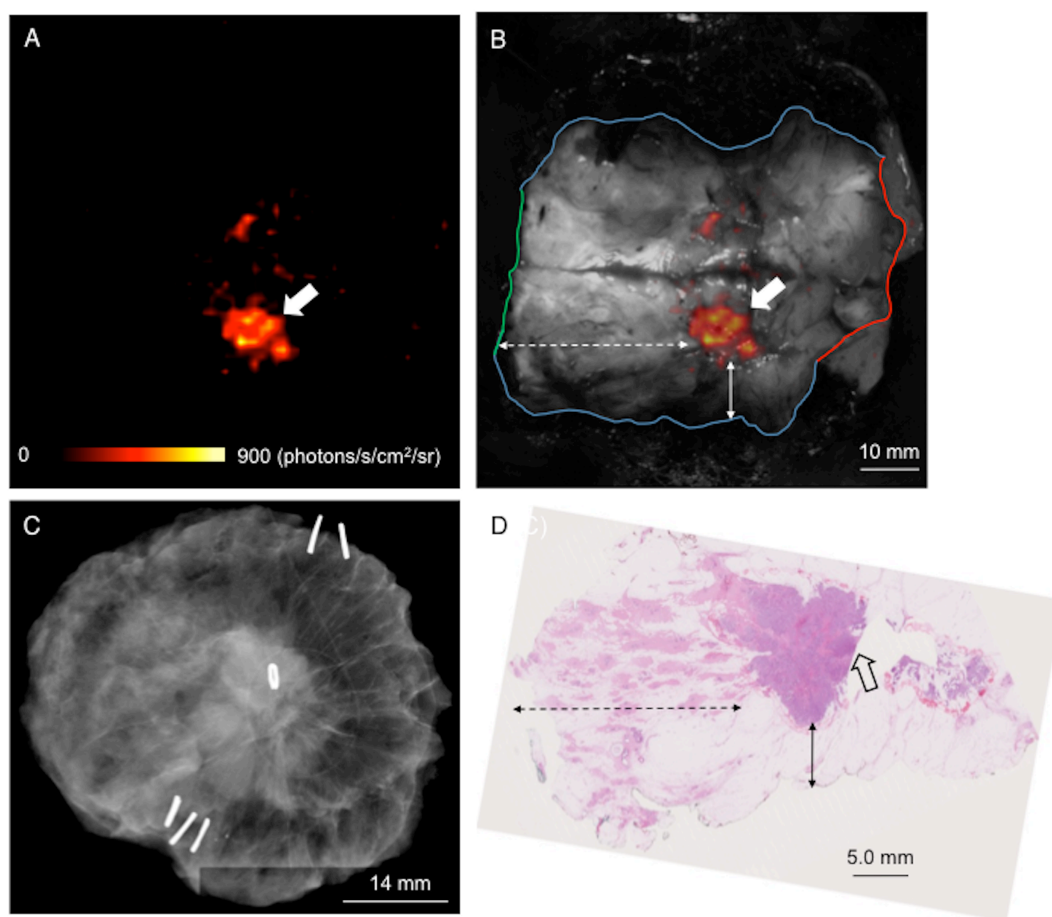
Figure 24: WLE specimen from a patient with a grade 3, ER+/HER2-, NST admixed with DCIS. (A) Cerenkov image; (B) Grey-scale photographic image overlaid with Cerenkov signal. An elevated signal (white arrow) from the tumour can be seen. Mean radiance is 637 ± 47 photons/s/cm^2/sr; mean TBR is 1.63. Both surgeons measured the posterior margin (outlined in blue; measurement shown with solid arrow), medial margin (outlined in green; measurement shown with dashed arrow) and lateral margin (outlined in red) distances as >5 mm; a cavity shaving would not have been performed based on the CLI image. The tumour size in the medial-lateral direction was 12 mm and 10 mm as measured by surgeons 1 and 2, respectively. (C) Specimen radiography image with three sets of surgical clips for reliable specimen orientation: 1 clip = anterior, 2 clips = superior, 3 clips = inferior/nipple. All four radial margins were >5 mm as measured by both surgeons and did not prompt resection of cavity shave margins. Medial-lateral tumour size measured by surgeon 1 and 2 was 17 mm and 20 mm, respectively. (D) Histopathology image from large-format pathology block. The image is rotated to facilitate correlation of histopathology and CLI. Part of the primary tumour was taken for storage in the Tissue Biobank (open arrow). The tumour is >5 mm from the posterior margin (inked black and shown with solid arrow), medial margin (dashed arrows) and lateral margin (not visible in image). The invasive and whole tumour size both measured 14 mm microscopically.

178

Tumour margin assessment on CLI using intact WLE specimen images could not be performed due to image artefacts created by the monopolar diathermy (Figure 25). This artefact provided a focal signal with a radiance that often exceeded the tumour radiance observed on incised CLI specimen images, and it was therefore not possible to discriminate between Cerenkov luminescence from tumour cells close or at the margin of excision on intact WLE specimens, and luminescence from the diathermy artefact.
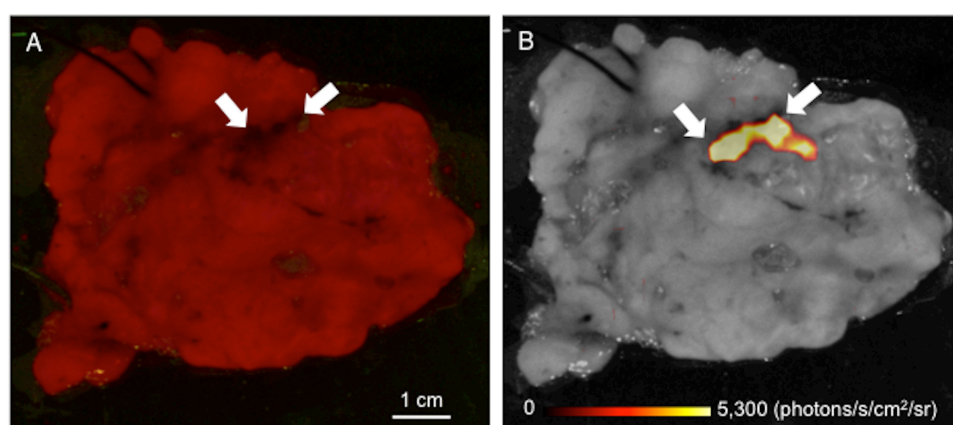
Figure 25: Intact WLE specimen showing image artefact from tissue excision with monopolar diathermy device. (A) Colour image (B) Grey-scale photographic image overlaid with Cerenkov signal. An elevated radiance from cauterised tissue can be seen (white arrows). Mean radiance is 3100 ± 930 photons/s/cm^2/sr. This patient did not receive ^{18}F-FDG, and the elevated radiance is therefore not Cerenkov luminescence from ^{18}F containing tumour cells. Note that the radiance is approximately 3 times higher than the tumour radiance observed on incised WLE specimen images (Table 17).

In 8 of the 10 patients tumour size could be measured on CLI, and compared to histopathology; the agreement is shown in Table 17. Invasive tumour size showed excellent agreement; mean difference for both surgeons combined was -0.84 ± 2.8 mm. ICC was 0.84 and 0.81 for surgeons 1 and 2, respectively. Whole tumour size (i.e. invasive carcinoma with surrounding DCIS) was underestimated on CLI; mean difference for both surgeons combined was -4.7 ± 5.0 mm. ICC was 0.65 and 0.69 for surgeons 1 and 2, respectively. Inter-rater agreement between surgeons was excellent (ICC = 0.97).

The agreement between invasive tumour size on histopathology and on radiography was good; mean difference for both surgeons combined was 1.0 ± 3.1 mm. ICC was 0.56 and 0.58 for surgeons 1 and 2, respectively. Whole tumour size was underestimated on radiography; mean difference for both surgeons combined was -5.2 ± 8.9 mm.

CLI image quality in the 10 patients with successful CLI was scored as 4.3 (range 4 – 5) by both surgeons.

3.4.3.2 Sentinel lymph node detection and intraoperative CLI of lymph nodes

SLNB was performed in 21 of the 22 patients; 1 patient underwent an ALND. SLNs were successfully identified in all 21 patients. A total of 43 SLNs were removed. The average number of SLNs per patient was 2 (range 1 – 4). Two of the 21 SLNB patients had macrometastatic SLNs.

The mean gamma probe signal of the 'hottest' SLN per patient was 4991 ± 2521 cps (range 8500 – 170). The mean gamma probe signal of the 'second hottest' SLN was 2505 ± 2632 cps (range 7368 – 50). Mean axillary background signal, measured in 13 patients, was 192 ± 70 cps (range 55 – 270). This signal is lower than the ^{18}F-FDG gamma probe cross-talk measured in the lead-in PET patient study (Section 3.3.3.2), and is mainly due to the longer time between ^{18}F-FDG injection and SLNB (mean 93 ± 34 min). A total of 7 nodes had a gamma probe signal below the background signal; 6 of these were blue. This indicates the importance of using the combined technique of radioisotope and blue dye in ^{18}F-FDG CLI guided breast surgery, as low-uptake nodes may be missed if gamma probe detection is used alone.

All SLNB procedures were performed with the monopolar diathermy device and due to the observed image artefact from diathermy on CLI, the SLN images

could not be analysed. The patient that underwent an ALND had one palpable lymph node that was intraoperatively dissected from the ALND specimen with a surgical scalpel. This lymph node showed an elevated radiance measuring 10 mm in longest dimension (Figure 26). Mean radiance was 468 ± 10 photons/s/cm^2/sr; signal-to-empty background ratio was 3.1. On histopathology a 9 mm macrometastasis was found. The increased signal-to-empty background ratio, and the correspondence between CLI signal dimension and tumour size, illustrates the potential of CLI for intraoperative identification of positive lymph nodes.
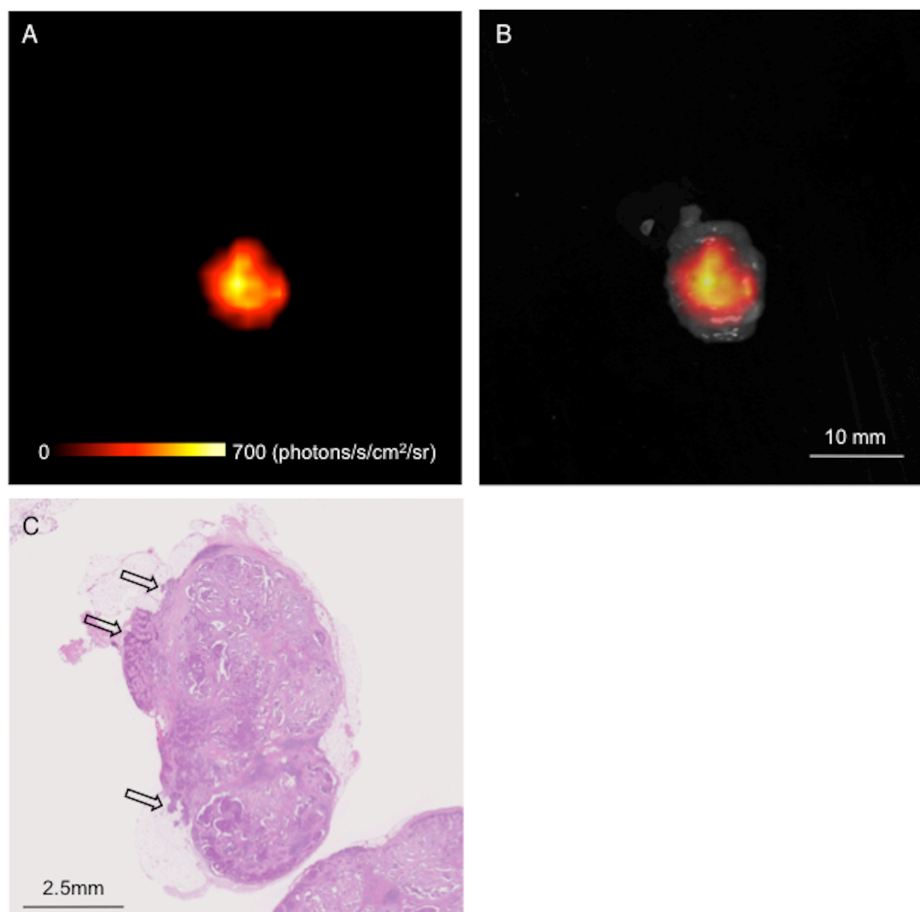
Figure 26: Macrometastatic lymph node. (A) Cerenkov image (B) grey-scale photographic image overlaid with Cerenkov signal. CLI imaging was performed intraoperatively after the lymph node was excised from the ALND specimen using a surgical scalpel. An elevated radiance can be observed measuring 10mm in longest dimension. Mean radiance is 468 ± 10 photons/s/cm^2/sr. (C) Histopathology image from lymph node showing a 9mm macrometastasis. Extranodal spread can also be seen (open arrow).

3.4.3.3 Radiation dose to staff

A summary of the whole body effective radiation dose to primary personnel from all 22 procedures is shown in Table 18. Surgeons received the highest mean and maximum dose of 34 μSv and 74 μSv, respectively. Mean duration of surgery was 39 ± 11 min (range 21 – 61) during which the surgeon was generally <0.5 meters from the patient. Mean radiation dose to the left and right hand of the surgeon was 126 ± 95 μSv (0 – 250) and 78 ± 75 μSv (0 – 200), respectively. A conservative estimate of the annual number of procedures is shown in Table 18. If the surgeons received the maximum measured whole body dose per procedure, then an individual surgeon could perform 270 and 676 procedures before reaching the United Kingdom and United States dose limits, respectively.

Mean and maximum radiation dose received by the anaesthetist standing at approximately 1 meter from the patient, with closer patient contact at the time of induction of anesthesia and at the end of the procedure, was 11 μSv and 18 μSv respectively.

Surgical equipment had low levels of radioactive contamination, which was undetectable 1-3 days later. No staff members were found to be contaminated with radioactivity after the procedures.

Table 18: Measured effective radiation doses by occupation from 22 surgical procedures.

Staff Group	N[1]	Mean Effective Dose per procedure ± std (µSv)	Range (µSv)	Estimated number of procedures per individual per year[2] ICRP[3] (20 mSv annual limit)	Estimated number of procedures per individual per year[2] USNRC[4] (50 mSv annual limit)
Surgeon	46	34 ± 15	8 – 74	270	676
Anaesthetist	22	11 ± 5	0 – 18	1111	2778
NM technologist	22	9 ± 4	1 – 15	1333	3333
Anaesthetist assistant	22	6 ± 3	0 – 11	1818	4545
Trial Co-coordinator	21	5 ± 2	1 – 10	2000	5000
Recovery Nurse	43	4 ± 3	0 – 14	1429	3571
Scrub Nurse	22	2 ± 1	0 – 5	4000	10000
Periphery Nurse	23	1 ± 1	0 – 4	5000	12500
Research fellow	36	1 ± 2	0 – 13	1538	3846
Ward Nurse	15	0	0 – 1	20000	50000
Tissue Biobank Practitioner	14	0	0 – 1	20000	50000

1. N: number of measurements
2. Based on maximum dose per procedure per staff group
3. ICRP: International Commission on Radiological Protection
4. USNRC: United States Nuclear Regulatory Commission

3.4.4 Discussion

This first-in-human study evaluated the feasibility of intraoperative ^{18}F-FDG CLI for assessing tumour margin status in patients with invasive breast cancer undergoing BCS, and SLNB or ALND. Tumour margin assessment on CLI could be performed in 10 of the 12 patients in the analysis dataset, and there was good agreement on margin width between CLI and definitive histopathology. An exploratory outcome measure assessed the correlation between tumour size on CLI and histopathology; the size on CLI and histopathology correlated well for invasive cancer, while whole tumour size (invasive with associated DCIS) was underestimated on CLI. Results from the radiation-monitoring program demonstrated that the procedure can be carried out safely while maintaining low radiation exposures to the staff involved.

In 2 patients margin assessment could not be performed because the tumours did not display elevated radiance on CLI. The absence of signal in these patients is probably due to the small tumor size, a factor known to be associated with lower ^{18}F-FDG uptake (389), and the late time points at which these tumors were imaged (135 min and 180 min post ^{18}F-FDG injection; the first and third longest injection-imaging time of all patients). Unsuccessful CLI imaging due to the absence of a detectable tumor signal highlights the importance of ongoing developments focused on improving detection sensitivity of CLI camera systems to aid detection of tumours with low ^{18}F-FDG uptake including lower grade tumours and DCIS (390).

Since its discovery in 2009, CLI has rapidly emerged as a powerful technique for cancer imaging. Three clinical pilot studies of CLI have been published to date. These have focused on the use of CLI to image radiopharmaceutical uptake in the thyroid, CLI for non-invasive detection of nodal

disease, and Cerenkov luminescence endoscopy to aid detection of cancerous lesions in the GI tract (348,349,379). To our knowledge, this is the first clinical report of intraoperative CLI. The feasibility of intraoperative CLI as shown in this study in combination with the wide applicability of ^{18}F-FDG across a range of solid cancers provides a stepping stone for clinical evaluation of this technology in other cancer types.

The low radiation exposure to staff found in this study is in accordance with previously reported exposure levels from ^{18}F-FDG guided breast surgery procedures (369,371), and comparable to the radiation dose reported for interventional cardiology procedures (1 – 50 μSv) (391). Surgeons received the highest maximum dose per procedure: 74 μSv (Table 18). The number of ^{18}F-FDG CLI-guided BCS procedures that could be performed in a routine clinical setting depends on the occupational radiation exposure limits per country (Table 18). In the United Kingdom these limits are based upon the recommendations of the International Commission on Radiological Protection (ICRP) (392), with an occupational annual dose limit of 20 mSv (386). In the United States, the annual occupational limit is set by the United States Nuclear Regulatory Commission (USNRC) at 50 mSv (393). It should be noted that surgeons and theatre staff might perform other work involving radiation, which should also be considered as part of their annual exposure. Furthermore, good practice would dictate that the radiation exposure from a procedure should be kept As Low As Reasonable Achievable (ALARP), i.e. well below the dose limits. In practice in the UK, if a worker is likely to receive annually more than 6mSv they would be designated a classified worker, necessitating annual medical surveillance and longer term record keeping of their radiation exposure. Decisions on whether it is justified to classify workers

performing higher radiation dose procedures would have to take into careful consideration the potential clinical and societal benefit of the technique.

Image artefacts on CLI from tissue excised with the monopolar diathermy device prevented tumour margin assessment on intact WLE specimens and assessment of SLNs. Although the source of this 'false-signal' is not yet fully understood, current evidence from pre-clinical experiments points towards long-lived, thermally-induced chemiluminescence (394). Since the emission seems to be related to temperature, which can reach up to 250°C at the tip of the diathermy device, an electrosurgical device (PEAK Plasmablade, Medtronic, USA) that operates at much lower temperature is currently being tested (395). In addition to potentially facilitating margin assessment on intact WLE specimens, an advantage of low-temperature devices over monopolar diathermy is the reduced collateral tissue damage, which could also improve the accuracy of assessing tumour resection margins on histopathology (396).

Although CLI imaging of incised WLE specimens is feasible for assessing tumour margin status, this approach has some important limitations over margin assessment on intact specimens. Firstly, migration of the wet pathology ink onto the margin edge immediately after specimen incision can hinders margin interpretation with CLI. Methods to accelerate drying of inks by applying acetic acid to the painted tissue or by using fast drying inks may be solutions to this problem, but this has not been tested in this study. Secondly, in our institution, as per the guidance of the breast histopathologist (S.E.P.), specimen incision could only be performed through the posterior margin to ensure accurate postoperative histological assessment of radial margins. Consequently, only a limited number of margins could be assessed with CLI per patient. A general limitation of using incised WLE specimens to assess tumour margins is that only a small part of the

specimen is exposed, and as with conventional histopathology this increases the likelihood of sampling errors. Due to the aforementioned limitations, the only two histologically positive margins were 'missed' as they were not visible on the CLI image. Hence, whilst the current dataset does demonstrate correlation between CLI and histopathological clear margins, it does not contain data to confirm that intraoperative ^{18}F-FDG CLI enables accurate assessment of close or positive margins <1 mm. In order to assess more margins per patient using incised specimens, specimen incision may be performed in multiple planes, but good communication between surgeons and pathologists is paramount in order to not compromise patient care.

A randomised, controlled, multi centre clinical study sponsored by Lightpoint medical is scheduled to commence in late 2016 to evaluate the effect of intraoperative ^{18}F-FDG CLI on re-operation rate and quality of life in breast-conserving surgery (ClinicalTrials.gov identifier NCT02666079). The study will run across an anticipated 7 study sites in the UK and Germany, recruiting a total of 442 female patients. Apart from a reduced age limit of ≥18 years of age, the inclusion and exclusion criteria are the same as in the current study. Randomisation will be done prior to surgery in a 1:1 ratio. In the treatment arm, patients will receive 5 MBq/kg 18F-FDG prior to surgery, and 150 MBq 99mTc-nanocolloid and blue dye if SLNB is performed (similar to the present study). To minimize the image artefact from the monopolar diathermy device, surgeons are recommended to perform tissue dissection using the PEAK Plasmablade or scissors/scalpel. Specimen imaging will be performed intraoperatively using the CE-marked LightPath™ Imaging System (Lightpoint Medical Ltd, UK). The smaller FOV of 6 x 6 cm and improved imaging software of this device may provide substantial improvements in sensitivity over the investigational CLI camera used

in the present study. The CLI images will be assessed intraoperatively to inform the surgeons on the margin status of the WLE specimen, aiming to achieve more complete tumour excision. In the control arm BCS with or without SLNB will be performed according to local practice. The primary outcome measure is the recommendation by the study site's multidisciplinary team to re-operate within 1 to 6 weeks post-initial surgery according to local practice. Secondary outcome measures include volume of excision, duration of surgery (skin to skin), SLN identification rate (if performed), radiation dose to staff, quality of life, cosmesis, disease specific survival and overall survival. To allow site familiarisation with the study procedures, the LightPath™ system and the Plasmablade device (if used), the first 25 patients will be included in the lead-in phase of the study. Upon completion of the lead-in phase, the study will be temporarily paused to analyse the data and identify potential areas for improvement. This will enable determining whether CLI images from intact WLE specimens excised with the Plasmablade and/or scalpel and/or scissors can be used to assess tumour margin status. In order to accurately discriminate between negative and positive tumour margins on intact specimen images, it is of key importance to identify signal characteristics (e.g. signal intensity or signal focality) that enable discrimination between 'true signals' and 'false signals'. This will also be required in order to use CLI for intraoperative assessment of lymph nodes, which is an exploratory outcome measure of the randomised controlled study. By analysing larger subgroups of patients with a range of tumour types (including pure DCIS), tumour sizes, histological grade and hormone receptor status, further insight should be obtained into which breast-cancer patient populations may most benefit from CLI-guided surgery.

4. General discussion and future work

This thesis evaluated two novel imaging techniques, TPI and CLI, that have been developed to assess tumour resection margins intraoperatively in patients undergoing BCS, with a view to reducing re-operation rates. The performance of both techniques was assessed in a first-in-human, single centre study intending to demonstrate proof-of-principle and feasibility in a clinical environment.

The TPI study evaluated a TPI handheld imaging probe that enables non-invasive assessment of WLE specimens. This device was used to measure freshly excised breast samples in an *ex vivo* setting (Section 2.3). Histopathological analysis of the 46 samples included for analysis showed that >85% of the tumour data (98 of the 115 pixels) was obtained from samples with a low-to-moderate percentage of tumour cells, which closely resembles the mixture of benign and tumour tissue commonly seen at the resection border of WLE specimens from patients with positive margins. To our knowledge this is the first time TPI has been evaluated on a dataset that is clinically representative for BCS. By incorporating the histopathological information on tissue type and cell density in the protocol used for subsequent data analysis and tissue classification, it was found that tissue composition is a key factor for the performance of TPI in breast cancer. In our study the highest accuracy for discriminating benign from malignant breast cancer on the full dataset was 75%, while earlier work by Fitzgerald *et al.* and Truong *et al.* using data from homogeneous breast samples (>50% of one tissue type) reported an accuracy of 92% and 93%, respectively (314,323). When excluding high dense fibrous tissue containing >80% fibrous cells from our dataset, accuracy increased to 88% in our study. These findings highlight the importance for future clinical TPI studies to obtain in-depth histopathological information from the samples included in the analysis, and to assure that the diagnostic accuracy of TPI

is assessed on a dataset that is truly reflective of the clinical situation where the intension is to use the device.

The CLI study evaluated ^{18}F-FDG CLI for intraoperative assessment of WLE specimens and lymph nodes using a prototype CLI imaging device. Results from two lead-in studies showed that in order to successfully perform SLNB at the time of intraoperative CLI with a ^{18}F-FDG dose of 5MBq/kg, it is required to use an increased ^{99m}Tc dose of 150 MBq, and a high-energy gamma probe collimator (Section 3.3). To our knowledge no reports have been published so far on the ability to successfully perform SLNB in combination with ^{18}F-FDG guided breast surgery. If ^{18}F-FDG intraoperative CLI is to be used in other solid cancer types that routinely perform ^{99m}Tc-guided SLNB at the time of primary tumour excision (e.g head and neck cancers and melanoma), experiments should be performed prior to clinical use to establish the required ^{99m}Tc dose and optimal SLNB protocol.

In the main study to evaluate ^{18}F-FDG CLI for assessing tumour margin and lymph node status, good agreement was found between the margin width on CLI and histopathology using incised WLE specimens (Section 3.4). However, due to the small sampling area and the potentially limited number of margins that can be assessed, the clinical applicability of this approach may require refining. Planar imaging of intact WLE specimens would enable margin assessment of a much larger surface area, thereby significantly reducing the likelihood for sampling errors. Moreover, by using intact specimens there is no need for specimen inking or physical tissue disruption, thus improving the ease-of-use of the technology while preventing potential margin interpretation errors from migration of the wet pathology ink. In order to potentially enable tumour margin assessment on intact WLE specimens it is of key importance to gain a better understanding of the image artefact caused by the monopolar diathermy device. This phenomenon seems to

have not yet been described in published literature to date. A key experiment that should be conducted is to obtain the wavelength spectrum of the diathermy-induced optical signal. By using bandpass filters with a wavelength ranging between 400 – 900 nm, the emission spectrum of the artefact can be compared to the Cerenkov radiation spectrum. The Cerenkov signal is heavily weighted towards the blue end of the visible spectrum (400 – 450 nm) (Section 3.1.1), so if the diathermy signal is predominantly present at higher wavelengths, optical filters can be installed in the filter-wheel of the LightPath™ system to filter out the 'unwanted' higher-wavelength photons, while minimizing CLI signal loss. In theory this could even prevent the need to change current surgical practice by allowing surgeons to use conventional electrosurgery when performing CLI-guided surgery.

Both the TPI study and CLI study did not include data from patients with pure DCIS, so a key question that remains unanswered is the ability of the TPI handheld imaging probe and ^{18}F-FDG CLI to accurately detect DCIS. The TPS study performed by Ashworth *et al.* showed that breast cancer had a higher index of refraction than fibrous and adipose breast tissue respectively, and concluded that this difference enabled discrimination of benign from malignant breast tissue on TPI (274). Unfortunately they did not specify the tumour types included in their analysis. Repeating their measurements on a variety of breast cancers including pure DCIS would provide valuable information on the optical properties of each tumour type in the terahertz frequency range. This information would help in gaining further insight in the applicability of TPI to different types of breast cancer.

The success of emerging technologies for intraoperative tumour margin assessment, and the ability for rapid translation from bench to bedside, will rely upon a variety of factors that are outlined in Section 1.5. Amongst these are spatial resolution and penetration depth, turnaround time, practicality and

implementability into existing clinical workflows, cost-effectiveness, diagnostic accuracy and ultimately reduction in re-excision rate. This thesis provides a unique opportunity to compare the pros and cons of TPI and CLI based on some of these criteria.

Both techniques employ a broadband wavelength range, 0.17 – 3.0 mm for TPI and 400 – 900 nm for CLI, and because of the longer wavelength of terahertz radiation the fundamental resolution of TPI is inferior to optical imaging techniques that use light in the visible or NIR wavelength range such as OCT and NIRF imaging. However, since the Cerenkov photons in ^{18}F-FDG CLI are indirectly produced by the positrons from ^{18}F-decay, the fundamental resolution of CLI is determined by the distance over which the positrons emit light. For ^{18}F this is 0.3 mm (Table 12). Thus, although the fundamental resolution of ^{18}F-FDG CLI is still superior to the fundamental resolution of TPI for the vast majority of the 0.1 – 1.8 THz spectrum of the TPI handheld probe, the differences are less profound in comparison to other emerging optical imaging techniques. The pixel resolution of both devices is excellent; 0.6 mm for the TPI handheld probe and 1.25 mm for the prototype CLI imaging camera when 8x8 binning is used as per the current image protocol. Depending on the sensitivity of the Lightpath™ device the pixel resolution in the RCT may be further improved by using lower binning settings (e.g. 4x4 or 2x2).

Both TPI and ^{18}F-FDG CLI have a tissue penetration depth in the range of 5 mm or less, which is perfectly suited for the 'no tumour on ink', '≥1 mm' or '≥2 mm' guidelines that are currently being used in clinical practice (Table 1). The limited tissue penetration could be an advantage over the established imaging techniques for margin assessment (IDSR and IOUS), and some of the emerging imaging techniques that employ light in the NIR frequency range (Raman spectroscopy,

OCT and NIRF imaging). X-ray radiation and ultrasound waves penetrate tissue up to several tenth of centimetres, while depending on the frequency, NIR light can be detected at a depth of 10 – 15 mm (344). This may cause errors in tumour margin assessment if histopathological negative margins are wrongly diagnosed as involved on intraoperative imaging.

Techniques for intraoperative assessment of tumour margins in BCS should provide a diagnosis within 20 – 30 minutes maximum. Both techniques meet this requirement. The acquisition time of TPI and CLI in the current studies was 20 seconds and 5 minutes, respectively. Due to the small 15x2 mm scan area of the TPI handheld probe multiple measurements should be performed to adequately assess each tumour margin. The optimal number of measurement points per margin depends on the balance between sampling accuracy and acquisition time. Most studies evaluating the MarginProbe, a handheld device that also has a small fingerprint, report a maximum number of 8 measurements per margin. Based on the measurement time of 20 seconds used in the current TPI study, and 8 measurements per margin, assessing all six margins would require 16 minutes. Increasing the number of measurement points may be feasible, but would require a reduction in acquisition time per measurement to stay within time-window considered acceptable for intraoperative tumour margin assessment in BCS. Whether the TPI acquisition time can be reduced depends on the signal-to-noise ratio required for maintaining optimal diagnostic accuracy, and this should be explored in the next TPI study. For CLI a maximum of 3 to 4 images from an intact WLE specimen is likely to be sufficient to capture all 6 margins because multiple margins can be assessed per image. Due to the limited tissue surface that is exposed, assessment of tumour margin status on incised specimens only requires acquisition of a single image. Thus, regardless of whether incised or intact

specimens are used, CLI imaging can be performed within 20 to 25 minutes. Since the Lightpath™ system that will be used in the RCT is expected to have an improved sensitivity, it would be interesting to evaluate whether the acquisition time can be reduced without compromising diagnostic accuracy.

TPI can be easily introduced into existing clinical workflows because the technique does not require the use of an exogenous contrast agent to discriminate benign from malignant breast tissue, and the non-ionizing energy level of terahertz radiation means that for scanning excised WLE specimens there are no safety concerns for patients and staff. In contrast, the ionizing radiation from radiotracers required for CLI provides some important logistical and regulatory challenges for clinical adoption (Section 3.1.2 and Section 3.4). From our own experience another key factor for successful implementation of CLI in clinical practice is thorough and careful education of patients and all staff involved in the patient care pathway. These training sessions should provide adequate and understandable information on the radiation exposure levels of ^{18}F-FDG CLI, and address common misconceptions around the perceived and actual dose-related health risks.

According to the results from the meta-analysis of St John *et al.,* the diagnostic accuracy of emerging techniques should at least meet the 53 – 91% sensitivity and 81 – 96% specificity of the established techniques for intraoperative margin assessment (183). The results of the current study show that for invasive cancer the handheld TPI probe does provide sufficient performance in terms of sensitivity (≥86%), but currently underperforms with regards to specificity (≤66%). Note that these results are obtained from a first-in-human proof of principle study. By improving the system's signal stability and/or correct for instabilities through calibration, there may be room for significant improvement in diagnostic accuracy. Similar to TPI, CLI is still at very early stage

of development with only one clinical pilot study conducted so far. The sensitivity and specificity of intraoperative ^{18}F-FDG CLI in the current study could not be determined because the imaging dataset did not contain data from histologically positive margins. A challenge of performing CLI with ^{18}F-FDG is that this tracer is not tumour-specific, and the uptake is dependent on metabolic activity, which varies amongst other factors between tumour types (invasive ductal carcinomas usually have a higher FDG uptake than invasive lobular carcinoma and DCIS), and tumour grade (higher grade tumours generally take up more FDG) (397). However, an important strength of CLI is the ability to use a spectrum of radiotracers, and there are some breast tumour specific tracers currently being trialled for market approval including ^{18}F-FES (targeting the ER-receptor) and ^{89}Zr-trastuzumab (targeting HER-2) (361). Although these tracers may not be currently available, they could aid in improving diagnostic accuracy of CLI in the near future. Ultimately both TPI and CLI need to demonstrate a significant reduction in re-operation rate and an improved cost-effectiveness, and the ability of these techniques do so remains to be determined in future studies.

5. Conclusion

The work described in this thesis has demonstrated that both TPI and CLI hold promise for intraoperative assessment of tumour resection margins in patients with invasive breast cancer.

The TPI handheld probe discriminates malignant from benign breast tissue with a high sensitivity and an encouraging degree of accuracy. The main challenge for TPI is accurate discrimination of cancer from tissue containing a high percentage of fibrous cells due to the similarities in the THz pulse between these two types of tissue.

Intraoperative ^{18}F-FDG CLI is feasible and a low risk procedure. There was good agreement in margin width between CLI and histopathology in showing clear margins of excision. Due to a lack of positive histological margins in the dataset diagnostic accuracy could not be assessed. Sentinel nodes were successfully detected in all patients using an increased ^{99m}Tc dose of 150 MBq and a high-energy collimator to facilitate SLN detection against the gamma-probe background signal from ^{18}F-FDG. Radiation dose to staff was low. Elimination of image artefacts from tissue dissection with the monopolar diathermy device is needed to further improve the applicability of ^{18}F-FDG CLI.

Larger studies to assess the diagnostic accuracy of each technique in patients with both invasive cancer and DCIS, and the impact on re-operation rate, are warranted and due to commence soon. The outcome of these studies will determine the true value of both techniques in improving quality of care in BCS, and will inform further research to evaluate this technology for other solid cancer types.

6. References

1. Ferlay J., Soerjomataram I., Ervik M., et al. GLOBOCAN 2012 v1.0, Cancer Incidence and Mortality Worldwide: IARC CancerBase No. 11. 2012.

2. Ferlay J, Steliarova-Foucher E, Lortet-Tieulent J, et al. Cancer incidence and mortality patterns in Europe: estimates for 40 countries in 2012. *Eur J Cancer.* 2013;49:1374-1403.

3. CRUK. Lifetime risk of breast cancer. http://www.cancerresearchuk.org/health-professional/cancer-statistics/statistics-by-cancer-type/breast-cancer/incidence-invasive - heading-Four. Accessed 21-07-2016, 2016.

4. Siegel R. SH, Naishadham D., Jemal A. Cancer statistics. *CA Cancer J Clin.* 2012;62:10-29.

5. Elston CW, Ellis IO, Pinder SE. Pathological prognostic factors in breast cancer. *Crit Rev Oncol Hematol.* 1999;31:209-223.

6. Sharma GN, Dave R, Sanadya J, Sharma P, Sharma KK. Various types and management of breast cancer: an overview. *Journal of Advanced Pharmaceutical Technology & Research.* 2010;1:109-126.

7. WHO. Tumours of the breast In: Tavassoli A., P. D, eds. *Tumours of the breast and female genital organs*: WHO; 2003:9 - 112.

8. Ellis IO, Carder P, Hales S, et al. *Pathology reporting of breast disease in surgical excision specimens incorporating the dataset for histological reporting of breast cancer*: The Royal College of Pathologists; 2016.

9. Harvey JM, Clark GM, Osborne CK, Allred DC. Estrogen receptor status by immunohistochemistry is superior to the ligand-binding assay for predicting response to adjuvant endocrine therapy in breast cancer. *J Clin Oncol.* 1999;17:1474-1481.

10. Dunnwald LK, Rossing MA, Li CI. Hormone receptor status, tumor characteristics, and prognosis: a prospective cohort of breast cancer patients. *Breast Cancer Res.* 2007;9:R6.

11. Fisher B, Redmond C, Fisher ER, Caplan R. Relative worth of estrogen or progesterone receptor and pathologic characteristics of differentiation as indicators of prognosis in node negative breast cancer patients: findings from National Surgical Adjuvant Breast and Bowel Project Protocol B-06. *J Clin Oncol.* 1988;6:1076-1087.

12. Walker RA, Bartlett JM, Dowsett M, et al. HER2 testing in the UK: further update to recommendations. *J Clin Pathol.* 2008;61:818-824.

13. Bartlett JM, Starczynski J, Atkey N, et al. HER2 testing in the UK: recommendations for breast and gastric in-situ hybridisation methods. *J Clin Pathol.* 2011;64:649-653.

14. Ross JS, Fletcher JA. The HER-2/neu oncogene in breast cancer: prognostic factor, predictive factor, and target for therapy. *Stem Cells.* 1998;16:413-428.

15. Foulkes WD, Smith IE, Reis-Filho JS. Triple-negative breast cancer. *New England Journal of Medicine.* 2010;363:1938-1948.

16. Montagna E, Maisonneuve P, Rotmensz N, et al. Heterogeneity of Triple-Negative Breast Cancer: Histologic Subtyping to Inform the Outcome. *Clinical Breast Cancer.* 2013;13:31-39.

17. Dent R, Trudeau M, Pritchard KI, et al. Triple-negative breast cancer: clinical features and patterns of recurrence. *Clin Cancer Res.* 2007;13:4429-4434.

18. Qiu J, Xue X, Hu C, et al. Comparison of Clinicopathological Features and Prognosis in Triple-Negative and Non-Triple Negative Breast Cancer. *J Cancer.* 2016;7:167-173.

19. Perou CM, Sorlie T, Eisen MB, et al. Molecular portraits of human breast tumours. *Nature.* 2000;406:747-752.

20. Sørlie T, Perou CM, Tibshirani R, et al. Gene expression patterns of breast carcinomas distinguish tumor subclasses with clinical implications. *Proceedings of the National Academy of Sciences of the United States of America.* 2001;98:10869-10874.

21. Prat A, Parker JS, Karginova O, et al. Phenotypic and molecular characterization of the claudin-low intrinsic subtype of breast cancer. *Breast Cancer Res.* 2010;12:R68.

22. Dawson SJ, Rueda OM, Aparicio S, Caldas C. A new genome-driven integrated classification of breast cancer and its implications. *EMBO J.* 2013;32:617-628.

23. Curtis C, Shah SP, Chin SF, et al. The genomic and transcriptomic architecture of 2,000 breast tumours reveals novel subgroups. *Nature.* 2012;486:346-352.

24. van de Vijver MJ, He YD, van't Veer LJ, et al. A gene-expression signature as a predictor of survival in breast cancer. *N Engl J Med.* 2002;347:1999-2009.

25. Győrffy B, Hatzis C, Sanft T, Hofstatter E, Aktas B, Pusztai L. Multigene prognostic tests in breast cancer: past, present, future. *Breast Cancer Research : BCR.* 2015;17:11.

26. Smith JA, Andreopoulou E. An overview of the status of imaging screening technology for breast cancer. *Ann Oncol.* 2004;15 Suppl 1:I18-I26.

27.   Skaane P. Ultrasonography as adjunct to mammography in the evaluation of breast tumors. *Acta Radiol Suppl.* 1999;420:1-47.

28.   Kolb TM, Lichy J, Newhouse JH. Occult cancer in women with dense breasts: detection with screening US--diagnostic yield and tumor characteristics. *Radiology.* 1998;207:191-199.

29.   Sadigh G, Carlos RC, Neal CH, Wojcinski S, Dwamena BA. Impact of breast mass size on accuracy of ultrasound elastography vs. conventional B-mode ultrasound: a meta-analysis of individual participants. *Eur Radiol.* 2012.

30.   Bosch AM, Kessels AG, Beets GL, et al. Interexamination variation of whole breast ultrasound. *Br J Radiol.* 2003;76:328-331.

31.   Satake H, Shimamoto K, Sawaki A, et al. Role of ultrasonography in the detection of intraductal spread of breast cancer: correlation with pathologic findings, mammography and MR imaging. *Eur Radiol.* 2000;10:1726-1732.

32.   Boetes C, Mus RD, Holland R, et al. Breast tumors: comparative accuracy of MR imaging relative to mammography and US for demonstrating extent. *Radiology.* 1995;197:743-747.

33.   Berg WA, Gutierrez L, NessAiver MS, et al. Diagnostic accuracy of mammography, clinical examination, US, and MR imaging in preoperative assessment of breast cancer. *Radiology.* 2004;233:830-849.

34.   Van Goethem M, Schelfout K, Dijckmans L, et al. MR mammography in the pre-operative staging of breast cancer in patients with dense breast tissue: comparison with mammography and ultrasound. *Eur Radiol.* 2004;14:809-816.

35.   Houssami N, Hayes DF. Review of preoperative magnetic resonance imaging (MRI) in breast cancer: should MRI be performed on all women with newly diagnosed, early stage breast cancer? *CA Cancer J Clin.* 2009;59:290-302.

36.   Mann RM, Hoogeveen YL, Blickman JG, Boetes C. MRI compared to conventional diagnostic work-up in the detection and evaluation of invasive lobular carcinoma of the breast: a review of existing literature. *Breast Cancer Res Treat.* 2008;107:1-14.

37.   Medeiros LR, Duarte CS, Rosa DD, et al. Accuracy of magnetic resonance in suspicious breast lesions: a systematic quantitative review and meta-analysis. *Breast Cancer Res Treat.* 2011;126:273-285.

38.   Peters NH, Borel Rinkes IH, Zuithoff NP, Mali WP, Moons KG, Peeters PH. Meta-analysis of MR imaging in the diagnosis of breast lesions. *Radiology.* 2008;246:116-124.

39.   Houssami N, Ciatto S, Macaskill P, et al. Accuracy and surgical impact of magnetic resonance imaging in breast cancer staging: systematic review and meta-analysis in detection of multifocal and multicentric cancer. *J Clin Oncol.* 2008;26:3248-3258.

40.   Turnbull L, Brown S, Harvey I, et al. Comparative effectiveness of MRI in breast cancer (COMICE) trial: a randomised controlled trial. *Lancet.* 2010;375:563-571.

41.   Peters NH, van Esser S, van den Bosch MA, et al. Preoperative MRI and surgical management in patients with nonpalpable breast cancer: the MONET - randomised controlled trial. *Eur J Cancer.* 2011;47:879-886.

42.   Pengel KE, Loo CE, Teertstra HJ, et al. The impact of preoperative MRI on breast-conserving surgery of invasive cancer: a comparative cohort study. *Breast Cancer Res Treat.* 2009;116:161-169.

43.   Bleicher RJ, Ciocca RM, Egleston BL, et al. Association of routine pretreatment magnetic resonance imaging with time to surgery, mastectomy rate, and margin status. *J Am Coll Surg.* 2009;209:180-187; quiz 294-185.

44.   Fancellu A, Turner RM, Dixon JM, Pinna A, Cottu P, Houssami N. Meta-analysis of the effect of preoperative breast MRI on the surgical management of ductal carcinoma in situ. *Br J Surg.* 2015;102:883-893.

45.   Sardanelli F, Boetes C, Borisch B, et al. Magnetic resonance imaging of the breast: recommendations from the EUSOMA working group. *Eur J Cancer.* 2010;46:1296-1316.

46.   Halsted WS. I. The results of operations for the cure of cancer of the breast performed at the Johns Hopkins Hospital from June, 1889, to January, 1894. *Ann Surg.* 1894;20:497-555.

47.   Halsted WS. I. The results of radical operations for the cure of carcinoma of the breast. *Ann Surg.* 1907;46:1-19.

48.   Patey DH, Dyson WH. The prognosis of carcinoma of the breast in relation to the type of operation performed. *Br J Cancer.* 1948;2:7-13.

49.   Patey DH. A review of 146 cases of carcinoma of the breast operated on between 1930 and 1943. *Br J Cancer.* 1967;21:260-269.

50.   Fisher B, Montague E, Redmond C, et al. Comparison of radical mastectomy with alternative treatments for primary breast cancer. A first report of results from a prospective randomized clinical trial. *Cancer.* 1977;39:2827-2839.

51.   Fisher B, Bauer M, Margolese R, et al. Five-year results of a randomized clinical trial comparing total mastectomy and segmental mastectomy with or without radiation in the treatment of breast cancer. *New England Journal of Medicine.* 1985;312:665-673.

52.   Fisher B, Anderson S, Bryant J, et al. Twenty-year follow-up of a randomized trial comparing total mastectomy, lumpectomy, and lumpectomy plus irradiation for the treatment of invasive breast cancer. *N Engl J Med.* 2002;347:1233-1241.

53.   Veronesi U, Salvadori B, Luini A, et al. Breast conservation is a safe method in patients with small cancer of the breast. Long-term results of three randomised trials on 1,973 patients. *Eur J Cancer.* 1995;31A:1574-1579.

54.   Veronesi U, Cascinelli N, Mariani L, et al. Twenty-year follow-up of a randomized study comparing breast-conserving surgery with radical mastectomy for early breast cancer. *N Engl J Med.* 2002;347:1227-1232.

55.   Lichter AS, Lippman ME, Danforth DN, et al. Mastectomy versus breast-conserving therapy in the treatment of stage I and II carcinoma of the breast: a randomized trial at the National Cancer Institute. *Journal of Clinical Oncology.* 1992;10:976-983.

56.   Sarrazin D, Le MG, Arriagada R, et al. Ten-year results of a randomized trial comparing a conservative treatment to mastectomy in early breast cancer. *Radiother Oncol.* 1989;14:177-184.

57.   van Dongen JA, Bartelink H, Fentiman IS, et al. Randomized clinical trial to assess the value of breast-conserving therapy in stage I and II breast cancer, EORTC 10801 trial. *J Natl Cancer Inst Monogr.* 1992:15-18.

58.   Blichert-Toft M, Rose C, Andersen JA, et al. Danish randomized trial comparing breast conservation therapy with mastectomy: six years of life-table analysis. Danish Breast Cancer Cooperative Group. *J Natl Cancer Inst Monogr.* 1992:19-25.

59.   Fisher B, Costantino J, Redmond C, et al. Lumpectomy compared with lumpectomy and radiation therapy for the treatment of intraductal breast cancer. *N Engl J Med.* 1993;328:1581-1586.

60.   Amichetti M, Caffo O, Richetti A, et al. Ten-year results of treatment of ductal carcinoma in situ (DCIS) of the breast with conservative surgery and radiotherapy. *Eur J Cancer.* 1997;33:1559-1565.

61.   Solin LJ, Kurtz J, Fourquet A, et al. Fifteen-year results of breast-conserving surgery and definitive breast irradiation for the treatment of ductal carcinoma in situ of the breast. *J Clin Oncol.* 1996;14:754-763.

62.   Bijker N, Meijnen P, Peterse JL, et al. Breast-conserving treatment with or without radiotherapy in ductal carcinoma-in-situ: ten-year results of European Organisation for Research and Treatment of Cancer randomized phase III trial 10853--a study by the EORTC Breast Cancer Cooperative Group and EORTC Radiotherapy Group. *J Clin Oncol.* 2006;24:3381-3387.

63.   Darby S, McGale P, Correa C, et al. Effect of radiotherapy after breast-conserving surgery on 10-year recurrence and 15-year breast cancer death: meta-analysis of individual patient data for 10,801 women in 17 randomised trials. *Lancet.* 2011;378:1707-1716.

64. Cariati M, Holmberg L, Mansi J, et al. Breast Cancer. In: Warrel DA, Cox TM, Firth DJ, eds. *Oxford Textbook of Medicine.* Vol 2: Oxford Unversity Press; 2010:1928 - 1940.

65. McGuire KP, Santillan AA, Kaur P, et al. Are mastectomies on the rise? A 13-year trend analysis of the selection of mastectomy versus breast conservation therapy in 5865 patients. *Ann Surg Oncol.* 2009;16:2682-2690.

66. Jeevan R, Browne J, Van der Meulen J, et al. *First annual report of the national mastectomy and breast reconstruction audit 2008* 2008.

67. Ahmed M, Rubio IT, Klaase JM, Douek M. Surgical treatment of nonpalpable primary invasive and in situ breast cancer. *Nat Rev Clin Oncol.* 2015;12:645-663.

68. Volleamere AJ, Kirwan CC. National survey of breast cancer specimen orientation marking systems. *Eur J Surg Oncol.* 2013;39:255-259.

69. Estourgie SH, Nieweg OE, Olmos RA, Rutgers EJ, Kroon BB. Lymphatic drainage patterns from the breast. *Ann Surg.* 2004;239:232-237.

70. Luini A, Gatti G, Ballardini B, et al. Development of axillary surgery in breast cancer. *Ann Oncol.* 2005;16:259-262.

71. Veronesi U, Paganelli G, Viale G, et al. A randomized comparison of sentinel-node biopsy with routine axillary dissection in breast cancer. *N Engl J Med.* 2003;349:546-553.

72. Purushotham AD, Upponi S, Klevesath MB, et al. Morbidity after sentinel lymph node biopsy in primary breast cancer: results from a randomized controlled trial. *J Clin Oncol.* 2005;23:4312-4321.

73. Mansel RE, Fallowfield L, Kissin M, et al. Randomized multicenter trial of sentinel node biopsy versus standard axillary treatment in operable breast cancer: the ALMANAC Trial. *J Natl Cancer Inst.* 2006;98:599-609.

74. Berg JW. The significance of axillary node levels in the study of breast carcinoma. *Cancer.* 1955;8:776-778.

75. Veronesi U, Luini A, Galimberti V, Marchini S, Sacchini V, Rilke F. Extent of metastatic axillary involvement in 1446 cases of breast cancer. *Eur J Surg Oncol.* 1990;16:127-133.

76. Krag DN, Weaver DL, Alex JC, Fairbank JT. Surgical resection and radiolocalization of the sentinel lymph node in breast cancer using a gamma probe. *Surg Oncol.* 1993;2:335-339; discussion 340.

77. Giuliano AE, Kirgan DM, Guenther JM, Morton DL. Lymphatic mapping and sentinel lymphadenectomy for breast cancer. *Ann Surg.* 1994;220:391-398; discussion 398-401.

78. Krag DN, Anderson SJ, Julian TB, et al. Sentinel-lymph-node resection compared with conventional axillary-lymph-node dissection in clinically node-negative patients with breast cancer: overall survival findings from the NSABP B-32 randomised phase 3 trial. *Lancet Oncol.* 2010;11:927-933.

79. Veronesi U, Viale G, Paganelli G, et al. Sentinel lymph node biopsy in breast cancer: ten-year results of a randomized controlled study. *Ann Surg.* 2010;251:595-600.

80. McMasters KM, Tuttle TM, Carlson DJ, et al. Sentinel lymph node biopsy for breast cancer: a suitable alternative to routine axillary dissection in multi-institutional practice when optimal technique is used. *J Clin Oncol.* 2000;18:2560-2566.

81. NICE. *Early and locally advanced breast cancer: diagnosis and treatment*: National Institute for Health and Clinical Excellence; 2009.

82. Layfield DM, Agrawal A, Roche H, Cutress RI. Intraoperative assessment of sentinel lymph nodes in breast cancer. *Br J Surg.* 2011;98:4-17.

83. Edge S, Byrd DR, Compton CC, Fritz AG, Greene FL, Trotti A. *AJCC Cancer Staging Manual.* 7th ed: Springer; 2010.

84. Lyman GH, Giuliano AE, Somerfield MR, et al. American Society of Clinical Oncology guideline recommendations for sentinel lymph node biopsy in early-stage breast cancer. *J Clin Oncol.* 2005;23:7703-7720.

85. Giuliano AE, Hunt KK, Ballman KV, et al. Axillary dissection vs no axillary dissection in women with invasive breast cancer and sentinel node metastasis: a randomized clinical trial. *JAMA.* 2011;305:569-575.

86. Donker M, van Tienhoven G, Straver ME, et al. Radiotherapy or surgery of the axilla after a positive sentinel node in breast cancer (EORTC 10981-22023 AMAROS): a randomised, multicentre, open-label, phase 3 non-inferiority trial. *Lancet Oncol.* 2014;15:1303-1310.

87. Senkus E, Kyriakides S, Ohno S, et al. Primary breast cancer: ESMO Clinical Practice Guidelines for diagnosis, treatment and follow-up. *Ann Oncol.* 2015;26 Suppl 5:v8-30.

88. Stuart KE, Houssami N, Taylor R, Hayen A, Boyages J. Long-term outcomes of ductal carcinoma in situ of the breast: a systematic review, meta-analysis and meta-regression analysis. *BMC Cancer.* 2015;15:890.

89. Bartelink H, Horiot JC, Poortmans PM, et al. Impact of a higher radiation dose on local control and survival in breast-conserving therapy of early breast cancer: 10-year results of the randomized boost versus no boost EORTC 22881-10882 trial. *J Clin Oncol.* 2007;25:3259-3265.

90. Houssami N, Macaskill P, Marinovich ML, Morrow M. The association of surgical margins and local recurrence in women with early-stage invasive breast

cancer treated with breast-conserving therapy: a meta-analysis. *Ann Surg Oncol.* 2014;21:717-730.

91. Poortmans PM, Collette L, Horiot JC, et al. Impact of the boost dose of 10 Gy versus 26 Gy in patients with early stage breast cancer after a microscopically incomplete lumpectomy: 10-year results of the randomised EORTC boost trial. *Radiother Oncol.* 2009;90:80-85.

92. Sadek BT, Homayounfar G, Abi Raad RF, et al. Is a higher boost dose of radiation necessary after breast-conserving therapy for patients with breast cancer with final close or positive margins? *Breast Cancer Res Treat.* 2015;154:71-79.

93. Nilsson C, Valachis A. The role of boost and hypofractionation as adjuvant radiotherapy in patients with DCIS: a meta-analysis of observational studies. *Radiother Oncol.* 2015;114:50-55.

94. Barry M, Ho A, Morrow M. The evolving role of partial breast irradiation in early-stage breast cancer. *Annals of Surgical Oncology.* 2013;20:2534-2540.

95. Esposito E, Anninga B, Harris S, et al. Intraoperative radiotherapy in early breast cancer. *Br J Surg.* 2015;102:599-610.

96. Vaidya JS, Wenz F, Bulsara M, et al. Risk-adapted targeted intraoperative radiotherapy versus whole-breast radiotherapy for breast cancer: 5-year results for local control and overall survival from the TARGIT-A randomised trial.[Erratum appears in Lancet. 2014 Feb 15;383(9917):602]. *Lancet.* 2014;383:603-613.

97. Veronesi U, Orecchia R, Maisonneuve P, et al. Intraoperative radiotherapy versus external radiotherapy for early breast cancer (ELIOT): a randomised controlled equivalence trial. *Lancet Oncology.* 2013;14:1269-1277.

98. Smith BD, Arthur DW, Buchholz TA, et al. Accelerated partial breast irradiation consensus statement from the American Society for Radiation Oncology (ASTRO). *Int J Radiat Oncol Biol Phys.* 2009;74:987-1001.

99. Polgar C, Van Limbergen E, Potter R, et al. Patient selection for accelerated partial-breast irradiation (APBI) after breast-conserving surgery: recommendations of the Groupe Europeen de Curietherapie-European Society for Therapeutic Radiology and Oncology (GEC-ESTRO) breast cancer working group based on clinical evidence (2009). *Radiother Oncol.* 2010;94:264-273.

100. Bouganim N, Tsvetkova E, Clemons M, Amir E. Evolution of sites of recurrence after early breast cancer over the last 20 years: implications for patient care and future research. *Breast Cancer Res Treat.* 2013;139:603-606.

101. Effects of chemotherapy and hormonal therapy for early breast cancer on recurrence and 15-year survival: an overview of the randomised trials. *Lancet.* 2005;365:1687-1717.

102. Early Breast Cancer Trialists' Collaborative G. Comparisons between different polychemotherapy regimens for early breast cancer: meta-analyses of long-term outcome among 100 000 women in 123 randomised trials. *The Lancet.*379:432-444.

103. Palmieri C, Jones A. The 2011 EBCTCG polychemotherapy overview. *Lancet.* 2012;379:390-392.

104. Mieog JS, van der Hage JA, van de Velde CJ. Neoadjuvant chemotherapy for operable breast cancer. *Br J Surg.* 2007;94:1189-1200.

105. Sainsbury R. The development of endocrine therapy for women with breast cancer. *Cancer Treat Rev.* 2013;39:507-517.

106. Fisher B, Costantino J, Redmond C, et al. A randomized clinical trial evaluating tamoxifen in the treatment of patients with node-negative breast cancer who have estrogen-receptor-positive tumors. *N Engl J Med.* 1989;320:479-484.

107. Stewart HJ. The Scottish trial of adjuvant tamoxifen in node-negative breast cancer. Scottish Cancer Trials Breast Group. *J Natl Cancer Inst Monogr.* 1992:117-120.

108. Henry NL. Endocrine therapy toxicity: management options. *Am Soc Clin Oncol Educ Book.* 2014:e25-30.

109. Early Breast Cancer Trialists' Collaborative G. Aromatase inhibitors versus tamoxifen in early breast cancer: patient-level meta-analysis of the randomised trials. *The Lancet.*386:1341-1352.

110. Coates AS, Winer EP, Goldhirsch A, et al. Tailoring therapies--improving the management of early breast cancer: St Gallen International Expert Consensus on the Primary Therapy of Early Breast Cancer 2015. *Ann Oncol.* 2015;26:1533-1546.

111. Hudis CA. Trastuzumab--mechanism of action and use in clinical practice. *N Engl J Med.* 2007;357:39-51.

112. Gianni L, Dafni U, Gelber RD, et al. Treatment with trastuzumab for 1 year after adjuvant chemotherapy in patients with HER2-positive early breast cancer: a 4-year follow-up of a randomised controlled trial. *Lancet Oncol.* 2011;12:236-244.

113. Joensuu H, Bono P, Kataja V, et al. Fluorouracil, epirubicin, and cyclophosphamide with either docetaxel or vinorelbine, with or without trastuzumab, as adjuvant treatments of breast cancer: final results of the FinHer Trial. *J Clin Oncol.* 2009;27:5685-5692.

114. Slamon D, Eiermann W, Robert N, et al. Adjuvant trastuzumab in HER2-positive breast cancer. *N Engl J Med.* 2011;365:1273-1283.

115. Long HD, Lin YE, Zhang JJ, Zhong WZ, Zheng RN. Risk of congestive heart failure in early breast cancer patients undergoing adjuvant treatment with trastuzumab: a meta-analysis. *Oncologist.* 2016;21:547-554.

116. Guarneri V, Frassoldati A, Bottini A, et al. Preoperative chemotherapy plus trastuzumab, lapatinib, or both in human epidermal growth factor receptor 2-positive operable breast cancer: results of the randomized phase II CHER-LOB study. *J Clin Oncol.* 2012;30:1989-1995.

117. Bundred N, Cameron D, Armstrong A, et al. Effects of perioperative lapatinib and trastuzumab, alone and in combination, in early HER2+ breast cancer - the UK EPHOS-B trial. *European Breast Cancer Conference.* Amsterdam; 2016.

118. de Azambuja E, Holmes AP, Piccart-Gebhart M, et al. Lapatinib with trastuzumab for HER2-positive early breast cancer (NeoALTTO): survival outcomes of a randomised, open-label, multicentre, phase 3 trial and their association with pathological complete response. *Lancet Oncol.* 2014;15:1137-1146.

119. Wang SY, Chu H, Shamliyan T, et al. Network meta-analysis of margin threshold for women with ductal carcinoma in situ. *J Natl Cancer Inst.* 2012;104:507-516.

120. Dunne C, Burke JP, Morrow M, Kell MR. Effect of margin status on local recurrence after breast conservation and radiation therapy for ductal carcinoma in situ. *J Clin Oncol.* 2009;27:1615-1620.

121. NCCN. *Clinical practise guidelines in oncology: breast cancer*: National Comprehensive Cancer Network; 2016.

122. Gnant M, Thomssen C, Harbeck N. St. Gallen/Vienna 2015: a brief summary of the consensus discussion. *Breast Care (Basel).* 2015;10:124-130.

123. ABS. Consensus on margins in breast conservation. Paper presented at: Association of Breast Surgery Annual Conference, 2015; Bournemouth.

124. Moran MS, Schnitt SJ, Giuliano AE, et al. Society of Surgical Oncology-American Society for Radiation Oncology consensus guideline on margins for breast-conserving surgery with whole-breast irradiation in stages I and II invasive breast cancer. *Ann Surg Oncol.* 2014;21:704-716.

125. Tucker FL. Imaging-assisted large-format breast pathology: program rationale and development in a nonprofit health system in the United States. *Int J Breast Cancer.* 2012;2012:171792.

126. Guidi AJ, Connolly JL, Harris JR, Schnitt SJ. The relationship between shaved margin and inked margin status in breast excision specimens. *Cancer.* 1997;79:1568-1573.

127. Moo TA, Choi L, Culpepper C, et al. Impact of margin assessment method on positive margin rate and total volume excised. *Ann Surg Oncol.* 2014;21:86-92.

128. Hodi Z, Ellis IO, Elston CW, et al. Comparison of margin assessment by radial and shave sections in wide local excision specimens for invasive carcinoma of the breast. *Histopathology.* 2010;56:573-580.

129. Molina MA, Snell S, Franceschi D, et al. Breast specimen orientation. *Ann Surg Oncol.* 2009;16:285-288.

130. Graham RA, Homer MJ, Katz J, Rothschild J, Safaii H, Supran S. The pancake phenomenon contributes to the inaccuracy of margin assessment in patients with breast cancer. *Am J Surg.* 2002;184:89-93.

131. Yeap BH, Muniandy S, Lee SK, Sabaratnam S, Singh M. Specimen shrinkage and its influence on margin assessment in breast cancer. *Asian J Surg.* 2007;30:183-187.

132. Williams AS, Hache KD. Recognition and discrimination of tissue-marking dye color by surgical pathologists: recommendations to avoid errors in margin assessment. *Am J Clin Pathol.* 2014;142:355-361.

133. Hassani A, Griffith C, Harvey J. Size does matter: High volume breast surgeons accept smaller excision margins for wide local excision--a national survey of the surgical management of wide local excision margins in UK breast cancer patients. *Breast.* 2013;22:718-722.

134. Harness JK, Giuliano AE, Pockaj BA, Downs-Kelly E. Margins: a status report from the Annual Meeting of the American Society of Breast Surgeons. *Annals of Surgical Oncology.* 2014;21:3192-3197.

135. Anderson SJ, Wapnir I, Dignam JJ, et al. Prognosis after ipsilateral breast tumor recurrence and locoregional recurrences in patients treated by breast-conserving therapy in five National Surgical Adjuvant Breast and Bowel Project protocols of node-negative breast cancer. *J Clin Oncol.* 2009;27:2466-2473.

136. Moran MS, Houssami N, Schnitt SJ, Morrow M. In Reply to Dixon and Thomas. *Int J Radiat Oncol Biol Phys.* 2014;89:1139-1141.

137. Dixon JM, Thomas J. In regard to Moran et al. *Int J Radiat Oncol Biol Phys.* 2014;89:1139.

138. Dixon JM, Thomas J, Kerr GR, et al. A study of margin width and local recurrence in breast conserving therapy for invasive breast cancer. *European Journal of Surgical Oncology (EJSO).* 2016;42:657-664.

139. Lowery AJ, Kell MR, Glynn RW, Kerin MJ, Sweeney KJ. Locoregional recurrence after breast cancer surgery: a systematic review by receptor phenotype. *Breast Cancer Research and Treatment.* 2012;133:831-841.

140. Houssami N, Morrow M. Margins in breast conservation: a clinician's perspective and what the literature tells us. *J Surg Oncol.* 2014;110:2-7.

141. Fisher ER, Sass R, Fisher B, Gregorio R, Brown R, Wickerham L. Pathologic findings from the National Surgical Adjuvant Breast Project (protocol 6). II. Relation of local breast recurrence to multicentricity. *Cancer.* 1986;57:1717-1724.

142. Blair SL, Thompson K, Rococco J, Malcarne V, Beitsch PD, Ollila DW. Attaining Negative Margins in Breast-Conservation Operations: Is There a Consensus among Breast Surgeons? *Journal of the American College of Surgeons.* 2009;209:608-613.

143. Ashken L, Ives C, Kim B, et al. Variation in the management of ductal carcinoma in situ in the UK: Results of the Mammary Fold National Practice Survey. *European Journal of Surgical Oncology (EJSO).* 2016;42:1153-1161.

144. Holland R, Hendriks JH, Vebeek AL, Mravunac M, Schuurmans Stekhoven JH. Extent, distribution, and mammographic/histological correlations of breast ductal carcinoma in situ. *Lancet.* 1990;335:519-522.

145. Holland R, Veling SH, Mravunac M, Hendriks JH. Histologic multifocality of Tis, T1-2 breast carcinomas. Implications for clinical trials of breast-conserving surgery. *Cancer.* 1985;56:979-990.

146. Shiyanbola OO, Sprague BL, Hampton JM, et al. Emerging trends in surgical and adjuvant radiation therapies among women diagnosed with ductal carcinoma in situ. *Cancer.* 2016.

147. NHS breast screening programme and association of breast surgery. An audit of screen detected breast cancers for the year of screening April 2013 to March 2014. 2015.

148. Solin LJ, Fourquet A, Vicini FA, et al. Long-term outcome after breast-conservation treatment with radiation for mammographically detected ductal carcinoma in situ of the breast. *Cancer.* 2005;103:1137-1146.

149. Rudloff U, Jacks LM, Goldberg JI, et al. Nomogram for predicting the risk of local recurrence after breast-conserving surgery for ductal carcinoma in situ. *J Clin Oncol.* 2010;28:3762-3769.

150. Van Zee KJ, Subhedar P, Olcese C, Patil S, Morrow M. Relationship Between Margin Width and Recurrence of Ductal Carcinoma In Situ: Analysis of 2996 Women Treated With Breast-conserving Surgery for 30 Years. *Ann Surg.* 2015;262:623-631.

151. Sahoo S, Recant WM, Jaskowiak N, Tong L, Heimann R. Defining negative margins in DCIS patients treated with breast conservation therapy: The University of Chicago experience. *Breast J.* 2005;11:242-247.

152. Silverstein MJ, Lagios MD, Groshen S, et al. The influence of margin width on local control of ductal carcinoma in situ of the breast. *N Engl J Med.* 1999;340:1455-1461.

153. Kim H, Noh JM, Choi DH, et al. Excision alone for small size ductal carcinoma in situ of the breast. *Breast.* 2014;23:586-590.

154. MacDonald HR, Silverstein MJ, Mabry H, et al. Local control in ductal carcinoma in situ treated by excision alone: incremental benefit of larger margins. *Am J Surg.* 2005;190:521-525.

155. MacAusland SG, Hepel JT, Chong FK, et al. An attempt to independently verify the utility of the Van Nuys Prognostic Index for ductal carcinoma in situ. *Cancer.* 2007;110:2648-2653.

156. Van Cleef A, Altintas S, Huizing M, Papadimitriou K, Van Dam P, Tjalma W. Current view on ductal carcinoma in situ and importance of the margin thresholds: A review. *Facts Views Vis Obgyn.* 2014;6:210-218.

157. van der Heiden-van der Loo M, de Munck L, Visser O, et al. Variation between hospitals in surgical margins after first breast-conserving surgery in the Netherlands. *Breast Cancer Res Treat.* 2012;131:691-698.

158. Thomas J, Evans A, Macartney J, et al. Radiological and pathological size estimations of pure ductal carcinoma in situ of the breast, specimen handling and the influence on the success of breast conservation surgery: a review of 2564 cases from the Sloane Project. *Br J Cancer.* 2010;102:285-293.

159. Talsma AK, Reedijk AM, Damhuis RA, Westenend PJ, Vles WJ. Re-resection rates after breast-conserving surgery as a performance indicator: introduction of a case-mix model to allow comparison between Dutch hospitals. *Eur J Surg Oncol.* 2011;37:357-363.

160. McCahill LE, Single RM, Aiello Bowles EJ, et al. Variability in reexcision following breast conservation surgery. *JAMA.* 2012;307:467-475.

161. Jeevan R, Cromwell DA, Trivella M, et al. Reoperation rates after breast conserving surgery for breast cancer among women in England: retrospective study of hospital episode statistics. *BMJ.* 2012;345:e4505.

162. Isaacs AJ, Gemignani ML, Pusic A, Sedrakyan A. Association of breast conservation surgery for cancer with 90-Day reoperation rates in New York State. *JAMA Surg.* 2016.

163. Lovrics PJ, Cornacchi SD, Farrokhyar F, et al. Technical factors, surgeon case volume and positive margin rates after breast conservation surgery for early-stage breast cancer. *Can J Surg.* 2010;53:305-312.

164. Xue DQ, Qian C, Yang L, Wang XF. Risk factors for surgical site infections after breast surgery: a systematic review and meta-analysis. *Eur J Surg Oncol.* 2012;38:375-381.

165. Heil J, Breitkreuz K, Golatta M, et al. Do reexcisions impair aesthetic outcome in breast conservation surgery? Exploratory analysis of a prospective cohort study. *Ann Surg Oncol.* 2012;19:541-547.

166. Arora D, Hasan S, Male E, et al. Cost analysis of re-excisions for breast conserving surgery in Central Texas. Paper presented at: ASCO Annual Meeting, 2015.

167. Landercasper J, Whitacre E, Degnim AC, Al-Hamadani M. Reasons for re-excision after lumpectomy for breast cancer: insight from the American Society of Breast Surgeons Mastery(SM) database. *Ann Surg Oncol.* 2014;21:3185-3191.

168. Kobbermann A, Unzeitig A, Xie XJ, et al. Impact of routine cavity shave margins on breast cancer re-excision rates. *Ann Surg Oncol.* 2011;18:1349-1355.

169. Unzeitig A, Kobbermann A, Xie XJ, et al. Influence of surgical technique on mastectomy and reexcision rates in breast-conserving therapy for cancer. *Int J Surg Oncol.* 2012;2012:725121.

170. Huston TL, Pigalarga R, Osborne MP, Tousimis E. The influence of additional surgical margins on the total specimen volume excised and the reoperative rate after breast-conserving surgery. *Am J Surg.* 2006;192:509-512.

171. Guidroz JA, Larrieux G, Liao J, Sugg SL, Scott-Conner CE, Weigel RJ. Sampling of secondary margins decreases the need for re-excision after partial mastectomy. *Surgery.* 2011;150:802-809.

172. Jones V, Linebarger J, Perez S, et al. Excising Additional Margins at Initial Breast-Conserving Surgery (BCS) Reduces the Need for Re-excision in a Predominantly African American Population: A Report of a Randomized Prospective Study in a Public Hospital. *Ann Surg Oncol.* 2016;23:456-464.

173. Chagpar AB, Killelea BK, Tsangaris TN, et al. A Randomized, Controlled Trial of Cavity Shave Margins in Breast Cancer. *N Engl J Med.* 2015;373:503-510.

174. Chagpar AB, Horowitz NR, Killelea BK, et al. Economic Impact of Routine Cavity Margins Versus Standard Partial Mastectomy in Breast Cancer Patients: Results of a Randomized Controlled Trial. *Ann Surg.* 2016.

175. Clough KB, Kaufman GJ, Nos C, Buccimazza I, Sarfati IM. Improving breast cancer surgery: a classification and quadrant per quadrant atlas for oncoplastic surgery. *Ann Surg Oncol.* 2010;17:1375-1391.

176. De La Cruz L, Blankenship SA, Chatterjee A, et al. Outcomes After Oncoplastic Breast-Conserving Surgery in Breast Cancer Patients: A Systematic Literature Review. *Ann Surg Oncol.* 2016.

177. Mansfield L, Agrawal A, Cutress RI. Oncoplastic breast conserving surgery. *Gland Surg.* 2013;2:158-162.

178. Losken A, Dugal CS, Styblo TM, Carlson GW. A meta-analysis comparing breast conservation therapy alone to the oncoplastic technique. *Ann Plast Surg.* 2014;72:145-149.

179. Santos G, Urban C, Edelweiss MI, et al. Long-Term Comparison of Aesthetical Outcomes After Oncoplastic Surgery and Lumpectomy in Breast Cancer Patients. *Ann Surg Oncol.* 2015;22:2500-2508.

180. Hargreaves AC, Mohamed M, Audisio RA. Intra-operative guidance: methods for achieving negative margins in breast conserving surgery. *Journal of Surgical Oncology.* 2014;110:21-25.

181. Angarita FA, Nadler A, Zerhouni S, Escallon J. Perioperative measures to optimize margin clearance in breast conserving surgery. *Surg Oncol.* 2014;23:81-91.

182. Butler-Henderson K, Lee AH, Price RI, Waring K. Intraoperative assessment of margins in breast conserving therapy: a systematic review. *Breast.* 2014;23:112-119.

183. St John ER, Al-Khudairi R, Ashrafian H, et al. Diagnostic Accuracy of Intraoperative Techniques for Margin Assessment in Breast Cancer Surgery: A Meta-analysis. *Ann Surg.* 2016.

184. Bathla L, Harris A, Davey M, Sharma P, Silva E. High resolution intra-operative two-dimensional specimen mammography and its impact on second operation for re-excision of positive margins at final pathology after breast conservation surgery. *Am J Surg.* 2011;202:387-394.

185. Kaufman CS, Jacobson L, Bachman BA, et al. Intraoperative digital specimen mammography: rapid, accurate results expedite surgery. *Ann Surg Oncol.* 2007;14:1478-1485.

186. Britton PD, Sonoda LI, Yamamoto AK, Koo B, Soh E, Goud A. Breast surgical specimen radiographs: how reliable are they? *Eur J Radiol.* 2011;79:245-249.

187. James TA, Harlow S, Sheehey-Jones J, et al. Intraoperative Ultrasound Versus Mammographic Needle Localization for Ductal Carcinoma In Situ. *Annals of Surgical Oncology.* 2009;16:1164-1169.

188. Ahmed M, Douek M. Intra-operative ultrasound versus wire-guided localization in the surgical management of non-palpable breast cancers: systematic review and meta-analysis. *Breast Cancer Res Treat.* 2013;140:435-446.

189. Krekel NM, Haloua MH, Lopes Cardozo AM, et al. Intraoperative ultrasound guidance for palpable breast cancer excision (COBALT trial): a multicentre, randomised controlled trial. *Lancet Oncol.* 2013;14:48-54.

190. Haloua MH, Volders JH, Krekel NM, et al. Intraoperative Ultrasound Guidance in Breast-Conserving Surgery Improves Cosmetic Outcomes and Patient Satisfaction: Results of a Multicenter Randomized Controlled Trial (COBALT). *Ann Surg Oncol.* 2016;23:30-37.

191. Krekel NM, Lopes Cardozo AM, Muller S, Bergers E, Meijer S, van den Tol MP. Optimising surgical accuracy in palpable breast cancer with intra-operative

breast ultrasound--feasibility and surgeons' learning curve. *European Journal of Surgical Oncology.* 2011;37:1044-1050.

192. Esbona K, Li Z, Wilke LG. Intraoperative imprint cytology and frozen section pathology for margin assessment in breast conservation surgery: a systematic review. *Ann Surg Oncol.* 2012;19:3236-3245.

193. Riedl O, Fitzal F, Mader N, et al. Intraoperative frozen section analysis for breast-conserving therapy in 1016 patients with breast cancer. *Eur J Surg Oncol.* 2009;35:264-270.

194. Cendan JC, Coco D, Copeland EM, 3rd. Accuracy of intraoperative frozen-section analysis of breast cancer lumpectomy-bed margins. *J Am Coll Surg.* 2005;201:194-198.

195. Osborn JB, Keeney GL, Jakub JW, Degnim AC, Boughey JC. Cost-effectiveness analysis of routine frozen-section analysis of breast margins compared with reoperation for positive margins. *Ann Surg Oncol.* 2011;18:3204-3209.

196. Cox CE, Hyacinthe M, Gonzalez RJ, et al. Cytologic evaluation of lumpectomy margins in patients with ductal carcinoma in situ: clinical outcome. *Ann Surg Oncol.* 1997;4:644-649.

197. Valdes EK, Boolbol SK, Ali I, Feldman SM, Cohen JM. Intraoperative touch preparation cytology for margin assessment in breast-conservation surgery: does it work for lobular carcinoma? *Ann Surg Oncol.* 2007;14:2940-2945.

198. Weinberg E, Cox C, Dupont E, et al. Local recurrence in lumpectomy patients after imprint cytology margin evaluation. *American Journal of Surgery.* 2004;188:349-354.

199. Ruidiaz ME, Blair SL, Kummel AC, Wang-Rodriguez J. Computerized decision support system for intraoperative analysis of margin status in breast conservation therapy. *ISRN Surg.* 2012;2012:546721.

200. James TA, Harlow S, Sheehey-Jones J, et al. Intraoperative ultrasound versus mammographic needle localization for ductal carcinoma in situ. *Annals of Surgical Oncology.* 2009;16:1164-1169.

201. Thill M. MarginProbe: intraoperative margin assessment during breast conserving surgery by using radiofrequency spectroscopy. *Expert Review of Medical Devices.* 2013;10:301-315.

202. Pappo I, Spector R, Schindel A, et al. Diagnostic performance of a novel device for real-time margin assessment in lumpectomy specimens. *J Surg Res.* 2010;160:277-281.

203. Schnabel F, Boolbol SK, Gittleman M, et al. A randomized prospective study of lumpectomy margin assessment with use of MarginProbe in patients with nonpalpable breast malignancies. *Annals of Surgical Oncology.* 2014;21:1589-1595.

204. Allweis TM, Kaufman Z, Lelcuk S, et al. A prospective, randomized, controlled, multicenter study of a real-time, intraoperative probe for positive margin detection in breast-conserving surgery. *Am J Surg.* 2008;196:483-489.

205. Thill M, Roder K, Diedrich K, Dittmer C. Intraoperative assessment of surgical margins during breast conserving surgery of ductal carcinoma in situ by use of radiofrequency spectroscopy. *Breast.* 2011;20:579-580.

206. Rivera RJ, Holmes DR, Tafra L. Analysis of the Impact of Intraoperative Margin Assessment with Adjunctive Use of MarginProbe versus Standard of Care on Tissue Volume Removed. *Int J Surg Oncol.* 2012;2012:868623.

207. Bigio IJ, Bown SG, Briggs G, et al. Diagnosis of breast cancer using elastic-scattering spectroscopy: preliminary clinical results. *J Biomed Opt.* 2000;5:221-228.

208. Bydlon TM, Kennedy SA, Richards LM, et al. Performance metrics of an optical spectral imaging system for intra-operative assessment of breast tumor margins. *Opt Express.* 2010;18:8058-8076.

209. Laughney AM, Krishnaswamy V, Rizzo EJ, et al. Spectral discrimination of breast pathologies in situ using spatial frequency domain imaging. *Breast Cancer Research.* 2013;15:R61.

210. Keller MD, Majumder SK, Kelley MC, et al. Autofluorescence and diffuse reflectance spectroscopy and spectral imaging for breast surgical margin analysis. *Lasers Surg Med.* 2010;42:15-23.

211. Brown JQ, Bydlon TM, Kennedy SA, et al. Optical spectral surveillance of breast tissue landscapes for detection of residual disease in breast tumor margins. *PLoS ONE [Electronic Resource].* 2013;8:e69906.

212. Dhar S, Lo JY, Palmer GM, et al. A diffuse reflectance spectral imaging system for tumor margin assessment using custom annular photodiode arrays. *Biomed Opt Express.* 2012;3:3211-3222.

213. Drexler W. *Optical Coherence Tomography: Technology and Applications*. 2nd ed: Springer; 2015.

214. Nguyen FT, Zysk AM, Chaney EJ, et al. Intraoperative Evaluation of Breast Tumor Margins with Optical Coherence Tomography. *Cancer Research.* 2009;69:8790-8796.

215. Zysk AM, Chen K, Gabrielson E, et al. Intraoperative Assessment of Final Margins with a Handheld Optical Imaging Probe During Breast-Conserving Surgery May Reduce the Reoperation Rate: Results of a Multicenter Study. *Ann Surg Oncol.* 2015;22:3356-3362.

216. Erickson-Bhatt SJ, Nolan RM, Shemonski ND, et al. Real-time Imaging of the Resection Bed Using a Handheld Probe to Reduce Incidence of Microscopic Positive Margins in Cancer Surgery. *Cancer Res.* 2015;75:3706-3712.

217. Kennedy BF, McLaughlin RA, Kennedy KM, et al. Investigation of Optical Coherence Microelastography as a Method to Visualize Cancers in Human Breast Tissue. *Cancer Res.* 2015;75:3236-3245.

218. South FA, Chaney EJ, Marjanovic M, Adie SG, Boppart SA. Differentiation of ex vivo human breast tissue using polarization-sensitive optical coherence tomography. *Biomed Opt Express.* 2014;5:3417-3426.

219. Grieve K, Mouslim K, Assayag O, et al. Assessment of Sentinel Node Biopsies With Full-Field Optical Coherence Tomography. *Technol Cancer Res Treat.* 2016;15:266-274.

220. Valic M, Leong WL, Done SJ, et al. Wide-field optical coherence tomography (WF-OCT) for near real-time, point-of-care assessment of margin status in breast-conserving surgery specimens: Results of a feasibility study at a high-volume single-centre. *38th Annual San Antonio Breast Cancer Symposium.* San Antonio; 2016.

221. Savastru D, Chang EW, Miclos S, Pitman MB, Patel A, Iftimia N. Detection of breast surgical margins with optical coherence tomography imaging: a concept evaluation study. *J Biomed Opt.* 2014;19:056001.

222. Kong K, Kendall C, Stone N, Notingher I. Raman spectroscopy for medical diagnostics--From in-vitro biofluid assays to in-vivo cancer detection. *Adv Drug Deliv Rev.* 2015;89:121-134.

223. Haka AS, Volynskaya Z, Gardecki JA, et al. Diagnosing breast cancer using Raman spectroscopy: prospective analysis. *J Biomed Opt.* 2009;14:054023.

224. Deng K, Zhu C, Ma X, et al. Rapid Discrimination of Malignant Breast Lesions from Normal Tissues Utilizing Raman Spectroscopy System: A Systematic Review and Meta-Analysis of In Vitro Studies. *PLoS One.* 2016;11:e0159860.

225. Shim MG, Wilson BC. The effects of ex vivo handling procedures on the near-infrared Raman spectra of normal mammalian tissues. *Photochem Photobiol.* 1996;63:662-671.

226. Haka AS, Volynskaya Z, Gardecki JA, et al. In vivo margin assessment during partial mastectomy breast surgery using raman spectroscopy. *Cancer Research.* 2006;66:3317-3322.

227. Horsnell JD, Smith JA, Sattlecker M, et al. Raman spectroscopy--a potential new method for the intra-operative assessment of axillary lymph nodes. *Surgeon.* 2012;10:123-127.

228. Jeong S, Kim YI, Kang H, et al. Fluorescence-Raman dual modal endoscopic system for multiplexed molecular diagnostics. *Sci Rep.* 2015;5:9455.

229. Mohs AM, Mancini MC, Singhal S, et al. Hand-held spectroscopic device for in vivo and intraoperative tumor detection: contrast enhancement, detection sensitivity, and tissue penetration. *Anal Chem.* 2010;82:9058-9065.

230. Vahrmeijer AL, Hutteman M, van der Vorst JR, van de Velde CJ, Frangioni JV. Image-guided cancer surgery using near-infrared fluorescence. *Nat Rev Clin Oncol.* 2013;10:507-518.

231. de Boer E, Harlaar NJ, Taruttis A, et al. Optical innovations in surgery. *Br J Surg.* 2015;102:e56-72.

232. Chi C, Du Y, Ye J, et al. Intraoperative imaging-guided cancer surgery: from current fluorescence molecular imaging methods to future multi-modality imaging technology. *Theranostics.* 2014;4:1072-1084.

233. Garland M, Yim JJ, Bogyo M. A Bright Future for Precision Medicine: Advances in Fluorescent Chemical Probe Design and Their Clinical Application. *Cell Chem Biol.* 2016;23:122-136.

234. Frangioni JV. Translating in vivo diagnostics into clinical reality. *Nat Biotechnol.* 2006;24:909-913.

235. Nunn AD. The cost of developing imaging agents for routine clinical use. *Invest Radiol.* 2006;41:206-212.

236. Rosenthal EL, Warram JM, Bland KI, Zinn KR. The status of contemporary image-guided modalities in oncologic surgery. *Ann Surg.* 2015;261:46-55.

237. Whitley MJ, Cardona DM, Blazer DG, et al. Intraoperative molecular imaging with protease-activated fluorescent imaging agent. *106th Annual Meeting of the American Association for Cancer Research*. Philadelphia; 2015.

238. Balog J, Sasi-Szabó L, Kinross J, et al. Intraoperative Tissue Identification Using Rapid Evaporative Ionization Mass Spectrometry. *Science Translational Medicine.* 2013;5:194ra193.

239. St John ER, Al-Khudairi R, Balog J, et al. Rapid evaporative ionisation mass spectrometry towards real time intraoperative oncological margin status determination in breast conserving surgery. *38th Annual San Antonio Breast Cancer Symposium*. San Antonio; 2016.

240. Valluru KS, Wilson KE, Willmann JK. Photoacoustic Imaging in Oncology: Translational Preclinical and Early Clinical Experience. *Radiology.* 2016;280:332-349.

241. Maeda A, Bu J, Chen J, Zheng G, DaCosta RS. Dual in vivo photoacoustic and fluorescence imaging of HER2 expression in breast tumors for diagnosis, margin assessment, and surgical guidance. *Mol Imaging.* 2014;13.

242. Li R, Wang P, Lan L, et al. Assessing breast tumor margin by multispectral photoacoustic tomography. *Biomed Opt Express.* 2015;6:1273-1281.

243. Xi L, Grobmyer SR, Wu L, et al. Evaluation of breast tumor margins in vivo with intraoperative photoacoustic imaging. *Opt Express.* 2012;20:8726-8731.

244. Dixon JM, Renshaw L, Young O, et al. Intra-operative assessment of excised breast tumour margins using ClearEdge imaging device. *European Journal of Surgical Oncology (EJSO).*

245. Karni T, Pappo I, Sandbank J, et al. A device for real-time, intraoperative margin assessment in breast-conservation surgery. *Am J Surg.* 2007;194:467-473.

246. Wilke LG, Brown JQ, Bydlon TM, et al. Rapid noninvasive optical imaging of tissue composition in breast tumor margins. *Am J Surg.* 2009;198:566-574.

247. Auston DH. Picosecond optoelectronic switching and gating in silicon. *Applied Physics Letters.* 1975;26:101-103.

248. Moulton PF. Spectroscopic and laser characteristics of Ti:Al2O3. *Journal of the Optical Society of America* 1986;3:125-133.

249. Fan S, He Y, Ung BS, Pickwell-MacPherson E. The growth of biomedical terahertz research. *Journal of Physics D: Applied Physics.* 2014;47.

250. Yu C, Fan S, Sun Y, Pickwell-Macpherson E. The potential of terahertz imaging for cancer diagnosis: A review of investigations to date. *Quant Imaging Med Surg.* 2012;2:33-45.

251. Parrott EPJ, Sy SMY, Blu T, Wallace VP, Pickwell-MacPherson E. Terahertz pulsed imaging in vivo: measurements and processing methods. *Journal of Biomedical Optics.* 2011;16.

252. Choi H, Son JH. Terahertz sources and detectors. In: Son JH, ed. *Terahertz biomedical science and technology*: Taylor & Francis Group; 2014:9-28.

253. Pickwell-MacPherson E, Wallace VP. Terahertz pulsed imaging—A potential medical imaging modality? *Photodiagnosis and Photodynamic Therapy.* 2009;6:128-134.

254. Fitzgerald AJ, Berry E, Zinovev NN, Walker GC, Smith MA, Chamberlain JM. An introduction to medical imaging with coherent terahertz frequency radiation. *Physics in Medicine and Biology.* 2002;47:R67.

255. Pickwell-MacPherson E. Practical considerations for in vivo THz imaging. 2010.

256. Hu BB, Nuss MC. Imaging with terahertz waves. *Optics Letters.* 1995;20:1716-1718.

257. Ashworth PC. *Biomedical applications of terahertz technology.*: Semiconductor Physics Group, Cavendish Laboratory University of Cambridge; 2010.

258. Choi H, Son JH. Terahertz imaging and tomorgraphy techniques. In: Son JH, ed. *Terahertz biomedical science and technology*: Taylor & Francis Group 2014:47-66.

259. Wallace VP, MacPherson E, Zeitler JA, Reid C. Three-dimensional imaging of optically opaque materials using nonionizing terahertz radiation. *J Opt Soc Am A.* 2008;25:3120-3133.

260. Oh SJ, Haam S, Suh JS. Terahertz characteristics of water and liquids. In: Son JH, ed. *Terahertz biomedical science and technology*: Taylor & Francis Group; 2014:117-134.

261. Cerussi A, Shah N, Hsiang D, Durkin A, Butler J, Tromberg BJ. In vivo absorption, scattering, and physiologic properties of 58 malignant breast tumors determined by broadband diffuse optical spectroscopy. *J Biomed Opt.* 2006;11:044005.

262. Chen JH, Avram HE, Crooks LE, Arakawa M, Kaufman L, Brito AC. In vivo relaxation times and hydrogen density at 0.063-4.85 T in rats with implanted mammary adenocarcinomas. *Radiology.* 1992;184:427-434.

263. de Boer LL, Molenkamp BG, Bydlon TM, et al. Fat/water ratios measured with diffuse reflectance spectroscopy to detect breast tumor boundaries. *Breast Cancer Res Treat.* 2015;152:509-518.

264. Bruehlmeier M, Roelcke U, Bläuenstein P, et al. Measurement of the Extracellular Space in Brain Tumors Using 76Br-Bromide and PET. *Journal of Nuclear Medicine.* 2003;44:1210-1218.

265. Fung BM, Wassil DA, Durham DL, Chesnut RW, Durham NN, Berlin KD. Water in normal muscle and muscle with a tumor. *Biochimica et Biophysica Acta (BBA) - General Subjects.* 1975;385:180-187.

266. Ross KFA, Gordon RE. Water in malignant tissue, measured by cell refractometry and nuclear magnetic resonance. *Journal of Microscopy.* 1982;128:1365-2818.

267. Berry E, Handley JW, Fitzgerald AJ, et al. Multispectral classification techniques for terahertz pulsed imaging: an example in histopathology. *Med Eng Phys.* 2004;26:423-430.

268. Knobloch P, Schildknecht C, Kleine-Ostmann T, et al. Medical THz imaging: an investigation of histo-pathological samples. *Physics in Medicine and Biology.* 2002;47:3875.

269. Png CM, Flook R, Ng BW, Abbott D. Terahertz spectroscopy of snap-frozen human brain tissue: an initial study. *Electronics Letters.* 2009;45:343-345.

270. Sun Y, Zhu Z, Chen S, et al. Observing the Temperature Dependent Transition of the GP2 Peptide Using Terahertz Spectroscopy. *PLoS ONE.* 2012;7:e50306.

271. Joseph CS, Yaroslavsky AN, Al-Arashi M, et al. Terahertz spectroscopy of intrinsic biomarkers for non-melanoma skin cancer. *Terahertz Technology and Applications II.* 2009;7215.

272. Fitzgerald AJ, Pickwell-MacPherson E, Wallace VP. Use of finite difference time domain simulations and Debye theory for modelling the terahertz reflection response of normal and tumour breast tissue. *PLoS One.* 2014;9:e99291.

273. Rayleigh. Investigations in optics, with special reference to the spectroscope. *Philosophical Magazine Series 5.* 1879;8:261-274.

274. Ashworth PC, Pickwell-MacPherson E, Provenzano E, et al. Terahertz pulsed spectroscopy of freshly excised human breast cancer. *Opt Express.* 2009;17:12444-12454.

275. Wilmink GJ, Grundt JE. Invited Review Article: Current State of Research on Biological Effects of Terahertz Radiation. *Journal of Infrared, Millimeter, and Terahertz Waves.* 2011;32:1074-1122.

276. Sun Y, Sy MY, Wang YJ, Ahuja AT, Zhang Y, Pickwell-MacPherson E. A promising diagnostic method: Terahertz pulsed imaging and spectroscopy. *World journal of radiology.* 2011;3:55 - 65.

277. Titova LV, Hegmann FA, Kovalchuk O. Biological effects of broadband terahertz pulses. In: Son JH, ed. *Terahertz biomedical science and technology* Taylor & Francis Group; 2014:241-263.

278. Scarfì MR, RomanÒ M, Di Pietro R, et al. THz Exposure of Whole Blood for the Study of Biological Effects on Human Lymphocytes. *Journal of Biological Physics.* 2003;29:171-176.

279. Zeni O, Gallerano GP, Perrotta A, et al. Cytogenetic observations in human peripheral blood leukocytes following in vitro exposure to THz radiation: a pilot study. *Health Phys.* 2007;92:349-357.

280. Bogomazova AN, Vassina EM, Goryachkovskaya TN, et al. No DNA damage response and negligible genome-wide transcriptional changes in human embryonic stem cells exposed to terahertz radiation. *Sci Rep.* 2015;5:7749.

281. Hintzsche H, Jastrow C, Heinen B, et al. Terahertz radiation at 0.380 THz and 2.520 THz does not lead to DNA damage in skin cells in vitro. *Radiat Res.* 2013;179:38-45.

282. Hintzsche H, Jastrow C, Kleine-Ostmann T, Karst U, Schrader T, Stopper H. Terahertz electromagnetic fields (0.106 THz) do not induce manifest genomic damage in vitro. *PLoS One.* 2012;7:e46397.

283. Titova LV, Ayesheshim AK, Golubov A, et al. Intense THz pulses cause H2AX phosphorylation and activate DNA damage response in human skin tissue. *Biomedical Optics Express.* 2013;4:559-568.

284. Alexandrov BS, Phipps ML, Alexandrov LB, et al. Specificity and Heterogeneity of Terahertz Radiation Effect on Gene Expression in Mouse Mesenchymal Stem Cells. *Scientific Reports.* 2013;3:1184.

285. Kim KT, Park J, Jo SJ, et al. High-power femtosecond-terahertz pulse induces a wound response in mouse skin. *Sci Rep.* 2013;3:2296.

286. Titova LV, Ayesheshim AK, Purschke D, et al. Effect of intense THz pulses on expression of genes associated with skin cancer and inflammatory skin conditions. Paper presented at: Optical Interactions with Tissue and Cells XXV; and Terahertz for Biomedical Application, 2014; San Francisco.

287. Korenstein-Ilan A, Barbul A, Hasin P, Eliran A, Gover A, Korenstein R. Terahertz radiation increases genomic instability in human lymphocytes. *Radiat Res.* 2008;170:224-234.

288. Alexandrov BS, Rasmussen KO, Bishop AR, et al. Non-thermal effects of terahertz radiation on gene expression in mouse stem cells. *Biomed Opt Express.* 2011;2:2679-2689.

289. De Amicis A, Sanctis SD, Cristofaro SD, et al. Biological effects of in vitro THz radiation exposure in human foetal fibroblasts. *Mutat Res Genet Toxicol Environ Mutagen.* 2015;793:150-160.

290. Sim YC, Ahn KM, Park JY, Park CS, Son JH. Temperature-dependent terahertz imaging of excised oral malignant melanoma. *IEEE J Biomed Health Inform.* 2013;17:779-784.

291. Sim YC, Park JY, Ahn KM, Park C, Son JH. Terahertz imaging of excised oral cancer at frozen temperature. *Biomed Opt Express.* 2013;4:1413-1421.

292. Hou D, Li X, Cai J, et al. Terahertz spectroscopic investigation of human gastric normal and tumor tissues. *Phys Med Biol.* 2014;59:5423-5440.

293. Wahaia F, Kasalynas I, Seliuta D, et al. Study of gastric cancer samples using terahertz techniques. *Second International Conference on Applications of Optics and Photonics.* Vol 9286; 2014.

294. Meng K, Chen TN, Chen T, et al. Terahertz pulsed spectroscopy of paraffin-embedded brain glioma. *J Biomed Opt.* 2014;19:077001.

295. Jung E-A, Lim M-H, Moon K-W, et al. Terahertz Pulse Imaging of Micro-metastatic Lymph Nodes in Early-stage Cervical Cancer Patients. *J Opt Soc Korea.* 2011;15:155-160.

296. O'Toole E. Tumours of the skin. In: Warrel DA, Cox TM, Firth DJ, eds. *Oxford Textbook of Medicine.* Vol 3. Oxford: Oxford University Press; 2010:4705-4715.

297. Cartee TV, Monheit GD. How many sections are required to clear a tumor? Results from a web-based survey of margin thresholds in Mohs micrographic surgery. *Dermatol Surg.* 2013;39:179-186.

298. Mudigonda T, Pearce DJ, Yentzer BA, Williford P, Feldman SR. The economic impact of non-melanoma skin cancer: a review. *J Natl Compr Canc Netw.* 2010;8:888-896.

299. Woodward RM, Wallace VP, Pye RJ, et al. Terahertz pulse imaging of ex vivo basal cell carcinoma. *J Invest Dermatol.* 2003;120:72-78.

300. Wallace VP, Fitzgerald AJ, Shankar S, et al. Terahertz pulsed imaging of basal cell carcinoma ex vivo and in vivo. *Br J Dermatol.* 2004;151:424-432.

301. Wallace VP, Fitzgerald AJ, Pickwell E, et al. Terahertz pulsed spectroscopy of human Basal cell carcinoma. *Appl Spectrosc.* 2006;60:1127-1133.

302. Joseph CS, Yaroslavsky AN, Neel VA, Goyette TM, Giles RH. Continuous wave terahertz transmission imaging of nonmelanoma skin cancers. *Lasers Surg Med.* 2011;43:457-462.

303. Joseph CS, Patel R, Neel VA, Giles RH, Yaroslavsky AN. Imaging of ex vivo nonmelanoma skin cancers in the optical and terahertz spectral regions Optical and Terahertz skin cancers imaging. *Journal of Biophotonics.* 2014;7:295-303.

304. Freeman AH. Radiology of the gastrointestinal tract. In: Warrel DA, Cox TM, Firth DJ, eds. *Oxford Textbook of Medicine.* Vol 2: Oxford University Press; 2010:2219-2225.

305. Reid CB, Fitzgerald A, Reese G, et al. Terahertz pulsed imaging of freshly excised human colonic tissues. *Phys Med Biol.* 2011;56:4333-4353.

306. Eadie LH, Reid CB, Fitzgerald A, Wallace V. Optimizing multi-dimensional terahertz imaging analysis for colon cancer diagnosis. *Expert Systems with Applications.* 2013;40:2043-2050.

307. Wang K, Mittleman DM. Metal wires for terahertz wave guiding. *Nature.* 2004;432:376-379.

308. Ji YB, Lee ES, Kim SH, Son JH, Jeon TI. A miniaturized fiber-coupled terahertz endoscope system. *Opt Express.* 2009;17:17082-17087.

309. You B, Chen H-Z, Lu J. Terahertz endoscope based on anti-resonant reflecting hollow core waveguide. *Optical Society of America*. Baltimore, Maryland; 2011.

310. Doradla P, Alavi K, Joseph C, Giles R. Single-channel prototype terahertz endoscopic system. *J Biomed Opt.* 2014;19:080501.

311. Fitzgerald AJ, Wallace VP, Pye R, et al. Terahertz imaging of breast cancer, a feasibility study. Paper presented at: Infrared and Millimeter Waves, 2004 and 12th International Conference on Terahertz Electronics, 2004 Conference Digest of the 2004 Joint 29th International Conference on; 27 Sept.-1 Oct. 2004, 2004.

312. Fitzgerald AJ, Wallace VP, Jimenez-Linan M, et al. Terahertz pulsed imaging of human breast tumors. *Radiology.* 2006;239:533-540.

313. Woodward RM, Cole BE, Wallace VP, et al. Terahertz pulse imaging in reflection geometry of human skin cancer and skin tissue. *Phys Med Biol.* 2002;47:3853-3863.

314. Fitzgerald AJ, Pinder S, Purushotham AD, O'Kelly P, Ashworth PC, Wallace VP. Classification of terahertz-pulsed imaging data from excised breast tissue. *J Biomed Opt.* 2012;17:016005.

315. Ashworth PC, O'Kelly P, Purushotham AD, et al. An intra-operative THz probe for use during the surgical removal of breast tumors. Paper presented at: Infrared, Millimeter and Terahertz Waves, 2008 IRMMW-THz 2008 33rd International Conference on; 15-19 Sept. 2008, 2008.

316. Park CC, Mitsumori M, Nixon A, et al. Outcome at 8 years after breast-conserving surgery and radiation therapy for invasive breast cancer: influence of margin status and systemic therapy on local recurrence. *J Clin Oncol.* 2000;18:1668-1675.

317. Khan KS, Chien PF. Evaluation of a clinical test. I: assessment of reliability. *BJOG.* 2001;108:562-567.

318. Bewick V, Cheek L, Ball J. Statistics review 13: Receiver operating characteristic curves. *Critical Care.* 2004;8:1-5.

319. Shalabi A, Inoue M, Watkins J, De Rinaldis E, Coolen AC. Bayesian clinical classification from high-dimensional data: Signatures versus variability. *Stat Methods Med Res.* 2016.

320. Gaussian derivatives. *Front-End Vision and Multi-Scale Image Analysis: Multi-Scale Computer Vision Theory and Applications, written in Mathematics.* Dordrecht: Springer Netherlands; 2003:53-69.

321. Ferguson B, Abbott D. De-noising techniques for terahertz responses of biological samples. *Microelectronics Journal.* 2001;32:943-953.

322. Chen Y, Huang S, Pickwell-MacPherson E. Frequency-Wavelet Domain Deconvolution for terahertz reflection imaging and spectroscopy. *Opt Express.* 2010;18:1177-1190.

323. Truong BC, Tuan HD, Fitzgerald AJ, Wallace VP, Nguyen HT. A dielectric model of human breast tissue in terahertz regime. *IEEE Trans Biomed Eng.* 2015;62:699-707.

324. Stomper PC, D'Souza DJ, DiNitto PA, Arredondo MA. Analysis of parenchymal density on mammograms in 1353 women 25-79 years old. *AJR Am J Roentgenol.* 1996;167:1261-1265.

325. Dillon MF, Mc Dermott EW, O'Doherty A, Quinn CM, Hill AD, O'Higgins N. Factors affecting successful breast conservation for ductal carcinoma in situ. *Ann Surg Oncol.* 2007;14:1618-1628.

326. Robertson R, Germanos MS, Li C, Mitchell GS, Cherry SR, Silva MD. Optical imaging of Cerenkov light generation from positron-emitting radiotracers. *Phys Med Biol.* 2009;54:N355-365.

327. Xu Y, Liu H, Cheng Z. Harnessing the power of radionuclides for optical imaging: Cerenkov luminescence imaging. *J Nucl Med.* 2011;52:2009-2018.

328. Thorek D, Robertson R, Bacchus WA, et al. Cerenkov imaging - a new modality for molecular imaging. *Am J Nucl Med Mol Imaging.* 2012;2:163-173.

329. Das S, Thorek DL, Grimm J. Cerenkov imaging. *Adv Cancer Res.* 2014;124:213-234.

330. Spinelli AE, Boschi F. Novel biomedical applications of Cerenkov radiation and radioluminescence imaging. *Phys Med.* 2015;31:120-129.

331. Tanha K, Pashazadeh AM, Pogue BW. Review of biomedical Cerenkov luminescence imaging applications. *Biomed Opt Express.* 2015;6:3053-3065.

332. Mitchell GS, Gill RK, Boucher DL, Li C, Cherry SR. In vivo Cerenkov luminescence imaging: a new tool for molecular imaging. *Philos Trans A Math Phys Eng Sci.* 2011;369:4605-4619.

333. Ma X, Wang J, Cheng Z. Cerenkov Radiation: A Multi-functional Approach for Biological Sciences. *Frontiers in Physics.* 2014;2.

334. Jelley JV. Cerenkov radiation and its applications. *British Journal of Applied Physics.* 1955;6:227.

335. Gill RK, Mitchell GS, Cherry SR. Computed Cerenkov luminescence yields for radionuclides used in biology and medicine. *Phys Med Biol.* 2015;60:4263-4280.

336. Liu H, Ren G, Miao Z, et al. Molecular optical imaging with radioactive probes. *PLoS One.* 2010;5:e9470.

337. Ackerman NL, Graves EE. The potential for Cerenkov luminescence imaging of alpha-emitting radionuclides. *Phys Med Biol.* 2012;57:771-783.

338. Ruggiero A, Holland JP, Lewis JS, Grimm J. Cerenkov luminescence imaging of medical isotopes. *J Nucl Med.* 2010;51:1123-1130.

339. Boschi F, Meo SL, Rossi PL, Calandrino R, Sbarbati A, Spinelli AE. Optical imaging of alpha emitters: simulations, phantom, and in vivo results. *J Biomed Opt.* 2011;16:126011.

340. Spinelli AE, Lo Meo S, Calandrino R, Sbarbati A, Boschi F. Optical imaging of Tc-99m-based tracers: in vitro and in vivo results. *J Biomed Opt.* 2011;16:116023.

341. Boschi F, Pagliazzi M, Rossi B, et al. Small-animal radionuclide luminescence imaging of thyroid and salivary glands with Tc99m-pertechnetate. *J Biomed Opt.* 2013;18:76005.

342. Kondakov AK, Gubskiy IL, Znamenskiy IA, Chekhonin VP. Possibilities of optical imaging of the (99m)Tc-based radiopharmaceuticals. *J Biomed Opt.* 2014;19:046014.

343. Pagliazzi M, Boschi F, Spinelli AE. Imaging of luminescence induced by beta and gamma emitters in conventional non-scintillating materials. *RSC Advances.* 2014;4:13687-13692.

344. Chin PT, Welling MM, Meskers SC, Valdes Olmos RA, Tanke H, van Leeuwen FW. Optical imaging as an expansion of nuclear medicine: Cerenkov-based luminescence vs fluorescence-based luminescence. *Eur J Nucl Med Mol Imaging.* 2013;40:1283-1291.

345. Abouzied MM, Crawford ES, Nabi HA. 18F-FDG imaging: pitfalls and artifacts. *J Nucl Med Technol.* 2005;33:145-155; quiz 162-143.

346. Xu Y, Chang E, Liu H, Jiang H, Gambhir SS, Cheng Z. Proof-of-concept study of monitoring cancer drug therapy with cerenkov luminescence imaging. *J Nucl Med.* 2012;53:312-317.

347. Zhang X, Kuo C, Moore A, Ran C. In vivo optical imaging of interscapular brown adipose tissue with (18)F-FDG via Cerenkov luminescence imaging. *PLoS One.* 2013;8:e62007.

348. Hu H, Cao X, Kang F, et al. Feasibility study of novel endoscopic Cerenkov luminescence imaging system in detecting and quantifying gastrointestinal disease: first human results. *Eur Radiol.* 2015;25:1814-1822.

349. Thorek DLJ, Riedl C, Grimm J. Clinical Cerenkov Luminescence Imaging of 18F-FDG. *Journal of Nuclear Medicine.* 2014.

350. Robertson R, Germanos MS, Manfredi MG, Smith PG, Silva MD. Multimodal imaging with (18)F-FDG PET and Cerenkov luminescence imaging after MLN4924 treatment in a human lymphoma xenograft model. *J Nucl Med.* 2011;52:1764-1769.

351. Timmermand OV, Tran TA, Strand SE, Axelsson J. Intratherapeutic biokinetic measurements, dosimetry parameter estimates, and monitoring of treatment efficacy using cerenkov luminescence imaging in preclinical radionuclide therapy. *J Nucl Med.* 2015;56:444-449.

352. Hu Z, Qu Y, Wang K, et al. In vivo nanoparticle-mediated radiopharmaceutical-excited fluorescence molecular imaging. *Nat Commun.* 2015;6:7560.

353. Cao X, Chen X, Kang F, et al. Performance evaluation of endoscopic Cerenkov luminescence imaging system: in vitro and pseudotumor studies. *Biomed Opt Express.* 2014;5:3660-3670.

354. Holland JP, Normand G, Ruggiero A, Lewis JS, Grimm J. Intraoperative imaging of positron emission tomographic radiotracers using Cerenkov luminescence emissions. *Mol Imaging.* 2011;10:177-186, 171-173.

355. Natarajan A, Habte F, Liu H, et al. Evaluation of 89Zr-rituximab tracer by Cerenkov luminescence imaging and correlation with PET in a humanized transgenic mouse model to image NHL. *Mol Imaging Biol.* 2013;15:468-475.

356. Hu Z, Liang J, Yang W, et al. Experimental Cerenkov luminescence tomography of the mouse model with SPECT imaging validation. *Opt Express.* 2010;18:24441-24450.

357. Hu Z, Yang W, Ma X, et al. Cerenkov luminescence tomography of aminopeptidase N (APN/CD13) expression in mice bearing HT1080 tumors. *Mol Imaging.* 2013;12:173-181.

358. Lohrmann C, Zhang H, Thorek DL, et al. Cerenkov Luminescence Imaging for Radiation Dose Calculation of a (9)(0)Y-Labeled Gastrin-Releasing Peptide Receptor Antagonist. *J Nucl Med.* 2015;56:805-811.

359. Agdeppa ED, Spilker ME. A review of imaging agent development. *AAPS J.* 2009;11:286-299.

360. Mahajan A, Goh V, Basu S, et al. Bench to bedside molecular functional imaging in translational cancer medicine: to image or to imagine? *Clin Radiol.* 2015;70:1060-1082.

361. van Es SC, Venema CM, Glaudemans AW, et al. Translation of New Molecular Imaging Approaches to the Clinical Setting: Bridging the Gap to Implementation. *J Nucl Med.* 2016;57 Suppl 1:96S-104S.

362. Franc BL, Mari C, Johnson D, Leong SP. The role of a positron- and high-energy gamma photon probe in intraoperative localization of recurrent melanoma. *Clin Nucl Med.* 2005;30:787-791.

363. Gulec SA. PET probe-guided surgery. *J Surg Oncol.* 2007;96:353-357.

364. Povoski SP, Chapman GJ, Murrey DA, Jr., Lee R, Martin EW, Jr., Hall NC. Intraoperative detection of (1)(8)F-FDG-avid tissue sites using the increased probe counting efficiency of the K-alpha probe design and variance-based statistical analysis with the three-sigma criteria. *BMC Cancer.* 2013;13:98.

365. Mourant JR, Fuselier T, Boyer J, Johnson TM, Bigio IJ. Predictions and measurements of scattering and absorption over broad wavelength ranges in tissue phantoms. *Appl Opt.* 1997;36:949-957.

366. Weissleder R. A clearer vision for in vivo imaging. *Nat Biotechnol.* 2001;19:316-317.

367. Brix G, Nosske D, Lechel U. Radiation exposure of patients undergoing whole-body FDG-PET/CT examinations: an update pursuant to the new ICRP recommendations. *Nuklearmedizin.* 2014;53:217-220.

368. Mahesh M. Fluoroscopy: patient radiation exposure issues. *Radiographics.* 2001;21:1033-1045.

369. Heckathorne E, Dimock C, Dahlbom M. Radiation dose to surgical staff from positron-emitter-based localization and radiosurgery of tumors. *Health Phys.* 2008;95:220-226.

370. Povoski SP, Sarikaya I, White WC, et al. Comprehensive evaluation of occupational radiation exposure to intraoperative and perioperative personnel from 18F-FDG radioguided surgical procedures. *Eur J Nucl Med Mol Imaging.* 2008;35:2026-2034.

371. Andersen PA, Chakera AH, Klausen TL, et al. Radiation exposure to surgical staff during F-18-FDG-guided cancer surgery. *Eur J Nucl Med Mol Imaging.* 2008;35:624-629.

372. ICRP. *Recommendations of the International Commission on Radiological Protection* ICRP; 2007.

373. Fan D, Zhang X, Zhong L, et al. (68)Ga-labeled 3PRGD2 for dual PET and Cerenkov luminescence imaging of orthotopic human glioblastoma. *Bioconjug Chem.* 2015;26:1054-1060.

374. Liu H, Carpenter CM, Jiang H, et al. Intraoperative imaging of tumors using Cerenkov luminescence endoscopy: a feasibility experimental study. *J Nucl Med.* 2012;53:1579-1584.

375. Carpenter CM, Ma X, Liu H, et al. Cerenkov luminescence endoscopy: improved molecular sensitivity with beta--emitting radiotracers. *J Nucl Med.* 2014;55:1905-1909.

376. Song T, Liu X, Qu Y, et al. A Novel Endoscopic Cerenkov Luminescence Imaging System for Intraoperative Surgical Navigation. *Mol Imaging.* 2015;14:443-449.

377. Madru R, Tran TA, Axelsson J, et al. (68)Ga-labeled superparamagnetic iron oxide nanoparticles (SPIONs) for multi-modality PET/MR/Cherenkov luminescence imaging of sentinel lymph nodes. *Am J Nucl Med Mol Imaging.* 2013;4:60-69.
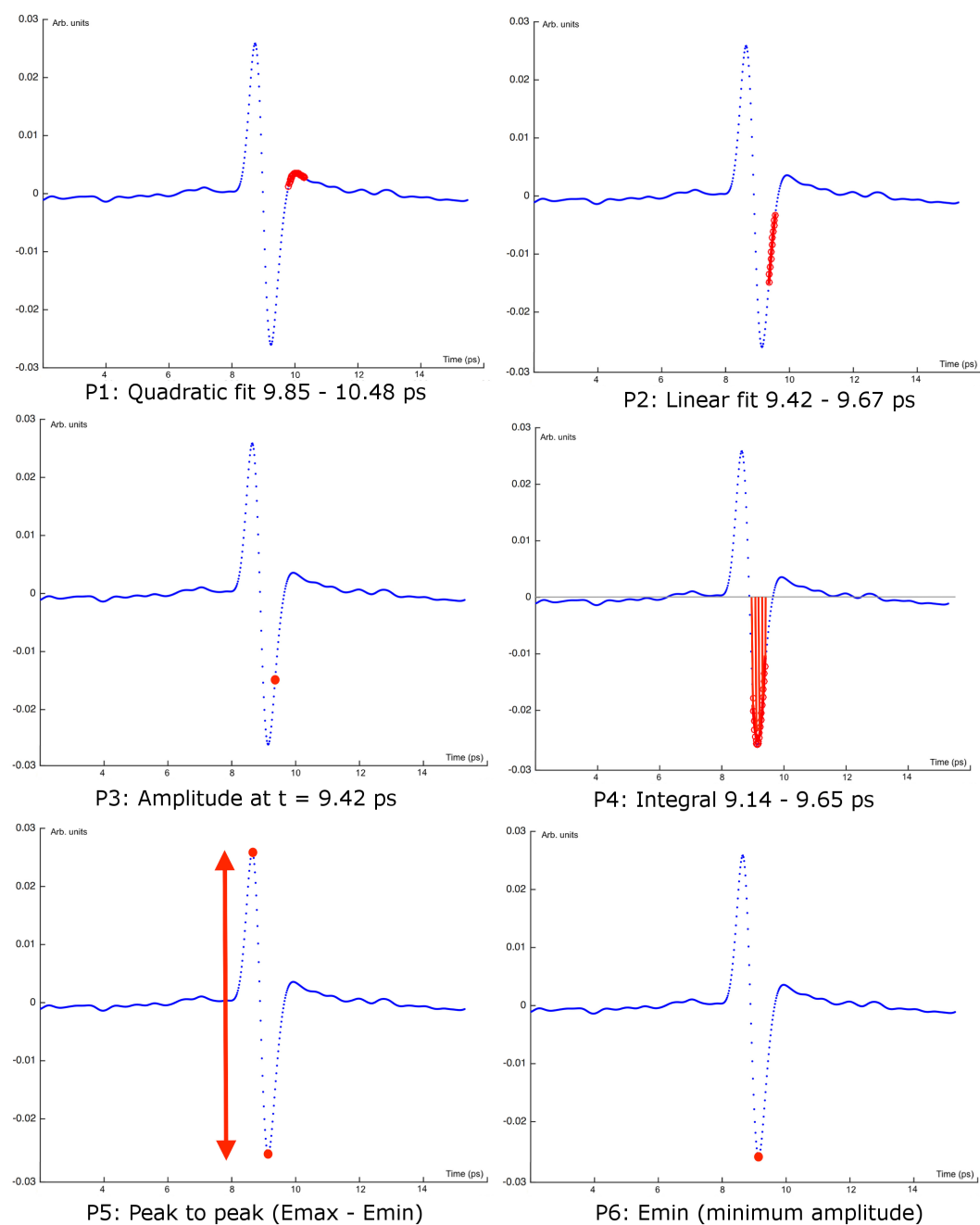
378. Thorek DL, Abou DS, Beattie BJ, et al. Positron lymphography: multimodal, high-resolution, dynamic mapping and resection of lymph nodes after intradermal injection of 18F-FDG. *J Nucl Med.* 2012;53:1438-1445.

379. Spinelli AE, Ferdeghini M, Cavedon C, et al. First human Cerenkography. *J Biomed Opt.* 2013;18:20502.

380. Britten A, Newey VR, Clarke R. A computerized gamma probe simulator to train surgeons in the localization of sentinel nodes. *Nucl Med Commun.* 2007;28:225-229.

381. Mathelin C, Salvador S, Huss D, Guyonnet JL. Precise localization of sentinel lymph nodes and estimation of their depth using a prototype intraoperative mini gamma-camera in patients with breast cancer. *J Nucl Med.* 2007;48:623-629.

382. Giammarile F, Alazraki N, Aarsvold JN, et al. The EANM and SNMMI practice guideline for lymphoscintigraphy and sentinel node localization in breast cancer. *Eur J Nucl Med Mol Imaging.* 2013;40:1932-1947.

383. Rubello D, Zavagno G, Bozza F, et al. Analysis of technical and clinical variables affecting sentinel node localization in patients with breast cancer after a single intradermal injection of 99mTc nanocolloidal albumin. *Nucl Med Commun.* 2004;25:1119-1124.

384. Mansel RE, MacNeill F, Horgan K, et al. Results of a national training programme in sentinel lymph node biopsy for breast cancer. *Br J Surg.* 2013;100:654-661.

385. Waddington WA, Keshtgar MR, Taylor I, Lakhani SR, Short MD, Ell PJ. Radiation safety of the sentinel lymph node technique in breast cancer. *Eur J Nucl Med.* 2000;27:377-391.

386. The Ionising Radiations Regulations 1999 No. 3232. Health and Safety Executive. 1999.

387. Ionising Radiation (Medical Exposure) Regulations 2000 (IRMER). Department of Health. 2012.

388. The environmental permitting (England and Wales) regulations 2010. Department for environment, food and rural affairs; 2010.

389. Kumar R, Chauhan A, Zhuang H, Chandra P, Schnall M, Alavi A. Clinicopathologic factors associated with false negative FDG-PET in primary breast cancer. *Breast Cancer Res Treat.* 2006;98:267-274.

390. Kalinyak JE, Berg WA, Schilling K, Madsen KS, Narayanan D, Tartar M. Breast cancer detection using high-resolution breast PET compared to whole-body PET or PET/CT. *Eur J Nucl Med Mol Imaging.* 2014;41:260-275.
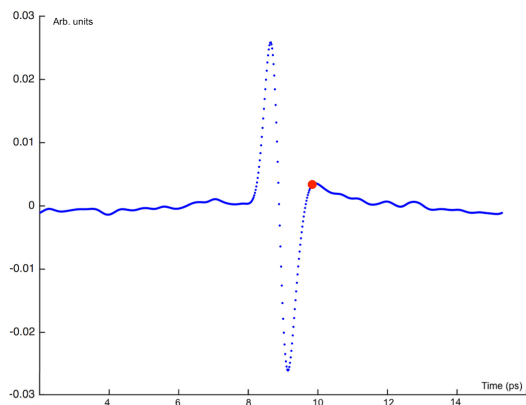
391. Duran A, Hian SK, Miller DL, Le Heron J, Padovani R, Vano E. Recommendations for occupational radiation protection in interventional cardiology. *Catheter Cardiovasc Interv.* 2013;82:29-42.

392. The 2007 Recommendations of the International Commission on Radiological Protection. ICRP publication 103. Ann. ICRP 37 (2-4). International Commission on Radiological Protection; 2007.

393. USNRC. Standards for protection against radiation. 10 CFR PART 20.

394. Sun JS, Tsuang YH, Chen IJ, Huang WC, Hang YS, Lu FJ. An ultra-weak chemiluminescence study on oxidative stress in rabbits following acute thermal injury. *Burns.* 1998;24:225-231.

395. Loh SA, Carlson GA, Chang EI, Huang E, Palanker D, Gurtner GC. Comparative healing of surgical incisions created by the PEAK PlasmaBlade, conventional electrosurgery, and a scalpel. *Plast Reconstr Surg.* 2009;124:1849-1859.

396. Ruidiaz ME, Cortes-Mateos MJ, Sandoval S, et al. Quantitative comparison of surgical margin histology following excision with traditional electrosurgery and a low-thermal-injury dissection device. *J Surg Oncol.* 2011;104:746-754.

397. Groheux D, Espie M, Giacchetti S, Hindie E. Performance of FDG PET/CT in the clinical management of breast cancer. *Radiology.* 2013;266:388-405.
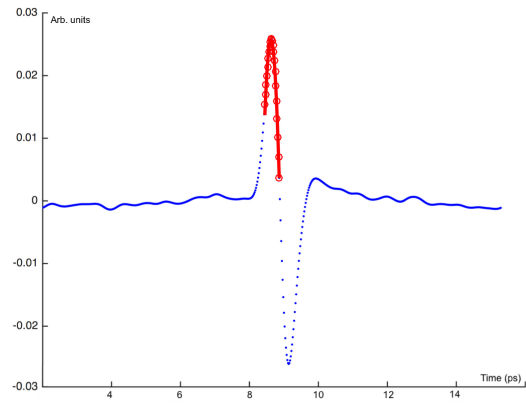
7. Appendix

7.1 Appendix 1: Supplementary data terahertz pulsed imaging study

Appendix Figure 27: Visualisation of the selected parameters used in SVM classification. Each parameter is displayed in red.
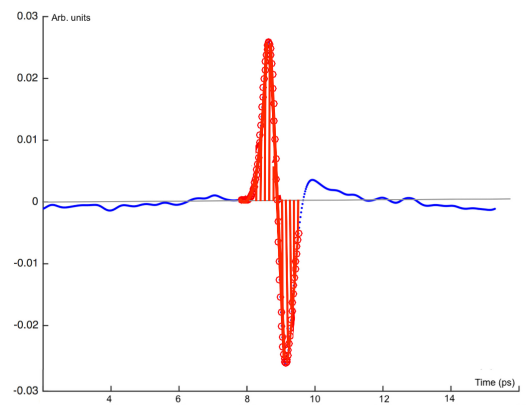
P7: Amplitude at t = 10.05 ps

P8: Quadratic fit 8.26 - 8.79 ps

P9: Integral 7.47 - 9.62 ps

P10: Emax (maximum amplitude)

P11: Power frequency = 1.11 THz

229
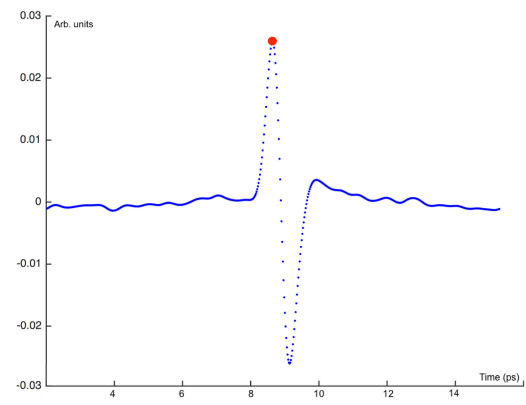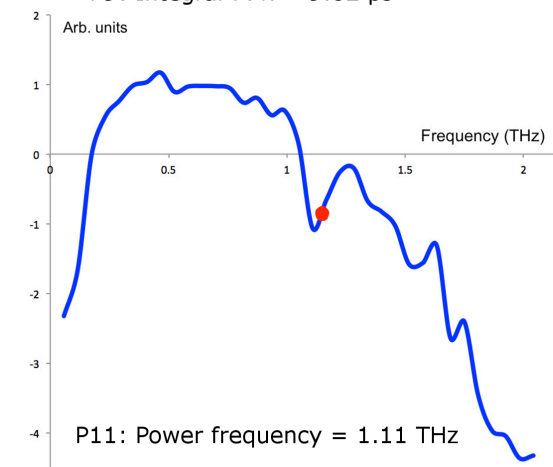
Appendix Table 19: SVM classification results for all possible combinations of 2 uncorrelated parameters. PPV = positive predictive value; NPV = negative predictive value.

		Accuracy (%)	Sensitivity (%)	Specificity (%)	PPV (%)	NPV (%)
P1	P2	68	77	61	62	76
P1	P3	68	76	61	61	76
P1	P4	70	77	63	63	78
P1	P5	73	83	65	66	82
P1	P6	75	86	66	67	85
P1	P8	71	90	56	62	87
P1	P9	68	77	61	61	77
P1	P10	65	77	55	58	74
P1	P11	71	77	65	64	78
P11	P2	74	82	69	67	82
P11	P3	73	81	67	66	81
P11	P4	71	78	65	64	79
P11	P5	72	83	63	65	85
P11	P6	68	74	63	62	75
P11	P7	60	59	61	55	65
P11	P8	65	76	57	59	74
P11	P9	55	55	56	50	60
P11	P10	65	75	56	58	73
P7	P2	68	78	61	62	77
P7	P3	69	78	62	63	78
P7	P4	69	78	61	62	78
P7	P6	67	80	57	59	77
P7	P8	63	81	48	56	76
P7	P9	67	82	55	59	79
P9	P2	68	77	61	61	76
P9	P3	67	77	58	60	75
P9	P4	64	75	56	58	73
P9	P5	62	77	51	56	73
P9	P6	63	79	51	57	75
P9	P8	60	77	45	53	71
P9	P10	70	74	67	64	76

Appendix Table 20: SVM classification results for all possible combinations of 3 uncorrelated parameters. PPV = positive predictive value; NPV = negative predictive value.

			Accuracy (%)	Sensitivity (%)	Specificity (%)	PPV (%)	NPV (%)
P1	P2	P9	61	66	56	55	67
P1	P2	P11	65	66	65	60	70
P1	P3	P9	61	67	56	55	68
P1	P3	P11	65	66	63	59	70
P1	P4	P9	62	70	56	56	69
P1	P4	P11	66	67	65	61	71
P1	P5	P9	64	76	55	58	74
P1	P5	P11	67	70	65	62	72
P1	P6	P9	61	70	54	55	69
P1	P6	P11	71	72	70	66	76
P1	P8	P9	62	74	53	56	71
P1	P8	P11	66	67	65	61	71
P1	P10	P9	65	72	59	59	72
P1	P10	P11	68	66	70	64	72
P7	P2	P9	63	65	61	57	68
P7	P2	P11	61	61	61	56	66
P7	P3	P9	61	64	59	56	67
P7	P3	P11	61	60	62	56	66
P7	P4	P9	61	63	60	56	67
P7	P4	P11	61	61	61	56	66
P7	P6	P9	65	72	59	59	72
P7	P6	P11	61	58	63	56	65
P7	P8	P9	64	70	58	58	71
P7	P8	P11	59	56	61	54	63
P9	P11	P1	64	57	70	61	67
P9	P11	P2	68	62	74	66	70
P9	P11	P3	68	61	73	65	70
P9	P11	P4	67	61	71	63	69
P9	P11	P5	60	58	62	55	65
P9	P11	P6	63	56	69	59	66
P9	P11	P7	55	48	61	50	59
P9	P11	P8	54	49	58	48	58
P9	P11	P10	55	51	58	50	60

Appendix Table 21: SVM classification results for all possible combinations of 4 uncorrelated parameters. PPV = positive predictive value; NPV = negative predictive value.

				Accuracy (%)	Sensitivity (%)	Specificity (%)	PPV (%)	NPV (%)
P1	P2	P9	P11	63	52	72	60	65
P1	P3	P9	P11	63	51	72	60	65
P1	P4	P9	P11	63	52	71	59	65
P1	P5	P9	P11	66	56	74	63	67
P1	P6	P9	P11	67	56	75	65	68
P1	P8	P9	P11	64	51	74	61	65
P1	P10	P9	P11	66	52	77	65	66
P7	P2	P9	P11	58	50	65	54	62
P7	P3	P9	P11	58	49	65	53	61
P7	P4	P9	P11	60	51	66	55	63
P7	P6	P9	P11	59	54	63	54	63
P7	P8	P9	P11	55	43	65	50	59

7.2 Appendix 2: Gamma probe cross-talk study documents

7.2.1 Patient information sheet

Study Title: Gamma probe cross talk from 18F-FDG in technetium-99m energy window

Sponsor: Kings College London / Guy's and St Thomas' NHS Trust

Principal Investigator: Professor Gary Cook

PATIENT INFORMATION SHEET

Invitation to take part in this research study

We would like to invite you to take part in a research study. Before deciding, it is important to understand why the research is being done and what it would involve for you. Please take time to read the following information carefully, discuss it with people who are close to you and do not hesitate to ask us any question. Participation in the study is entirely voluntary. Your level of care will not be affected whether you take part in the study or not.

Why have I been invited?

You are being invited to take part in this research study because you are about to have a PET-scan during which you will receive an injection of a radioisotope called 18F-FDG. A maximum of 20 patients will take part in the study. The study is only taking place at this hospital.

What is the purpose of the study?

The study is to measure the highest and lowest signal from the radioisotope (18F-FDG) that is injected as part of your PET-scan. The signal will be measured in the left and right

armpit, using a handheld detection device (called a gamma probe) that is currently being used to detect other radioisotopes during surgery.

We are hoping to use the results of this study in a new surgical device trial that may help surgeons detect during surgery whether all the breast tumour (cancer) has been removed. Removing all cancer will reduce the need for further surgery, and thus benefit future patients with breast cancer.

Do I have to take part?

No, it is up to you to decide whether you would like to join this research study. If you agree to take part, we will ask you to sign a consent form. If you do not want to take part in the study or withdraw at any time without giving a reason, the treatment and care you receive from the doctors and nurses here at Guy's and St Thomas' Foundation Trust will be no different than you would normally receive.

What will happen to me if I take part?

All patients taking part in this study will receive the same level of care and same treatment as those who are not.

If you choose to take part in the study, some basic information about you will be collected - for example, your age, height, weight and the reason why you are undergoing a PET-scan.

As part of the routine PET scanning procedure, you will receive a radioisotope injection and you will need to wait for 90 minutes before your scan can be done. This period of time allows the tracer to circulate in the blood stream and go into the tissues. We will take our measurements during your waiting time, so we will not be interfering with your scan.

We will position a handheld detection device (called a gamma probe) in your right armpit and measure the highest and lowest signal. We will then measure the highest and lowest signal in your left armpit. The head of the probe will be placed against your skin to take the readings and is approximately the size of a ten pence coin. You will only feel a slight pressure against your skin.

The measurements will take just a few minutes and will not affect you or your treatment in any way. Your participation will end once the measurements have been completed. There is no follow up in this study.

The information from these measurements will help us to design an accurate protocol for another research study to help surgeons detect during surgery whether all of a breast tumour (cancer) has been removed.

What are the possible disadvantages and risks of taking part?

There are no risks or side effects associated with this research study. You will not receive any drugs or undergo any invasive procedures as part of this study. Your routine care will not be affected in any way.

What are the possible benefits of taking part?

There are no direct benefits to you from taking part in this research. Future patients that undergo surgery for breast cancer may benefit if the technique works.

What if there is a problem?

The trial does not affect your treatment and does not involve any invasive procedures so it is highly unlikely that anything will go wrong with your treatment or care. The research team will always be available in the event of any problems or if you have any queries (contact numbers are listed at the end of this document). If you wish to complain about any aspect of

Patient information sheet – CLI PET study.   *Version 2 dated 24.01.2014*   3

the way you have been approached or treated during the course of the study, you can do so using the National Health Service (NHS) complaints procedure.

There are no special compensation arrangements as we do not anticipate any adverse events. However, the healthcare professionals working on the clinical studies are covered by NHS Indemnity, which covers harm due to medical negligence.

Any concerns should be raised by speaking to a member of staff at your at your hospital or by talking the local Patient Advice and Liaison Service (PALS) which has been established in every NHS Trust and Primary Care Trust (PCT).

Will my taking part in this study be kept confidential?

Yes. We will follow all ethical and legal regulations and all information about you will be handled in confidence. Only Guy's and St Thomas' staff will collect information about you during the course of the research and this will remain confidential and be stored in a secure area of the hospital.

What will happen to the results of the research study?

At the end of the study the results will be included in a report. You will not be identified in this, or any other written report. The report may form part of an application to the Regulatory Authorities. You will not be identified in the report.

What is organizing and funding the research study?

The research is being organized by Guy's and St Thomas' Foundation Trust. This study is not funded.

Who has reviewed the study?

All research in Guy's and St Thomas' NHS Foundation Trust is reviewed by an independent group of people called an Ethics Committee to protect your safety, rights and wellbeing. This study has been reviewed by from the South East Scotland Research Ethics Committee..

Involvement of the General Practitioner/Family doctor (GP)

Your doctor (general practitioner) will be notified of your involvement in this study

Further information and contact details

If you have any questions or wish to obtain any further information later, please contact the following individuals:

Research Nurse: Vernie Ramalingam   02071880743

Research Fellow: Maarten Grootendorst   02071880743

Clinical Trials Coordinator: Sweta Sethi   02071880743/ 07795646473

For an independent opinion please contact:

Fernanda Castro   02071886380

Thanks

Thank you for your time and for considering participating in this research study.

7.2.2 Consent form

King's College London
University of London

Guy's and St Thomas' NHS
NHS Foundation Trust

Study Title:	Gamma probe cross talk from 18F-FDG in technetium-99m energy window
Sponsor:	King's College London / Guy's and St Thomas' NHS Trust
Principal Investigator:	Professor Gary Cook

INFORMED CONSENT FORM

Please read carefully and initial each of the boxes below:

1. I confirm that I have read and understood the Patient Information sheet version 2, dated 24/01/2014, about the study named above. I have been given the opportunity to take the information into consideration, ask questions and have had these answered to my satisfaction. ☐

2. I am fully aware that participation is voluntary and that I have the right to withdraw at any time, without mentioning any reasons and without this having any influence on my medical treatment or legal rights. ☐

3. I understand that the collected data may be assessed during this study by representatives of an ethics committee or health authorities. I give my consent for these people to have access to my data. ☐

4. I understand that the study data will be kept for a period of 15 years after the end of the study. ☐

5. I consent to my GP being informed of my participation in this study. ☐

6. I agree to participate in this study ☐

Name of patient	Date	Signature

Name of person taking consent	Date	Signature

Complete in duplicate, one copy to be given to the patient and another copy to be stored in the study file.

Consent Form: CLI PET study   *Version 2 dated 14.01.2014*   1

238

7.2.3 GP letter

Date

Dear Dr   ,

Patients name:

Patient's address:

Gamma probe detection in patients undergoing a PET-scan study

Your patient has consented to participate in this observational study that has been designed to measure the amount of cross talk between a gamma-probe signal from 18F-FDG and the gamma-probe signal from 99mTc (Technetium-99m) in patients undergoing a diagnostic PET scan.

Patients that are about to have a routine PET-scanning procedure will be receive an injection of the radioisotope 18F-FDG for the PET scan. After they have been given the injection, a gamma probe will be placed in their right and then left armpit. The highest and lowest signal will be measured.

A copy of the patient information sheet is enclosed, but if you require further information please do not hesitate to contact us.

Yours sincerely,

Gary Cook

Professor of Clinical PET Imaging/ Honorary Consultant

GP letter version 1.0
24 January 2014
REC Ref: 14/SS/0013

7.3 Appendix 3: Intraoperative ¹⁸F-FDG Cerenkov luminescence imaging clinical study documents

7.3.1 Patient information sheet and consent form

Short Title:	**The CLI Specimen Analyser study**
Study Title:	**A pilot study to evaluate Cerenkov Luminescence Imaging for measuring margin and lymph node status in breast cancer surgical specimens.**
Sponsor:	**Lightpoint Medical Limited**
Study Code:	**LPM-001**
Principal Investigator:	**Professor Arnie Purushotham**

PATIENT INFORMATION SHEET

Invitation to take part in this research study

We would like to invite you to take part in a research study. It is important you understand why the research is being done and what it would involve for you before making your decision. Take your time to read the following information carefully and please talk to friends and family members about the study if you wish.

Participation in the study is entirely voluntary. If you have any questions about the study after you have read this information, please discuss this with the study doctor or study staff. When you believe that you have sufficient information, you can decide whether or not you wish to take part in the study.

What is the research testing?

This study is testing a new device that could help surgeons know if they have removed all of a tumour (cancer) during surgery. The device is known as the CLI Specimen Analyser (see picture below). This new device is use to look at the lump and any other tissue removed from your breast during surgery.

Picture 1
The CLI Specimen Analyser
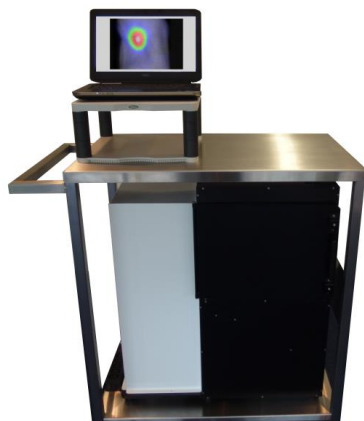
What is the purpose of the study?

The purpose of this study is to find out if this new device can be used, in the future, to detect cancer in tissue removed during surgery. This is a small pilot study to help researchers understand more about how the device works. Some people have already taken part in this study and we know that we can use the new device to look at the cancer that has been removed during surgery. However, we need some more people to take part in the study, so that we can understand how best to use the new device. The results of this study will be used to make improvements to the device and to plan larger studies to test how well the device works.

Why have I been invited?

You are being invited to join this research study because you are about to have surgery for breast cancer. A maximum of 30 people will take part in the study, which is only taking place at this hospital.

Do I have to take part?

It is up to you to decide to join this research study. A member of the research team will describe the study and go through this form with you. You will be given as much time as you need to read and understand the information leaflet and make your decision. You may want to talk to your family or GP about taking part and you will be given the opportunity to do so. If you agree to take part, we will then ask you to sign a consent form. If you do not want to take part in the study, the treatment and care you receive from the doctors and nurses here at Guy's Hospital will be exactly the same as you would normally receive.

What will happen to me if I take part?

All patients taking part in this study will receive the same level of care and same treatment as those who are not.

If you choose to take part in the study, some basic information about you will be collected. For example, your age, height, weight and the reason you are having surgery. On the day of surgery, your blood sugar level will be measured. This is done by pricking your finger with a small needle (lancet) and collecting a drop of blood. If your blood sugar level is too high (12 mmol/l or higher), you will not be able to take any further part in the study.

Patients who take part in the study will be given an injection of a radioactive compound called fluorine FDG (18F-FDG) just before their surgery. This is a sugar substance that is taken up in many types of cancer. It is normally used during a test called a PET scan, which helps to show your doctor where cancer cells are located. This injection is given during the study because the new device being tested detects very low level light given off by cancer cells containing fluorine FDG. The radioactivity from the injection leaves your body quickly and will not make you feel unwell. As radiation can harm unborn children, if you are interested in taking part in the study you will be asked if it is possible that you could be pregnant. You may be asked to take a pregnancy test.

If your doctor is planning to perform a sentinel lymph node biopsy during your surgery, you will normally be given another radioactive compound called ^{99m}Tc-colliod (technetium colloid). If you take part in the study, you will be given more ^{99m}Tc-colliod than normal (150 MBq instead of 20-40 MBq)

Once surgery has begun, the surgeon will perform the operation as normal. The lump and any tissue that is removed from your breast during the operation will be examined using the CLI device. We will also examine any lymph nodes that are removed from the armpit. The CLI device will take pictures of the tissue, like Picture 2 below.

The tissue will then be sent to the laboratory to be examined for cancer using standard tests. The results from the CLI device will not be known until after your operation and will not be used to make any decisions about your care. You will not be provided with the results from the CLI device.

Picture 2
A picture of breast tissue taken in the CLI Specimen Analyser. The orange-coloured areas show where there is tumour.
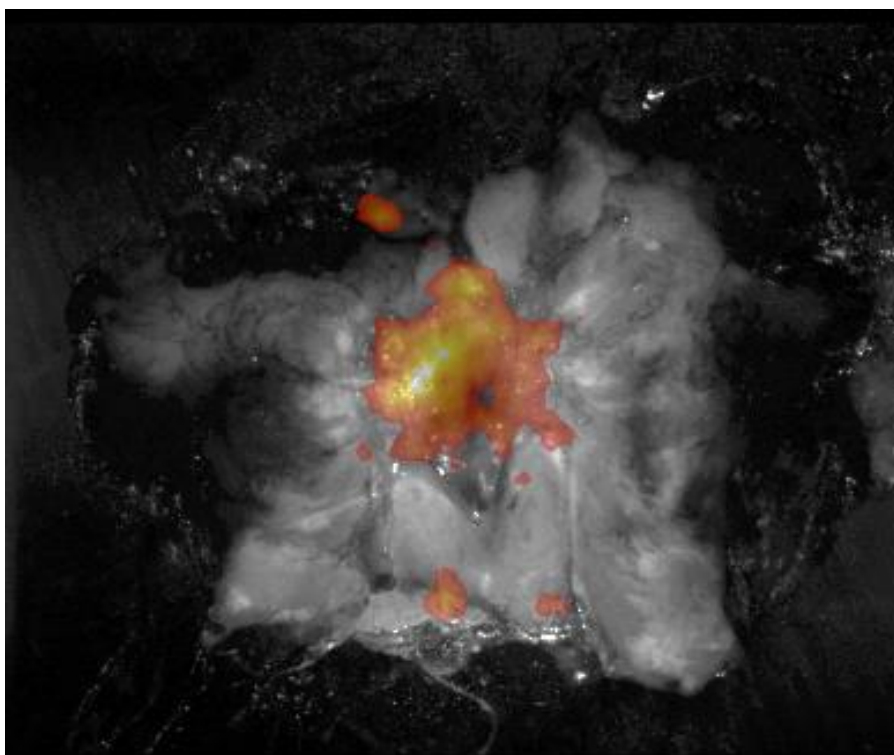
What are the alternatives for treatment?
Taking part in this study will not change the treatment you receive in any way. The results from tests using the CLI Specimen Analyser will not be used to make any decisions about your treatment. You doctor will provide the best treatment that is available to you.

What are the possible disadvantages and risks of taking part?

Patients taking part in the study will be given an injection of fluorine FDG and technetium colloid which are radioactive tracers required for the study. Both tracers are used routinely; fluorine FDG in PET-CT scanning and technetium colloid in sentinel node biopsy procedures. For this study the amount of fluorine FDG is the same as is given for a standard PET-CT scan. The amount of radiation for the technetium colloid is greater than standard care. The amount of radiation you will receive from the injection reduces rapidly over a few hours and by the time you leave the operating theatres the amount of radiation left in you so small that it is safe for you to travel home and be with your family and friends.

The amount of radiation you will receive in this study is 6.4milliSieverts (mSv). This is similar to:

- The radiation dose from a typical chest CT scan (7.0mSv).
- Around 3 years' natural background radiation. Natural background radiation is approximately 2.2mSv per year in the UK. In some places, the natural background radiation is higher - the average annual background radiation dose to a person living in Cornwall is slightly higher (7.8mSv) than the amount of radiation you will receive in this study.
- Around 300 transatlantic flights (a 7 hour flight is 0.02mSv).

It is known that high levels of radiation can cause cancer. While the amount of radiation you receive if you take part in the study is small, it is possible that this may increase the risk of developing cancer later on in life. This risk changes depending on your age now. If you are in your thirties, the additional risk of developing cancer later on in life because of the radiation exposure is 1 in 2,300. This means that if 2,300 people aged 30-39 were exposed to the level of radiation received from taking part in this study, 1 of them would develop cancer later in life because of the radiation. The table below shows the increase in risk for each age group.

Age now	Increased risk of cancer later in life
30-39	1 in 2300 (0.043%)
40-49	1 in 2700 (0.037%)
50-59 years	1 in 3500 (0.029%)
60-69 years	1 in 5000 (0.020%)
70-79 years	1 in 8700 (0.011%)
80-89 years	1 in 20,000 (0.005%)
90-99 years	1 in 1,000,000 (0.0001%)

What are the possible benefits of taking part?

There are no direct benefits to you from taking part in this research.

The goal of this research study and future studies is to find better ways to see cancer during surgery so that surgeons can be sure all the cancer has been removed. It is hoped

that the findings of this research will help develop devices which will in the future benefit not just women with breast cancer, but men and women with all types of cancer.

244

What will happen if I do not want to carry on with the study?

You have the right to stop taking part in the study at any time without mentioning any reasons. This decision will not affect your current treatment and care or any future treatment and care you receive in our hospital.

What if there is a problem?

If you have a concern about any aspects of this study, you should ask to speak to the researchers who will do their best to answer your questions. If you remain unhappy and wish to complain formally, you can do this by following the hospital complaints procedure. To find out about it, ask a member of staff, look on the hospital website or contact the Patient Advice and Liaison Service (PALS) on 020 7188 8801 or 020 7188 8803 for more information.

We will provide compensation for any injury caused by taking part in this study in accordance with national guidelines. We will pay compensation where the injury probably resulted from any procedure you received as part of the study. Any payment would be without legal commitment. (Please ask if you wish to receive more information on this). We would not be bound by these guidelines to pay compensation where the injury resulted from a procedure outside of the study or the study protocol was not followed. Insurance has been taken out by the study sponsor to cover injury or death resulting from participation in the study.

If you have private medical insurance you should check with the insurance company that your insurance status would not be affected before agreeing to take part in the study.

Will my taking part in this study be confidential?

If you agree to take part in the study you will be given a unique study number. Any data collected will be recorded using only your study number to identify you. We will not collect any personal identifiable information (names, addresses, telephone numbers) for the trial.

The data that is collected for the study will be kept for up to 15 years after the end of the study. No information that could identify you will be used in any publications about the study.

In the UK, all research involving patients is reviewed by an ethics committee. This is to ensure that the research is carried out safely and according to regulations.

Lightpoint Medical (the company sponsoring the study) will also appoint authorized representatives to compare the collected study data with the data in your medical file. This will only be the information relating to your cancer diagnosis and your participation in the study. This is to check that all data has been accurately recorded.

We will ask for your consent to allow the use of your data and medical records as mentioned above. All information collected will be treated with the strictest confidence; and your study doctor will be responsible for ensuring the confidential handling of your data.

Notifying your General Practitioner

We will ask for your consent to inform your general practitioner (GP) that you have decided to take part in this study. If you have any objections to your GP being contacted, please speak to your study doctor.

What will happen to any samples I give?

No samples will be collected for this study. While tissue from your breast and lymph nodes removed during surgery will be examined immediately using the CLI Specimen Analyser, these will be handled as normal afterwards, and sent to the laboratory for examination.

Will any genetic tests be done?

No.

What will happen to the results of the research study?

At the end of the study the results will be included in a report. You will not be named in this, or any other document about the study. The report may form part of an application to Regulatory Authorities. This study has been placed on internet directories of clinical trials (http://isrctn.org/ and www.clinicaltrials.gov) and the result, once available will be posted here. Your study team will also send you a copy of the results upon request.

Who is organising and funding the research?

Lightpoint Medical Ltd, a Biotechnology company, is organising this study in partnership with Guy's and St Thomas' NHS Foundation Trust and King's College London. The study is funded by the Technology Strategy Board.

Who has reviewed the study?

To protect your safety, rights and wellbeing, all research in Guy's and St Thomas' NHS Foundation Trust is reviewed by an independent group of people called an Ethics Committee. This study has obtained ethical approval from the West Midlands - Edgbaston ethics committee.

Further information and contact details

If you wish to receive additional information or if you still have any questions after having read this information sheet or before or during the study, you can always contact members of the research team below:

Professor Purushotham (breast surgeon)   Tel: 02071883027

Vernie Ramalingam (research nurse)   Tel: 0207188 0743

Sweta Sethi (clinical trial coordinator)   Tel: 02071880743

In cases of emergency you can call our hospital through the general telephone number: 020 7188 7188.

A description of this research study will be available on the following websites http://public.ukcrn.org.uk/search/, http://isrctn.org/ and http://www.ClinicalTrials.gov. These websites will not include information that can identify you. At most, the websites will include a summary of the results. You can search these websites at any time.

Signing the Informed Consent Form

If you decide to take part in the study, we will ask you to sign a form in duplicate. You may keep one copy yourself and give the other copy to your study doctor, who will ensure it is filed in your medical records. By signing this form (i.e. an Informed Consent Form or simply Informed Consent), you agree to take part in this study. You will remain free to decide to stop taking part in the study for whatever reason relevant to you. The study doctor will also sign the form and confirm that he or she has informed you about the study, that he or she has given you this patient information sheet and that he or she is prepared to answer any questions that may arise.

CONCLUSION

You must only sign the Informed Consent Form if all of the following are true:

- You have read and understood this patient information sheet.

- All your questions about taking part in this study have been answered to your satisfaction.

- You understand all information provided concerning this study.

- You have voluntarily decided to take part in this study.

Thank you for taking the time to read this information.

Short Title:	**The CLI Specimen Analyser study**
Study Title:	**A pilot study to evaluate Cerenkov Luminescence Imaging for measuring margin status in breast cancer surgical specimens.**
Sponsor:	**Lightpoint Medical Limited**
Study Code:	**LPM-001**
Principal Investigator:	**Professor Arnie Purushotham**

INFORMED CONSENT FORM

Please read carefully and initial each of the boxes below:

1. I confirm that I have read and understood the Patient Information Sheet (version 1.3 dated: 03 February 2016) about the study named above. I have been given the opportunity to take the information into consideration, ask questions and have had these answered to my satisfaction.

2. I am fully aware that participation is voluntary and that I have the right to withdraw at any time, without mentioning any reasons and without this having any influence on my medical treatment or legal rights.

3 I understand that I will receive a radioactive injection as part of the study. All risks have been explained to me

3. I understand that relevant information from my medical data and other collected data may be assessed during this study by representatives of Lightpoint Medical Ltd, companies acting on their behalf, an ethics committee or health authorities. I give my consent for these people to have access to my data.

4. I understand that the study data will be kept for a period of up to 15 years after the end of the study.

5. I agree that my general practitioner (GP) will be informed about my participation in this study.

6. I agree to participate in this study.

Please write your name, today's date and sign below.

Name of patient	Date	Signature

Name of person taking consent	Date	Signature

249

7.3.2 GP letter

GENERAL PRACTITIONER INFORMATION

Patient's Name:

Date of Birth:

Address:

Dear ……,

A pilot study to evaluate Cerenkov Luminescence Imaging for measuring margin and lymph node status in breast cancer surgical specimens

I wish to inform you that the above patient has agreed to participate in a clinical performance study of an in-vitro diagnostic device. This patient was invited to participate in the study as she is scheduled to have Breast Conserving Surgery for breast cancer at Guy's Hospital.

This study of 30 patients will test the feasibility of using a new medical technology known as Cerenkov Luminescence Imaging, or CLI. The study device is a specimen analyser intended for the ex-vivo visualisation of surgical specimens to assess tumour margin and lymph node metastatic status during surgery.

In addition to routine care, your patient will have their blood glucose checked on the day of surgery, receive an additional intravenous injection of a PET radiotracer (18F-FDG) and, if the patient is having a sentinel lymph node biopsy, an increased quantity of technetium 99m.

The study has been reviewed by an independent Research Ethics Committee and it has been agreed that it may go ahead.

I would be grateful if you could inform me immediately of any concerns you may have with your patient entering this study.

Please do not hesitate to contact me if you have any questions.

Yours sincerely,

Professor Arnie Purushotham

7.4 Appendix 4: Overview of prizes, papers, oral presentations and grants arising from work in this thesis

Prizes

- Winner Poster Prize, Division of Cancer Studies Symposium, 2015

- Runner-up Nuclear Oncology Young Investigator Award, Society of Nuclear Medicine and Molecular Imaging Annual Meeting, 2015

- Runner-up Three Minute Thesis Competition, King's College London, 2014

Papers

Cerenkov Luminescence Imaging (CLI) for image-guided cancer surgery

Grootendorst MR, Cariati M, Kothari A, Tuch DS, Purushotham A. Published in Clinical and Translation Imaging (April 2016)

Application of Terahertz Technology to Breast Cancer

Grootendorst MR, Cariati M, Ashworth PC, Fitzgerald AJ, Purushotham A, Wallace VP. Published as book chapter in 'Terahertz Biomedical Science and Technology' (May 2014)

Intraoperative Assessment of Tumor Resection Margins in Breast-Conserving Surgery using ^{18}F-FDG Cerenkov Luminescence Imaging –
A First-in-Human Feasibility Study

Grootendorst MR, Cariati M, Pinder SE, Kothari A, Douek M, Kovacs T, Hamed H, Pawa A, Nimmo F, Owen J, Ramalingam V, Sethi S, Mistry S, Vyas K, Tuch D, Britten A, Van Hemelrijck M, Cook G, Sibley-Allen C, Allen S, Purushotham A. Re-submitted to the Journal of Nuclear Medicine following minor revisions (September 2016)

The use of a handheld Terahertz pulsed imaging device to differentiate benign and malignant breast tissue

Grootendorst MR, *Fitzgerald AJ, Brouwer de Koning SG, Santaolalla A, Portieri A, Van Hemelrijck M, Young MR, Cariati M, Pepper M, Wallace VP, Pinder SE, Purushotham A. Submitted to British Journal of Surgery (October 2016)*

Oral presentations

Intraoperative assessment of tumour resection margins in breast-conserving surgery using Cerenkov Luminescence Imaging (CLI)

Presented at British Breast Group Meeting, Edinburg, United Kingdom, 2016

Grootendorst MR, *Cariati M, Kothari A, Douek M, Kovacs T, Hamed H, Pawa A, Nimmo F, Ramalingam V, Sethi S, Mistry S, Vyas K, Tuch D, Britten A, Van Hemelrijck M, Cook G, Allen S, Sibley-Allen C, Pinder S, Purushotham A*

Cerenkov luminescence imaging in surgery

Presented in Plenary Session at British Nuclear Medicine Society Autumn Meeting, London, United Kingdom, 2015

Grootendorst MR, *Purushotham A*

Clinical feasibility of intraoperative ^{18}F-FDG Cerenkov Luminescence Imaging in breast cancer surgery

Presented in Poster Prize Session at Association of Breast Surgery Annual Conference, Bournemouth, United Kingdom, 2015

Grootendorst MR, Kothari A, Cariati M, Cook G, Allen S, Sibley-Allen C, Britten A, Tuch D, Pinder S, Purushotham A on behalf of the Cerenkov Luminescence Imaging Study Group

Clinical feasibility of intraoperative ^{18}F-FDG Cerenkov Luminescence Imaging in breast cancer surgery

Presented in Nuclear Oncology Young Investigator Award Session at Society of Nuclear Medicine and Molecular Imaging Annual Meeting, Baltimore, United States, 2015

Grootendorst MR, Kothari A, Cariati M, Cook G, Allen S, Sibley-Allen C, Britten A, Tuch D, Pinder S, Purushotham A on behalf of the Cerenkov Luminescence Imaging Study Group

Gamma probe cross talk from ^{18}F-FDG in ^{99m}Tc energy window when performing sentinel lymph node biopsy

Presented at Association of Breast Surgery London Regional Breast Symposium, London, United Kingdom, 2014

Grootendorst MR, Voskuilen V, John J, Woods E, Sethi S, Britten A, Allen S, Cook G, Purushotham A

Differentiating benign and malignant breast tissue using a handheld Terahertz probe

Presented in Breast Imaging Session at Radiological Society of North America Annual Meeting, Chicago, United States, 2015

Maarten Grootendorst, Susan Brouwer de Koning, Tony Fitzgerald, Alessia Portieri, Aida Santa Olalla, Massi Cariati, Michael Pepper, Vincent Wallace, Sarah Pinder, Arnie Purushotham

The use of a handheld Terahertz pulsed imaging device to differentiate benign and malignant breast tissue with a view to reducing re-operation rates in breast-conserving surgery

Presented in Ronald Raven Prize Session at British Association of Surgical Oncology – Royal Society of Medicine Conference, London, United Kingdom, 2015

Grootendorst MR, Brouwer de Koning S, Fitzgerald T, Portieri A, Santa Olalla A, Cariati M, Pepper M, Wallace W, Pinder S, Purushotham

Grants

Pioneering a centre of excellence for intraoperative molecular imaging in cancer surgery

Co-author on Guy's and St Thomas' Charity Health Innovation Fund Grant

Grant total: £950,259

7.5 Appendix 5: Papers and book chapter

CrossMark

REVIEW ARTICLE

Cerenkov luminescence imaging (CLI) for image-guided cancer surgery

M. R. Grootendorst[1,2] · M. Cariati[1,2] · A. Kothari[2] · D. S. Tuch[3] · A. Purushotham[1,2]

© The Author(s) 2016. This article is published with open access at Springerlink.com

Abstract Cerenkov luminescence imaging (CLI) is a novel molecular optical imaging technique based on the detection of optical Cerenkov photons emitted by positron emission tomography (PET) imaging agents. The ability to use clinically approved tumour-targeted tracers in combination with small-sized imaging equipment makes CLI a particularly interesting technique for image-guided cancer surgery. The past few years have witnessed a rapid increase in proof-of-concept preclinical studies in this field, and several clinical trials are currently underway. This article provides an overview of the basic principles of Cerenkov radiation and outlines the challenges of CLI-guided surgery for clinical use. The preclinical and clinical trial literature is examined including applications focussed on image-guided lymph node detection and Cerenkov luminescence endoscopy, and the ongoing clinical studies and technological developments are highlighted. By intraoperatively guiding the oncosurgeon towards more accurate and complete resections, CLI has the potential to transform current surgical practice, and improve oncological and cosmetic outcomes for patients.

Keywords Cerenkov luminescence imaging · Image-guided surgery · Cerenkov luminescence endoscopy · Tumour margins · Lymph nodes

✉ M. R. Grootendorst
maarten.grootendorst@kcl.ac.uk

1 Department of Research Oncology, 3rd Floor Bermondsey Wing, King's College London, London SE1 9RT, UK

2 Department of Breast Surgery, 3rd Floor Tower Wing, Guy's Hospital, London SE1 9RT, UK

3 Lightpoint Medical Ltd, The Island, Moor Road, HP5 1NZ Chesham, UK

Introduction

Cancer surgery

The International Agency for Research on Cancer (IARC) reports that 14.1 million new cancer cases were diagnosed in 2012 worldwide, with 8.2 million cancer-related deaths. By 2030, these figures will grow to 21.7 million new cases and 13 million deaths, simply due to population growth and ageing [2]. Of the estimated 21.7 million global new cancer patients in 2030, 17.3 million, or approximately 80 %, will need surgery as the main form of treatment [3].

For cancer surgery to have curative intent, complete tumour resection (i.e. excision of all cancer tissue with no residual loco-regional disease) is mandatory. To achieve this, surgeons try to identify a tumour's extent, and aim to excise the lesion with a surrounding margin of healthy tissue. In an effort to minimise functional loss and/or cosmetic impairment, the goal is to remove the least possible amount of healthy tissue without compromising oncological safety [4].

Palpation and visual inspection—combined with a surgeon's experience and judgement—are currently the only widely available 'modalities' to guide resection. These are frequently inaccurate at discriminating between malignant and normal tissue, resulting in positive tumour margin rates of up to 50 % in some cancers [5–7]. Positive margins are associated with a higher risk of local recurrence and poor prognosis [8–11]. Adjuvant treatments such as radiotherapy, hormone therapy or chemotherapy, and repeat operations to excise residual disease are often indicated to reduce the likelihood of local recurrence, but these treatments can impact on quality of life by causing significant physical and emotional distress, and suboptimal cosmetic outcome [12, 13].

⚝ Springer

With the above in mind, continuing efforts have been made to assist surgeons in the process of determining which tissue needs to be excised during cancer surgery. Currently used clinical techniques include ultrasonography, specimen radiography, and intraoperative histology and cytology techniques. Although all of these techniques are used to varying degrees in cancer surgery, none has quite solved the Goldilocks problem of margins, due to limitations in sensitivity, specificity, accuracy, or costs [14, 15].

Cerenkov luminescence imaging

Cerenkov luminescence imaging (CLI) is a novel imaging modality that has great potential for image-guided surgery in general, and the issue of surgical margins in particular. CLI is based on the detection of Cerenkov photons emitted by positron emission tomography (PET) imaging agents. Cerenkov photons are emitted by a charged particle (positron or electron) when travelling through a dielectric medium at a velocity greater than the velocity of light in that medium. The Cerenkov phenomenon seems to have been first observed by Marie Curie in the late 19th century. In her biography, she describes observing a pale blue glow from the radium-containing bottles in her laboratory. The first person to systematically describe Cerenkov radiation was Pavel Cerenkov, and together with Il'ja Mikhailovic Frank and Igor Yevgenyevich Tamm who developed the theoretical framework, they won the Nobel Prize in Physics in 1958 for their contribution to the discovery of the Cerenkov effect. In the lay mind, Cerenkov radiation is known as the blue glow in the cooling water basins that surround nuclear reactors.

By detecting the optical photons from PET imaging tracers, CLI combines optical and molecular imaging. Robertson et al. were the first who demonstrated that CLI with PET agents can be used to image cancer in vivo [16], and since then, this technology has rapidly emerged in the field of biomedical imaging. In recent years, several review papers have outlined the various applications of CLI including its use in Cerenkov luminescence imaging dosimetry (CLID), radionuclide therapy monitoring, tumour response monitoring and photoactivation therapy [17–21]. An in-depth explanation of the complex physics underlying Cerenkov radiation and CLI has also been reported [22, 23].

The aim of this review paper is to provide an overview on the use of CLI for image-guided interventions with a specific focus on image-guided cancer surgery. The first section of this paper outlines the characteristics of Cerenkov radiation and CLI. Rather than describing these characteristics using complex physical equations as already done by others, this review provides a simplified explanation with an emphasis on the features that are relevant to image-guided surgery. The second section of this paper contains an overview of the published work in this field to date, and the last section will highlight the ongoing clinical studies and technological developments.

Cerenkov radiation: the basics

Cerenkov radiation is produced when a charged particle travels through a dielectric medium, i.e. a medium that can be polarised by an electric field, with a speed faster than the speed of light in that medium [24]. When propagating, the charged particle (a positively charged positron or negatively charged electron) induces a local polarisation by displacing the positive and negative charges of the atoms in the medium (Fig. 1). In a situation where the particle's velocity does not exceed the speed of light in that medium, the polarisation field surrounding the particle is perfectly symmetrical, and there is no electric field at larger distances. The net result is that no Cerenkov radiation is emitted. When the particle's speed exceeds the speed of light, however, the polarisation becomes asymmetrical along the track of the particle, resulting in a dipole electric field at larger distances from the particle. As the particle passes the electrons of the atoms return to their ground state, thereby emitting the transferred energy as optical photons that are known as Cerenkov radiation. Thus, Cerenkov radiation is produced as secondary emission; it is not the charged particle generating light, but the medium as a reaction to the particle.

For Cerenkov radiation to be emitted, the charged particle needs to exceed a certain energy threshold. This threshold is expressed by $v \geq c/\eta$, where v is the charged particle's velocity, c is the speed of light in vacuum, and η is the refraction index of the medium. From this expression, it becomes clear that the Cerenkov threshold is related to the refractive index of the medium. Using the relationship between the velocity of the particle and its energy as described by equations 2 and 3 in Gill et al., it is found that in water with a refractive index of 1.33, the threshold is 0.264 MeV [25]. In soft tissues, the refractive index typically ranges from 1.36 to 1.40, resulting in a threshold for the production of Cerenkov radiation of approximately 0.219–0.250 MeV. These thresholds are lower than the beta particle energies from radionuclides used in PET, and these radionuclides thus emit Cerenkov radiation in both water and tissue [26]. As the charged particle travels through the medium, it loses energy due to interactive processes with its surroundings including
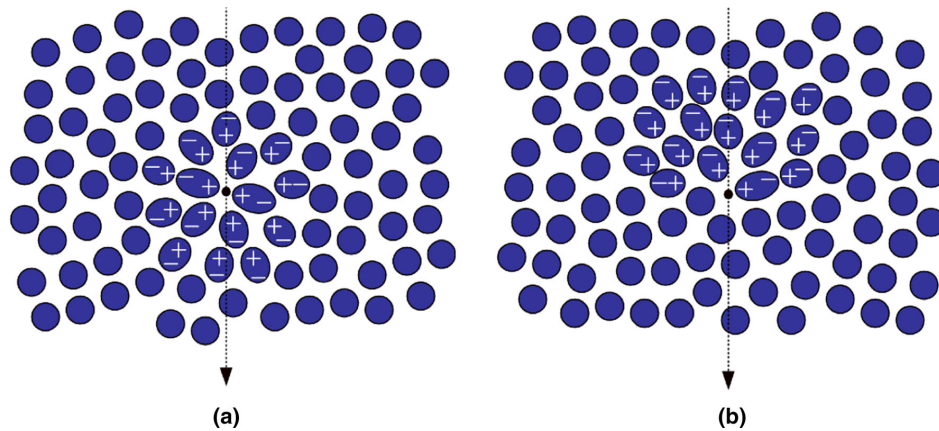
(a)   **(b)**

Fig. 1 A charged particle, in this case an electron, passing through a dielectric medium with **a** a particle speed (*v*) lower than speed of light in that medium (*c*/η), **b** a particle speed larger than speed of light in that medium. The condition such that Cerenkov luminescence is produced along the particle's track requires $v \geq c/\eta$

absorption and scattering, and eventually, its energy falls below the threshold, and Cerenkov light is no longer produced. For the much heavier alpha particles, the Cerenkov threshold in water and tissue is 1926 and 1673 MeV, respectively [27]. Although none of the energies from existing alpha-emitting radionuclides come near this threshold (typical alpha particle energies range between 3 and 7 MeV), studies have shown emission of Cerenkov photons by alpha emitters [27–29]. There are two explanations for this observation, depending on the type of radionuclide: either photons arise from the short-lived beta-emitting daughter radionuclides of some alpha emitters (e.g. Actinium-225), or they are produced by electrons that arise from Compton scattered high-energy gamma photons. Regardless of the mechanism, Cerenkov radiation from alpha emitters is, thus, produced indirectly by secondary beta particles. The pure gamma-emitter Technetium-99 m (^{99m}Tc) is also able to produce optical photons as shown by several groups [30–32]. Although the mechanism of this optical emission is not yet fully understood, it is assumed to be from OH radicals that are excited by the low energy Compton electrons [30] or from gamma excitation of the luminophores that are present in ^{99m}Tc based tracers (e.g. the amino acids in ^{99m}Tc-macroaggregates albumin) [32]. This form of luminescence is known as radioluminescence and differs from Cerenkov radiation; it has a different wavelength spectrum, and its signal intensity is lower in tissue [33]. The latter may provide additional challenges for its use in image-guided interventions. In the remainder of this review, our focus will, therefore, solely be on Cerenkov radiation.

The number of Cerenkov photons *N* emitted per distance travelled *x* can be calculated using equation 1, which is derived from the Frank–Tamm equation [25]:

$$\frac{dN}{dx} = 2\pi\alpha\left(1 - \frac{1}{\beta^2\eta^2}\right)\int_{\lambda_1}^{\lambda_2}\frac{1}{\lambda^2}d\lambda$$

Here, α is the fine structure constant (1/137), β is the ratio between particle's velocity and the speed of light in vacuum (v/c), and the integral is over the interval λ_1 to λ_2. From this equation, it follows that the intensity of the Cerenkov radiation depends on a particle's velocity, and thus, its energy. Fluorine-18 (^{18}F), the most commonly used radionuclide in PET imaging, has an average and maximum β-energy of 250 and 633 keV, respectively. As a result, only 47 % of the decays produce a positron that exceeds the energy threshold for production of Cerenkov radiation in water [22]. Yttrium-90 (^{90}Y), a radionuclide often used in radiation therapy, has a much higher average and maximum β-energy of 934 keV and 2.28 MeV, respectively, and 90 % of its produced electrons are above the Cerenkov threshold in water. Gill et al. recently studied 47 radionuclides widely used in nuclear medicine, and used Monte Carlo simulations to quantify the expected Cerenkov light yield (photons/decay) for each radionuclide in tissue ($\eta = 1.4$) [25]. They found that ^{18}F emits 2.58 photons per decay in tissue; approximately 23 times less than the 58.5 photons per decay emitted by ^{90}Y. The light yield from some commonly used radionuclides in order from high to low is shown in Table 1. Although it is important to realise that the reported light yields do not take into account the wavelength-dependent absorption and

Table 1 Relevant characteristics of Cerenkov radiation and CLI for image-guided cancer surgery

Cerenkov radiation definition	Optical radiation emitted by charged particles when travelling through a dielectric medium with a speed larger than the speed of light in that medium
Threshold energy for Cerenkov radiation emission [25]	Water ($\eta = 1.33$): 0.264 MeV
	Biological tissue ($\eta = 1.36$–1.40): 0.219–0.250 MeV
Cerenkov radiation is emitted by	β^+, β^-, and α-emitting radionuclides
Cerenkov intensity from radionuclides most commonly used in clinic in order from high to low [25]	^{90}Y > ^{68}Ga > ^{15}O > ^{124}I > ^{11}C > ^{89}Zr > ^{18}F > ^{131}I > ^{64}Cu
Cerenkov radiation spectrum [16]	350–900 nm
Fundamental resolution [22]	0.3–2.00 mm
Camera requirements for Cerenkov radiation detection	High-sensitivity optical cameras with single-photon detection capability
Typical penetration depth in tissue [70]	$\sim$1–2 cm
Typical CLI acquisition times	1–5 min
Types of images acquired with CLI	Photographic image: anatomical information
	Functional image: information on the uptake and location of the radiopharmaceutical
Advantages of CLI for image-guided cancer surgery	Ability to use clinically approved tumour-targeted radiopharmaceuticals
	Potential for multi-modality imaging with the same tracer: preoperative imaging with gamma-camera, PET or SPECT, intraoperative imaging using CLI $\pm$ beta-probe or gamma-probe
	Small form factor of CLI equipment allowing implementation of CLI technology in intraoperative specimen chamber, flexible endoscope and rigid laparoscope
	External excitation source not required: less tissue autofluorescence
Challenges of CLI for image-guided cancer surgery	Faint signal
	Light-tight imaging conditions required
	Radiation dose to patient and staff
	Strict regulations for use of radiotracers
	Complex logistics that requires close multi-disciplinary team work

wavelength-dependent scattering that would occur in human tissue—this would reduce the number of detectable photons—it is clear that the signal intensity of CLI can be improved significantly using higher-energetic isotopes. However, even with the use of such isotopes, the Cerenkov light yield from a single radioactive decay process is low in comparison to, for example, the light yield from a single fluorescent molecule. Fluorescein and Indocyanine green (ICG), fluorophores used in fluorescence image-guided surgery, emit roughly three orders of magnitude more photons [34]. This low light yield requires strict control of the light environment to obtain a sufficient signal-to-background ratio (SBR) when using CLI in an intraoperative setting as explained below.

Another characteristic of Cerenkov light is its broad emission spectrum that ranges from approximately 350 to 900 nm [16]. The light intensity is inversely proportional to the square of the wavelength ($1/\lambda^2$). This is why Cerenkov radiation is strongest towards the blue end of the visible spectrum, and hence why Cerenkov radiation appears blue.

The fundamental resolution of Cerenkov radiation is determined by the distance over which a β-particle emits light. It was found that for ^{90}Y and ^{18}F, this distance is approximately 2 and 0.3 mm, respectively [22]. This shows that lower-energetic tracers have a better physical resolution limit, but the downside is a lower light yield, and thus, sensitivity.

Characteristics of CLI from an image-guided surgery perspective

CLI images can be acquired by detecting the Cerenkov light from PET tracers using ultra-high-sensitivity optical cameras such as electron-multiplying charge-coupled device (EMCCD) cameras. The CLI image can be analysed semiquantitatively in photon radiance. CLI and PET are directly correlated due to both techniques measuring the photons produced by positron-emitting radiopharmaceuticals; PET measures the annihilation photons, and CLI measures the Cerenkov photons. Several studies have shown a strong correlation between CLI and PET for different radiopharmaceuticals in vitro, ex vivo and in vivo, thus demonstrating the feasibility of CLI for molecular

Table 2 Literature overview on the correlation of CLI and PET

CLI parameter	PET parameter	Correlation between CLI and PET	Radiopharmaceutical	In vivo, in vitro, ex vivo	Refs.
Radiance	%ID/g	$R^2 = 0.93, 0.95, 0.93, 0.89$	^{18}F-FDG	In vivo	[71]
Radiance	%ID/g	$R^2 = 0.97$	^{18}F-FDG	In vivo	[26]
Radiance	Activity	$R^2 = 0.95$	^{18}F-FDG	In vivo	[72]
Radiance	Activity	$R^2 = 0.98$	^{18}F-FDG	In vivo	[73]
Radiance	PET±	$P = 0.02$	^{18}F-FDG	In vivo	[61]
Radiance	%ID/cm^3	$R^2 = 0.83$	^{18}F-FDG	In vivo	[74]
Radiance	%ID	$R^2 = 0.82$	^{18}F-FDG	In vivo	[74]
Radiant vol.	Glycolytic vol.	$R^2 = 0.99$	^{18}F-FDG	In vivo	[74]
Radiance	Activity	$R^2 = 0.99$	^{18}F	In vitro	[75]
Radiance	Activity	$R^2 = 0.97$	^{18}F-FDG	In vitro	[64]
Radiance	Activity conc.	$R^2 = 0.99$	^{18}F-FDG	In vitro	[61]
Radiance	Activity	$R^2 = 0.97$	^{18}F-FDG	Ex vivo	[72]
Intensity	Activity conc.	$R^2 = 0.98$	^{68}Ga	In vitro	[76]
Intensity	Activity conc.	$R^2 = 0.99$	^{68}Ga	In vivo	[76]
Radiance	%ID/g	R = 0.89	^{89}Zr-trastuzumab	In vivo	[1]
Radiance	%ID/g	R = 0.98	^{89}Zr-J591	In vitro	[28]
Radiance	Activity conc.	R = 0.98	^{89}Zr-J591	In vitro	[28]
Radiance	%ID/g	$R^2 = 0.85$	^{89}Zr-rituximab	In vivo	[77]
Radiance	Activity	$R^2 = 0.98$	Na-^{131}I	In vitro	[68]
Radiance	Activity	$R^2 = 0.99$	^{131}I-NGR	In vitro	[78]
Radiance	%IA/g	$R^2 = 0.94, 0.98$	^{90}Y-DOTA-AR	In vivo	[79]
Radiance	%IA/g	$R^2 = 0.91, 0.99$	^{90}Y-DOTA-AR	Ex vivo	[79]

imaging of living subjects. An overview of the published literature on the correlation between CLI and PET is provided in Table 2. Results on the correlation between CLI and radiotracer activity are also included in this table.

There are several reasons why CLI has sparked so much interest in the field of biomedical imaging, and why it is a promising technology to guide surgical resection. Firstly, CLI images can be acquired with clinically approved tumour-targeted radiopharmaceuticals that have been used for over two decades in molecular medical imaging [26]. This provides great potential for rapid translation of CLI into clinical practice. Especially, the possibility to use the most commonly used PET radiopharmaceutical 2-deoxy-2-(^{18}F)fluoro-D-glucose (abbreviated ^{18}F-FDG) facilitates wide clinical adoption of CLI, as this is a versatile tracer that can be used in several solid cancers, including lung cancer, colorectal cancer, melanoma, head and neck cancer, breast cancer and oesophageal cancer [35].

The ability to use clinically approved tumour-specific tracers is an important advantage over conventional optical imaging techniques, such as targeted fluorescence imaging, as to date, there are no tumour-specific fluorescent tracers that have been approved by the FDA or EMA [36]. Targeted fluorescence imaging faces a significant commercial hurdle for clinical adoption, because the process of obtaining regulatory and reimbursement approval is costly and lengthy

[37], while the revenue of imaging agents is often low compared to therapeutic agents, which makes it a significantly less interesting investment for industry [38, 39].

In addition to the already approved PET tracers, a significant number of new tracers are being developed for market approval including ^{68}Ga-PSMA, ^{68}Ga-DOTATOC, ^{18}F-NaF, ^{18}F-Choline, and ^{18}F-FDOPA [40].

The ability to use the same tracer for both CLI and PET or SPECT enables dual-modality molecular imaging. PET and SPECT provide preoperative information on the location and extent of the tumour, while CLI can be used as an intraoperative adjunct to aid lesion identification and guide surgical resection. The use of the same tracer ensures visualisation of the same structures and facilitates a more accurate comparison between modalities. Depending on the patient pathway and half-life of the tracer, preoperative and intraoperative imaging could be performed using only one tracer injection, or by reinjecting the tracer. By capturing a white-light image with a standard camera at the time of CLI image acquisition, the functional information from the CLI image can be combined with the anatomical and structural information from the photograph, thereby providing the surgeon unprecedented information on the nature, location, and extent of the cancerous tissue.

Beta-emitting radiopharmaceuticals can also be detected by a beta probe or gamma probe [41–43], so these tools

could potentially be used in addition to CLI-guided surgery to overcome the limited penetration depth of CLI as a result of absorption and scattering, thereby further ensuring successful tumour resection.

Another advantage of CLI is that the optical imaging systems required to acquire an image can be small in dimension or use fibre-optics or laparoscopic capabilities. Unlike a PET system, this provides the ability to use CLI in an operating theatre or in endoscopy equipment, and examples of such applications are provided in the next section.

CLI faces a number of challenges for routine clinical adoption. As mentioned earlier, Cerenkov luminescence is very faint due to the small number of optical Cerenkov photons emitted by charged particles. In biological applications, the signal intensity is further reduced by strong tissue attenuation from chromophores like (oxy)haemoglobin and light scattering which is more pronounced in the 400–650 nm range [44, 45]. Consequently, the acquisition time required to obtain high-resolution images with a sufficient signal-to-noise ratio (SNR) is longer than with conventional optical imaging. Typical imaging times in preclinical and clinical CLI studies range from 1 to 5 min (Table 3). Although these images are not available in 'real-time', these acquisition times are considered feasible for most intraoperative applications. However, when imaging with handheld devices (e.g. endoscopes), it is essential that during image acquisition, the device is not

moved as this causes blurring of the image resulting in a reduced image quality. In an in vivo environment, this may prove especially difficult due to bowel activity and breathing artefacts, and motion-correction algorithms may be needed to correct for this.

The weak light intensity also requires a light-tight environment as any leakage of ambient light will overwhelm the CLI signal. Since Cerenkov radiation is strongest in the visible wavelengths, it cannot be spectrally separated from the much brighter ambient lights currently used in operating theatres. Control of the light environment is, therefore, currently achieved by imaging in a light-tight specimen chamber or room with light-sealed doors, or in anatomical areas that provide natural darkness (e.g. gastrointestinal tract).

An often mentioned limitation of optical imaging, in general, is the limited light penetration depth, and thereby, the inability to image deep located tissue. This was nicely illustrated by Chin et al. who calculated the reduction in signal intensity from one ^{18}F-isotope and one ICG molecule in 1 mm of tissue, and found a reduction in signal intensity of 77 and 39 %, respectively [34]. Because Cerenkov light is 'blue-weighted' and tissue absorption and scattering are significantly increased for these wavelengths, CLI is mainly applicable for imaging superficially located tissue.

Table 3 Overview of published studies on CLI-guided surgery

Preclinical or clinical	Indication	Tumour type	Tracer	Dose	CLI device	Acquisition time	Refs.
Preclinical	CLI-guided tumour resection	HER2+ breast cancer	^{89}Zr-DFO-trastuzumab	4 MBq	Ivis optical imager	2–5 min	[1]
Preclinical	CLI-guided tumour resection	Glioblastoma	^{68}Ga-3PRGD2	3.7 MBq	Ivis optical imager	1–5 min	[80]
Preclinical	Cerenkov luminescence endoscopy	Brain glioma	^{18}F-FDG	37 MBq	Custom-build flexible fibre endoscope light-tight box	5 min	[62]
Preclinical	Cerenkov luminescence endoscopy	Glioblastoma	^{90}Y-PRGD2, ^{18}F-FP-PRGD2	8.1 MBq, 33 MBq	Custom-build flexible fibre endoscope light-tight box	6 min	[81]
Preclinical	Cerenkov luminescence endoscopy	Colon cancer	^{18}F-FDG	24 MBq	Clinically approved rigid laparoscope coupled to EMCCD camera in light-tight box	5 min	[82]
Clinical	Cerenkov luminescence endoscopy	Rectal cancer	^{18}F-FDG	9.25 MBq/kg	Clinically approved flexible fibre endoscope coupled to EMCCD camera	5 min	[73]
Preclinical	CLI-guided lymph node mapping	N/A	^{68}Ga-SPIONs[a]	5–10 MBq	CCD camera positioned in light-tight box	2–10 min	[53]
Preclinical	CLI-guided lymph node mapping	N/A	^{18}F-FDG	1.2 MBq	Ivis optical imager	2 min	[52]

[a] Superparamagnetic iron oxide particles (SPIONs)

Due to the half-life dependency of radiotracers, the window in which CLI imaging needs to be performed to obtain a sufficient SNR and image quality is limited. Well-designed logistics and close collaboration between nuclear medicine, radiology and surgical departments are, therefore, a prerequisite for the successful implementation of CLI in current clinical and surgical workstreams.

A challenge for CLI-guided surgery in particular is the radiation exposure to patients and theatre staff from using radiopharmaceuticals. For patients, the effective dose from a 300 MBq ^{18}F-FDG injection is approximately 6 mSv; this is comparable to the radiation dose for a typical chest CT scan [46] and much lower than the 20–2500 mSv radiation exposure from diagnostic and interventional fluoroscopy procedures [47]. Staff that work in close proximity of the patient during surgery are also exposed to radiation. The received radiation dose is dependent on the time between injection and the start of the interventional procedure, as well as the duration of the procedure. Various groups have published staff radiation doses from ^{18}F-FDG-guided cancer surgery procedures [48–50], and have shown that the radiation dose received per procedure is generally low. For example, for a 105 min procedure starting approximately 1 h after injection of 370 MBq ^{18}F-FDG, the exposure to the surgeon was 42 μSv [48]. However, depending on the national annual occupational dose limit (50 mSv in the United States, and 20 mSv in most other countries) and type of procedure, the number of procedures an individual can perform per year without exceeding the permissible limits for professional workers may be restricted. Regardless of these limits, there are strict requirements for the use of radioactivity in clinical practice. For example, routine staff monitoring is a requisite for each institution that conducts radiotracer guided procedures, strict regulations need to be followed with regards to clinical waste disposal and handling of radioactive specimens, and staff need to attend radiation safety training prior to participation in any procedure involving radiation [51]. These requirements could hinder adoption of radio-guided surgical technologies, especially in small district hospitals that do not have access to nuclear medicine or radiation safety departments. The aforementioned characteristics of Cerenkov radiation and CLI in light of image-guided surgical applications are summarised in Table 1.

Applications of CLI for image-guided surgery and ongoing clinical trials

After it was first described in 2009, CLI has gained significant scientific interest. A search of Embase and Medline performed on 28 December 2015 using the keywords 'Cerenkov Luminescence Imaging' provided a total of 103 and 59 articles, respectively. Despite the limitations mentioned in the previous section, various research groups have been successful in using CLI for image-guided surgical interventions. An overview of the results published to date is provided in Table 3. The majority of this work is pre-clinical, although one clinical study was also published recently. In addition to the tumour types shown in Table 3, CLI-guided surgery could also be applied to other superficial malignancies where precision surgery is essential for preserving organ function, such as neoplasms in the oral cavity and genital tract. However, publications of CLI in these malignancies have not yet emerged.

The published studies show the ability to perform CLI-guided surgical excision of tumours using a variety of radiopharmaceuticals and different CLI embodiments, including standard IVIS optical imaging systems, custom-build flexible fibre endoscope systems, and clinically approved rigid laparoscope and flexible endoscope systems coupled to EMCCD cameras. An example that nicely illustrates CLI-guided tumour excision is shown in Fig. 2.

An important advantage of using CLI in an endoscopic setting is that these make use of anatomical dark chambers, so that there is no interference from external light sources. Besides, this technology can also be implemented in other types of endoscopes, such as a bronchoscope or hysteroscope, and future applications of CLI could, for example, focus on lung cancer, endometrial cancer and metastatic lymph nodes in the abdomen, pelvis and thorax.

CLI has also been successfully used for lymph node identification and image-guided lymph node excision using ^{18}F-FDG and ^{68}Ga-labelled superparamagnetic iron oxide particles (SPIONs) [52, 53].

Another interesting application of CLI, although not directly related to image-guided surgery, has been published by Spinelli et al. [54]. They imaged the thyroid gland of a patient treated for hyperthyroidism who received 550 MBq of Iodine-131 (^{131}I). Using an EMCCD camera positioned in a light-tight room, tracer uptake in the thyroid could be visualised with a 2-min exposure time. This application is of clinical interest as imaging the uptake of beta-emitting radiopharmaceuticals could provide a rapid and inexpensive alternative for monitoring radiation doses given to superficial organs.

The successful applications of CLI for image-guided cancer surgery have resulted in several clinical studies that are currently ongoing to evaluate the feasibility of this technique in different tumour types. At Guy's Hospital (London, UK), a first-in-woman pilot study evaluates intraoperative CLI for measuring tumour resection margins and lymph node status in 30 patients undergoing breast-conserving surgery (BCS) (ClinicalTrials.gov identifier NCT02037269). Patients receive an intravenous standard of care PET dose of 5 MBq/kg ^{18}F-FDG, and excised wide
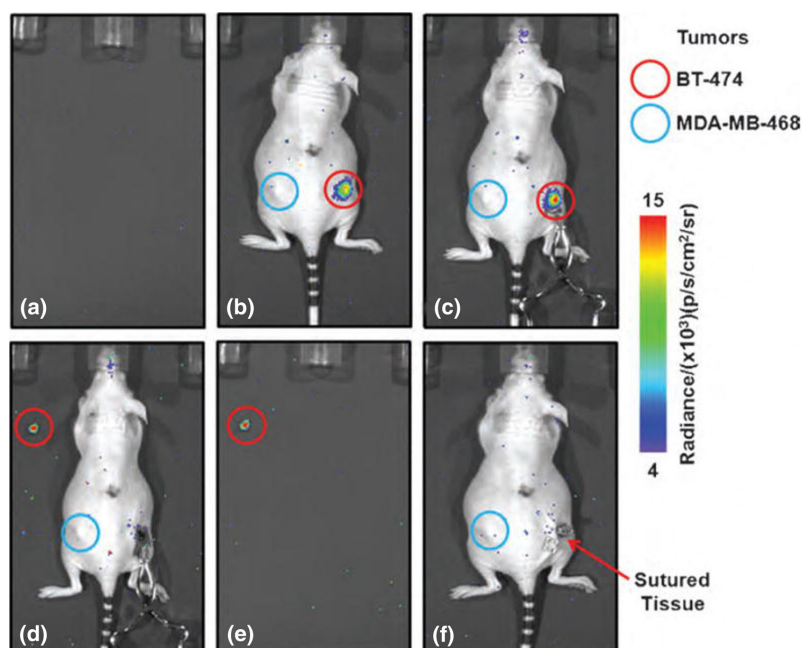
Fig. 2 ^{89}Zr-DFO-trastuzumab CLI-guided tumour excision. **a** Empty background image acquired prior to surgery. **b** Image acquired pre-incision and **c** post-incision after removal of the skin. An elevated tumour radiance is visible in the HER2/neu positive tumour (*red circle*); ^{89}Zr-DFO-trastuzumab is not taken up in the HER2/neu negative tumour, and this tumour, therefore, does not display an elevated radiance (*blue circle*). Note the increase in radiance due to a reduction in tissue absorption and scattering after removal of the skin. **d** Image of the surgical cavity after excision of the HER2/neu positive tumour. An elevated radiance from the excised tumour specimen is visible (*red circle*). No CLI signal is left at the excision site indicating complete tumour resection. **e** Image of excised tumour alone. **f** Image acquired straight after the surgical wound was closed with sutures. This research was originally published in Molecular Imaging [1]

local excision (WLE) specimens and lymph nodes are imaged within 1–3 h post-injection using an investigational intraoperative CLI specimen camera (Lightpoint Medical Ltd, UK) (Fig. 3). The investigational CLI camera consists of a light-tight sample chamber, a radiation-shielded thermoelectrically-cooled EMCCD camera, and a f/0.95 lens. The camera provides 8×8 cm field of view and 156 μm intrinsic spatial resolution. Interim results show that elevated radiances are detected in cancer compared to normal breast tissue, and that the radiation exposure to surgical staff is low [55, 56]. The results from comparing CLI resection margin status and lymph node status to the gold-standard, histopathology, are being prepared for publication at the time of writing. An example of a CLI image from a WLE specimen that was scanned intraoperatively in this clinical study is shown in Fig. 4. This image illustrates that CLI provides high-resolution functional information that allows surgeons to accurately assess tumour margins during surgery.

To evaluate the effect of intraoperative 18F-FDG CLI on reoperation rate and quality of life in BCS, a randomised, controlled, multi-centre clinical study is scheduled to commence in mid-2016 (ClinicalTrials.gov identifier NCT02666079). This will run across an anticipated eight study sites in the UK and Germany, and use the CE-marked LightPath^{TM} Imaging System (Lightpoint Medical Ltd, UK).

Another CLI study that is currently being conducted at Guy's Hospital and University College London Hospital focusses on tumour margin evaluation in prostate cancer (ClinicalTrials.gov identifier NCT02151097). Patients undergoing a therapeutic radical prostatectomy receive a 370 MBq intravenous injection of ^{18}F-Choline, and the margins of the resected prostatectomy specimen are imaged using the investigational intraoperative CLI camera. The initial results show that intraoperative ^{18}F-Choline CLI is a feasible and low-risk procedure [57]. Elevated radiances were present in all three primary tumours (tumour-to-background ratio between 2.49 and 4.90), and CLI imaging did not add additional time to surgery. The assisting surgeon and scrub nurse received the highest body dose; 110–180 and 40–80 μSv, respectively. Work is
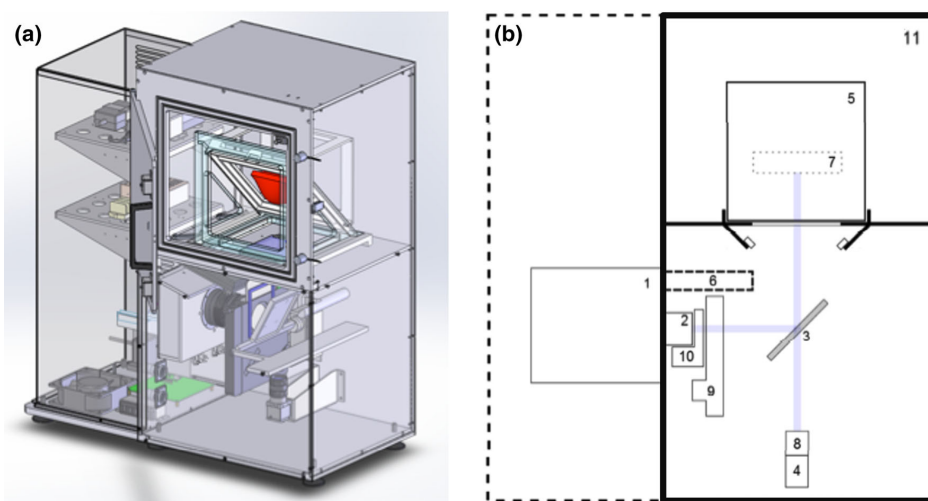
Fig. 3 Investigational intraoperative CLI imaging system used in breast-conserving surgery trial. **a** Computer aided design (CAD) rendering. The *red* object indicates the location of the tissue specimen within the specimen chamber. **b** Schematic diagram showing: (*1*) thermoelectrically-cooled EMCCD camera, (*2*) *f*/0.95 lens, (*3*) hinged reflex mirror, (*4*) CMOS reference camera for anatomical imaging, (*5*) specimen holder, (*6*) lead radiation shielding for EMCCD camera, (*7*) focal zone, (*8*) fixed lens for reference camera, (*9*) filter wheel, (*10*) LED RGB light array, (*11*) specimen chamber. The *purple line* shows the optical paths for the EMCCD camera and the reference camera as determined by the angle of the reflex mirror

currently being done to perform CLI imaging with the Gallium-68 (^{68}Ga) labelled prostate specific membrane antigen (PSMA); a tracer that has strong advantages over ^{18}F-Choline. PSMA is a cell surface target that is highly expressed by nearly all prostate cancers, and ^{68}Ga-PSMA is, therefore, highly taken up in prostate cancer cells [58]. The Cerenkov radiance from ^{68}Ga in tissue ($\eta = 1.4$) is approximately 17 times higher compared to ^{18}F, which could facilitate a reduction in tracer dose, thereby lowering the radiation exposure to theatre staff. The shorter ^{68}Ga half-life of 68 min means that contaminated surgical instruments and surgical waste can be cleaned and disposed much quicker. Another advantage is that besides imaging the primary tumour, this tracer also holds promise for visualising small lymph node metastases [59].

In addition to imaging resected WLE specimens ex vivo, scanning the post-resection surgical cavity for residual tumour that cannot be identified by visual inspection or palpation could further aid achieving complete excision of cancers. Detection of beta-radiation with handheld betascopes can identify small areas of malignant cells [60], and clinical studies to test the combination of in vivo betascope detection and ex vivo CLI will soon commence in gastrointestinal cancers (ClinicalTrials.gov identifier NCT02446379) and breast cancer (ClinicalTrials.gov identifier NCT02151071).

Another interesting application of CLI that is currently being evaluated is the non-invasive detection of nodal disease in a preoperative clinical setting (ClinicalTrials.gov Identifier NCT01664936). In this observational study, patients with lymphoma, leukaemia and metastatic lymphadenopathy scheduled to undergo standard clinical ^{18}F-FDG PET are included. CLI imaging is performed immediately after the PET-scan in a dark room with a single-photon sensitive camera positioned on a standard photography tripod. The preliminary results of this study from four patients (two lymphoma, one lung cancer and one breast cancer) showed that metastatic lymph nodes in the neck or axilla, located at 1.6 ± 0.5 cm under the skin, had a statistically significant higher Cerenkov signal than negative nodes ($P = 0.02$), and this finding strongly correlated with the results from PET [61]. Examples of patient population that can benefit from accurate preoperative identification of nodal disease are breast cancer patients with involved lymph nodes. If positive lymph nodes are identified preoperatively on CLI, their treatment could convert from sentinel lymph node biopsy (SLNB) to immediate axillary node clearance (ANC), thus preventing the patient from undergoing an unnecessary surgical procedure. Alternatively, these patients may undergo neoadjuvant chemotherapy followed by SLNB $\pm$ ANC. Completion of this study will provide further insight in the
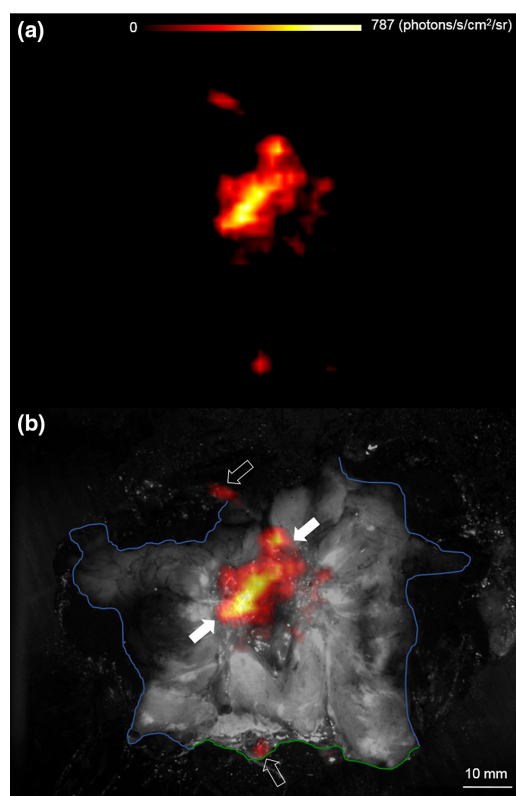
Fig. 4 Wide local excision specimen from a patient with a 22 mm, grade 2, ER+/HER2− invasive lobular carcinoma. The specimen was incised to expose the primary tumour and margins of excision, and subsequently scanned with the investigational CLI camera. **a** Cerenkov image, **b** white-light photograph (*black* and *white*) overlaid with Cerenkov signal. An increased radiance from the tumour is visible (*white arrows*); mean radiance is 544.0 (SD 71.0) photons/s/cm^2/sr. The tumour-to-tissue background ratio is 2.44. Phosphorescent signals from the pathology inks used to orientate the specimen prior to incision are also present (*open arrows*). The posterior margin (*blue*) and superior margin (*green*) are visible; both margins were clear (≥5 mm) on CLI and histopathology, respectively

real value of preoperative CLI imaging in aiding surgical and medical decision-making.

Future technical developments

CLI has only recently been introduced as a modality for imaging biological tissue, and this technique is, therefore, still in its infancy. In the last decade, advances in optical imaging devices in the biophotonics field have progressed rapidly with the development of highly sensitive, charge-coupled detectors (CCD), and current technological developments focus on further increasing the sensitivity of this imaging technology. This would facilitate a reduction in acquisition time, and a reduction in the administered radiopharmaceutical dose.

Improvements in detection sensitivity can be achieved using more specialised optics and more sensitive detectors. For example, the Schott-75 glass used in the CLI prototype device of Liu et al. transmits only 40 % of light at 500 nm, and impurities in the glass scintillate gamma photons, which increase background noise [62]. The use of fused silica, which transmits further in the violet and ultraviolet wavelengths and has fewer impurities, would significantly improve detection sensitivity.

In non-invasive CLI imaging, improvements in sensitivity may be obtained by using CCD cameras that are optimised to detect Cerenkov radiation in the UV for surface imaging, or in the near-infrared (NIR) for deep imaging. Spinelli et al. showed in a theoretical analysis that a CCD detector with a quantum efficiency peak in the NIR range could enhance the number of detected Cerenkov photons by 35 %, especially for Cerenkov source located deeper inside the tissue [63].

As already described in the section 'Cerenkov radiation', Cerenkov light is mainly weighted towards the ultraviolet (UV) and blue part of the spectrum. The high absorption and scattering of these frequencies in biological tissue hampers CLI detection and quantification. To overcome these limitations, current work focusses on shifting the CLI emission spectrum to NIR wavelengths by ways of Cerenkov radiation energy transfer (CRET). Different research groups have done this using fluorescent quantum dots (QDs) or other fluorophores, in vitro and in vivo animal models [64–66]. The broad excitation spectrum that matches the CR spectrum and the narrow emission spectrum make QDs specifically favourable. NIR wavelength light would enable the use of spectral filters to reduce interference from external light source, thus facilitating the use of CLI in the intraoperative suite. However, as with targeted fluorescent probes, nanoparticles have not yet received marked approval, and these approaches can, therefore, not be used clinically yet.

Another interesting development in the field of CLI is the acquisition of three-dimensional (3D) images by means of Cerenkov luminescence tomography (CLT). Different reconstruction approaches have been proposed using multi-view [67, 68] or multi-spectral [69] imaging methods, all showing a good correlation in radiotracer distribution on CLT and PET or SPECT, respectively. Although each method is currently still limited in terms of acquisition time or spatial resolution and has only been used preclinically, the ability of CLT to provide 3D information on the in vivo distribution of radiopharmaceuticals could provide a more

accurate depiction of the location and extent of the tumour, thereby aiding the surgeon in more accurate tumour excision.

Conclusions

CLI is a fast-emerging optical imaging technology that has rapidly progressed from bench to bedside. This rapid development has been facilitated by the ability to use clinically approved tumour-targeted PET tracers. Due to its high-resolution, wide applicability across a range of solid cancers and small size imaging equipment, CLI is of particular interest in the field of image-guided surgery. Challenges for the clinical implementation of this technique include the low signal intensity, the requirement for light-tightness, the minute-scale image acquisition times and the logistical issues associated with using radiotracers intraoperatively. Preclinical studies have shown that CLI can be successfully used to guide surgical resection of tumours and lymph nodes, as well as to detect cancerous lesions using Cerenkov luminescence endoscopy. Several clinical studies on the preoperative and intraoperative use of CLI in breast cancer, prostate cancer, gastrointestinal cancer and metastatic lymph nodes are currently underway. Results from these studies, together with ongoing developments in ultra-sensitive camera technology will help drive widespread clinical adoption. By improving the accuracy of surgical resections, CLI has the potential to become a disruptive technology in cancer surgery.

Compliance with ethical standards

References

1. Holland JP, Normand G, Ruggiero A, Lewis JS, Grimm J (2011) Intraoperative imaging of positron emission tomographic radiotracers using Cerenkov luminesence emissions. Mol Imaging 10(3):177–186 **(171–173)**
2. Bray F, Jemal A, Grey N, Ferlay J, Forman D (2012) Global cancer transitions according to the Human Development Index (2008-2030): a population-based study. Lancet Oncol 13(8):790–801. doi:10.1016/s1470-2045(12)70211-5
3. Sullivan R, Alatise OI, Anderson BO, Audisio R, Autier P, Aggarwal A, Balch C, Brennan MF, Dare A, D'Cruz A, Eggermont AM, Fleming K, Gueye SM, Hagander L, Herrera CA, Holmer H, Ilbawi AM, Jarnheimer A, Ji JF, Kingham TP, Liberman J, Leather AJ, Meara JG, Mukhopadhyay S, Murthy SS, Omar S, Parham GP, Pramesh CS, Riviello R, Rodin D, Santini L, Shrikhande SV, Shrime M, Thomas R, Tsunoda AT, van de Velde C, Veronesi U, Vijaykumar DK, Watters D, Wang S, Wu YL, Zeiton M, Purushotham A (2015) Global cancer surgery: delivering safe, affordable, and timely cancer surgery. Lancet Oncol 16(11):1193–1224. doi:10.1016/s1470-2045(15)00223-5
4. Keereweer S, Van Driel PB, Snoeks TJ, Kerrebijn JD, Baatenburg de Jong RJ, Vahrmeijer AL, Sterenborg HJ, Lowik CW (2013) Optical image-guided cancer surgery: challenges and limitations. Clin Cancer Res 19(14):3745–3754. doi:10.1158/1078-0432.ccr-12-3598
5. Waljee JF, Hu ES, Newman LA, Alderman AK (2008) Predictors of re-excision among women undergoing breast-conserving surgery for cancer. Ann Surg Oncol 15(5):1297–1303. doi:10.1245/s10434-007-9777-x
6. Iczkowski KA, Lucia MS (2011) Frequency of positive surgical margin at prostatectomy and its effect on patient outcome. Prostate Cancer 2011:673021. doi:10.1155/2011/673021
7. McMahon J, O'Brien CJ, Pathak I, Hamill R, McNeil E, Hammersley N, Gardiner S, Junor E (2003) Influence of condition of surgical margins on local recurrence and disease-specific survival in oral and oropharyngeal cancer. Br J Oral Maxillofac Surg 41(4):224–231
8. Menes TS, Tartter PI, Bleiweiss I, Godbold JH, Estabrook A, Smith SR (2005) The consequence of multiple re-excisions to obtain clear lumpectomy margins in breast cancer patients. Ann Surg Oncol 12(11):881–885. doi:10.1245/aso.2005.03.021
9. Raziee HR, Cardoso R, Seevaratnam R, Mahar A, Helyer L, Law C, Coburn N (2012) Systematic review of the predictors of positive margins in gastric cancer surgery and the effect on survival. Gastric Cancer 15(Suppl 1):S116–124. doi:10.1007/s10120-011-0112-7
10. Luryi AL, Chen MM, Mehra S, Roman SA, Sosa JA, Judson BL (2015) Treatment factors associated with survival in early-stage oral cavity cancer: analysis of 6830 cases from the National Cancer Data Base. JAMA Otolaryngol Head Neck Surg 141(7):593–598. doi:10.1001/jamaoto.2015.0719
11. Silberstein JL, Eastham JA (2014) Significance and management of positive surgical margins at the time of radical prostatectomy. Indian J Urol 30(4):423–428. doi:10.4103/0970-1591.134240
12. Munshi A, Kakkar S, Bhutani R, Jalali R, Budrukkar A, Dinshaw KA (2009) Factors influencing cosmetic outcome in breast conservation. Clin Oncol (R Coll Radiol) 21(4):285–293. doi:10.1016/j.clon.2009.02.001
13. Zelefsky MJ, Harrison LB, Fass DE, Armstrong JG, Shah JP, Strong EW (1993) Postoperative radiation therapy for squamous cell carcinomas of the oral cavity and oropharynx: impact of therapy on patients with positive surgical margins. Int J Radiat Oncol Biol Phys 25(1):17–21

14. Butler-Henderson K, Lee AH, Price RI, Waring K (2014) Intra-operative assessment of margins in breast conserving therapy: a systematic review. Breast 23(2):112–119. doi:10.1016/j.breast.2014.01.002

15. Handgraaf HJ, Boonstra MC, Van Erkel AR, Bonsing BA, Putter H, Van De Velde CJ, Vahrmeijer AL, Mieog JS (2014) Current and future intraoperative imaging strategies to increase radical resection rates in pancreatic cancer surgery. Biomed Res Int 2014:890230. doi:10.1155/2014/890230

16. Robertson R, Germanos MS, Li C, Mitchell GS, Cherry SR, Silva MD (2009) Optical imaging of Cerenkov light generation from positron-emitting radiotracers. Phys Med Biol 54(16):N355–365. doi:10.1088/0031-9155/54/16/n01

17. Xu Y, Liu H, Cheng Z (2011) Harnessing the power of radionuclides for optical imaging: Cerenkov luminescence imaging. J Nucl Med 52(12):2009–2018. doi:10.2967/jnumed.111.092965

18. Thorek D, Robertson R, Bacchus WA, Hahn J, Rothberg J, Beattie BJ, Grimm J (2012) Cerenkov imaging—a new modality for molecular imaging. Am J Nucl Med Mol Imaging 2(2):163–173

19. Das S, Thorek DL, Grimm J (2014) Cerenkov imaging. Adv Cancer Res 124:213–234. doi:10.1016/b978-0-12-411638-2.00006-9

20. Spinelli AE, Boschi F (2015) Novel biomedical applications of Cerenkov radiation and radioluminescence imaging. Phys Med 31(2):120–129. doi:10.1016/j.ejmp.2014.12.003

21. Tanha K, Pashazadeh AM, Pogue BW (2015) Review of biomedical Cerenkov luminescence imaging applications. Biomed Opt Express 6(8):3053–3065. doi:10.1364/boe.6.003053

22. Mitchell GS, Gill RK, Boucher DL, Li C, Cherry SR (2011) In vivo Cerenkov luminescence imaging: a new tool for molecular imaging. Philos Trans A Math Phys Eng Sci 369(1955):4605–4619. doi:10.1098/rsta.2011.0271

23. Ma X, Wang J, Cheng Z (2014) Cerenkov radiation: a multi-functional approach for biological sciences. Front Phys. doi:10.3389/fphy.2014.00004

24. Jelley JV (1955) Cerenkov radiation and its applications. Br J Appl Phys 6(7):227

25. Gill RK, Mitchell GS, Cherry SR (2015) Computed Cerenkov luminescence yields for radionuclides used in biology and medicine. Phys Med Biol 60(11):4263–4280. doi:10.1088/0031-9155/60/11/4263

26. Liu H, Ren G, Miao Z, Zhang X, Tang X, Han P, Gambhir SS, Cheng Z (2010) Molecular optical imaging with radioactive probes. PLoS ONE 5(3):e9470. doi:10.1371/journal.pone.0009470

27. Ackerman NL, Graves EE (2012) The potential for Cerenkov luminescence imaging of alpha-emitting radionuclides. Phys Med Biol 57(3):771–783. doi:10.1088/0031-9155/57/3/771

28. Ruggiero A, Holland JP, Lewis JS, Grimm J (2010) Cerenkov luminescence imaging of medical isotopes. J Nucl Med 51(7):1123–1130. doi:10.2967/jnumed.110.076521

29. Boschi F, Meo SL, Rossi PL, Calandrino R, Sbarbati A, Spinelli AE (2011) Optical imaging of alpha emitters: simulations, phantom, and in vivo results. J Biomed Opt 16(12):126011. doi:10.1117/1.3663441

30. Spinelli AE, Lo Meo S, Calandrino R, Sbarbati A, Boschi F (2011) Optical imaging of Tc-99 m-based tracers: in vitro and in vivo results. J Biomed Opt 16(11):116023. doi:10.1117/1.3653963

31. Boschi F, Pagliazzi M, Rossi B, Cecchini MP, Gorgoni G, Salgarello M, Spinelli AE (2013) Small-animal radionuclide luminescence imaging of thyroid and salivary glands with Tc99 m-pertechnetate. J Biomed Opt 18(7):76005. doi:10.1117/1.jbo.18.7.076005

32. Kondakov AK, Gubskiy IL, Znamenskiy IA, Chekhonin VP (2014) Possibilities of optical imaging of the (99 m)Tc-based radiopharmaceuticals. J Biomed Opt 19(4):046014. doi:10.1117/1.jbo.19.4.046014

33. Pagliazzi M, Boschi F, Spinelli AE (2014) Imaging of luminescence induced by beta and gamma emitters in conventional non-scintillating materials. RSC Adv 4(26):13687–13692. doi:10.1039/C3RA47102K

34. Chin PT, Welling MM, Meskers SC, Valdes Olmos RA, Tanke H, van Leeuwen FW (2013) Optical imaging as an expansion of nuclear medicine: Cerenkov-based luminescence vs fluorescence-based luminescence. Eur J Nucl Med Mol Imaging 40(8):1283–1291. doi:10.1007/s00259-013-2408-9

35. Abouzied MM, Crawford ES, Nabi HA (2005) 18F-FDG imaging: pitfalls and artifacts. J Nucl Med Technol 33(3):145–155 (quiz 162–143)

36. Rosenthal EL, Warram JM, Bland KI, Zinn KR (2015) The status of contemporary image-guided modalities in oncologic surgery. Ann Surg 261(1):46–55. doi:10.1097/sla.0000000000000622

37. Frangioni JV (2006) Translating in vivo diagnostics into clinical reality. Nat Biotechnol 24(8):909–913. doi:10.1038/nbt0806-909

38. Agdeppa ED, Spilker ME (2009) A review of imaging agent development. AAPS J 11(2):286–299. doi:10.1208/s12248-009-9104-5

39. Nunn AD (2006) The cost of developing imaging agents for routine clinical use. Invest Radiol 41(3):206–212. doi:10.1097/01.rli.0000191370.52737.75

40. Mahajan A, Goh V, Basu S, Vaish R, Weeks AJ, Thakur MH, Cook GJ (2015) Bench to bedside molecular functional imaging in translational cancer medicine: to image or to imagine? Clin Radiol 70(10):1060–1082. doi:10.1016/j.crad.2015.06.082

41. Franc BL, Mari C, Johnson D, Leong SP (2005) The role of a positron- and high-energy gamma photon probe in intraoperative localization of recurrent melanoma. Clin Nucl Med 30(12):787–791

42. Gulec SA (2007) PET probe-guided surgery. J Surg Oncol 96(4):353–357. doi:10.1002/jso.20862

43. Povoski SP, Chapman GJ, Murrey DA Jr, Lee R, Martin EW Jr, Hall NC (2013) Intraoperative detection of (1)(8)F-FDG-avid tissue sites using the increased probe counting efficiency of the K-alpha probe design and variance-based statistical analysis with the three-sigma criteria. BMC Cancer 13:98. doi:10.1186/1471-2407-13-98

44. Mourant JR, Fuselier T, Boyer J, Johnson TM, Bigio IJ (1997) Predictions and measurements of scattering and absorption over broad wavelength ranges in tissue phantoms. Appl Opt 36(4):949–957

45. Weissleder R (2001) A clearer vision for in vivo imaging. Nat Biotechnol 19(4):316–317. doi:10.1038/86684

46. Brix G, Nosske D, Lechel U (2014) Radiation exposure of patients undergoing whole-body FDG-PET/CT examinations: an update pursuant to the new ICRP recommendations. Nuklearmedizin 53(5):217–220. doi:10.3413/Nukmed-0663-14-04

47. Mahesh M (2001) Fluoroscopy: patient radiation exposure issues. Radiographics 21(4):1033–1045. doi:10.1148/radiographics.21.4.g01jl271033

48. Heckathorne E, Dimock C, Dahlbom M (2008) Radiation dose to surgical staff from positron-emitter-based localization and radiosurgery of tumors. Health Phys 95(2):220–226. doi:10.1097/01.hp.0000310962.96089.44

49. Povoski SP, Sarikaya I, White WC, Marsh SG, Hall NC, Hinkle GH, Martin EW Jr, Knopp MV (2008) Comprehensive evaluation of occupational radiation exposure to intraoperative and perioperative personnel from 18F-FDG radioguided surgical procedures. Eur J Nucl Med Mol Imaging 35(11):2026–2034. doi:10.1007/s00259-008-0880-4

50. Andersen PA, Chakera AH, Klausen TL, Binderup T, Grossjo-hann HS, Friis E, Palnaes Hansen C, Schmidt G, Kjaer A, Hesse B (2008) Radiation exposure to surgical staff during F-18-FDG-guided cancer surgery. Eur J Nucl Med Mol Imaging 35(3):624–629. doi:10.1007/s00259-007-0532-0

51. ICRP (2007) Recommendations of the International Commission on Radiological Protection. ICRP Publication 103, vol 37

52. Thorek DL, Abou DS, Beattie BJ, Bartlett RM, Huang R, Zan-zonico PB, Grimm J (2012) Positron lymphography: multimodal, high-resolution, dynamic mapping and resection of lymph nodes after intradermal injection of 18F-FDG. J Nucl Med 53(9):1438–1445. doi:10.2967/jnumed.112.104349

53. Madru R, Tran TA, Axelsson J, Ingvar C, Bibic A, Stahlberg F, Knutsson L, Strand SE (2013) (68)Ga-labeled superparamagnetic iron oxide nanoparticles (SPIONs) for multi-modality PET/MR/ Cherenkov luminescence imaging of sentinel lymph nodes. Am J Nucl Med Mol Imaging 4(1):60–69

54. Spinelli AE, Ferdeghini M, Cavedon C, Zivelonghi E, Calandrino R, Fenzi A, Sbarbati A, Boschi F (2013) First human Cerenkography. J Biomed Opt 18(2):20502. doi:10.1117/1.jbo. 18.2.020502

55. Grootendorst M, Purushotham A (2015) Clinical feasibility of intraoperative 18F-FDG Cerenkov Luminescence Imaging in breast cancer surgery. J Nucl Med 56:S3

56. Grootendorst MR, Kothari A, Cariati M, Hamed H, Douek M, Kovacs T, Cook G, Allen S, Sibley-Allen C, Britten A, Pawa A, Nimmo F, Vyas K, Tuch D, Pinder S, Purushotham A (2015) P094. Clinical feasibility of Cerenkov Luminescence Imaging (CLI) for intraoperative assessment of tumour excision margins and sentinel lymph node metastases in breast-conserving surgery. Eur J Surg Oncol 41(6):S53. doi:10.1016/j.ejso.2015.03.132

57. Michel C, Freeman A, Jameson C, Waddington W, Tuch D, Harboe M, Cathcart P (2015) P7: intra-operative margin detection using Cerenkov Luminescence Imaging during radical prostate-ctomy; Initial results from the PRIME study. Eur J Surg Oncol 41(11):S271. doi:10.1016/j.ejso.2015.08.112

58. Afshar-Oromieh A, Avtzi E, Giesel FL, Holland-Letz T, Linhart HG, Eder M, Eisenhut M, Boxler S, Hadaschik BA, Kratochwil C, Weichert W, Kopka K, Debus J, Haberkorn U (2015) The diagnostic value of PET/CT imaging with the (68)Ga-labelled PSMA ligand HBED-CC in the diagnosis of recurrent prostate cancer. Eur J Nucl Med Mol Imaging 42(2):197–209. doi:10. 1007/s00259-014-2949-6

59. Afshar-Oromieh A, Haberkorn U, Schlemmer HP, Fenchel M, Eder M, Eisenhut M, Hadaschik BA, Kopp-Schneider A, Rothke M (2014) Comparison of PET/CT and PET/MRI hybrid systems using a 68 Ga-labelled PSMA ligand for the diagnosis of recur-rent prostate cancer: initial experience. Eur J Nucl Med Mol Imaging 41(5):887–897. doi:10.1007/s00259-013-2660-z

60. King MT, Carpenter CM, Sun C, Ma X, Le QT, Sunwoo JB, Cheng Z, Pratx G, Xing L (2015) Beta-Radioluminescence imaging: a comparative evaluation with Cerenkov luminescence imaging. J Nucl Med 56(9):1458–1464. doi:10.2967/jnumed.115. 158337

61. Thorek DL, Riedl CC, Grimm J (2014) Clinical Cerenkov luminescence imaging of (18)F-FDG. J Nucl Med 55(1):95–98. doi:10.2967/jnumed.113.127266

62. Liu H, Carpenter CM, Jiang H, Pratx G, Sun C, Buchin MP, Gambhir SS, Xing L, Cheng Z (2012) Intraoperative imaging of tumors using Cerenkov luminescence endoscopy: a feasibility experimental study. J Nucl Med 53(10):1579–1584. doi:10.2967/ jnumed.111.098541

63. Spinelli AE, Boschi F (2012) Optimizing in vivo small animal Cerenkov luminescence imaging. J Biomed Opt 17(4):040506. doi:10.1117/1.jbo.17.4.040506

64. Hu Z, Qu Y, Wang K, Zhang X, Zha J, Song T, Bao C, Liu H, Wang Z, Wang J, Liu Z, Liu H, Tian J (2015) In vivo nanoparticle-mediated radiopharmaceutical-excited fluorescence molecular imaging. Nat Commun 6:7560. doi:10.1038/ ncomms8560

65. Thorek DL, Ogirala A, Beattie BJ, Grimm J (2013) Quantitative imaging of disease signatures through radioactive decay signal conversion. Nat Med 19(10):1345–1350. doi:10.1038/nm.3323

66. Lewis MA, Kodibagkar VD, Oz OK, Mason RP (2010) On the potential for molecular imaging with Cerenkov luminescence. Opt Lett 35(23):3889–3891. doi:10.1364/ol.35.003889

67. Li C, Mitchell GS, Cherry SR (2010) Cerenkov luminescence tomography for small-animal imaging. Opt Lett 35(7):1109–1111. doi:10.1364/ol.35.001109

68. Hu Z, Liang J, Yang W, Fan W, Li C, Ma X, Chen X, Ma X, Li X, Qu X, Wang J, Cao F, Tian J (2010) Experimental Cerenkov luminescence tomography of the mouse model with SPECT imaging validation. Opt Express 18(24):24441–24450. doi:10. 1364/oe.18.024441

69. Spinelli AE, Kuo C, Rice BW, Calandrino R, Marzola P, Sbarbati A, Boschi F (2011) Multispectral Cerenkov luminescence tomography for small animal optical imaging. Opt Express 19(13):12605–12618. doi:10.1364/oe.19.012605

70. Ma X, Yang W, Zhou S, Ma W, Hu Z, Liang J, Wang J (2012) Study of penetration depth and resolution of Cerenkov lumines-cence emitted from (18)F-FDG and (131)I. J Nucl Med 53:S1

71. Xu Y, Chang E, Liu H, Jiang H, Gambhir SS, Cheng Z (2012) Proof-of-concept study of monitoring cancer drug therapy with cerenkov luminescence imaging. J Nucl Med 53(2):312–317. doi:10.2967/jnumed.111.094623

72. Zhang X, Kuo C, Moore A, Ran C (2013) In vivo optical imaging of interscapular brown adipose tissue with (18)F-FDG via Cer-enkov luminescence imaging. PLoS ONE 8(4):e62007. doi:10. 1371/journal.pone.0062007

73. Hu H, Cao X, Kang F, Wang M, Lin Y, Liu M, Li S, Yao L, Liang J, Liang J, Nie Y, Chen X, Wang J, Wu K (2015) Feasi-bility study of novel endoscopic Cerenkov luminescence imaging system in detecting and quantifying gastrointestinal disease: first human results. Eur Radiol 25(6):1814–1822. doi:10.1007/ s00330-014-3574-2

74. Robertson R, Germanos MS, Manfredi MG, Smith PG, Silva MD (2011) Multimodal imaging with (18)F-FDG PET and Cerenkov luminescence imaging after MLN4924 treatment in a human lymphoma xenograft model. J Nucl Med 52(11):1764–1769. doi:10.2967/jnumed.111.091710

75. Timmermand OV, Tran TA, Strand SE, Axelsson J (2015) Intratherapeutic biokinetic measurements, dosimetry parameter estimates, and monitoring of treatment efficacy using cerenkov luminescence imaging in preclinical radionuclide therapy. J Nucl Med 56(3):444–449. doi:10.2967/jnumed.114.148544

76. Cao X, Chen X, Kang F, Lin Y, Liu M, Hu H, Nie Y, Wu K, Wang J, Liang J, Tian J (2014) Performance evaluation of endoscopic Cerenkov luminescence imaging system: in vitro and pseudotumor studies. Biomed Opt Express 5(10):3660–3670. doi:10.1364/boe.5.003660

77. Natarajan A, Habte F, Liu H, Sathirachinda A, Hu X, Cheng Z, Nagamine CM, Gambhir SS (2013) Evaluation of 89Zr-rituximab tracer by Cerenkov luminescence imaging and correlation with PET in a humanized transgenic mouse model to image NHL. Mol Imaging Biol 15(4):468–475. doi:10.1007/s11307-013-0624-0

78. Hu Z, Yang W, Ma X, Ma W, Qu X, Liang J, Wang J, Tian J (2013) Cerenkov luminescence tomography of aminopeptidase N (APN/CD13) expression in mice bearing HT1080 tumors. Mol Imaging 12(3):173–181

79. Lohrmann C, Zhang H, Thorek DL, Desai P, Zanzonico PB, O'Donoghue J, Irwin CP, Reiner T, Grimm J, Weber WA (2015)

Cerenkov luminescence imaging for radiation dose calculation of a (9)(0)Y-labeled gastrin-releasing peptide receptor antagonist. J Nucl Med 56(5):805–811. doi:10.2967/jnumed.114.149054

80. Fan D, Zhang X, Zhong L, Liu X, Sun Y, Zhao H, Jia B, Liu Z, Zhu Z, Shi J, Wang F (2015) (68)Ga-labeled 3PRGD2 for dual PET and Cerenkov luminescence imaging of orthotopic human glioblastoma. Bioconjug Chem 26(6):1054–1060. doi:10.1021/acs.bioconjchem.5b00169

81. Carpenter CM, Ma X, Liu H, Sun C, Pratx G, Wang J, Gambhir SS, Xing L, Cheng Z (2014) Cerenkov luminescence endoscopy: improved molecular sensitivity with beta–emitting radiotracers. J Nucl Med 55(11):1905–1909. doi:10.2967/jnumed.114.139105

82. Song T, Liu X, Qu Y, Liu H, Bao C, Leng C, Hu Z, Wang K, Tian J (2015) A novel endoscopic Cerenkov luminescence imaging system for intraoperative surgical navigation. Mol Imaging 14:443–449

16

Application of Terahertz Technology to Breast Cancer

Maarten
R. Grootendorst
King's College London

Massimiliano
Cariati
King's College London

Philip C. Ashworth
University of Cambridge

Anthony
J. Fitzgerald
University of Western Australia

Arnie Purushotham
King's College London

Vincent P. Wallace
University of Western Australia

16.1 Introduction to Breast Cancer

16.1.1 Breast Cancer Key Facts

Breast cancer is by far the most common cancer among women, both in developed and in developing regions. Worldwide, an estimated 1.38 million women are diagnosed with the disease each year, making it the second most frequently diagnosed cancer after lung cancer (Ferlay et al. 2010). Among men, breast cancer is far less common, accounting for <1% of male cancer cases.

The incidence rate of breast cancer in women is higher in developed countries compared with other countries; Western Europe has the highest incidence rate (89.7 per 100,000) and Middle Africa the lowest (19.3 per 100,000). A range of factors contribute to this variation in incidence rates, particularly relating to lifestyle (Youlden et al. 2012). In the United Kingdom and other parts of Western Europe, the incidence rate of breast cancer has increased by almost 50% in the period 1980–2008. Currently, the estimated lifetime risk of developing breast cancer in women in the United Kingdom and the United States is one in eight (Cancer Research UK 2012a; Siegel et al. 2012).

297

Although the incidence rate is significantly higher in developed countries, the range in mortality rate is much less (6–19 per 100,000). This is due to a combination of factors, including earlier detection, favorable treatment modalities, and better access to these modalities. However, with approximately 189,000 deaths per annum, breast cancer is, together with lung cancer, the most frequent cause of cancer death in women in the world, both in developed and developing regions.

Breast cancer therefore remains a large health problem, despite the fact that early diagnosis and more effective treatment have lowered the mortality rate in several countries. Therefore, there is a need to improve and optimize breast cancer care globally.

16.1.2 Types of Breast Cancer

There are various types of breast cancer, each type presents with different symptoms and characteristics. Although it was previously believed that in some cases breast cancer arose in the ducts and in other cases in the lobules, it is now clear that this disease derives from the terminal ductal lobular unit (TDLU) (see Figure 16.1). Breast cancer can be roughly divided into noninvasive and invasive cancer.

Noninvasive breast cancers are cancers that have not yet broken through the myoepithelial layer and basement membrane and hence are confined within the ductolobular units and are termed carcinoma in situ. Ductal carcinoma in situ (DCIS) is the most common form of in situ breast cancer and starts within the duct system, involving almost always a single duct within the breast. DCIS generally has no signs or symptoms, although a small number of patients may present with a small palpable lump. If DCIS cells die and pile up, tiny specks of calcium form within the broken cells (called calcifications or microcalcifications). These calcifications are usually very small and therefore difficult to identify by imaging techniques.

Over time, cancer cells can penetrate through the wall of the ducts and lobules, thereby infiltrating the breast stroma. If this occurs, the cancer is called invasive. The most common form of invasive breast cancer,
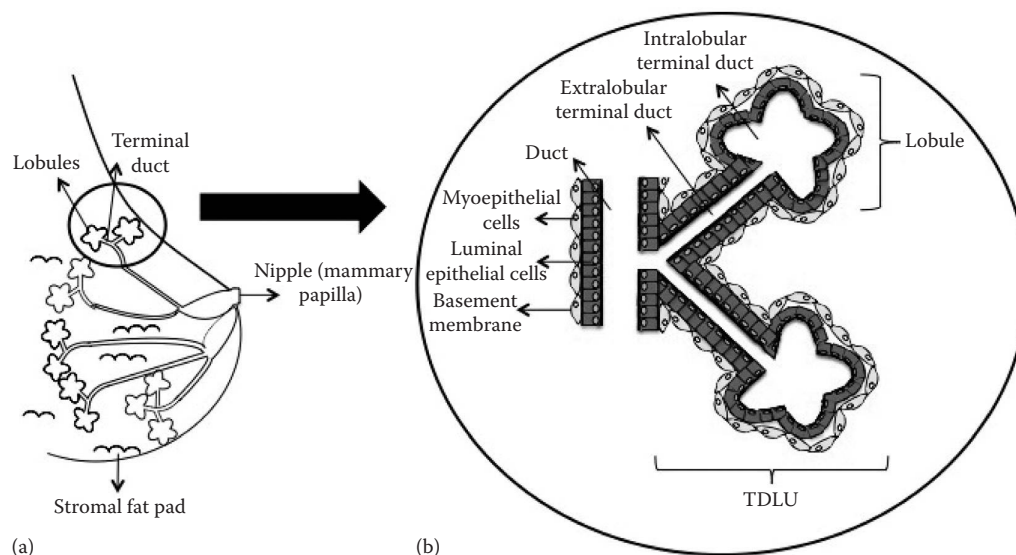
FIGURE 16.1 Schematic of the human mammary gland. (a) The human mammary gland is organized into lobules interconnected by a network of branched ducts. (b) The ducts consist of an inner layer of luminal epithelial cells and an outer layer of myoepithelial cells. The large duct separates into extralobular ducts, which then separate into intralobular ducts. The main functional unit of the breast is the TDLU that consists of the lobule, intralobular terminal ducts, and the extralobular terminal ducts.

and breast cancer in general, is invasive ductal carcinoma (IDC). IDC is diagnosed in more than 80% of all breast cancer patients (Cancer Research UK 2012b) and is more common as women grow older. Invasive lobular carcinoma is the second most common invasive cancer and accounts for 10% of all invasive cancers.

Invasive carcinomas tend to form hard, palpable lesions, while DCIS is mostly nonpalpable. This presents additional challenges for accurate preoperative and intraoperative identification.

16.1.3 Breast Cancer Surgery

Most women with breast cancer undergo some type of surgery to remove the primary tumor, which has moved from radical to more conservative over the last century. Breast cancer surgery can roughly be divided in breast-conserving surgery (BCS) and mastectomy (i.e., the complete removal of the breast). The choice between BCS or mastectomy depends on several factors, including the size of the tumor relative to the size of the breast, its location, the presence of diffuse microcalcifications (DCIS), and patient's preference. The purpose of adopting BCS is to minimize the psychological and physical morbidity associated with mastectomy.

16.1.3.1 Breast-Conserving Surgery

A combination of patient and physician awareness and increased use of screening mammography has significantly impacted on the stage at which cancers are diagnosed. Women with stage 0 (carcinoma in situ), stage 1 (invasive tumor <2 cm), or stage 2 (invasive tumor <5 cm) are ideal candidates for BCS, and due to the earlier stage of diagnoses, approximately two-thirds of newly diagnosed breast cancer patients in the United Kingdom and the United States undergo BCS as initial treatment (Jeevan et al. 2011; Katipamula et al. 2009).

The aim of BCS is to remove the primary tumor while conserving as much healthy breast tissue if possible to provide good cosmetic outcome and to reduce physical trauma. BCS is often followed by a course of postoperative radiotherapy, and the combination of BCS with radiotherapy provides similar survival rates to those achieved with mastectomy alone for women with invasive disease (Fisher et al. 2002). However, incomplete removal of the tumor results in involved tumor margins and involved margins are one of the main risk factors for local recurrence and affect disease-free survival (Singletary 2002; Veronesi et al. 2002).

There are various imaging techniques used to diagnose breast cancer, including x-ray mammography, ultrasound (US) imaging, and magnetic resonance imaging (MRI). These *preoperative* imaging techniques provide information on the location and size of the tumor, but these techniques have limited intraoperative capabilities. The correlation between tumor size estimation with preoperative imaging techniques and histopathological size remains suboptimal, thereby creating an element of uncertainty when deciding how much tissue is to be excised during surgery. Hence, surgeons can use this information only as a rough guide to define the margins of the tumor.

The techniques used to obtain intraoperative information on tumor margins depend on whether the tumor is palpable or nonpalpable. Palpable tumors are localized with the tip of the surgeon's thumb and index fingers, a technique known as palpation-guided surgery. By feeling for the tumor, the surgeon can determine the extent of the tumor, and after the boundaries are identified, the surgeon aims to excise the tumor together with a region of healthy tissue. One can appreciate that this is a very subjective method. Nonpalpable tumors cannot be identified by *touch*, so additional techniques are required to localize the lesion and to determine its boundaries. The various techniques that are available are outlined in Section 16.2 and make use of a wire, radioactive material, or US waves. The surgeon uses these techniques to guide the excision of the lesion, thereby aiming to obtain an adequate margin of healthy tissue.

The aforementioned surgical guidance techniques provide macroscopic information on tumor margins, and in order to determine if the tumor is excised completely, the tumor margins of the excised specimen need to be analyzed on a microscopic level. These so-called microscopic margins are determinative to whether a procedure is considered successful. There are currently two techniques available to assess the microscopic margins *intraoperatively*: frozen section analysis and touch print cytology.
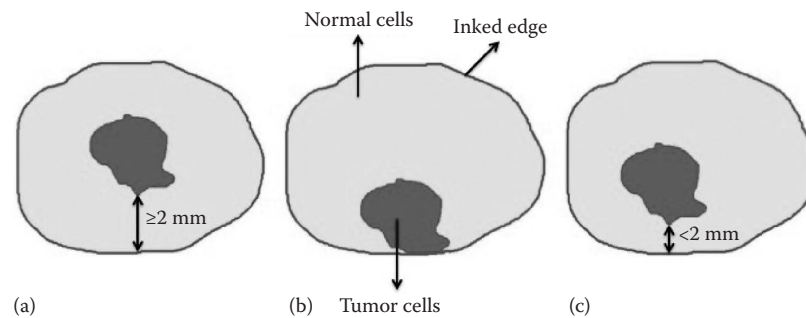
FIGURE 16.2   Negative margin (a), positive margin (b), and close margin (c).

However, as explained in more detail in Section 16.2, both techniques have disadvantages, and therefore, only a small number of hospitals utilize these techniques.

The golden standard for assessing microscopic margins is postoperative histological examination. During this procedure, the pathologist inks the surface of the excised specimen, and the closest distance of an inked surface to tumor cells is reported within several days after surgery. Most institutions consider a margin width of >2 mm as negative, 0–2 mm as close, and 0 mm as positive (Houssami et al. 2010; Morrow et al. 2012) (see Figure 16.2). Although there is no consensus on what constitutes an adequate microscopic margin, the majority of centers advise patients with positive or close margins to undergo a reoperation to remove residual disease.

During a reoperation, the surgeon reopens the site of the original surgery and removes a further slice of tissue of the margin reported to be involved. The reexcised tissue then undergoes a similar postoperative histological examination procedure as the BCS specimen to determine if all the cancer has been excised, and a second or third reexcision operation may be required if the reexcision did not result in clear margins. A mastectomy is performed in cases where an attempt to reexcise the residual disease fails multiple times. Approximately 10% of patients with BCS as primary surgery eventually undergo a mastectomy to obtain clear margins (McCahill et al. 2012; Waljee et al. 2008).

The need to perform a reoperation in patients with involved margins after initial BCS has various undesirable consequences. It most likely will cause a delay in adjuvant treatment, and there is evidence that patients with positive margins after initial BCS have a higher chance of local recurrence (Kouzminova et al. 2009). Reoperations will result in a significantly poorer cosmetic outcome, for both reexcisions and mastectomies (Munshi et al. 2009). The additional procedures also increase the health economic costs, thus representing a burden to the health-care system. The last and probably the most important consequence of reoperations is the emotional distress patients experience after being told their cancer is not removed completely. This may result in delays in recovery, causing adverse socioeconomic effects because patients cannot resume work or other activities.

Due to a lack of adequate intraoperative tools to identify and assess tumor margins in current clinical care, positive resection margins have been reported in up to 41% of patients and are more likely in patients with a carcinoma in situ component (Jeevan et al. 2012; Talsma et al. 2011; Waljee et al. 2008). Because of the high percentage of patients that currently need to undergo a reoperation as a consequence of positive margins, there is a clear need for new, intraoperative techniques to accurately assess resection margins in patients undergoing BCS.

16.1.3.2 Mastectomy

A mastectomy is a surgical procedure that involves removal of all breast tissue to ensure no disease is left behind. This procedure is more extensive than BCS and is associated with more postsurgery side effects and a longer recovery time. Reconstruction surgery can be carried out at the same time as the mastectomy (immediate reconstruction) or sometime after the initial mastectomy surgery (delayed reconstruction).

Mastectomies are generally performed in patients that are not suitable for BCS, including patients with a large tumor (particularly in women with small breasts), a tumor in the middle of the breast, multifocal disease or areas of DCIS in the rest of the breast, or in patients where the initial BCS along with one or more reexcisions has not completely removed the cancer.

Due to the earlier stage at which breast cancer is currently being diagnosed in most developed countries, mastectomies are performed much less often than BCS as initial treatment.

There are different types of mastectomies, varying from removal of only breast tissue to a more radical procedure where in addition to removal of the breast, the lymph nodes in the armpit (axilla) and the chest wall muscles under the breast are also removed. Each type of mastectomy encompasses the removal of all breast tissue, and therefore positive tumor margins resulting from incomplete removal of the tumor rarely occur.

16.1.4 Conclusion

A key problem that currently hampers the success of BCS is the lack of accurate, real-time techniques that provide intraoperative information on tumor margins. This leads to reexcision in up to 41% of patients. Reoperations have a significant physical and emotional impact on patients and cause a financial burden for the health-care sector. Therefore, there is a need for a technique that can accurately assess tumor margins intraoperatively, thereby reducing the number of reoperations.

THz radiation possesses a number of properties that make it a viable technique for tumor margin assessment. Section 16.3 will focus on the interaction of THz radiation with human breast tissue and cancer and the results that have been obtained with different THz imaging devices. The other techniques for intraoperative assessment of tumor margins are outlined in Section 16.2.

16.2 Other Techniques for Intraoperative Assessment of Tumor Margins

There are a number of techniques, either in current use, in clinical trials, or in the research phase, that provide the surgeon with intraoperative information on tumor margins. All these techniques aim to reduce the reexcision rate. However, in choosing or developing such techniques, there are important clinical criteria to consider, including time, detection depth, and sampling area.

This paragraph gives an overview of the performance, advantages, and limitations of techniques that are currently available as well as techniques that are in the development phase. The currently available techniques can be divided into intraoperative tumor localization techniques and intraoperative pathological techniques. The former provides information on tumor margins at a macroscopic level, while the latter assesses tumor margins microscopically.

16.2.1 Currently Available Intraoperative Tumor Localization Techniques

16.2.1.1 Wire-Guided Localization

Approximately 35% of breast cancers smaller than 5 cm are nonpalpable (Lovrics et al. 2009; Skinner et al. 2001), and the most commonly used technique to determine the location of these tumors is wire-guided localization (WGL).

The wire used for localizing the lesion is 20–25 cm long and bent at the tip to form a V-shaped hook. A needle is used to target the lesion guided by x-ray, US, or MRI. After introduction of the needle, a wire is threaded down through the needle (hook end first) to lodge at the target tissue. The needle is then removed, and the hook expands upon removal of the needle, thereby anchoring the wire in the lesion. Mammography is used to confirm the wire is positioned correctly, and after confirmation, the external part of the wire is taped to the body to prevent displacement.

During the operation, the surgeon views the mammograms to get an indication of the tumor localization, and the wire is used as a guide to find the nonpalpable lesion. Since the tip of the wire is in the lesion, the surgeon needs to deviate from the wire before he or she reaches the tip to obtain an adequate margin of healthy tissue.

Literature shows that 30%–37% of wire-guided procedures result in positive margins (Gajdos et al. 2002; Lovrics et al. 2009). From these results can be concluded that WGL is suboptimal in aiding complete excision of nonpalpable breast cancers.

One of the reasons for the high positive margin rate is that the guide wire does not provide a clear three-dimensional perspective on the various tumor edges, and the required extent of resection needed to achieve negative margins still remains an estimate. Furthermore, the guide wire is prone to move before or during surgery and may therefore provide inadequate information on tumor localization. Other disadvantages include the time required to place the wire and the associated patient discomfort, resulting in increased levels of stress and arousal (Kelly and Winslow 1996). Because of the high reexcision rates and patient discomfort, other techniques have been developed to assess tumor margins.

16.2.1.2 Radioisotope Labeled Localization

Radioisotope labeled localization is an alternative technique to WGL for intraoperative localization and simultaneous resection of nonpalpable breast tumors. There are two variations of this technique: radioguided occult lesion localization (ROLL) and radioguided seed localization (RSL). In ROLL, a radioactive tracer is injected into the tumor preoperatively, and a gamma probe is used to guide the resection during surgery. To facilitate correct positioning, the injection of the radioactive tracer is performed under stereotactic or ultrasonographic guidance. After the primary tumor is excised, the gamma probe can be used to search and identify residual disease in the breast cavity. RSL is almost identical to ROLL, but instead of a radiotracer, a radioactive seed is used.

Numerous studies have been performed to evaluate the oncologic safety of the ROLL and RSL procedures (Barentsz et al. 2013; Donker et al. 2013; Hughes et al. 2008; Lovrics et al. 2011; Medina-Franco et al. 2008; Monti et al. 2007; Sarlos et al. 2009; Thind et al. 2011). Positive margins varied from 4% to 27%, although Sarlos et al. reported a 35% positive margin rate in patients with DCIS. Hughes et al. compared RSL with WGL and found significantly lower positive margin rates with RSL as compared to wire localization, while Lovrics et al. reported similar positive margin rates. A recently published large multicenter clinical trial compared ROLL to WGL in patients with invasive breast carcinoma (Postma et al. 2012). They found similar positive margin rates for ROLL and WGL, and ROLL was considered comparable in terms of complete tumor excision and reexcision rates. However, they found a larger excision volume in the ROLL group and concluded that ROLL cannot replace WGL as standard of care.

Although the oncologic safety of ROLL and RSL might be similar to WGL, both techniques have several advantages over WGL. They are easy-to-perform radiological and surgical procedures, and the tumor can be identified in three dimensions allowing for more precise excision. More importantly, both techniques are more patient friendly; hence, the pain rankings reported by patients are significantly lower (Lovrics et al. 2011; Rampaul et al. 2004). However, these guidance tools are still invasive like WGL and therefore associated with patient discomfort. Moreover, the use of radioactive material exposes patients and health-care workers to radiation, is heavenly controlled by legislation, and is available only in hospitals with a nuclear medicine department.

16.2.1.3 Intraoperative Ultrasound–Guided Resection

Intraoperative US (IOUS) is a method of excising a tumor under direct visualization, thus providing the surgeon with real-time information of the tumor extent.

Immediately after excision, ex vivo US examination of the specimen is performed in the operating theater to check the completeness of the specimen. In case of positive or close margins, residual disease is removed by shaving the patient's cavity margins.

The COBALT trial compared IOUS-guided resection with palpation-guided resection for invasive *palpable* tumors and found tumor-involved margins in 11% of the IOUS-guided group and 28% in the palpation-guided group (p = 0.0031) (Krekel et al. 2012). Besides, IOUS-guided surgery resulted in significantly smaller excision volumes. Moore et al. also found a significant improvement in margin status in IOUS-guided surgery compared to palpation-guided surgery (Moore et al. 2001).

For *nonpalpable* invasive breast cancers, positive margins were found after IOUS-guided surgery in 4.3%–19% of patients (Bennett et al. 2005; Krekel et al. 2011; Ngô et al. 2007; Rahusen et al. 2002; Snider and Morrison 1999). Rahusen et al. reported significantly improved margin status using IOUS compared to WGL (11% vs. 45%, respectively), and this finding was supported by Krekel et al. Besides, Snider et al. found a smaller resection volume compared to WGL.

These results indicate that IOUS-guided surgery can lower the proportion of tumor-involved resection margins compared to palpation-guided and wire-guided localization, while decreasing resection volumes. US is widely available, does not require radiation, and minimizes patient trauma and discomfort as there is no need for additional interventions (i.e., a wire or material). However, IOUS also has some important disadvantages. The technique is not suitable for detecting microcalcifications as these are not sonographically visible, and DCIS can therefore not be identified. Besides, the lesion must be above a certain size to be imaged, and it is shown that 50% of nonpalpable tumors are missed (Klimberg 2003). Other possible restrictions are that the technique does not have the sensitivity and resolution to find residual disease after excision of the primary tumor and that a radiologist must be present in the operating theater during the procedure.

16.2.1.4 Intraoperative Specimen Radiography

Intraoperative specimen radiography is a technique often used to image the excised specimen in patients with nonpalpable breast tumors. In conventional specimen radiography, the surgical specimen is transported from the operating theater to the diagnostic imaging department, while intraoperative digital specimen mammography (IDSM) entails imaging in the operating theater. The former can entail significant time for transport (≈30 min). If specimen radiographs reveal involved margins, the surgeon can shave the associated cavity edges to remove any residual malignant disease.

In 2007, Kaufman et al. compared IDSM with CRF for assessing tumor margins. The sensitivity of IDSM and CRF for detecting positive margins was 36% and 31%; specificity was 71% and 74% (Kaufman et al. 2007). More recently, Bathla et al. evaluated the performance of an IDSM device for intraoperative margin assessment and found a sensitivity and specificity of 58.5% and 91.8%, respectively (Bathla et al. 2011). The positive predictive value was 82.7%; the negative predictive value was 76.7%.

A disadvantage of intraoperative specimen radiography is that in situ cancers will show up only if there is sufficient contrast or microcalcifications associated with it. Thus, even if the tumor seems to be adequately removed on the radiography image, reoperation may still be needed if histopathology identifies an in situ component near or at the margin. Besides, specimen radiography provides information on margin status at a macroscopic level and can therefore not be relied on solely.

16.2.2 Currently Available Intraoperative Pathological Techniques

A disadvantage related to all the aforementioned techniques is that no information is provided on the microscopic margin status. Therefore, some centers use additional intraoperative pathological techniques to provide the surgeons with information on the microscopic extent of the tumor. The most commonly used intraoperative pathological techniques are frozen section analysis (FSA) and touch imprint cytology (TIC).

16.2.2.1 Frozen Section Analysis

FSA is used to intraoperatively assess microscopic margin status in many oncologic procedures, including breast cancer. While the patient is still on the operating table, the excised specimen is inked, sliced, frozen, and analyzed microscopically by an experienced histopathologist (Weber et al. 2008).

This takes approximately 30 min. Surgery continues during the pathological analysis, and the surgeon closes the wound if the pathological result takes longer than the surgical procedure. In case involved margins are identified, the wound of the patient is reopened and additional cavity shaving is performed.

Reported sensitivity rates for the assessment of resection margin status range between 73% and 83%, whereas specificity rates are in between 87.5% and 99% (Esbona and Wilke 2012; Hunt et al. 2007; Olson et al. 2007; Weber et al. 2008). The lower sensitivity is mainly a result of unreliable detection of small tumors (<10 mm) and microcalcifications (i.e., DCIS). Two large studies evaluated the number of reoperations after FSA, and both studies demonstrated that frozen section leads to low reoperation rates (9% and 10%, respectively) (Esbona and Wilke 2012; Riedl et al. 2009). Apart from the unreliable detection of small tumors and microcalcifications, FSA does not provide the surgeon with information on tumor extent prior to excision, therefore not aiding in decreasing resection volumes. Furthermore, FSA is labor intensive and requires an experienced on-site pathologist and may therefore not be performed in hospitals where the pathology department is located outside of the hospital. Besides, FSA requires a relatively large part of the specimen, which may compromise postoperative evaluation by the pathologist, and freezing artifacts are common in fatty tissue, which may interfere with accurate identification of cell types.

16.2.2.2 Touch Imprint Cytology

Intraoperative TIC is a simple and rapid alternative to FSA. The excised specimen is oriented and pressed onto specifically coated slides, making an imprint of all six margins. Cells sticking to the glass surface are then fixed, stained, and microscopically analyzed (Klimberg et al. 1998). This technique is based on the difference in cellular surface characteristics between malignant cells and mammary fat; malignant cells will adhere to the slides and adipose cells will not.

The results of TIC are reported within 15 min, which is definitely quicker than FSA, and for most surgeries, the result is received before the wound is closed. Another advantage over FSA is that it saves tissue for permanent sectioning and histopathological examination, and that it is less expensive than FSA.

Esbona et al. performed a systematic review on reexcision rates, sensitivity, and specificity of TIC and compared the performance with FSA and postoperative histopathological evaluation (Esbona and Wilke 2012). The reexcision rate of TIC was 11%, against 10% and 35% for FSA and postoperative histopathology. The sensitivity and specificity were 72% and 92%, respectively, compared to 83% and 95% for FSA. In line with the results for FSA as described previously, most false-negative results with TIC were observed in tumors with in situ disease. However, there was a greater degree of variation present in the sensitivity of TIC. The difference in cytopathological proficiency between pathologists may account for the degree of variation, as the technique requires extensive cytology expertise.

Although the results of this technique seem very promising, so far it has not been as widely used as FSA. One of the explanations is that close margins are not taken into account, because only superficial tumor cells are detected with the technique. Therefore, no information is gathered on margin width, multifocality, and quantity of cancerous cells approaching the cut edge (Pleijhuis et al. 2009). There is also the potential of artifacts caused by draught and surface cautery, and TIC seems less effective in identifying lobular carcinoma (Valdes et al. 2007).

16.2.3 Techniques under Development

The previously described techniques all have certain disadvantages and result in positive resection margins in a significant amount of patients. The main disadvantage of all these techniques is the inaccuracy in detecting DCIS, and the need to detect DCIS is significant as it is considered a more challenging intraoperative assessment target. Currently, several techniques are being developed for assessing tumor margins intraoperatively, with a particular focus on techniques that are able to identify DCIS. A nonexhaustive list of these new, innovative techniques is provided later.

16.2.3.1 Radiofrequency Spectroscopy: MarginProbe®

The MarginProbe (Dune Medical Devices, Framingham, USA) uses radiofrequency spectroscopy to detect minute differences in electromagnetic properties of tissue with and without cancer, and provides this key information as a *positive* or *negative* readout to breast surgeons intraoperatively. The device consists of a console and a disposable handheld probe with an effective measurement area of 7 mm and a detection depth of about 1 mm.

A prospective, randomized, multicenter trial was conducted to evaluate the performance of the device in assessing surgical margins (Allweis et al. 2008). After excision of the main lumpectomy specimen, patients were randomized to a device and a control arm. In the device arm, the surgeon applied the device to the six margins (medial, lateral, superior, inferior, deep, and anterior), and reexcised tissue if the device indicated positive margins. In the device arm, 60% of the involved margins were correctly identified and reexcised, compared with 40% in the control arm (p = 0.044). The percentage of patients with correctly identified margins in a nonpalpable subgroup was also higher (69% vs. 39%, respectively). The need for reoperation in case of positive margins was not defined or dictated by the study, so the actual decrease in reexcision rate from using the device cannot be determined from this study.

One of the advantages of the technique is the potential to detect DCIS (Pappo et al. 2010; Thill et al. 2011), so the MarginProbe can be of special interest for this group of patients. Other advantages include a short measurement time (1–2 s per measurement) and controlled, user-independent tissue measurements using a vacuum-based mechanism. The main disadvantage of this technique is that the performance of the device decreases for tissue with a more heterogeneous composition, that is, the probe is less sensitive to measurement sites with a small cancer feature size (Pappo et al. 2010). Consequently, patients with small tumors might still need to undergo a second surgery to obtain clear margins. Besides, the technique samples only an area of 7 mm, and positive margins can be missed if the surgeon does not accurately cover each entire margin.

16.2.3.2 Diffuse Reflectance Spectroscopy

Diffuse reflectance spectroscopy (DRS) can identify tissue characteristics by measuring their intrinsic light absorption and scattering properties at different wavelengths in the UV–visible range. Diffuse reflectance spectra can be obtained by illuminating tissue with a selected light spectrum, and these spectra reflect the absorption and scattering properties of the tissue. The absorption coefficient is directly related to the concentration of physiologically relevant absorbers in the tissue, which include oxygenated and deoxygenated hemoglobin. The scattering coefficient reflects the size and density of scattering centers in tissue, such as cells and nuclei. Since changes in human tissue associated with malignant transformation include alterations in cellular composition, metabolic rate, and tissue morphologic characters, the reflectance spectra can be used to differentiate tumor from normal tissue.

Bigio et al. performed one of the earliest studies on the applicability of DRS for assessing tumor margins (Bigio et al. 2000). They used elastic scattering spectroscopy (a variant of DRS) implemented in a fiber-optic probe assembly and measured diffuse reflectance spectra from the tumor cavity in vivo after resection. The probe had a sensing depth of 300 μm, which is sufficient to detect disease at the surface. The measured tissue was biopsied for pathologic correlation, and the spectra were fed into classification algorithms to provide estimations for the presence of residual disease. They measured 72 breast tissue sites, and the sensitivity and specificity were 69% and 85%, respectively.

More recently, a biomedical group from the Duke University has developed a diffuse reflectance imaging device and studied 55 resection margins in an ex vivo setting in 48 patients. They were able to detect positive margins, regardless of pathology or depth from the margin, with 79% sensitivity and 67% specificity (Ramanujam et al. 2009; Wilke et al. 2009) (see Figure 16.3). Interestingly, positive margins for DCIS were correctly identified in eight of nine margins, corresponding with a sensitivity of 89%. However, of the eight patients who received neoadjuvant therapy, only four patients had their margins assessed correctly, indicating the inability of the current device to identify positive margins in this patient group.
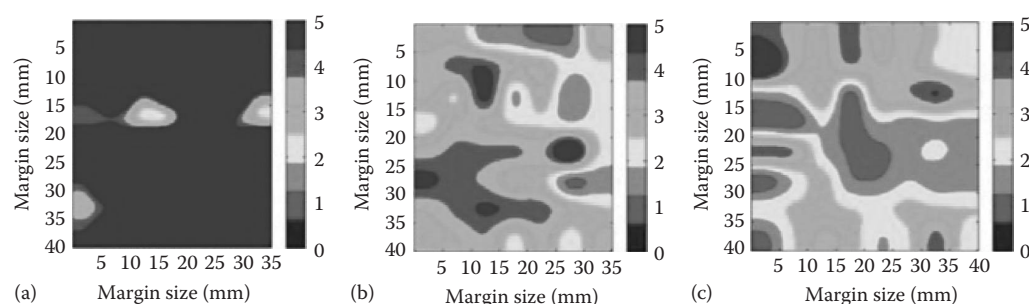
FIGURE 16.3   (See color insert.) Diffuse reflectance spectroscopy for tumor margin assessment. Parameter maps per margin were obtained from the ratio of β-carotene (absorption parameter) and the wavelength-averaged reduced scattering coefficient (scattering parameter). Blue areas generally represent healthy tissue, whereas red areas represent tumor. (a) Pathologically confirmed negative margin. (b) Pathologically confirmed margin positive for DCIS. (c) Pathologically confirmed margin positive for IDC. (Reproduced from Wilke, L. G., J. Brown, T. M. Bydlon et al., *Am. J. Surg.*, 198, 566, 2009, with permission from Elsevier.)

Another group combined diffuse reflectance and autofluorescence spectroscopy (Keller et al. 2010). Excised specimens were measured by a fiber-optic probe, and diffuse reflectance and autofluorescence spectra were then classified as benign or malign using a two-part classification method. Tissues from 32 patients were measured, and the sensitivity and specificity were 85% and 96%, respectively.

These preliminary results suggest that DRS (in combination with autofluorescence) could provide a useful tool to assess tumor margins intraoperatively. The potential to detect DCIS is of particular interest, as all currently available techniques lack the ability to accurately detect DCIS. However, due to the small scan area of the current probes, which is restricted by the output of the optical fibers, only a small tissue volume can be scanned. Hence, in order to cover the entire margin, multiple sites must be measured, which is time consuming and subject to user errors. Therefore, an important challenge for this technique is to increase the scan volume to make the technique suitable for intraoperative use.

16.2.3.3 Spatially Offset Raman Spectroscopy

Another optical technique that can potentially be used for breast tumor margin evaluation is Raman spectroscopy. Raman spectroscopy is a form of vibrational spectroscopy. Laser light (mostly in the visible, near-infrared (NIR), or near-ultraviolet range) is nonelastically scattered from molecules that are excited by the incident light, and this inelastic scattering can be used to identify organic molecules, such as fat, collagen, cell cytoplasm, and nucleus. These molecules have been shown to provide a signature associated with abnormality (Frank et al. 1995), thus providing the possibility for margin assessment.

Keller et al. used spatially offset Raman spectroscopy (SORS), which is a variant of Raman spectroscopy, for breast tumor surgical margin evaluation (Keller et al. 2011). They developed a SORS probe with one source fiber and multiple detection fibers, allowing the detection of spectral signatures from tumor within the first 2 mm in depth from the tissue surface. A total of 35 excised specimens were scanned: 15 samples with negative margins (>2 mm) and 20 samples with positive invasive tumor margins (<2 mm). The spectra were then classified to predict if a margin was positive or negative. They found a sensitivity, specificity, negative predictive value, and positive predictive value of 95%, 100%, 94%, and 100%. Although their findings are based on a small data set and did not include actual reexcision rates, their results seem very promising. However, the diameter of their probe is approximately 5 mm, thus covering only a small tissue area. The biggest challenge for this technique is therefore similar to DRS: adapt the probe to interrogate larger areas of tissue in order to meet the clinical criteria of sufficient area sampling within practical time constraints.

16.2.3.4 Optical Coherence Tomography

In the last decade, optical coherence tomography (OCT) has emerged as a high-resolution optical diagnostic imaging modality that is currently being used in ophthalmology and dermatology. More recently, OCT has been investigated as a technique to assess breast tumor margins. OCT is an optical equivalent of US, but instead of acoustic waves, it is based on the reflection of light from a low-coherence broadband light source (typically employing NIR light). By measuring backscattered or back-reflected light, cross-sectional tomographic images of the tissue microstructure can be obtained with a similar resolution as histopathology (μm).

Nguyen et al. at the University of Illinois used OCT images to intraoperatively assess exposed tumor margins (Nguyen et al. 2009). Their system operates in the spectral region around 1300 nm, providing a lateral and axial resolution of 35 and 5.9 μm in tissue, respectively. They scanned excised specimens (including DCIS) from 37 patients. The OCT images from the first 17 patients were used to establish imaging protocols and OCT criteria for identifying positive margins, and the images from the remaining patients were used for the study set. Eleven margins were identified as positive and nine as negative on OCT imaging, giving a sensitivity, specificity, and overall accuracy of 100%, 82%, and 90%, respectively. The increased scattering, due to strong reflections from tightly packed cells, was the main feature for classifying margins as positive.

The main challenge for this technique is to decrease acquisition and processing time, allowing to scan larger areas in a shorter time interval. Recent developments in OCT technology may make it possible to decrease scanning times, but these advances will result in significant increases in data volume. This requires automated classification algorithms, as individual analysis and interpretation of the OCT images would be too time consuming. However, once these challenges are overcome, the technique may provide useful intraoperative information to reduce the number of reoperations.

16.2.3.5 Near-Infrared Fluorescence Imaging

In near-infrared fluorescence (NIRF) imaging, an NIR fluorophore is administered, after which the breast tissue is irradiated by an external laser in the NIR spectral range (650–900 nm). Upon excitation, the fluorophore will release photons of a higher NIR wavelength, which are captured by an NIRF camera system and digitally converted into a visible image. In the 650–900 nm range, the absorption coefficient in tissue is minimum, resulting in decreased light scattering and autofluorescence, and increased penetration depth compared to visible and UV light.

Fluorophores can be conjugated to a specific targeting ligand or monoclonal antibody to image tumor-targeted molecules that have been identified with breast cancer, including Her2/Neu receptor, vascular endothelial growth factor (EGF) receptor, and EGF. The tumor-specific binding properties of these so-called tumor-targeted fluorophores seem perfectly suitable for image-guided surgery, as it provides the surgeon with real-time, tumor-specific information on the location and extent of the lesion.

However, the need to administer exogenous fluorophores limits the clinical application of the technique due to the requirement to be approved for human use. Indocyanine green (ICG) is currently the most often used NIR fluorophore, but ICG does not offer the possibility of tumor-specific antigen coupling. Another reason why the development of this technique has been hampered is the lack of dedicated intraoperative imaging systems.

To date, a minimal number of studies have been published that use NIRF imaging to guide surgical excision in breast cancer. Mieog et al. used NIRF in a breast cancer rat model. Seventeen rats were operated on, resulting in a complete resection of seventeen out of seventeen tumors (Mieog et al. 2011). Moreover, the technique enabled the identification of remnant tumor in the surgical cavity, which is an important advantage over WGL and US. Aydogan et al. performed a feasibility study in two patients. They injected nontargeted ICG in the breast lesion under US guidance. Surgery was performed 1 h after injection, and in both patients, clear margins were obtained (Aydogan et al. 2012).

Overall, NIRF imaging seems a suitable candidate for early intraoperative introduction, as it is a fast and simple-to-operate technique, with a sufficient penetration depth to assess tumor margins. However, progress needs to be made with clinically available fluorophores and dedicated imaging systems. Furthermore, the technique does not provide information on microscopic margin status. Thus, it is likely that it will be used together with a technique that provides microscopic information on tumor margins.

16.2.4 Conclusion

The intraoperative techniques that are currently being used in BCS all have their limitations. The overall disadvantage of all these techniques is the inaccurate detection of DCIS, and this limitation will become of greater importance in the near future, as patients will be diagnosed at an earlier stage. The techniques that are currently in the clinical trial or research phase have the potential to assess tumor margins with a similar or even better accuracy than current techniques. Moreover, most of these techniques seem to be able to detect DCIS, thus providing additional value in this specific patient population. However, technological developments are required for these techniques to meet the clinical criteria of sufficient area sampling within practical time constraints, and further studies must be performed to elucidate their value in decreasing reoperation rates in BCS.

16.3 THz Technology in Breast Cancer

16.3.1 Introduction

In recent years, there has been growing interest in the application of terahertz (THz) technology to the field of biomedical research (Berry et al. 2004; Fitzgerald et al. 2006; Knab et al. 2007; Pickwell et al. 2004; Reid et al. 2007; Woodward et al. 2003). THz has been used to successfully characterize DNA (Nagel et al. 2006) and proteins (Knab et al. 2007) in this range, demonstrating the ability of the radiation to probe intermolecular interactions. Typical THz imaging systems produce radiation of wavelengths in the range of 3 mm to 80 μm; this is longer than that of the visible spectrum or infrared, so THz radiation is less susceptible to scattering within biological tissue (Han et al. 2000), and in general, scattering is assumed to be negligible. Due to the unique sensitivity of THz to water and the safe nature of the wavelengths used, THz techniques have been investigated for imaging of tissues (Arnone et al. 1999; Ashworth et al. 2006, 2008; Berry et al. 2004; Brucherseifer et al. 2000; Fitzgerald et al. 2006; Han et al. 2000; Markelz et al. 2000; Nagel et al. 2006; Nakajima et al. 2007; Pickwell et al. 2004). Many tissues in the human body are made up of about 70% water, and the adult human body is about 57% water by mass (Hall 2010). It is known that many cancers have a higher concentration of water than normal tissue. THz radiation is uniquely sensitive to water, which, together with the advantages listed earlier, makes it a viable tool for medical imaging and in particular of cancers.

Wallace et al. working at TeraView Ltd (Cambridge, UK) demonstrated the application of THz reflection images to differentiate between normal skin and cancerous skin on both ex vivo and in vivo samples (Fitzgerald et al. 2004; Pickwell et al. 2004; Wallace et al. 2006) and additionally performed THz spectroscopy to characterize the properties of different tissue types. Further work has been done to identify contrast between healthy colon tissue, dysplasia, and cancer by Reid et al. at University College, London (Reid 2009).

16.3.2 Application of THz Technology to Breast Cancer

The application of THz technology to breast cancer was first proposed by Fitzgerald et al. in 2004 (Fitzgerald et al. 2004). Using a portable THz pulsed imaging (TPI) system developed for use in a hospital environment, they measured samples of excised breast tissue. The system used photoconduction to

generate and detect THz pulses with a frequency content from 0.1 to 4 THz. Several freshly excised breast samples were imaged. Two parameters from the time domain impulse functions were used to produce images: the minimum of the THz impulse function, E_{min}, and the ratio of the E_{min} to the maximum of the impulse function, E_{max}. The images showed contrast between healthy and cancerous tissues with good agreement to histology. Interestingly, the images also highlighted DCIS. This preliminary study demonstrated the potential of TPI to image breast tumors and encouraged further studies to determine the ability of the technique to discriminate between different types of breast tissue (Fitzgerald et al. 2004).

A more comprehensive study performed in 2006 by Fitzgerald et al. (2006) confirmed that TPI could be used to identify contrast between healthy breast tissue and breast cancer by using E_{min} and E_{min}/E_{max}. The shape and size of the tumor on TPI correlated well with histopathology (see Figure 16.4). This work showed that THz can be used to distinguish invasive lobular and ductal breast cancer from normal and adipose breast tissue, and that it is likely that DCIS can be imaged as well (Fitzgerald et al. 2006).

Given it quasi-3D nature, THz imaging produces large volumes of data due to the two spatial and temporal components both being recorded. Fitzgerald et al. (2012) investigated data reduction methods prior to the classification of THz data from freshly excised breast cancer tissues. THz images have typically been formed using a range of parameters (or features), derived from the pulse or spectral profiles (Fitzgerald et al. 2002; Woodward et al. 2002). This heuristic approach to data reduction was compared to an unsupervised method that has traditionally been used in other areas, called principal component analysis (PCA) (Hutchings et al. 2009). PCA provides a theoretically optimal linear reduction, which requires no underlying assumptions about the statistical nature of the data. The PCA method was applied to the THz pulses and compared with the heuristic parameters. Classification for this study was performed using the support vector machine algorithm, which is well suited to finding complicated decision boundaries and has been used with good effect on other THz data sets (Yin et al. 2007). The classification results from the THz signals were then compared with histopathology. It was shown that using appropriate data reduction methods, based on parametric features and/or principal components, THz signals reflected from freshly excised breast cancer tissue can be classified with accuracies up to 92%.

This chapter provides further evidence on the efficacy of the technique and points to methods to improve classification of signals obtained when using THz in breast cancer. With these encouraging results, it was suggested that this technique of imaging could potentially be used to intraoperatively assess tumor margins in patients undergoing BCS, eventually aiming to reduce the number of reoperations (Wallace et al. 2005).
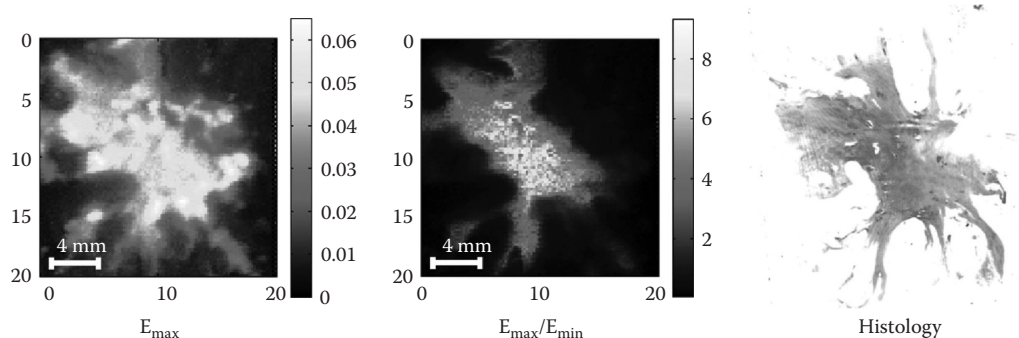
FIGURE 16.4   (See color insert.) This figure shows two terahertz images generated using the maximum of the reflected pulse (E_{max}) and the ratio between maximum and minimum of the reflected pulse (E_{max}/E_{min}). In the E_{max} image, all the tissues are shown, tumor with surrounding adipose tissue. In E_{max}/E_{min}, only the tumor is visible and correlated well with the tumor shown in the histology image. (Reproduced from Ashworth, P. C., E. Pickwell-MacPherson, E. Provenzano et al., *Opt. Exp.*, 17, 12444, 2009. With permission of Optical Society of America.)

16.3.3 Handheld THz Probe for Intraoperative Use

In order to use THz technology for intraoperative assessment of breast tumor margins, a handheld THz imaging probe has been developed (see Figure 16.5) (Wallace et al. 2005). The system uses a photoconductive emitter and receiver to produce and detect THz pulses of bandwidth 0.1–2.0 THz. The THz pulse beam is focused to the probe tip, from which they are reflected back, through a silicon lens and a system of Risley beam steering prisms. The THz pulse beam is scanned back and forth across the active area by controlled rotation of the Risley prisms, resulting in an imaging window with a length of 8 mm.

This probe has been used to study tissue samples, obtained from freshly excised lumpectomy and mastectomy specimens, from 37 patients at Guy's Hospital in London (Ashworth et al. 2008). Figure 16.6 shows typical impulse responses observed upon the reflection of THz pulses from the three main breast tissue types—adipose, fibrous, and cancerous. A number of distinguishing parameters (features) were identified, and Figure 16.7 shows the average values for four parameters for each of the three key tissue types. It is clear from these two figures that it is easy to identify differences between adipose tissue and cancer with the probe. However, as expected, the discrimination between fibrous tissue and cancer is more challenging. By examining the pulse integral and full width half maximum in Figure 16.7, we can see subtle differences in the average values of these parameters between fibrous tissue and cancer. PCA was applied to the full-time domain THz pulse data, and then linear discriminant analysis was used to predict the tissue types of individual specimens as listed in Table 16.1. This shows that a promising value of 90% was found for the sensitivity and 81% for specificity (Ashworth 2010).

It is clear that these studies with a handheld THz probe are promising; THz technology is now becoming sufficiently versatile that it is possible to build such a probe and achieve a good level of performance in a clinical environment. One of the limitations of the handheld probe is that due to the small imaging window, only a small tissue volume can be scanned. If in the near future the THz probe is used to scan complete lumpectomy specimens, multiple measurements per margin must be performed, which is time-consuming and sensitive to user errors. A potential limitation of the use of THz for assessing breast margins in general is the limited penetration depth as a result of high attenuation of THz in water. Tumor cells located at a depth >1 mm may therefore not be detected, but further studies are needed to determine the actual penetration depth of THz in breast tissue. There are still improvements that can be made in order to increase the SNR, reduce errors in data registration, and remove contaminant data from the training data set for discriminate analysis. These improvements may well bring the performance of the technique closer to routine use during surgery.
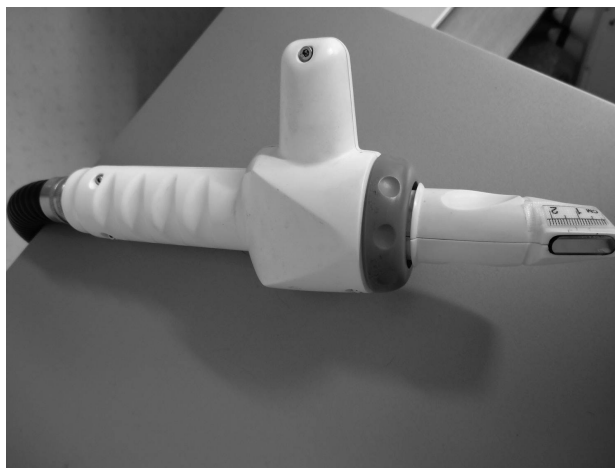

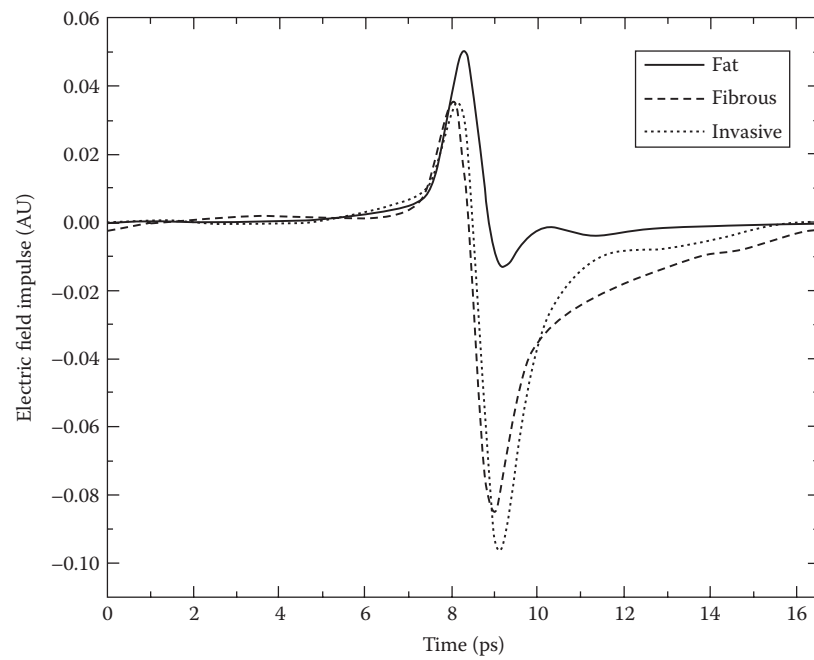**FIGURE 16.5**   THz handheld intraoperative probe; courtesy of TeraView Ltd. (patented).

FIGURE 16.6 Graph showing typical pulses obtained from three key tissue types found in tissue excised from a breast cancer patient.
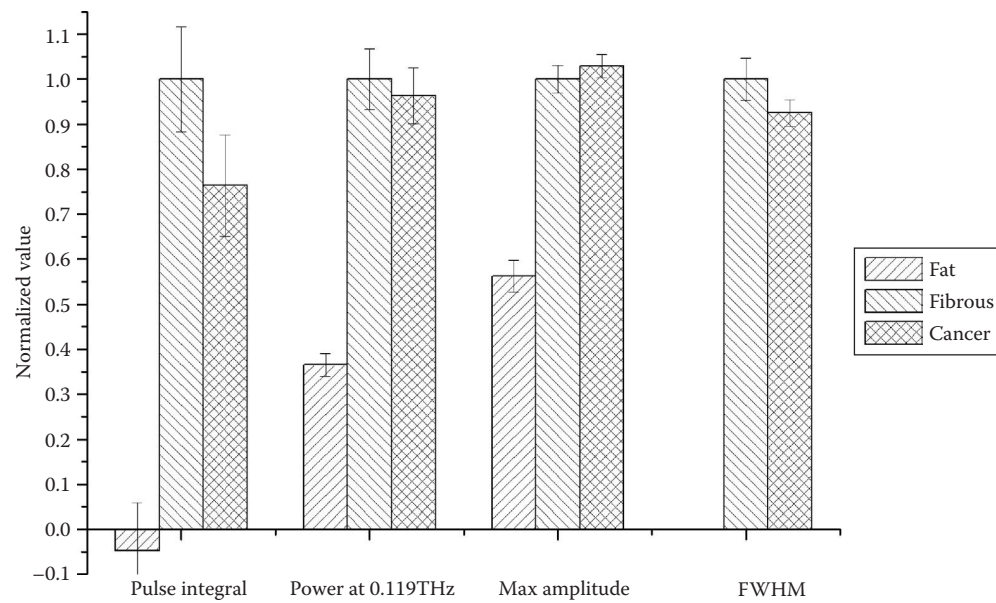

FIGURE 16.7 Bar graph showing the average values of four parameters for each of the three tissue types. Error bars represent 95% confidence intervals.

TABLE 16.1 Table Listing the Results of Linear Discriminant Analysis on Data Collected Using Handheld Probe

THz Prediction	Histology Result	
	Cancer	Healthy
Cancer	27	34
Healthy	3	142
Total N	30	176
Total correct	27	142
	Sensitivity	Specificity
	90%	81%

16.3.4 Understanding THz Signals from Breast Tissue

There is a need to understand the mechanisms that cause contrast in THz images of breast cancer and relate reflected pulse data to changes in tissue pathology. As a first step, Ashworth et al. measured the absorption and refractive indices of both healthy and diseased breast tissues in the THz region via time-domain THz pulsed spectroscopy (TPS) (Ashworth et al. 2009). THz transmission spectroscopy or TPS has previously been used to obtain the THz optical characteristics of skin tissue and basal cell carcinomas (BCCs) (Pickwell et al. 2004; Wallace et al. 2006), including the refractive index and absorption coefficient spectra. In the Ashworth study, 74 fresh breast tissue samples were measured, of these 33 were classified as *cancer*, 22 as *healthy fibrous*, and 19 as *healthy fat*. Figures 16.8 and 16.9 show the measured average absorption coefficient and refractive index for each of these groups, respectively. The error bars displayed
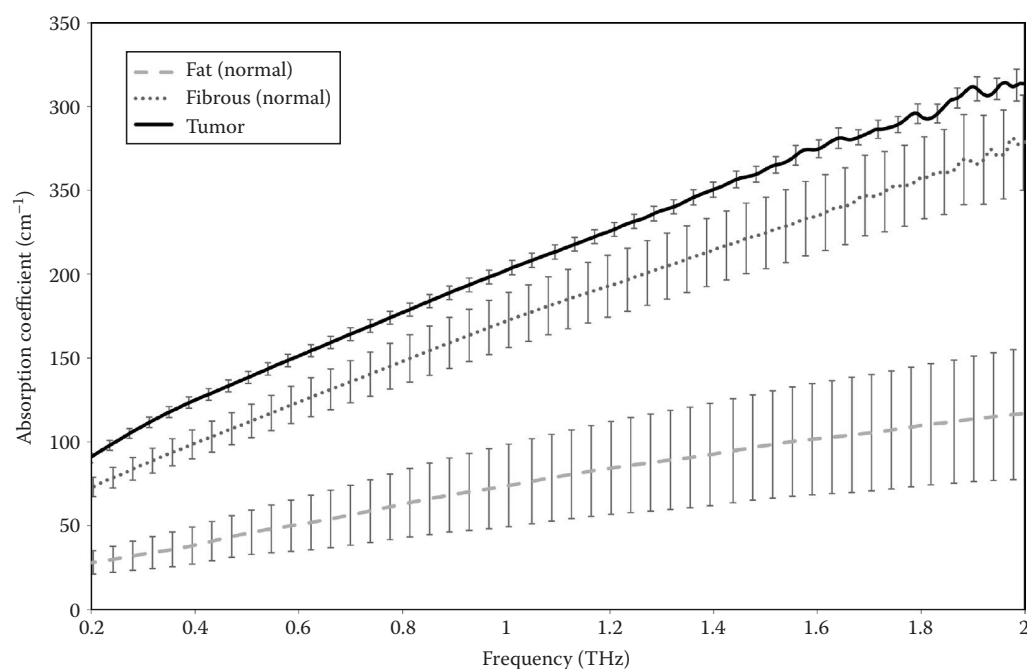

FIGURE 16.8 Graph showing average absorption coefficient spectra of groups of tissue types; error bars represent 95% confidence intervals.
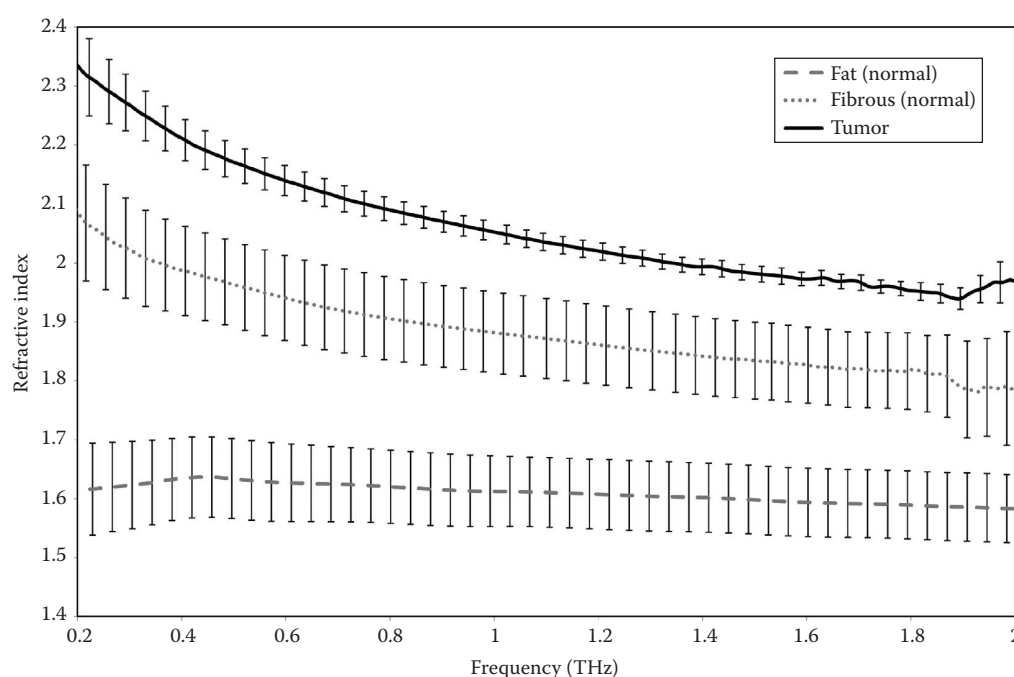
FIGURE 16.9 Graph showing average refractive index spectra of groups of tissue types; error bars represent 95% confidence intervals.

represent 95% confidence intervals derived from the standard error of the mean. The error bars for the refractive index are constant for fibrous tissue and fat but are slightly larger at high and low frequencies for the cancer samples. This is due to low signal in these ranges caused by attenuation through the sample.

Due to the nature of fibrous tissue within the breast, it was a challenging task isolating sufficient fibrous tissue from fatty tissue intact such that it would be suitable for our spectroscopy needs. As a result, the fibrous tissue group had a higher percentage fat than the tumor group, as tumors formed solid lumps that proved easier to separate.

There is a clear difference in the refractive indices between all pure tissue types and also a difference between the absorption coefficient of fat and the other two tissue types. In Figure 16.8, the shape of the spectrum of the cancer is very similar to fibrous tissue, but the transmitted signal is lower due to the increased attenuation in the cancer. The attenuation is a combination of absorption and scattering, and it would be impossible with this type of measurement to determine the contribution from each mechanism. As discussed previously, increased water content in the cancer tissue would lead to increased absorption, and in cancer tissue samples, we therefore assume absorption to be dominant and scattering negligible. But if one looks at studies on dehydrated, wax-embedded samples, attenuation also increases for regions of cancer, which can only result from structural changes, which, in turn, change the scattering properties (Berry et al. 2004; Nakajima et al. 2007). It is seen that breast tumor tissue has a higher refractive index than both healthy fatty and healthy fibrous tissues with the greatest difference being at 0.32 THz. Furthermore, around 0.32 THz, the absorption coefficient of breast tumor tissue increases slightly compared with fibrous breast tissue. Simulations were carried out to predict the impulse responses from performing THz pulsed reflection imaging on these tissues. A large difference was seen, as expected, between the impulse responses of healthy fat and those of healthy fibrous and breast tumor tissues. A difference in peak height of about 60% was seen on the impulse responses between cancer and healthy fibrous tissues.

In conclusion, the contrast seen when imaging breast cancer in reflection is mainly caused by an increase in the refractive index between cancer and healthy tissues and also in part due to an increase in the absorption coefficient. The root cause of the increases in these fundamental properties is yet to be determined.

Acquiring spectroscopic THz data allows us to simulate the reflected time domain response functions of healthy fibrous breast tissue and breast cancer tissue. Pickwell et al. have looked at the refractive index and absorption coefficient separately to characterize tissues. They have used the same model to investigate correlations between THz data and pathology and identify parameters of the simulated reflected impulse response function and corresponding spectroscopic properties with a view to improving our ability to distinguish between the fibrous and cancer tissues in the breast (Pickwell-Macpherson et al. 2012).

16.4 Conclusion

The field of medical imaging using THz technology is very much in its infancy, and there is a great deal of work yet to be done to show its true potential before the modality would be widely adopted by the medical community. At present, only skin, colon, and breast cancers have been examined in an ex vivo setting where the water content of the tissues is close to that of in vivo tissue. It would be interesting to look at the potential use of THz in identifying other cancers that can either be accessed topically or in cases where a conservative excision is required. These may, for example, include head and neck cancers such as mouth, throat, or brain cancers, cervical cancer, or rectal cancer. However, it is important not to lose focus and to ensure that the development of THz technology with a view to intraoperatively diagnosing those cancers for which contrasts have already been identified continues, and current techniques are improved.

There are several challenges to using this technique during surgery, such as the presence of blood and other fluids in the region, maintaining good contact of the probe with the breast tissue, and inter-patient variability. Although the presence of blood and other fluids can be managed during surgery, for example, through cauterization, this may also affect the THz response of the tissue to a varying degree and thus will require further study.

References

Allweis, T. M., Z. Kaufman, S. Lelcuk et al. 2008. A prospective, randomized, controlled, multicenter study of a real-time, intraoperative probe for positive margin detection in breast-conserving surgery. *The American Journal of Surgery* 196: 483–489.

Arnone, D. D., C. M. Ciesla, A. Corchia et al. 1999. Applications of terahertz (THz) technology to medical imaging. Presented at *Proceedings of SPIE* 3828: 209–219.

Ashworth, P. C. 2010. Biomedical applications of terahertz technology. Cambridge, U.K.: University of Cambridge. PhD.

Ashworth, P. C., P. O'Kelly, A. D. Purushotham et al. 2008. An intra-operative THz probe for use during the surgical removal of breast tumors. Presented at *33rd International Conference on Infrared, Millimeter and Terahertz Waves*, Pasadena, CA, pp. 1–3.

Ashworth, P. C., E. Pickwell-MacPherson, E. Provenzano et al. 2009. Terahertz pulsed spectroscopy of freshly excised human breast cancer. *Optics Express* 17: 12444–12454.

Ashworth, P. C., J. A. Zeitler, M. Pepper, and V. P. Wallace 2006. Terahertz spectroscopy of biologically relevant liquids at low temperatures. Presented at *31st International Conference on Infrared Millimeter Waves and 14th International Conference on Terahertz Electronics*, Shanghai, China, p. 184.

Aydogan, F., V. Ozben, E. Aytac et al. 2012. Excision of nonpalpable breast cancer with indocyanine green fluorescence-guided occult lesion localization (IFOLL). *Breast Care* 7: 48–51.

Barentsz, M. W., M. A. A. J. van den Bosch, W. B. Veldhuis et al. 2013. Radioactive seed localization for non-palpable breast cancer. *British Journal of Surgery* 100: 582–588.

Bathla, L., A. Harris, M. Davey, P. Sharma, and E. Silva. 2011. High resolution intra-operative two-dimensional specimen mammography and its impact on second operation for re-excision of positive margins at final pathology after breast conservation surgery. *The American Journal of Surgery* 202: 387–394.

Bennett, I. C., J. Greenslade, and H. Chiam. 2005. Intraoperative ultrasound-guided excision of nonpalpable breast lesions. *World Journal of Surgery* 29: 369–374.

Berry, E., J. W. Handley, A. J. Fitzgerald et al. 2004. Multispectral classification techniques for terahertz pulsed imaging: An example in histopathology. *Medical Engineering & Physics* 26: 423–430.

Bigio, I. J., S. G. Bown, G. Briggs et al. 2000. Diagnosis of breast cancer using elastic-scattering spectroscopy: Preliminary clinical results. *Journal of Biomedical Optics* 5: 221–228.

Brucherseifer, M., M. Nagel, P. Haring Bolivar et al. 2000. Label-free probing of the binding state of DNA by time-domain terahertz sensing. *Applied Physics Letters* 77: 4049–4051.

Cancer Research UK. 2012a. Breast cancer incidence statistics—lifetime risks. http://www.cancerresearchuk.org/cancer-info/cancerstats/types/breast/incidence/#risk, accessed June 25, 2013.

Cancer Research UK. 2012b. Invasive ductal breast cancer. http://www.cancerresearchuk.org/cancer-help/type/breast-cancer/%20about/types/invasive-ductal-breast-cancer, accessed June 25, 2013.

Donker, M., C. A. Drukker, R. A. V. Olmos et al. 2013. Guiding breast-conserving surgery in patients after neoadjuvant systemic therapy for breast cancer: A comparison of radioactive seed localization with the ROLL technique. *Annals of Surgical Oncology* 20: 1–7.

Esbona, K. and L. G. Wilke. 2012. Intraoperative imprint cytology and frozen section pathology for margin assessment in breast conservation surgery: A systematic review. *Annals of Surgical Oncology* 19: 3236–3245.

Ferlay, J. S., H. R. Shin, F. Bray et al. 2010. GLOBOCAN 2008, cancer incidence and mortality worldwide: IARC CancerBase No. 10. Presented at *International Agency for Research on Cancer 2010*, Lyon, France, p. 29.

Fisher, B., S. Anderson, J. Bryant et al. 2002. Twenty-year follow-up of a randomized trial comparing total mastectomy, lumpectomy, and lumpectomy plus irradiation for the treatment of invasive breast cancer. *New England Journal of Medicine* 347: 1233–1241.

Fitzgerald, A. J., E. Berry, N. N. Zinovev et al. 2002. An introduction to medical imaging with coherent terahertz frequency radiation. *Physics in Medicine and Biology* 47: R67.

Fitzgerald, A. J., S. Pinder, A. D. Purushotham et al. 2012. Classification of terahertz-pulsed imaging data from excised breast tissue. *Journal of Biomedical Optics* 17: 0160051–01600510.

Fitzgerald, A. J., V. P. Wallace, M. Jimenez-Linan et al. 2006. Terahertz pulsed imaging of human breast tumors. *Radiology* 239: 533–540.

Fitzgerald, A. J., V. P. Wallace, R. Pye et al. 2004. *Terahertz Imaging of Breast Cancer, a Feasibility Study*. New York: IEEE.

Frank, C. J., R. L. McCreery, and D. C. B. Redd. 1995. Raman spectroscopy of normal and diseased human breast tissues. *Analytical Chemistry* 67: 777–783.

Gajdos, C., P. I. Tartter, I. J. Bleiweiss et al. 2002. Mammographic appearance of nonpalpable breast cancer reflects pathologic characteristics. *Annals of Surgery* 235: 246.

Hall, J. E. 2010. *Guyton and Hall Textbook of Medical Physiology: Enhanced E-Book*. Philadelphia, PA: Elsevier Health Sciences.

Han, P. Y., G. C. Cho, and X.-C. Zhang. 2000. Time-domain transillumination of biological tissues with terahertz pulses. *Optics Letters* 25: 242–244.

Houssami, N., P. Macaskill, M. L. Marinovich et al. 2010. Meta-analysis of the impact of surgical margins on local recurrence in women with early-stage invasive breast cancer treated with breast-conserving therapy. *European Journal of Cancer* 46: 3219–3232.

Hughes, J. H., M. C. Mason, R. J. Gray et al. 2008. A multi-site validation trial of radioactive seed localization as an alternative to wire localization. *The Breast Journal* 14: 153–157.

Hunt, K. K., A. A. Sahin, H. M. Kuerer et al. 2007. Role for intraoperative margin assessment in patients undergoing breast-conserving surgery. *Annals of Surgical Oncology* 14: 1458–1471.

Hutchings, J., C. Kendall, B. Smith et al. 2009. The potential for histological screening using a combination of rapid Raman mapping and principal component analysis. *Journal of Biophotonics* 2: 91–103.

Jeevan, R., D. Cromwell, J. Browne, and J. Van Der Meulen. 2011. *National Mastectomy and Breast Reconstruction Audit 2011*. Leeds, U.K.: The NHS Information Centre.

Jeevan, R., D. A. Cromwell, M. Trivella et al. 2012. Reoperation rates after breast conserving surgery for breast cancer among women in England: Retrospective study of hospital episode statistics. *British Medical Journal* 345: e4505.

Katipamula, R., A. C. Degnim, T. Hoskin et al. 2009. Trends in mastectomy rates at the Mayo Clinic Rochester: Effect of surgical year and preoperative magnetic resonance imaging. *Journal of Clinical Oncology* 27: 4082–4088.

Kaufman, C. S., L. Jacobson, B. A. Bachman et al. 2007. Intraoperative digital specimen mammography: Rapid, accurate results expedite surgery. *Annals of Surgical Oncology* 14: 1478–1485.

Keller, M. D., S. K. Majumder, M. C. Kelley et al. 2010. Autofluorescence and diffuse reflectance spectroscopy and spectral imaging for breast surgical margin analysis. *Lasers in Surgery and Medicine* 42: 15–23.

Keller, M. D., E. Vargis, N. de Matos Granja et al. 2011. Development of a spatially offset Raman spectroscopy probe for breast tumor surgical margin evaluation. *Journal of Biomedical Optics* 16: 077006.

Kelly, P. and E. H. Winslow 1996. Needle wire localization for nonpalpable breast lesions: Sensations, anxiety levels, and informational needs. Presented at *Oncology Nursing Forum* 23: 639–645.

Klimberg, V. S. 2003. Advances in the diagnosis and excision of breast cancer. *The American Surgeon* 69: 11.

Klimberg, V. S., K. C. Westbrook, and S. Korourian. 1998. Use of touch preps for diagnosis and evaluation of surgical margins in breast cancer. *Annals of Surgical Oncology* 5: 220–226.

Knab, J. R., J.-Y. Chen, Y. He, and A. G. Markelz. 2007. Terahertz measurements of protein relaxational dynamics. *Proceedings of the IEEE* 95: 1605–1610.

Kouzminova, N. B., S. Aggarwal, A. Aggarwal, M. D. Allo, and A. Y. Lin. 2009. Impact of initial surgical margins and residual cancer upon re-excision on outcome of patients with localized breast cancer. *The American Journal of Surgery* 198: 771–780.

Krekel, N., M. H. Haloua, A. M. Lopes Cardozo et al. 2012. Intraoperative ultrasound guidance for palpable breast cancer excision (COBALT trial): A multicentre, randomised controlled trial. *The Lancet Oncology* 14: 48–54.

Krekel, N. M. A., B. M. Zonderhuis, H. B. A. C. Stockmann et al. 2011. A comparison of three methods for nonpalpable breast cancer excision. *European Journal of Surgical Oncology* 37: 109–115.

Lovrics, P. J., S. D. Cornacchi, F. Farrokhyar et al. 2009. The relationship between surgical factors and margin status after breast-conservation surgery for early stage breast cancer. *The American Journal of Surgery* 197: 740–746.

Lovrics, P. J., D. McCready, G. Gohla, C. Boylan, and M. Reedijk. 2011. A multicentered, randomized, controlled trial comparing radioguided seed localization to standard wire localization for nonpalpable, invasive and in situ breast carcinomas. *Annals of Surgical Oncology* 18: 3407–3414.

Markelz, A. G., A. Roitberg, and E. J. Heilweil. 2000. Pulsed terahertz spectroscopy of DNA, bovine serum albumin and collagen between 0.1 and 2.0 THz. *Chemical Physics Letters* 320: 42–48.

McCahill, L. E., R. M. Single, E. J. A. Bowles et al. 2012. Variability in reexcision following breast conservation surgery. *The Journal of the American Medical Association* 307: 467–475.

Medina-Franco, H., L. Abarca-Pérez, M. N. García-Alvarez et al. 2008. Radioguided occult lesion localization (ROLL) versus wire-guided lumpectomy for non-palpable breast lesions: A randomized prospective evaluation. *Journal of Surgical Oncology* 97: 108–111.

Mieog, J. S. D., M. Hutteman, J. R. van der Vorst et al. 2011. Image-guided tumor resection using real-time near-infrared fluorescence in a syngeneic rat model of primary breast cancer. *Breast Cancer Research and Treatment* 128: 679–689.

Monti, S., V. Galimberti, G. Trifiro et al. 2007. Occult breast lesion localization plus sentinel node biopsy (SNOLL): Experience with 959 patients at the European Institute of Oncology. *Annals of Surgical Oncology* 14: 2928–2931.

Moore, M. M., L. A. Whitney, L. Cerilli et al. 2001. Intraoperative ultrasound is associated with clear lumpectomy margins for palpable infiltrating ductal breast cancer. *Annals of Surgery* 233: 761.

Morrow, M., J. R. Harris, and S. J. Schnitt. 2012. Surgical margins in lumpectomy for breast cancer—Bigger is not better. *The New England Journal of Medicine* 367: 79–82.

Munshi, A., S. Kakkar, R. Bhutani et al. 2009. Factors influencing cosmetic outcome in breast conservation. *Clinical Oncology* 21: 285–293.

Nagel, M., M. Först, and H. Kurz. 2006. THz biosensing devices: Fundamentals and technology. *Journal of Physics: Condensed Matter* 18: S601.

Nakajima, S., H. Hoshina, M. Yamashita, C. Otani, and N. Miyoshi. 2007. Terahertz imaging diagnostics of cancer tissues with a chemometrics technique. *Applied Physics Letters* 90: 041102.

Ngô, C., A. G. Pollet, J. Laperrelle et al. 2007. Intraoperative ultrasound localization of nonpalpable breast cancers. *Annals of Surgical Oncology* 14: 2485–2489.

Nguyen, F. T., A. M. Zysk, E. J. Chaney et al. 2009. Intraoperative evaluation of breast tumor margins with optical coherence tomography. *Cancer Research* 69: 8790–8796.

Olson, T. P., J. Harter, A. Munoz, D. M. Mahvi, and T. M. Breslin. 2007. Frozen section analysis for intraoperative margin assessment during breast-conserving surgery results in low rates of re-excision and local recurrence. *Annals of Surgical Oncology* 14: 2953–2960.

Pappo, I., R. Spector, A. Schindel et al. 2010. Diagnostic performance of a novel device for real-time margin assessment in lumpectomy specimens. *Journal of Surgical Research* 160: 277–281.

Pickwell, E., B. E. Cole, A. J. Fitzgerald, M. Pepper, and V. P. Wallace. 2004. In vivo study of human skin using pulsed terahertz radiation. *Physics in Medicine and Biology* 49: 1595.

Pickwell-Macpherson, E., A. J. Fitzgerald, and V. P. Wallace 2012. Breast cancer tissue diagnosis at terahertz frequencies. In *Optical Interactions with Tissue and Cells XXIII*, eds. Jansen, E. D. and R. J. Thomas, Bellingham, WA: SPIE.

Pleijhuis, R. G., M. Graafland, J. De Vries, J. Bart, J. S. De Jong, and G. M. Van Dam. 2009. Obtaining adequate surgical margins in breast-conserving therapy for patients with early-stage breast cancer: current modalities and future directions. *Annals of Surgical Oncology* 16: 2717–2730.

Postma, E. L., H. M. Verkooijen, S. van Esser et al. 2012. Efficacy of "radioguided occult lesion localisation" (ROLL) versus "wire-guided localisation" (WGL) in breast conserving surgery for non-palpable breast cancer: A randomised controlled multicentre trial. *Breast Cancer Research and Treatment* 136: 469–478.

Rahusen, F. D., A. J. A. Bremers, H. F. J. Fabry, and R. P. A. Boom. 2002. Ultrasound-guided lumpectomy of nonpalpable breast cancer versus wire-guided resection: A randomized clinical trial. *Annals of Surgical Oncology* 9: 994–998.

Ramanujam, N., J. Q. Brown, T. M. Bydlon et al. 2009. Quantitative spectral reflectance imaging device for intraoperative breast tumor margin assessment. Presented at *Annual International Conference of the IEEE Engineering in Medicine and Biology Society*: 6554–6556.

Rampaul, R. S., M. Bagnall, H. Burrell et al. 2004. Randomized clinical trial comparing radioisotope occult lesion localization and wire-guided excision for biopsy of occult breast lesions. *British Journal of Surgery* 91: 1575–1577.

Reid, C. 2009. Spectroscopic methods for medical diagnosis at terahertz wavelengths. Doctoral Thesis, University College London, London, U.K.

Reid, C., A. P. Gibson, J. C. Hebden, and V. P. Wallace 2007. The use of tissue mimicking phantoms in analysing contrast in THz pulsed imaging of biological tissue. Presented at *Joint 32nd International Conference on Infrared and Millimeter Waves and the 15th International Conference on Terahertz Electronics*, Cardiff, U.K., pp. 567–568.

Riedl, O., F. Fitzal, N. Mader et al. 2009. Intraoperative frozen section analysis for breast-conserving therapy in 1016 patients with breast cancer. *European Journal of Surgical Oncology* 35: 264–270.

Sarlos, D., L. D. Frey, H. Haueisen et al. 2009. Radioguided occult lesion localization (ROLL) for treatment and diagnosis of malignant and premalignant breast lesions combined with sentinel node biopsy: A prospective clinical trial with 100 patients. *European Journal of Surgical Oncology* 35: 403–408.

Siegel, R., D. Naishadham, and A. Jemal. 2012. Cancer statistics, 2012. *CA: A Cancer Journal for Clinicians* 62: 10–29.

Singletary, S. E. 2002. Surgical margins in patients with early-stage breast cancer treated with breast conservation therapy. *The American Journal of Surgery* 184: 383–393.

Skinner, K. A., H. Silberman, and M. J. Silverstein. 2001. Palpable breast cancers are inherently different from nonpalpable breast cancers. *Annals of Surgical Oncology* 8: 705–710.

Snider Jr, H. C. and D. G. Morrison. 1999. Intraoperative ultrasound localization of nonpalpable breast lesions. *Annals of Surgical Oncology* 6: 308–314.

Talsma, A. K., A. M. J. Reedijk, R. A. M. Damhuis, P. J. Westenend, and W. J. Vles. 2011. Re-resection rates after breast-conserving surgery as a performance indicator: Introduction of a case-mix model to allow comparison between Dutch hospitals. *European Journal of Surgical Oncology* 37: 357–363.

Thill, M., K. Röder, K. Diedrich, and C. Dittmer. 2011. Intraoperative assessment of surgical margins during breast conserving surgery of ductal carcinoma in situ by use of radiofrequency spectroscopy. *Breast* 20: 579–580.

Thind, C. R., S. Tan, S. Desmond et al. 2011. SNOLL. Sentinel node and occult (impalpable) lesion localization in breast cancer. *Clinical Radiology* 66: 833–839.

Valdes, E. K., S. K. Boolbol, I. Ali, S. M. Feldman, and J.-M. Cohen. 2007. Intraoperative touch preparation cytology for margin assessment in breast-conservation surgery: Does it work for lobular carcinoma? *Annals of Surgical Oncology* 14: 2940–2945.

Veronesi, U., N. Cascinelli, L. Mariani et al. 2002. Twenty-year follow-up of a randomized study comparing breast-conserving surgery with radical mastectomy for early breast cancer. *New England Journal of Medicine* 347: 1227–1232.

Waljee, J. F., E. S. Hu, L. A. Newman, and A. K. Alderman. 2008. Predictors of re-excision among women undergoing breast-conserving surgery for cancer. *Annals of Surgical Oncology* 15: 1297–1303.

Wallace, V. P., A. J. Fitzgerald, E. Pickwell et al. 2006. Terahertz pulsed spectroscopy of human basal cell carcinoma. *Applied Spectroscopy* 60: 1127–1133.

Wallace, V. P., A. J. Fitzgerald, B. Robertson, E. Pickwell, and B. Cole 2005. Development of a hand-held TPI system for medical applications. In *2005 IEEE MTT-S International Microwave Symposium*, Vols. 1–4, Long Beach, CA, pp. 637–639. IEEE.

Weber, W. P., S. Engelberger, C. T. Viehl et al. 2008. Accuracy of frozen section analysis versus specimen radiography during breast-conserving surgery for nonpalpable lesions. *World Journal of Surgery* 32: 2599–2606.

Wilke, L. G., J. Brown, T. M. Bydlon et al. 2009. Rapid noninvasive optical imaging of tissue composition in breast tumor margins. *The American Journal of Surgery* 198: 566–574.

Woodward, R. M., B. E. Cole, V. P. Wallace et al. 2002. Terahertz pulse imaging in reflection geometry of human skin cancer and skin tissue. *Physics in Medicine and Biology* 47: 3853.

Woodward, R. M., V. P. Wallace, R. J. Pye et al. 2003. Terahertz pulse imaging of ex vivo basal cell carcinoma. *Journal of Investigative Dermatology* 120: 72–78.

Yin, X., B.-H. Ng, B. M. Fischer, B. Ferguson, and D. Abbott. 2007. Support vector machine applications in terahertz pulsed signals feature sets. *IEEE Sensors Journal* 7: 1597–1608.

Youlden, D. R., S. M. Cramb, N. A. Dunn et al. 2012. The descriptive epidemiology of female breast cancer: An international comparison of screening, incidence, survival and mortality. *Cancer Epidemiology* 36: 237–248.

Intraoperative Assessment of Tumor Resection Margins in Breast-Conserving Surgery using ^{18}F-FDG Cerenkov Luminescence Imaging – A First-in-Human Feasibility Study

Maarten R. Grootendorst[1,2]

Massimiliano Cariati[1,2]

Sarah E. Pinder[1]

Ashutosh Kothari[2]

Michael Douek[1,2]

Tibor Kovacs[2]

Hisham Hamed[2]

Amit Pawa[3]

Fiona Nimmo[4]

Julie Owen[1]

Vernie Ramalingam[2]

Sweta Sethi[2]

Sanjay Mistry[2]

Kunal Vyas[5]

David S. Tuch[6]

Alan Britten[7]

Mieke Van Hemelrijck[1]

Gary J. Cook[8]

Chris Sibley-Allen[9]

Sarah Allen[9]

Arnie Purushotham[1,2]

Running title: CLI for assessing breast tumor margins

Author affiliations:

[1] – King's College London, Division of Cancer Studies, London, UK;

[2] – Department of Breast Surgery, Guy's and St Thomas' NHS Foundation Trust, London, UK;

[3] – Anesthetic Department, Guy's and St Thomas' NHS Foundation Trust, London, UK;

[4] – Day Surgery Unit, Guy's and St Thomas' NHS Foundation Trust, London, UK;

[5] – Sagentia Ltd., Cambridge, UK;

[6] – Lightpoint Medical Ltd., Chesham, UK;

[7] – Medical Physics Department, St George's Hospital, London, UK;

[8] – King's College London, Division of Imaging Sciences and Biomedical Engineering, London, UK

[9] – Department of Nuclear Medicine, Guy's and St Thomas' NHS Foundation Trust, London, UK;

Conflicts of interest: David S. Tuch is an employee of and a shareholder in Lightpoint Medical Ltd. The other authors have no conflicts of interest to disclose.

Corresponding author

Name: Arnie Purushotham

Address: Department of Research Oncology, 3rd Floor Bermondsey Wing, Guy's Hospital, SE1 9RT, London

Phone: +44 (0) 207 188 3027

Email: arniepurushotham@gmail.com

First author

Name: Maarten Grootendorst (PhD student)

Address: Department of Research Oncology, 3rd Floor Bermondsey Wing, Guy's Hospital, SE1 9RT, London

Phone: +44 (0) 75 188 92692

Email: maarten.grootendorst@kcl.ac.uk

Word count: 6922

ABSTRACT

Rationale: In early-stage breast cancer, the primary treatment option for the majority of women is breast-conserving surgery (BCS). There is a clear need for more accurate techniques to assess resection margins intraoperatively, as on average 20% of patients require further surgery to achieve clear margins. Cerenkov luminescence imaging (CLI) combines optical and molecular imaging by detecting light emitted by 18F-fluorodeoxyglucose (^{18}F-FDG). Its high-resolution and small size imaging equipment makes CLI a promising technology for intraoperative margin assessment. A first-in-human study was conducted to evaluate the feasibility of ^{18}F-FDG CLI for intraoperative assessment of tumor margins in BCS.

Methods: Twenty-two patients with invasive breast cancer received 5 MBq/kg ^{18}F-FDG 45-60 min prior to surgery. Sentinel lymph node biopsy (SLNB) was performed using an increased technetium-99m (^{99m}Tc)-nanocolloid activity of 150 MBq to facilitate nodal detection against the gamma-probe background signal (cross-talk) from ^{18}F-FDG. The cross-talk and ^{99m}Tc dose required was evaluated in two lead-in studies. Immediately after excision, specimens were imaged intraoperatively in an investigational CLI imaging system. The first 10 patients were used to optimize the imaging protocol; the remaining 12 patients were included in the analysis dataset. CLI images from incised BCS specimens were analyzed postoperatively by two surgeons blinded to the histopathology results, and mean radiance and margin distance were measured. Agreement between margin distance on CLI and histopathology was assessed. Radiation doses to staff were measured.

Results: Ten of the 12 patients had an elevated tumor radiance on CLI. Mean radiance and tumor-to-background ratio were 560 ± 160 photons/s/cm^2/sr and 2.41 ± 0.54, respectively. All 15 assessable margins were clear on CLI and histopathology. Agreement in margin distance and inter-rater agreement was good (κ = 0.81 and 0.912, respectively). Sentinel lymph nodes (SLNs) were successfully detected in all patients. Radiation dose to staff was low; surgeons received a mean dose of 34 ± 15 µSv per procedure.

Conclusions: Intraoperative ^{18}F-FDG CLI is a promising, low-risk technique for intraoperative assessment of tumor margins in breast-conserving surgery. A randomized controlled trial will evaluate the impact of this technique on re-excision rates.

Key words: Cerenkov luminescence imaging; breast-conserving surgery; tumor margins; ^{18}F-FDG; sentinel lymph node biopsy

INTRODUCTION

In early-stage breast cancer, the primary treatment option for the majority of women is BCS by wide local excision (WLE) of the tumor. WLE often fails to achieve clear surgical margins, and on average 20% of patients who undergo BCS will require repeat surgery to achieve clear margins (*1*) (although this may vary since there is no global agreement of the definition of 'clear margins'). Re-operations potentially have several negative consequences including delayed commencement of adjuvant therapy, worse cosmesis, increased patient anxiety and costs (*2,3*).

There have been several attempts to assess surgical margins intraoperatively in order to reduce breast cancer re-operation rates post-WLE (*1*). Techniques evaluated to date include specimen radiography, intraoperative ultrasound, touch imprint cytology, frozen section, and radiofrequency spectroscopy. However, these all have limitations in terms of adequate performance, practicality and/or cost-effectiveness (*1*). Experimental methods evaluated include Raman spectroscopy, ambient mass spectrometry, optical coherence tomography, diffuse reflectance spectroscopy, confocal microscopy, and (targeted) fluorescence imaging (*1*). Each of these techniques have unique limitations, and the diagnostic performance remains to be evaluated in large-scale studies.

Positron emission tomography (PET) using ^{18}F-FDG is a powerful tool for *in vivo* imaging of breast cancer. While whole-body PET has limited diagnostic sensitivity for primary breast cancer, high-resolution PET imaging with positron emission mammography has shown high sensitivity (92-96%) and specificity (84-91%) for breast cancer diagnosis (*4-6*). Intraoperative high-resolution imaging of ^{18}F-FDG could therefore provide a powerful tool for surgical guidance. However, intraoperative PET is impractical due to the large size and expense of a PET scanner and PET's low spatial resolution. Development of a compact, high-resolution, intraoperative PET scanner could address these limitations.

Recently, it has been discovered that PET imaging agents emit optical photons via a phenomenon called Cerenkov luminescence (*7*). Cerenkov photons are generated by positrons travelling at super-relativistic speeds in tissue. Optical imaging of Cerenkov photons emitted by PET agents is an emerging imaging modality called CLI. CLI combines high diagnostic performance and clinical translatability of PET imaging with high spatial resolution and compactness of optical cameras,

thus making it a promising technology for intraoperative margin assessment in breast cancer surgery (*8*).

In this first-in-human clinical trial we evaluated the feasibility, safety, and preliminary performance of ^{18}F-FDG CLI using a novel intraoperative CLI camera to assess tumor margin status in breast cancer patients undergoing WLE with SLNB or with axillary lymph node dissection (ALND).

MATERIALS AND METHODS

Intraoperative ^{18}F-FDG CLI in breast-conserving surgery

Patient recruitment and patient preparation on the day of surgery. Research Ethics Committee approval was obtained prior to patient recruitment (ClinicalTrials.gov identifier NCT02037269). Between June 2014 and February 2016, patients with histologically confirmed invasive breast cancer on core biopsy with or without associated ductal carcinoma in situ (DCIS), due to undergo primary BCS and SLNB or ALND, were recruited at Guy's Hospital in London after written informed consent was obtained. Exclusion criteria were: age <30 years, previous surgery or radiotherapy to the ipsilateral breast in the preceding two years, neoadjuvant systemic therapy, pregnancy or lactation, blood glucose level of ≥12 mmol/l on the day of surgery and known hypersensitivity to ^{18}F-FDG. Females of childbearing age required a negative pregnancy test (by beta HCG qualitative analysis), history of surgical sterilization, or history of amenorrhea in the past twelve months.

On the day of surgery patients scheduled to undergo SLNB received a periareolar intradermal injection of 150 MBq ^{99m}Tc-albumin-nanocolloid (Nanocoll[TM], GE Healthcare, UK). The increased ^{99m}Tc activity of 150 MBq was calculated based on the results from two lead-in cross-talk studies (Supplemental Material). Patients were then injected intravenously with 5 MBq/kg ^{18}F-FDG (up to a maximum of 300 MBq) and typically 45-60 min post-^{18}F-FDG injection were taken to the operating theatre.

Surgery and intraoperative specimen radiography. Following induction of anesthesia, patients due to undergo SLNB received a periareolar subdermal injection of 2ml Patent Blue V and 3ml of normal saline. To minimize radiation exposure to theatre staff by reducing the time spent in close proximity to the patient, a standard breast operating set was pre-arranged on a sterile tray. Surgery to the breast

was performed ahead of SLNB/ALND to minimize signal intensity reduction from radiotracer decay in the time between ^{18}F-FDG injection and CLI imaging. The WLE specimen was excised using monopolar diathermy (Valleylab Force FX^{TM} electrosurgical generator with HCP-01 Skintact surgical pencil). The excised specimen was orientated with sutures and metal surgical clips as per local protocol.

Post-excision WLE specimens were x-rayed intraoperatively (Faxitron Bioptics, USA), and excision of cavity shave margins was performed if the tumor was deemed to be close to the edge of the specimen on radiography.

Following excision of the WLE specimen, SLNB or ALND was performed. For SLNB a Europrobe 3 gamma probe with a high-energy collimator was used (Eurorad SA, France). SLNs were defined as nodes that were radioactive, blue, or palpable (*9*). The number of excised SLNs, the *ex vivo* SLN gamma probe signal (counts per second), and the presence of blue nodal discoloration were recorded. Upon completion of the procedure the gamma probe background signal in the axilla was measured.

Intraoperative CLI of WLE specimens and lymph nodes. Following specimen radiography, CLI imaging of the WLE specimen was performed using an investigational intraoperative CLI imaging system (Lightpoint Medical Ltd, UK). This system consists of a custom-built light-tight dark box containing two optical pathways: one for CLI and one for white-light imaging for anatomic reference (Fig. 1A). The CLI imaging pathway includes a fast f/.95 lens and a reflex mirror to fold the optical pathway into an electron-multiplying charge coupled device (EMCCD) camera. The field-of-view of the CLI camera is 8×8 cm, and the acquisition matrix is 512×512 to give a pixel resolution of 156.25 μm. The EMCCD is thermoelectrically-cooled to -80°C and radiation-shielded with lead to prevent annihilation photons from scintillating in the EMCCD chip, i.e. "gamma strikes". The white-light imaging pathway provides a photographic reference image using a standard complementary metal-oxide-semiconductor camera.

The WLE specimen was positioned on a specimen table (Fig. 1B), the margin of interest placed in the center of the field-of-view by using the surgical sutures to guide orientation, and subsequently imaged.

Following intact WLE specimen imaging, the surface of the specimen was immediately inked intraoperatively in order to preserve its orientation for histopathological analysis (Supplemental Material Fig. 1A). Six distinct ink colors (Davidson[®], Bradley Products Inc., USA) were applied to the six margins. The inked specimen was then incised through the posterior margin to visualize the primary tumor and tumor margins, and the incised WLE specimen was imaged (Supplemental Material Figs. 1B and 1C). In one patient sequential image acquisition over a 50-minute time-period was performed to determine the half-life ($t_{1/2}$) of the radiance observed in the tumor.

The first 10 patients were included in the optimization dataset and the remaining 12 patients in the analysis dataset. In the first 10 patients, the image acquisition protocol was optimized by testing different image acquisition times (100, 300, 400 sec) and pixel binning settings (2x2, 4x4, 8x8). A 300-sec acquisition time and 8x8 pixel binning was found to provide sufficient sensitivity for tumor detection and acceptable spatial resolution (1.25 mm) within a time-window feasible for intraoperative use, and these setting were used in the remaining 12 patients included in the analysis dataset. Upon completion of WLE CLI, the activity of the WLE specimen was estimated using a scintillation monitor (Type 41/44A, ThermoScientific, USA) or handheld radiation spectrometer (Raymon10 GR1, Kromek PLC). SLNs were also imaged intraoperatively with CLI using the same imaging settings.

After imaging was completed, WLE specimens were sent for histopathological analysis as per standard practice.

Radiation safety monitoring. Radiation safety monitoring was performed to ensure safe working practices were maintained and that work was compliant with UK legislation regarding ionizing radiation (*10-12*). Prior to commencing the study all staff received training to become familiar with radiation control procedures, occupational risks, and learned how to minimize exposure without compromising patient care. Staff members were issued with electronic personal radiation dose monitors (PDM-112 and PDM-122, Hitachi-Aloka Medical Ltd., Japan) for the body, and thermo-stimulated luminescent ring dosimeters for extremities (Landauer, UK). Radiation contamination monitoring of staff, rooms, equipment and waste was carried out after each procedure using a scintillation monitor (Type 41/44A, Series 300 mini-monitor, ThermoScientific, USA). As ^{99m}Tc has a longer half-life (6.02 hours) than [18]F (110 min) the radioactive waste storage requirements for CLI procedures are similar to standard SLNB

procedures. The time taken for the various stages of the procedure, i.e. from induction of anesthesia to recovery, were recorded.

Histopathology. Histopathological analysis was performed as per UK National guidelines: the WLE specimen was sliced at 2 mm intervals, and representative sections of the tumor and all 6 relevant margins were selected by the pathologist, processed, paraffin wax embedded and 3 to 4 micron sections were cut and stained with hematoxylin and eosin. Microscopic margin distance measurements were performed by a Consultant breast pathologist (S.E.P.). Microscopic invasive tumor size and whole tumor size (including DCIS extending from the main invasive mass) were also measured. Positive margins were defined as invasive cancer or DCIS <1 mm from the specimen surface. The histological margin distances were reported in increments of 1 mm, but margins more than 5 mm were reported as >5 mm. The pathologist was blinded to the interpretation of the CLI images.

Image analysis. All CLI and radiography images were analyzed postoperatively in order to provide a controlled and standardized analysis environment. Measurements of the mean radiance (photons/s/cm^2/sr) were performed by drawing region-of-interests on the unprocessed CLI images. Region-of-interests were selected in areas showing increased signal intensity ('tumor') and no increased signal ('tissue background'). Tumor-to-background ratios (TBRs) were calculated. Gamma strikes were excluded from region-of-interest analysis. The tumor radiance from the sequential incised WLE images was fit to a monoexponential, to determine the radiance half-life.

Assessment of margin status on CLI was performed on the incised WLE specimen images. The analysis was done independently by two experienced breast surgeons (AP and AK), and performed prior to analysis of the radiography images to prevent potential confirmation bias from *a priori* knowledge of the radiological margin status. Prior to analysis CLI images were processed by applying a median filter (filter size range 5 – 10, filter threshold range 10 – 15) and Gaussian filter (filter width: 1, filter threshold: 0.5). A stronger Gaussian filter (filter width: 4 or 5) was applied to images with a low TBR to increase the visibility of the tumor. The preoperative diagnostic information that would typically be available to the surgeon was provided including patient age, clinical, mammographic and ultrasound tumor size, screen detected (Y/N), and histological tumor type, grade

and receptor status on core biopsy. Per patient, a color image containing information on specimen orientation was shown together with a grey-scale image and Cerenkov image. All images were displayed on a standard computer monitor (23", 1920 x 1080 pixels, 250 cd/m^2 luminance). The grey-scale image was overlaid with the Cerenkov signal to provide a fused image containing both functional and anatomical information. The leveling was set using the software's default leveling, and manually adjusted based on the surgeon's clinical judgment. Both surgeons then independently reported whether an elevated radiance from the tumor could be identified on CLI; in patients displaying an elevated tumor radiance the margin distance of the margins visible in the image was measured using the ruler function in the imaging software (Mirada XD3, Mirada Medical, Oxford, UK). The total time required to complete margin assessment was approximately 2 min per patient. As an exploratory outcome measure, tumor size was also measured. Upon completion of the measurements surgeons were asked whether, given the CLI image, they would have performed a cavity shaving had the image been available at the time of surgery. Surgeons also scored image quality on a 5-point Likert scale: 1 = very poor – image not interpretable, 2 = poor but interpretable, 3 = fair, 4 = good, 5 = very good.

Following CLI image analysis, specimen radiography image analysis was performed on a Coronis 3MP screen (20.8", 1536 x 2048 pixels, 500 cd/m^2 luminance) using standard GE PACS imaging software. Surgeons were presented with the same preoperative diagnostic information, but the images were shown in a different order to avoid potential sequential bias. The number of surgical marker clips was noted, and the reliability of specimen orientation assessed. If the orientation was considered reliable, the margin distance and tumor size on radiography was measured. Whether an additional cavity shaving would have been performed based on the radiography image was also noted.

The final histopathology results of the surgically excised tissue were not available at the time of CLI and radiography image analysis, and could therefore not bias the surgeon's assessment.

Statistics. Weighted Kappa coefficients were calculated to assess the agreement in margin distance between CLI and definitive histopathology, and to assess the inter-rater agreement between surgeons ('irr' package, version 3.2.2, R statistical software). A kappa coefficient (κ) greater than 0.75 was considered good agreement (*13*). Agreement between histological tumor size and tumor size on

CLI and radiography respectively was assessed by calculating the mean difference in tumor size ± std, and intraclass correlation coefficients (ICC) (SPSS® version 23.0; IBM, Chicago).

RESULTS

Intraoperative imaging of WLE specimens

A total of 22 patients were included in the study. The CLI results and postoperative histopathology results from the 12 patients included in the analysis dataset are shown in Table 1. The mean administered ^{18}F-FDG activity was 295 ± 18 MBq (range 259 – 325). The mean time between ^{18}F-FDG injection and WLE excision was 86 ± 26 min (range 50 – 146), and the mean time between ^{18}F-FDG injection and commencement of CLI image acquisition was 118 ± 26 min (range 88 – 180).

Tumor margin assessment was performed on incised WLE specimen images to allow for visualization of the tumor extent and to avoid image artifacts created by the monopolar diathermy. Ten of the 12 patients in the analysis dataset had elevated tumor radiance on CLI (Table 1). Mean tumor radiance and TBR in these 10 patients was 560 ± 160 photons/s/cm^2/sr (range 308 – 871) and 2.41 ± 0.54 (range 1.63 – 3.22). The half-life of the tumor radiance was 115.5 min, which is consistent with the 109.8-minute half-life of ^{18}F. This concordance supports that the detected tumor radiance is Cerenkov luminescence from ^{18}F-FDG. Mean radioactivity in the WLE specimen at the time of CLI imaging was 90 ± 48 kBq in patients with an elevated radiance; in the 2 patients without an elevated radiance radioactivity was 14 kBq and 19 kBq, respectively.

In the 10 patients with elevated tumor radiance, a total of 60 margins could be assessed histologically, 26 margins were evaluable on specimen radiography, and 15 margins were assessable on CLI. Of the 45 histological margins that were not evaluable on CLI, 40 were not in the field-of-view of the CLI image, and 5 could not be assessed due to migration of the specimen orientation ink onto the margin edge, preventing optical margin interrogation. Eighteen of the 60 histological margins were not assessable on specimen radiography due to the inability to reliably orientate the specimen on the radiography image, and 16 margins were not in the image field-of-view.

The margin distance from the 15 margins as measured on CLI and histopathology is shown in Table 1. Two margins measured between 1 and 5 mm on CLI and histopathology (Figs. 2 and 3); the remaining 13 margins were >5 mm by both modalities. There was good agreement between the histological margin distance and the margin distance on CLI as measured by both surgeon 1 and

surgeon 2, respectively (κ surgeon 1 = 0.76, κ surgeon 2 = 0.86). The agreement in margin distance between surgeons was also good (κ = 0.91).

Five margins could be assessed on both CLI and specimen radiography, and all were >5 mm on both modalities, as well as histologically. An example of a CLI, radiography and histopathology image from a patient with >5 mm resection margin widths is shown in Fig. 4.

Two patients (17%) had a positive margin on postoperative histopathological analysis; both were medial margins with DCIS <1 mm distant. These margins were not visible in the CLI image as specimen incision had only exposed the superior, inferior and posterior margins; the medial margin could therefore not be assessed.

In 8 of the 10 patients tumor size could be measured on CLI, and compared to histopathology: the agreement is shown in Table 1. In 2 patients the orientation inks prevented measurement of tumor size on CLI. Invasive tumor size showed excellent agreement; mean difference for both surgeons combined was -0.84 ± 2.8 mm. ICC was 0.84 and 0.81 for surgeons 1 and 2, respectively. Whole tumor size was underestimated on CLI; mean difference for both surgeons combined was -4.7 ± 5.0 mm. ICC was 0.65 and 0.69 for surgeons 1 and 2, respectively. Inter-rater agreement between surgeons was excellent (ICC = 0.97).

The agreement between invasive tumor size on histopathology and on radiography was good; mean difference for both surgeons combined was 1.0 ± 3.1 mm. ICC was 0.56 and 0.58 for surgeons 1 and 2, respectively. Whole tumor size was underestimated on radiography; mean difference for both surgeons combined was -5.2 ± 8.9 mm.

CLI image quality in the 10 patients with successful CLI was scored as 4.3 (range 4 – 5) by both surgeons.

Sentinel lymph node detection and ^{18}F-FDG Cerenkov lymph node imaging

SLNB was performed in 21 of the 22 patients; 1 patient underwent an ALND. SLNs were successfully identified in all 21 patients. A total of 43 SLNs were removed. The average number of SLNs per patient was 2 (range 1 – 4). Two of the 21 SLNB patients had macrometastatic SLNs.

The mean gamma probe signal of the 'hottest' SLN per patient was 4991 ± 2521 counts per second (range 8500 – 170). The mean gamma probe signal of the 'second hottest' SLN was 2505 ±

2632 counts per second (range 7368 – 50). Mean axillary background signal, measured in 13 patients, was 192 ± 70 counts per second (range 55 – 270). This signal is lower than the ^{18}F-FDG gamma probe cross-talk measured in the lead-in study (Supplemental Material), and is mainly due to the longer time between ^{18}F-FDG injection and SLNB (mean 93 ± 34 min). A total of 7 nodes had a gamma probe signal below the background signal; 6 of these were blue. This indicates the importance of using the combined technique of radioisotope and blue dye in ^{18}F-FDG CLI guided breast surgery, as low-uptake nodes may be missed if gamma probe detection is used alone.

All SLNB procedures were performed with the monopolar diathermy device and due to the observed image artifact from diathermy on CLI, the SLN images were uninterpretable.

Radiation dose to staff

A summary of the whole body effective radiation dose to primary personnel from all 22 procedures is shown in Table 2. Surgeons received the highest mean and maximum dose of 34 μSv and 74 μSv respectively. Mean duration of surgery was 39 ± 11 min (range 21 – 61) during which the surgeon was generally <0.5 meters from the patient. Mean radiation dose to the left and right hand of the surgeon was 126 ± 95 μSv (0 – 250) and 78 ± 75 μSv (0 – 200), respectively. Mean and maximum radiation dose received by the anesthetist standing at approximately 1 meter from the patient, with closer patient contact at the time of induction of anesthesia and at the end of the procedure, was 11 μSv and 18 μSv, respectively. Surgical equipment had low levels of radioactive contamination, which was undetectable 1-3 days later. No staff members were found to be contaminated with radioactivity after the procedures.

DISCUSSION

This first-in-human study evaluated the feasibility of intraoperative ^{18}F-FDG CLI for assessing tumor margin status in patients with invasive breast cancer undergoing BCS, and SLNB or ALND. Tumor margin assessment on CLI could be performed in 10 of the 12 patients in the analysis dataset, and there was strong agreement between CLI and definitive histopathology on margin width. An exploratory outcome measure assessed the correlation between tumor size on CLI and histopathology; the size on CLI and histopathology correlated well for invasive cancer, while whole tumor size (invasive with associated DCIS) was underestimated on CLI. Results from the radiation

monitoring program demonstrated that the procedure can be carried out safely while maintaining low radiation exposures to the staff involved.

In 2 patients margin assessment could not be performed because the tumors did not display elevated radiance on CLI. The absence of signal in these patients is probably due to the small tumor size, a factor known to be associated with lower ^{18}F-FDG uptake (*14*), and the late time points at which these tumors were imaged (135 min and 180 min post ^{18}F-FDG injection; the first and third longest injection-imaging time of all patients). Unsuccessful CLI imaging due to the absence of a detectable tumor signal highlights the importance of ongoing developments focused on improving detection sensitivity of camera systems to aid detection of tumors with low ^{18}F-FDG uptake including lower grade tumors and DCIS (*4*).

Since its discovery in 2009, CLI has rapidly emerged as a powerful technique for cancer imaging. CLI is readily translatable to the clinic due to existing regulatory approval and widespread availability of PET imaging agents (*15*). In contrast, targeted fluorescence imaging requires prohibitive clinical development times and capital investment for regulatory and reimbursement approval of novel imaging drugs (*16*). Three clinical pilot studies of CLI have been published to date. These have focused on the use of CLI to image radiopharmaceutical uptake in the thyroid, CLI for non-invasive detection of nodal disease, and Cerenkov luminescence endoscopy to aid detection of cancerous lesions in the GI tract (*17-19*). To our knowledge, this is the first report of intraoperative CLI. Its high-resolution, small size imaging equipment and minute-scale image acquisition (5 min) and image analysis (~2 min) times, make CLI of particular interest for image-guided surgery. The feasibility of intraoperative CLI as shown in this study in combination with the wide applicability of ^{18}F-FDG across a range of solid cancers provides a stepping stone for clinical evaluation of this technology in other cancer types.

The low radiation exposure to staff found in this study is in accordance with previously reported exposure levels from ^{18}F-FDG guided breast surgery procedures (*20,21*), and comparable to the radiation dose reported for interventional cardiology procedures (1 – 50 µSv) (*22*). The number of ^{18}F-FDG CLI-guided BCS procedures that could be performed in a routine clinical setting depends on the occupational limits on radiation exposure per country (Table 2). In the UK and US the occupational annual dose limit is 20 mSv (*23*) and 50 mSv (*24*), respectively. Good practice would dictate that the radiation exposure from a procedure should be kept As Low As Reasonable Achievable, i.e. well

below the dose limits. In practice in the UK, if a worker is likely to receive annually more than 6mSv they would be designated a classified worker, necessitating annual medical surveillance and longer term record keeping of their radiation exposure.

Image artifacts on CLI from tissue excised with the monopolar diathermy device prevented tumor margin assessment on intact WLE specimens and assessment of SLNs. Although the source of this 'false-signal' is not yet fully understood, current evidence from pre-clinical experiments points towards long-lived, thermally-induced chemiluminescence (*25*). Since the emission seems to be related to temperature, which can reach up to 250°C at the tip of the diathermy device, electrosurgical devices that operate at much lower temperatures are currently being tested (*26*). In addition to potentially facilitating margin assessment on intact WLE specimens, an advantage of low-temperature devices over monopolar diathermy is the reduced collateral tissue damage, which could also improve the accuracy of assessing tumor resection margins on histopathology (*27*).

Although CLI imaging of incised WLE specimens is feasible for assessing tumor margin status, this approach has some limitations over margin assessment on intact specimens. Firstly, migration of the wet pathology ink onto the margin edge immediately after specimen incision hinders margin interpretation with CLI. Methods to accelerate drying of inks by applying acetic acid to the painted tissue or by using fast drying inks may be solutions to this problem, but this has not been tested in this study. Secondly, in our institution specimen incision could only be performed through the posterior margin to ensure accurate postoperative histological assessment of radial margins. Consequently, only a limited number of margins could be assessed with CLI imaging per patient, and two histologically positive margins that were not visible in the CLI image were therefore missed. In order to assess more margins per patient specimen incision may be performed in multiple planes, but good communication between surgeons and pathologists is paramount in order to not compromise patient care.

A randomized, controlled, multi-center clinical study is scheduled to commence in late 2016 to evaluate the effect of intraoperative ^{18}F-FDG CLI on re-operation rate and Quality of Life in BCS (ClinicalTrials.gov identifier NCT02666079). The study will run across an anticipated 8 study sites in the UK and Germany and use the CE-marked LightPath[TM] Imaging System (Lightpoint Medical Ltd, UK). The smaller field-of-view of 6 x 6 cm and improved imaging software may provide substantial improvements in sensitivity over the investigational CLI camera used in the present study. By

analyzing larger subgroups of patients with a range of tumor types (including DCIS), size, histological grades and hormone receptor status, further insight should be obtained into which breast-cancer patient populations may most benefit from CLI-guided surgery.

CONCLUSION

Intraoperative ^{18}F-FDG CLI in BCS for invasive breast carcinoma is a promising and low-risk procedure. CLI imaging of incised WLE specimens provides high-resolution functional information that allows surgeons to accurately assess margin status with good correlation to gold-standard histopathological examination. Further work, focused on suppressing the optical signal from the monopolar diathermy device, will assist margin assessment on intact WLE specimens and potentially identification of SLN metastases on CLI. SLNB can be performed successfully during ^{18}F-FDG CLI-guided surgery by using 150 MBq ^{99m}Tc-nanocolloid and blue dye. Based on the results of this study a larger randomized controlled study is warranted to evaluate the impact of intraoperative ^{18}F-FDG on re-operation rate and Quality of Life in BCS.

DISCLOSURES

ACKNOWLEDGEMENTS

REFERENCES

1. St John ER, Al-Khudairi R, Ashrafian H, et al. Diagnostic Accuracy of Intraoperative Techniques for Margin Assessment in Breast Cancer Surgery: A Meta-analysis. *Ann Surg.* 2016.

2. Munshi A, Kakkar S, Bhutani R, Jalali R, Budrukkar A, Dinshaw KA. Factors influencing cosmetic outcome in breast conservation. *Clin Oncol (R Coll Radiol).* 2009;21:285-293.

3. Abe SE, Hill JS, Han Y, et al. Margin re-excision and local recurrence in invasive breast cancer: A cost analysis using a decision tree model. *J Surg Oncol.* 2015;112:443-448.

4. Kalinyak JE, Berg WA, Schilling K, Madsen KS, Narayanan D, Tartar M. Breast cancer detection using high-resolution breast PET compared to whole-body PET or PET/CT. *Eur J Nucl Med Mol Imaging.* 2014;41:260-275.

5. Narayanan D, Madsen KS, Kalinyak JE, Berg WA. Interpretation of positron emission mammography and MRI by experienced breast imaging radiologists: performance and observer reproducibility. *AJR Am J Roentgenol.* 2011;196:971-981.

6. Schilling K, Narayanan D, Kalinyak JE, et al. Positron emission mammography in breast cancer presurgical planning: comparisons with magnetic resonance imaging. *Eur J Nucl Med Mol Imaging.* 2011;38:23-36.

7. Das S, Thorek DL, Grimm J. Cerenkov imaging. *Adv Cancer Res.* 2014;124:213-234.

8. Grootendorst MR, Cariati M, Kothari A, Tuch DS, Purushotham A. Cerenkov luminescence imaging (CLI) for image-guided cancer surgery. *Clinical and Translational Imaging.* 2016:1-14.

9. Mansel RE, MacNeill F, Horgan K, et al. Results of a national training programme in sentinel lymph node biopsy for breast cancer. *Br J Surg.* 2013;100:654-661.

10. The ionising radiations regulations 1999. No. 3232.: Health and Safety Executive; 1999.

11. Ionising radiation (medical exposure) regulations 2000 (IRMER). Department of Health; 2012.

12. The environmental permitting (England and Wales) regulations 2010. Department for environment, food and rural affairs; 2010.

13. Khan KS, Chien PF. Evaluation of a clinical test. I: assessment of reliability. *BJOG.* 2001;108:562-567.

14. Kumar R, Chauhan A, Zhuang H, Chandra P, Schnall M, Alavi A. Clinicopathologic factors associated with false negative FDG-PET in primary breast cancer. *Breast Cancer Res Treat.* 2006;98:267-274.

15. Spinelli AE, Boschi F. Novel biomedical applications of Cerenkov radiation and radioluminescence imaging. *Phys Med.* 2015;31:120-129.

16. Agdeppa ED, Spilker ME. A review of imaging agent development. *AAPS J.* 2009;11:286-299.

17. Spinelli AE, Ferdeghini M, Cavedon C, et al. First human Cerenkography. *J Biomed Opt.* 2013;18:20502.

18. Thorek DL, Riedl CC, Grimm J. Clinical Cerenkov luminescence imaging of (18)F-FDG. *J Nucl Med.* 2014;55:95-98.

19. Hu H, Cao X, Kang F, et al. Feasibility study of novel endoscopic Cerenkov luminescence imaging system in detecting and quantifying gastrointestinal disease: first human results. *Eur Radiol.* 2015;25:1814-1822.

20. Heckathorne E, Dimock C, Dahlbom M. Radiation dose to surgical staff from positron-emitter-based localization and radiosurgery of tumors. *Health Phys.* 2008;95:220-226.

21. Andersen PA, Chakera AH, Klausen TL, et al. Radiation exposure to surgical staff during F-18-FDG-guided cancer surgery. *Eur J Nucl Med Mol Imaging.* 2008;35:624-629.

22. Duran A, Hian SK, Miller DL, Le Heron J, Padovani R, Vano E. Recommendations for occupational radiation protection in interventional cardiology. *Catheter Cardiovasc Interv.* 2013;82:29-42.

23. The 2007 recommendations of the international commission on radiological protection. ICRP publication 103. Ann. ICRP 37 (2-4). International Commission on Radiological Protection; 2007.

24. USNRC. Standards for protection against radiation. 10 CFR 20.1201.

25. Sun JS, Tsuang YH, Chen IJ, Huang WC, Hang YS, Lu FJ. An ultra-weak chemiluminescence study on oxidative stress in rabbits following acute thermal injury. *Burns.* 1998;24:225-231.

26. Loh SA, Carlson GA, Chang EI, Huang E, Palanker D, Gurtner GC. Comparative healing of surgical incisions created by the PEAK PlasmaBlade, conventional electrosurgery, and a scalpel. *Plast Reconstr Surg.* 2009;124:1849-1859.

27. Ruidiaz ME, Cortes-Mateos MJ, Sandoval S, et al. Quantitative comparison of surgical margin histology following excision with traditional electrosurgery and a low-thermal-injury dissection device. *J Surg Oncol.* 2011;104:746-754.

FIGURES WITH LEGENDS
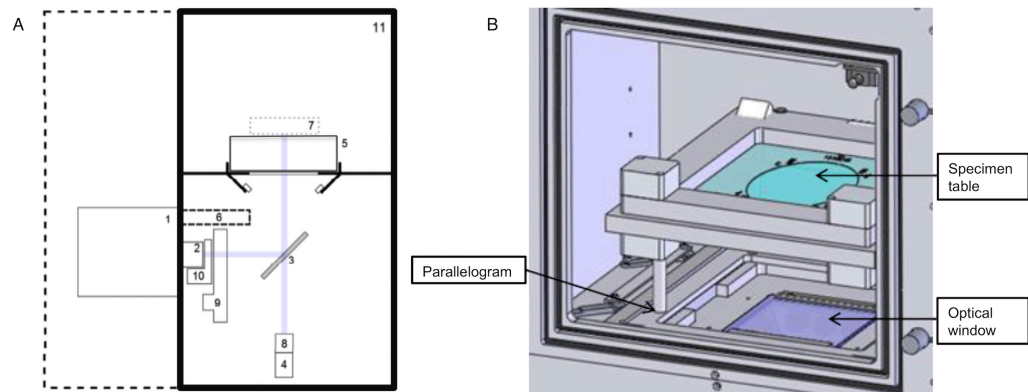
Figure 1: Investigational intraoperative CLI specimen camera. (A) Schematic diagram. Component labels: 1) EMCCD camera, 2) f/.95 lens, 3) Hinged reflex mirror, 4) Complementary metal-oxide-semiconductor reference camera, 5) Specimen table, 6) Lead radiation shielding for EMCCD camera, 7) Focal zone, 8) Fixed lens for reference camera, 9) Filter wheel, 10) LED RGB light array, 11) Specimen chamber. The purple line shows the optical paths for the EMCCD camera and the reference camera as determined by the angle of the reflex mirror. (B) Specimen chamber. The specimen table is placed on a parallelogram to facilitate accurate positioning of the specimen in the center of the image.

Figure 2: WLE specimen from a patient with a grade 3, ER-/HER2-, no special type (NST) carcinoma. (A) Cerenkov image; (B) Grey-scale photographic image overlaid with Cerenkov signal. An increased signal from the tumor is visible (white arrows); mean radiance is 871 ± 131 photons/s/cm^2/sr, mean TBR is 3.22. Both surgeon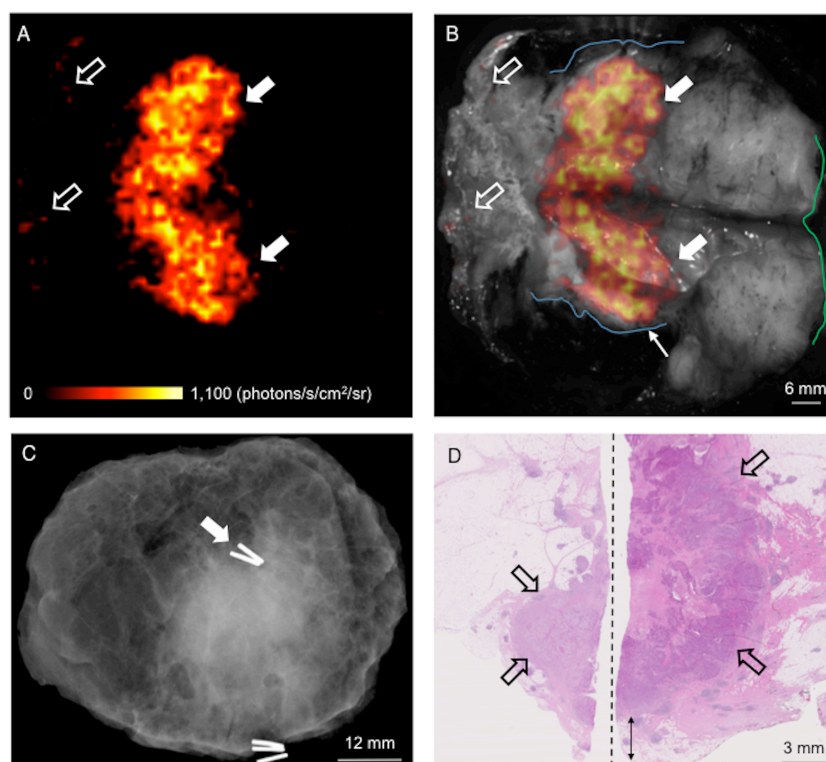s measured the posterior margin (outlined in blue) as 2 mm (small arrow); a cavity shaving would have been performed if the image had been available intraoperatively. The medial margin (outlined in green) measured >5 mm by both surgeons. Pathology ink prevented assessing the lateral margin; a phosphorescent signal is visible (open arrows). (C) Specimen radiography image. The absence of one surgical clip to mark the anterior margin, and the odd position of the superior margin clip (white arrow) prevented reliable margin assessment. (D) Combined histopathology image from two adjacent pathology slides on which the posterior margin (bottom of image) and part of the primary tumor are visible (open arrows). The distance from the posterior margin measured 3 mm microscopically (double arrow). The medial margin is > 5 mm (not present in image).

Figure 3: WLE specimen from a patient with a grade 3, ER+/HER2-, NST carcinoma admixed with high grade DCIS. (A) Cerenkov image; (B) Grey-scale photographic image overlaid with Cerenkov signal. An increased signal from the tumor is visible (white arrows); mean radiance is 406 ± 51 photons/s/cm^2/sr, mean TBR is 2.03. The posterior margin (outlined in blue) is 2 mm or 3 mm on CLI as measured by surgeons 1 and surgeon 2, respectively; both surgeons would have performed a cavity shaving. The medial margin (outlined in green) is >5 mm. (C) Specimen radiography image. All 4 radial margins were >5 mm, and both surgeons indicated they would not have performed a cavity shaving. (D) Histopathology image showing the posterior margin (left side of image) and part of the tumor (open arrows). The posterior margin was 5 mm distant histologically (double arrow).
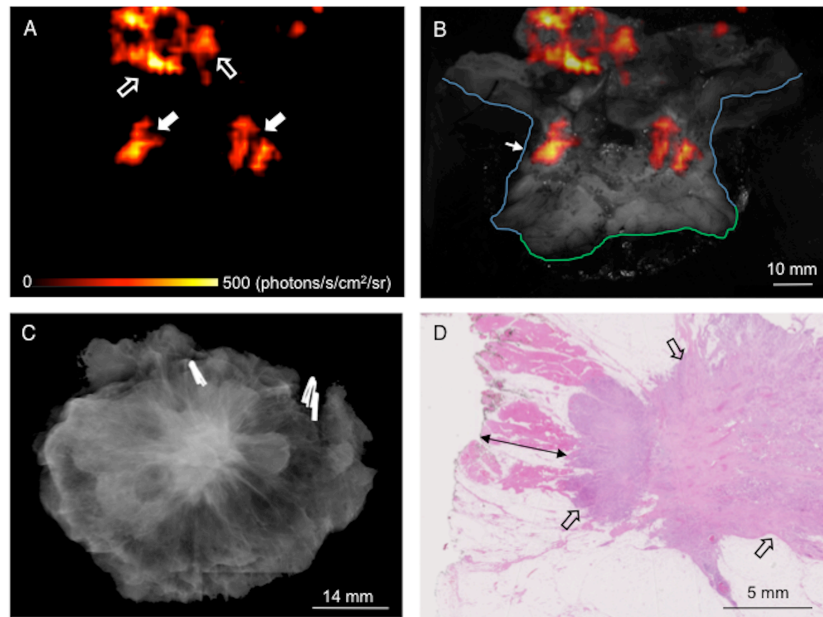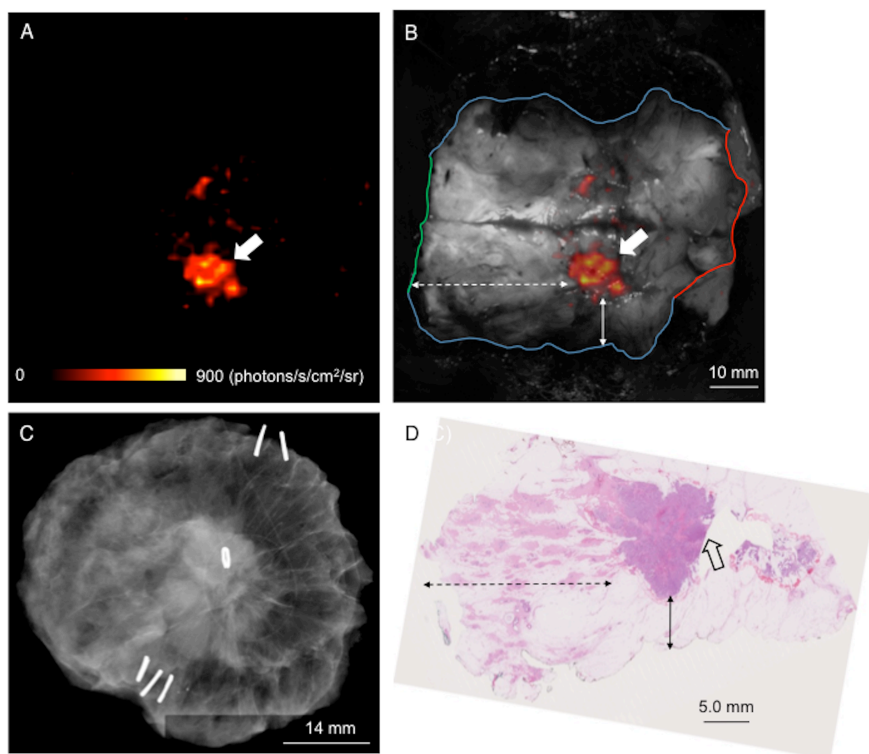
Figure 4: WLE specimen from a patient with a grade 3, ER+/HER2-, NST carcinoma admixed with high grade DCIS. (A) Cerenkov image; (B) Grey-scale photographic image overlaid with Cerenkov signal. An elevated signal (white arrow) from the tumor can be seen. Mean radiance is 637 ± 47 photons/s/cm^2/sr; mean TBR is 1.63. Both surgeons measured the posterior margin (outlined in blue), medial margin (outlined in green) and lateral margin (outlined in red) distances as >5 mm; a cavity shaving would not have been performed based on the CLI image. (C) Specimen radiography image. All 4 radial margins were >5 mm as measured by both surgeons and did not prompt resection of cavity shave margins (D) Histopathology image from large-format pathology block. The tumor is >5 mm from the posterior margin (solid arrow), medial margin (dashed arrow) and lateral margin (not visible in image).

Table 1: CLI and postoperative histopathology results for each patient in the analysis dataset.

Patient	Tumor type[1]	Histologic grade invasive (1 – 3)	ER/HER2 status of invasive cancer (Pos/Neg)[2]	Mean tumor radiance (photons/s/cm2/sr)	TBR[3]	Margin distance CLI surgeon 1, 2[7] (mm)	Margin distance histopath[5] (mm)	Tumor size CLI surgeon 1, 2[7] (mm)	Invasive tumor size histopath[8] (mm)	Whole tumor size histopath[8] (mm)
1	NST DCIS	2	Pos/Neg	-[4]	-	-	-	-	13	13
2	NST DCIS	3	Neg/Pos	453.59	2.34	6, 6	>5	*[6]	22	22
3	NST	3	Neg/Neg	871.16	3.22	2, 2 28, 30	3 >5	20, 18	20	20
4	NST DCIS	3	Neg/Neg	-[4]	-	-	-	-	14	14
5	NST DCIS	3	Pos/Neg	405.76	2.03	2, 3	5	18, 18	20	20
6	ILC	2	Pos/Neg	544.04	2.44	9, 9	>5	20, 19	22	22
7	NST	3	Pos/Neg	667.47	2.72	10, 11	>5	*[6]	25	25
8	NST DCIS	2	Pos/Neg	308.30	1.63	6, 8 16, 15	>5 >5	19,19	15	35
9	NST DCIS	3	Pos/Neg	593.93	3.08	14, 13 6, 7	>5 >5	14, 15	18	19
10	NST DCIS	3	Pos/Neg	648.29	2.46	8, 8	>5	22, 22	19	29
11	NST DCIS	2	Pos/Neg	466.03	2.54	15, 14	>5	13, 11	13	13
12	NST DCIS	3	Pos/Neg	637.08	1.63	9, 9 30, 31 22, 22	>5 >5 >5	12, 10	14	14

1. *NST: invasive carcinoma of ductal/no special type, DCIS: ductal carcinoma in situ, ILC: invasive lobular carcinoma*
2. *Pos: positive, Neg: negative*
3. *Tumor-to-background ratio*
4. *No elevated tumor radiance on CLI*
5. *Histopath: histopathology*
6. *Presence of orientation inks prevented measuring tumor size on CLI.*
7. *Margin distance and tumor size are shown for surgeon 1 and 2, respectively*
8. *The histopathological tumor size displayed in the table is the tumor size measured in the same direction as the tumor size measurement on CLI. In patient 3, 11 and 12 the largest invasive and whole tumor size (i.e. extent of DCIS and invasive cancer) was measured in a different direction, and was 32 mm, 33 mm and 25 mm, respectively*

Table 2: Measured effective radiation doses by occupation from 22 surgical procedures.

Staff Group	N[1]	Mean Effective Dose per procedure ± std (µSv)	Range (µSv)	Estimated number of procedures per individual per year[2] ICRP[3] (20 mSv annual limit)	Estimated number of procedures per individual per year[2] USNRC[4] (50 mSv annual limit)
Surgeon	46	34 ± 15	8 – 74	270	676
Anesthetist	22	11 ± 5	0 – 18	1111	2778
NM technologist	22	9 ± 4	1 – 15	1333	3333
Anesthetist assistant	22	6 ± 3	0 – 11	1818	4545
Trial Co-coordinator	21	5 ± 2	1 – 10	2000	5000
Recovery Nurse	43	4 ± 3	0 – 14	1429	3571
Scrub Nurse	22	2 ± 1	0 – 5	4000	10000
Periphery Nurse	23	1 ± 1	0 – 4	5000	12500
Research fellow	36	1 ± 2	0 – 13	1538	3846
Ward Nurse	15	0	0 – 1	20000	50000
Tissue Biobank Practitioner	14	0	0 – 1	20000	50000

1. N = number of measurements
2. Based on maximum Effective Dose per procedure per staff group
3. ICRP: International Commission on Radiological Protection
4. USNRC: United States Nuclear Regulatory Commission

SUPPLEMENTAL MATERIAL

METHODS

Standard practice requires the use of ^{99m}Tc–labeled radiopharmaceuticals for SLNB. The presence of ^{18}F-FDG in study subjects results in greater than normal background signal being detected by the handheld gamma probe used for SLNB, due to the down-scatter of 511keV Fluorine-18 (^{18}F) gamma photons into the ^{99m}Tc energy window. This cross-talk background could potentially hinder detection of low-activity SLNs. To assess the ^{18}F cross-talk and to determine the activity of ^{99m}Tc-nanocolloid required to successfully perform standard of care SLNB in patients undergoing ^{18}F-FDG CLI-guided surgery, two lead-in studies were conducted prior to commencing the CLI study.

Lead-in study I: SLNB simulations using the GAPS simulator

To determine the effects of the cross-talk background on the detectability of radioactive lymph nodes a simulation study was performed using the computerized gamma probe simulator (GAPS) (*1*). The GAPS system has previously been used in the UK national breast SLNB training program 'NEW START', and provides simulations of the radioactivity distribution and gamma probe response that allows accurate objective assessment of the surgeon's ability to localize SLNs on the surface of a manikin of the female breast and axilla.

The aim of the study was to measure the accuracy of gamma probe guided localization of nodes with varying levels of radioactivity and varying levels of cross-talk background.

The measurements were performed by two breast surgeons (AP and AK), with extensive experience of performing SLNB procedures. After one test case to familiarize the surgeons with the GAPS system, each surgeon was presented with 3 simulated SLNB cases individually. In each case the injection site, two SLNs and a spatially uniform ^{18}F background signal with Poisson distributed noise were simulated. The simulated SLN count rates ranged between 56 and 373 counts per second, and were based on a 150MBq ^{99m}Tc injection, a SLN tracer uptake ranging from 0.06% to 0.4% of the administered dose, an average SLN depth (30mm from the axillary skin surface) (*2*), and a time between tracer injection and SLN detection of 3 hours, which is common for 1-day SLNB protocols. The dose of 150MBq ^{99m}Tc is markedly higher than the standard dose of 20MBq used for 1-day SLNB procedures at Guy's Hospital. This increased dose was chosen to ensure a significant rise in SLN

count rate, thus facilitating SLN detection in a ^{18}F background, whilst keeping within a dose range that is well established (*3*). The range in SLN % tracer uptake covers the lower spectrum of tracer uptake reported in literature (*4*), thus assessing the surgeon's performance in the clinically most challenging situation of identifying SLNs with a low count rate. The ^{18}F background signal was set to a mean of 560 cps, corresponding to an ^{18}F-FDG dose of 5MBq/kg, which is the dose CLI study patients received. Calibration measurements of count rates from ^{99m}Tc and ^{18}F sources with the same gamma probe system and high-energy collimator as in the CLI study, the Europrobe 3 (Eurorad S.A., France), were used to set the count rates simulated by the GAPS system. The signal-to-noise ratio, defined as the ratio of the node count rate to the background count rate, varied from 0.67 and 0.10 in the simulations.

The surgeons performed surface scans with the GAPS gamma probe to localize as many nodes as they could, and to indicate when they thought they had localized a SLN. SLN detection was only considered successful if the surgeon indicated that they had located a node and if the position pointed at by the probe was within 10mm of the virtual node.

Lead-in study II: Gamma probe measurements in 18F-FDG PET patients

Following on from the SLNB simulations, gamma probe measurements of the axilla were performed in patients scheduled for a diagnostic ^{18}F-FDG PET scan to confirm that the simulated ^{18}F background signal corresponded to the gamma probe cross-talk found *in vivo*.

After research ethics committee approval and written informed consent was obtained, a total of 20 female patients were included at the PET Centre at St Thomas's Hospital (ISRCTN29552671). Approximately 60 minutes after receiving an intravenous injection of ^{18}F-FDG, but prior to PET imaging, the Europrobe 3 gamma probe with a high energy collimator was used to perform 10 second measurements of the lowest and highest count rates in the left and right axilla, respectively. The measurements of both axillae were performed shortly after each other (within 5 minutes) so that effects of radioactive decay between measurements were negligible. The background count rate was also measured, and the 10s count rates were averaged to give cps. The gamma probe system and configurations used to perform the ^{18}F-FDG axillary cross-talk measurements were the same as in the CLI study. The axilla was defined as the triangle between the pectoralis major, the latissimus dorsi and the edge of the breast. By placing the probe perpendicular to the skin, the entire axilla was scanned.

Patient and injection characteristics such as height, weight and injected activity were recorded. An independent samples t-test was performed to compare the highest signal in the right axilla and left axilla respectively, and a p-value of <0.05 was considered statistically significant.

RESULTS

## Lead-in study I: SLNB simulations using the GAPS simulator

The SLN detection results per surgeon can be found in Supplemental Table 1. The majority of the SLNs were accurately detected. Nodes with 0.4% (373 cps), 0.3% (280 cps) and 0.1% (93 cps) of injected activity were found by both surgeons, representing successful localization of nodes even with a signal-to-noise ratio as low as 0.17. Both surgeons missed the SLN with the lowest simulated uptake (0.06% uptake, 56 cps). The mean spatial accuracy for detected nodes was 2.6mm and 4.0mm for surgeon 1 and surgeon 2, respectively.

Lead-in study II: Gamma probe measurements in ^{18}F-FDG PET patients

The patient and ^{18}F-FDG injection characteristics can be found in Supplemental Table 2. The mean and standard deviation of the lowest and highest gamma probe signal in the right axilla was 310 ± 77 cps (range 133 – 488) and 372 ± 85 cps (range 233 – 616), respectively. The mean and standard deviation of the lowest and highest gamma probe signal in the left axilla was 299 ± 80 cps (range 161 – 553) and 359 ± 74 cps (range 236 – 582), respectively. These mean values are lower than the 560cps (5MBq/kg) used in the SLNB simulations, which were obtained from gamma probe calibration measurements with ^{18}F distributed in a water volume. The lower values probably reflect the renal excretion and non-uniform uptake *in vivo*. The highest count rate, which is clinically most relevant as it causes the greatest interference when detecting SLNs, did not differ between left and right axilla (p = 0.596), thus indicating that the cross-talk is similar in both axillae.

Based on the findings from both lead-in studies the investigators were confident that by using an increased administered activity of 150 MBq ^{99m}Tc-nanocolloid, a gamma probe collimator suitable for 511 keV energy photons and blue dye, SLNB could be performed safely and successfully, and patient recruitment to the CLI study commenced.

FIGURES FOR SUPPLEMENTAL MATERIAL
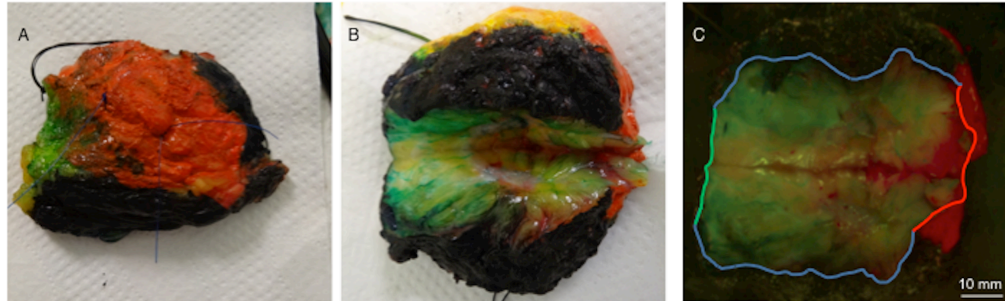
Supplemental Figure 1: Intraoperative inking and incising of WLE specimen. (A) Inks and sutures were applied to the WLE specimen to aid anatomical specimen orientation. (B) WLE specimen following initial incision through the posterior (black) margin, exposing the primary tumor and margins of excision. (C) White-light image of incised WLE specimen obtained with the CLI imaging system. Compared to (B) the specimen was further incised and opened to maximize the visibility of the posterior margin (outlined in blue), medial margin (outlined in green) and lateral margin (outlined in red). This image was used to assess tumor margins on CLI (Fig. 4B in manuscript).

TABLES FOR SUPPLEMENTAL MATERIAL

Supplemental Table 1: SLN detection results from SLNB simulations using the GAPS simulator.

Surgeon	Case	^{18}F BG[1] (cps)[2]	SLN 1 (cps)	SLN 1 detected?	Localization error SLN 1 (mm)	SLN 2 (cps)	SLN 2 detected?	Localization error SLN 2 (mm)
1	1	560	373	Y	2.50	93	Y	6.40
	2	560	280	Y	1.40	93	Y	2.43
	3	560	280	Y	0.50	56	N	-
2	1	560	373	Y	1.27	93	Y	3.99
	2	560	280	Y	3.00	93	Y	9.70
	3	560	280	Y	2.00	56	N	-

1. *BG = background signal*
2. *CPS = counts per second*

Supplemental Table 2: Patient and ^{18}F-FDG injection characteristics from the gamma probe cross-talk study in PET patients.

Characteristic	Mean (range)
Age (years)	61.5 (40-81)
Height (cm)	161 (145-178)
Weight (kg)	69.3 (45-101)
Blood glucose level (mmol/L)	5.7 (4.3-16.4)
Injected Activity (MBq)	343.8 (307.5-387.0)
Time between injection and first measurement (min)	59.7 (49-79)

REFERENCES FOR SUPPLEMENTAL MATERIAL

1. Britten A, Newey VR, Clarke R. A computerized gamma probe simulator to train surgeons in the localization of sentinel nodes. *Nucl Med Commun.* 2007;28:225-229.

2. Mathelin C, Salvador S, Huss D, Guyonnet JL. Precise localization of sentinel lymph nodes and estimation of their depth using a prototype intraoperative mini gamma-camera in patients with breast cancer. *J Nucl Med.* 2007;48:623-629.

3. Giammarile F, Alazraki N, Aarsvold JN, et al. The EANM and SNMMI practice guideline for lymphoscintigraphy and sentinel node localization in breast cancer. *Eur J Nucl Med Mol Imaging.* 2013;40:1932-1947.

4. Rubello D, Zavagno G, Bozza F, et al. Analysis of technical and clinical variables affecting sentinel node localization in patients with breast cancer after a single intradermal injection of 99mTc nanocolloidal albumin. *Nucl Med Commun.* 2004;25:1119-1124.

The use of a handheld Terahertz pulsed imaging device to differentiate benign and malignant breast tissue

Maarten R. Grootendorst[1,2]*, Anthony J. Fitzgerald[3]*, Susan G. Brouwer de Koning[1,2], Aida Santaolalla[1], Alessia Portieri[4], Mieke Van Hemelrijck[1], Matthew R. Young[2], Julie Owen[5], Massi Cariati[1,2], Michael Pepper[4,6], Vincent P. Wallace[3], Sarah E. Pinder[5], Arnie Purushotham[1,2]

*: joint first author

[1] – King's College London, Division of Cancer Studies, London, UK;

[2] – Department of Breast Surgery, Guy's and St Thomas' NHS Foundation Trust, London, UK;

[3] – School of Physics, University of Western Australia, Perth, Australia;

[4] – Teraview Ltd., Cambridge, UK;

[5] – King's College London, Division of Cancer Studies, King's Health Partners Cancer Biobank and Breast Pathology Research Group, London, UK;

[6] – London Centre for Nanotechnology, University College London, UK;

Corresponding author: Professor Arnie Purushotham, Department of Research Oncology, 3rd Floor Bermondsey Wing, Guy's Hospital, SE1 9RT, London. Email: arniepurushotham@gmail.com
Phone: +44 (0) 207 188 3027. Fax: +44 (0) 207 188 0919.

Running title (60 characters): Terahertz pulsed imaging for breast tumour margin assessment

Keywords (5): Terahertz pulsed imaging, breast-conserving surgery, tumour margins, diagnostic accuracy

Category of manuscript: Original paper

Word count: 3980

Surgical relevance (150 words)

There is a clear need for more accurate techniques to assess tumour resection margins intraoperatively in breast-conserving surgery (BCS), since approximately 10 – 30% of patients require further surgery to achieve clear margins. Due to the sensitivity of terahertz radiation to changes in water content and tissue composition, the millimetric penetration depth and submillimeter imaging resolution, Terahertz pulsed imaging (TPI) represents a promising technology for intraoperative margin assessment. A TPI handheld probe system (Teraview, Cambridge, UK) has been developed to facilitate the use of TPI to scan breast specimens *ex vivo*. In this study, we found that the TPI probe can discriminate invasive breast cancer from benign breast tissue with a high sensitivity (86%) and an encouraging degree of accuracy (75%). These promising results warrant larger studies to assess the diagnostic accuracy of TPI on different cancer types including ductal carcinoma in situ (DCIS), and its impact on re-operation rate.

Abstract

Background:

There is a clear need for developing new techniques to more accurately assess tumour resection margins during breast-conserving surgery (BCS), since currently approximately 10 – 30% of patients undergoing BCS require a re-operation to achieve clear margins. This study evaluates the diagnostic accuracy of a handheld terahertz pulsed imaging (TPI) system to discriminate benign from malignant breast tissue *ex vivo.*

Method:

A total of 46 freshly excised invasive breast cancer samples from 32 patients were scanned with a TPI handheld probe system (Teraview Ltd., UK). For each sample, detailed pathology data were obtained and correlated with the THz data. Two data reduction and classification methods were applied to the THz data to determine diagnostic accuracy: (1) heuristic parameters in combination with support vector machine (SVM) classification and (2) Gaussian wavelet deconvolution in combination with Bayesian classification.

Results:

On the full dataset accuracy, sensitivity, specificity, positive predictive value and negative predictive values were 75%, 86%, 66%, 67% and 85% for method 1, and 69%, 87%, 54%, 60%, 84% for method 2, respectively. These values increased to 88%, 87%, 96%, 98% and 61% when high percentage fibrous tissue was excluded from the analysis.

Conclusion:

The TPI handheld probe can discriminate invasive breast cancer from benign breast tissue with high sensitivity and an encouraging degree of accuracy. Accurate discrimination of cancer from tissue containing a high percentage of fibrous cells is challenging. Larger studies are warranted to assess the performance of this technique on different tumour types including DCIS, and its impact on re-operation rate.

Introduction

Breast cancer is by far the most common cancer among women worldwide[1]. A combination of an increased use of screening mammography, neoadjuvant chemotherapy and neoadjuvant endocrine therapy to downstage the size of the tumour, has significantly increased the number of patients suitable for breast-conserving surgery (BCS). Currently approximately two-thirds of newly diagnosed breast cancer patients in the United Kingdom and the United States undergo BCS as initial treatment[2, 3].

A key problem in BCS is that approximately 20% of patients in the UK require a re-operation because of close or positive tumour margins on postoperative histopathological analysis[4]. A positive margin, defined as 'tumour on ink', is associated with a 2-fold increased risk for developing local recurrence [5, 6]. Although what constitutes an adequate negative margin of excision is a subject of intense debate, the 2015 Association of Breast Surgery (ABS) of Great Britain and Ireland consensus agreement defined a clear histological margin for invasive cancer and ductal carcinoma *in situ* (DCIS) as tumour cells >1 mm from the inked resection edge[7].

Re-operations potentially have a significant impact on patients and healthcare systems. They can result in an increased rate of surgical complications[8], compromise cosmetic outcome[9], delay adjuvant therapy, and increase anxiety and stress for patients and their families. Re-excision surgery also presents a high cost burden to healthcare systems; a recent study in the United States showed that the costs for a re-excision was $4721 per patient[10].

In an attempt to decrease the re-operation rate, techniques to intraoperatively assess tumour resection margins have been developed. Clinically established techniques include specimen radiography, intraoperative ultrasound, radiofrequency spectroscopy, frozen section analysis and touch imprint cytology. However, these all have limitations in terms of diagnostic accuracy, logistical or technical demands or cost-effectiveness[11]. Emerging techniques include Raman spectroscopy[12], diffuse reflectance spectroscopy[13-17], optical coherence tomography[18-20], mass spectroscopy[21, 22], bio-impedance spectroscopy[23], and (targeted) fluorescence imaging[24]. These techniques each have unique limitations, and their potential value for improving quality of care and reducing healthcare costs is yet unknown.

Terahertz pulsed imaging (TPI) employs terahertz (THz) radiation (0.1 – 4 THz) for imaging biological tissue. Due to the millimetric penetration depth and sensitivity of THz radiation to changes in

water content and tissue composition, and the submillimeter imaging resolution of TPI, this technique holds promise for imaging cancer[25]. Work performed to date has shown the ability of TPI to discriminate malignant from benign tissue in skin, colon, oral, gastric, brain and breast cancer[26]. In 2006, Fitzgerald *et al.* were the first to demonstrate the potential of TPI for identifying breast cancer during BCS[27]. They measured 22 freshly excised breast tissue samples, and demonstrated a good correlation between tumour size and shape assessed by TPI compared with histopathology. To better understand the origin of the observed contrast on TPI, Ashworth *et al.* used THz spectroscopy and showed that the absorption coefficient and refractive index of tumour were different to that of normal breast tissue in the THz region of the spectrum[28]. Following from their initial work, Fitzgerald *et al.* imaged 51 breast samples and assessed the diagnostic accuracy of TPI by using a range of THz image parameters and classification techniques[29]. They demonstrated an accuracy, sensitivity and specificity of 92%, 90% and 92%, respectively. However, the TPI device used in their study is not suitable for intraoperative assessment of intact breast specimens due to the requirement for physical tissue disruption to obtain samples that fit the 20 x 20 mm sample holder. Importantly, the tissue samples included in their dataset had a 'homogeneous' tissue composition, i.e. contained more than 50% of a single tissue type. This is not an accurate representation of the tissue composition found at the resection border of patients with close or positive margins, as involved margins are often identified microscopically as a small number of tumour cells immersed in a 'background' of fibrous and/or adipose tissue[30]. Thus, the diagnostic accuracy of TPI for detecting tumour close or at the margin remains underdetermined.

To facilitate the use of TPI to scan tumour resection margins intraoperatively, Teraview Ltd. (Cambridge, UK) has developed a *handheld* probe system. Therefore, a single centre study was performed to evaluate the ability of the TPI handheld probe to discriminate benign from malignant breast tissue in an *ex vivo* setting. The aims of the study were to obtain a dataset that closely resembles the mixture of benign and tumour tissue commonly found at the resection border of patients with involved margins, and to evaluate the diagnostic performance of the TPI handheld probe in terms of accuracy, sensitivity, specificity and predictive values using two data analysis and classification methods.

Methods

TPI handheld probe system

The TPI handheld probe produces and detects THz pulses by guiding laser pulses from a femtosecond fibre laser (Menlo Systems GmbH, Martinsreid, Germany) down optical fibres to a photoconductive emitter and detector (Supplementary Material Figure 1**)**. The 0.1 – 1.8 THz pulses are then guided by an oscillating mirror via a monolithic silicon section onto a quartz window present at the tip of the probe, scanning 26 pixels in an area of 15 x 2 mm at a frequency of 4 Hz (Supplementary Material Figure 2). During scanning each pixel acquires THz pulses over time to form a TPI image (Figure 1).

Data acquisition

Between August 2013 and August 2014, following written, informed consent, breast tissue samples from patients who underwent BCS or mastectomy at Guy's Hospital in London were scanned with the TPI probe (REC 12-EE-0493). Within 60 minutes post-excision, BCS or mastectomy specimens were inked and sliced by an Advanced Practitioner in the King's Health Partners Cancer Biobank located adjacent to the operating theatre. Tissue samples were obtained for the study subject to the amount of tissue required for diagnostic purposes.

Prior to scanning the samples, a Tegaderm layer (3M Tegaderm Film, 3M, Bracknell, UK) was applied to the probe's quartz window, and the remainder of the probe was wrapped in a disposable protective sheath to prevent contamination from tissue. Data was collected from a 60 second water measurement to act as a control measurement and to assess the signal intensity and shape of the THz pulses emitted by the TPI system on each day of measurement. To enable consistent and controlled TPI measurements, tissue samples were placed in a standard histology cassette (Unisette^TM, Simport, Beloeil, Canada) that tightly fitted the head of the probe (Supplementary Material Figure 3). All samples were scanned for 20 seconds. Upon completion of each measurement a photograph of the sample in the cassette was taken to facilitate accurate correlation of the TPI data with the final histology slide.

After the sample was scanned, the Tegaderm layer was removed from the probe and a 60 second air measurement was performed that was used as a reference for data processing. For orientation purposes the top and the right surface of the sample were inked red and black respectively,

after which the histology cassette containing the sample was closed, and placed in formalin for 24-48 hours, processed and paraffin wax embedded. Three to 4 micron sections were then cut and stained with haematoxylin and eosin. The histology slides were digitalised, and subsequently viewed and analysed using histopathology slide viewer software (NDP.view2, Hamamatsu, UK).

TPI data processing

Each pixel of the TPI probe acquired raw THz pulses throughout the duration of the measurement. These pulses were deconvolved with the reference ("air without Tegaderm") pulses and a double Gaussian filter was applied to reduce noise. All pulses were aligned in time to compensate for small offsets in the phase of the detected pulses due to changes in the optical path length that occur when optical fibres deform slightly with movement during scanning. The deconvolved pulses – called impulse functions - of each pixel were then averaged over time, resulting in 26 impulse functions, one for each of the 26 pixels to be used for discriminating benign from malignant breast tissue (Figure 1).

Correlation of TPI with histopathology

By using the photograph depicting the imprint of the probe's scan window on the sample, and the clear contrast from the air-tissue interface and tissue composition on the TPI image, the 15 x 2 mm TPI scan area was mapped onto the digital histopathology image (Figure 1). To reduce potential inaccuracies in correlating TPI with histopathology, samples were excluded from further analysis if the number of tissue-containing pixels on TPI and histopathology differed by more than three.

Histopathological analysis and selection of TPI data

The digital histopathology slide of each sample was analysed in the viewer software by a Consultant breast histopathologist (S.E.P.), and the percentage of different tissue types, namely tumour, fibrous, and adipose, were recorded in 5% intervals. For a subset of samples an intra-rater variability analysis was performed to assess the ability of the histopathologist to consistently score the tissue samples. For this analysis, a total of 92 pixels from 7 tumour samples and 125 pixels from 7 benign samples were re-evaluated in a blinded method by the same histopathologist 8 weeks after the first analysis. Weighted kappa coefficients were calculated to assess the agreement in subgroup classification between evaluation 1 and 2 (*kappa 2* function of the 'irr' package v0.84, R statistical software v3.2.2).

A kappa coefficient (κ) greater than 0.80 was considered excellent agreement[31]. A Wilcoxon signed-rank test was performed to assess whether evaluation 1 was statistically significantly different from evaluation 2. The level of significance was defined as $p < 0.05$.

Based on the histopathological information, pixels were selected by drawing region of interests (ROIs) on the TPI images, and subsequently grouped according to tissue type and tissue percentage (Table 1). Pixels containing tumour tissue, and pixels containing pure fibrous tissue or a mixture of fibrous and adipose tissue, were divided into groups of 20% (i.e. 1 – 20%, 21 – 40%, 41 – 60%, 61 – 80%, and 81 – 100%). Pure adipose pixels were grouped separately in a "100% adipose" group.

TPI data analysis and classification

Classification of each of the selected impulse functions as malignant or benign was performed using two data analysis and classification methods: (1) heuristic parameters in combination with support vector machine (SVM) classification and (2) Gaussian wavelet deconvolution with Bayesian classification.

The impulse function of each pixel is made of values at 301 time points, and given that information from both the time and frequency domain can be used to classify pixels, it was advantageous to reduce the dimensionality of the data for classification. In method 1 this was done by using parameters that described significant features in the impulse function or spectrum. Since a large number of time points or frequency points can be selected to form a parameter, a Receiver operator Characteristics (ROC) analysis was used to select the optimal characterising parameters. The area under the ROC curve (AUROC) was used as an estimate of the classification ability of each parameter (illustrated in Supplementary Material Figure 4). AUROC analysis was performed on the data from 3 pathology groups; (i) the entire tumour and fibrous groups (excluding pure adipose), (ii) the tumour and 100% fibrous groups, and (iii) the tumour and 100% adipose groups. From this analysis the top 11 parameters were selected to be used for classification of the data in the SVM (Table 2). To avoid effects of overfitting, the parameters chosen were tested to ensure they were not correlated, eliminating any parameters with an absolute correlation coefficient of 0.7 or more. The SVM function used for classification was from the Matlab native functions *svmtrain.m* and *svmclassify.m* using a radial basis function as the kernel to form the decision boundaries (MATLAB 2013A, The Mathworks

Inc., Natick, MA, 2013). A grid search method was applied to optimise the sigma and box constraint terms as 0.3 and 1.1, respectively.

Tissue classification was also performed using Gaussian wavelet deconvolution in combination with a Bayesian classifier. In contrast to heuristic parameters, Gaussian wavelet deconvolution can be applied to the full impulse function. This method was considered a suitable approach because of the similarities between the signal features of a Gaussian function and its derivatives, and the TPI impulse functions from breast tissue. Gaussian derivatives of order 0 (normal Gaussian function), 1, 2, 3 and 4 were applied to the impulse function of each pixel. Higher order Gaussian derivatives were not used to avoid potential overfitting. The Gaussian deconvolved data were then fed into a Bayesian classification algorithm[32], and classified as tumour, fibrous or adipose, respectively. Pixels classified as adipose and fibrous were then grouped together as 'benign' in order to calculate the diagnostic performance of TPI. Similar to SVM, pixels were marked as tumour when containing any amount of cancer cells.

The SVM and Bayesian classifier were trained individually using the leave-one-out method (LOO); leaving out the pixels of a single sample to be classified, and training each classifier on the other samples. The trained classifiers were then applied to the pixels of the sample that was left out. This process was repeated for all the samples, leaving each of them out in turn, and the results compiled to give accuracy, sensitivity, specificity, positive predictive value, and negative predictive value for distinguishing malignant from benign tissue.

Results

Tissue sample characteristics and histopathology intra-rater reliability

In total, 126 samples from 106 patients were scanned; 46 samples from 32 patients met the strict criteria established to ensure accurate correlation of TPI with histology, i.e. a photograph was available of the sample in the histology cassette, and the number of tissue containing pixels on TPI and histopathology differed by 3 or less. These samples were included for analysis. Of these, 20 samples contained tumour; 16 invasive ductal/no special type (NST) carcinoma, 2 NST admixed with DCIS, 2 invasive lobular carcinoma (ILC). Twenty-two samples contained pure fibrous tissue or a mixture of fibrous and adipose tissue, and 4 samples contained pure adipose tissue. The total number of pixels for analysis was 257; the breakdown in terms of tissue composition is given in Table 1.

The intra-rater reliability analysis showed excellent agreement in cell density subgroup classification between histopathological evaluation 1 and evaluation 2 (κ = 0.89) (p = NS). This confirmed that the established subgroups reliably reflected the tissue composition of the samples, and thus could be used to evaluate the performance of the TPI handheld probe system for different tissue groups.

Heuristic parameters and SVM classification

A total of 11 parameters were selected based on the AUROC analysis: 10 time domain parameters and 1 frequency parameter (Table 2) (Supplementary Material Figure 5). Most of the time domain parameters capture the area around the minimum amplitude of the pulse, and the return to baseline after the minimum. P1 – P7 were selected based on their overall ability of discriminating tumour from fibrous tissue with adipose, while P8 – P11 were specifically selected to enhance the TPI probe's ability to discriminate tumour from pure fibrous tissue. All 11 parameters showed strong discriminative power to distinguish tumour from pure adipose tissue (mean AUROC = 0.97, range 0.84 – 1.0).

The SVM classification results of the individual parameters, and the combination of parameters that performed best in terms of accuracy, may be found in Table 3. Overall, the combination of P1 and P6 provided the best performance with an accuracy, sensitivity, specificity, positive predictive value (PPV) and negative predictive value (NPV) of 75%, 86%, 66%, 67% and 85%, respectively. These values were obtained as a result of 16 of the 115 tumour pixels being misclassified as benign; 48 of the 142 benign pixels were misclassified as tumour. All misclassified tumour pixels had a tumour content ≤60%. Of the 48 misclassified benign pixels, 46 were fibrous pixels containing 81 – 100% fibrous cells; only 2 of the 1 – 80% fibrous pixels were misclassified as tumour, and all 26 pure adipose pixels were correctly identified as benign. The two-dimensional parametric plot of P1 and P6 showed very little differences between tumour and high percentage fibrous tissue (Figure 2A); this provides an explanation for why most of the SVM classification errors occurred in these two tissue groups (Figure 2B). Pixels with a high adipose content (1 – 80% fibrous pixels and pure adipose pixels) were generally clearly different from pixels containing a high percentage of fibrous tissue (81 – 100%) and cancer (Figure 2A). The accuracy, sensitivity, specificity, PPV and NPV for discriminating 1 – 80% fibrous and pure adipose tissue from tumour (i.e. excluding the predominantly fibrous group with 81 – 100% purity) was 87%, 86%, 96%, 98%, 59%, respectively.

Gaussian wavelet deconvolution and Bayesian classification

The accuracy, sensitivity, specificity, PPV and NPV of Gaussian wavelet deconvolution and Bayesian classification was 69%, 87%, 54%, 60%, 84%, respectively (Table 3). Of the 115 tumour pixels, 15 were misclassified as benign. All misclassified pixels contained ≤60% tumour cells. Sixty-six of the 142 benign pixels were wrongly classified as tumour; 64 of these were 81 – 100% fibrous pixels, only two 1 – 80% fibrous pixels were misclassified. All pure adipose pixels were correctly classified. The accuracy, sensitivity, specificity, PPV and NPV of the handheld probe for discriminating 1 – 80% fibrous and pure adipose from tumour was 88%, 87%, 96%, 98% and 61%, respectively.

Discussion

This study has evaluated the performance of a TPI handheld probe system to discriminate breast cancer from benign breast tissue in an *ex vivo* setting. A total of 257 pixels acquired from scanning 46 breast tissue samples were included for analysis. The tumour samples predominantly contained low-to-moderate tumour cell percentages, resembling the tissue composition found at the resection border of breast specimens from patients with positive margins after BCS. Two data analysis and classification methods were assessed: (1) heuristic parameters in combination with SVM classification and (2) Gaussian wavelet deconvolution with Bayesian classification. On the full dataset the former provided the best performance in terms of accuracy (75%). Both methods had excellent sensitivity (86% and 87%, respectively) and thus show promise for identifying tumour cells close to or at the resection margins, allowing immediate further excision of appropriate margins and reducing subsequent second operations/re-excision rates if the TPI handheld probe had been used intraoperatively. Specificity however, was 66% and 54% for SVM and Bayesian respectively; for both methods the lower specificity was due to pixels with 81 – 100% fibrous tissue that were wrongly classified as tumour. The accuracy, sensitivity and specificity increased to 88%, 87%, and 96% respectively after excluding the 81 – 100% fibrous tissue from the classification results.

The reported pooled sensitivity and specificity of the established techniques to intraoperatively assess tumour margins during BCS are 53% (95% CI 45 – 61%) and 84% (95% CI 77 – 89%) for specimen radiography, 59% (95% CI 36 – 79%) and 81% (95% CI 66 – 91%) for ultrasound imaging, 71% and 68% for radiofrequency spectroscopy, 86% (95% CI 78 – 91%) and 96% (95% CI 92 – 98%) for frozen section analysis, and 91% (95% IC 71 – 97%) and 95% (95% IC 90 – 98%) for imprint

cytology, respectively[11]. Thus, based on the results of the present study, the TPI handheld probe appears to perform similarly or better in terms of sensitivity, while the performance in terms of specificity is lower. Compared to specimen radiography and ultrasound, which are also imaging technologies, TPI has the potential advantage that image interpretation is not needed as the device can provide a binary read-out (tumour or no tumour). This may overcome the need for the training required for obtaining ultrasound accreditation[33]. Potential advantages over the histopathological techniques frozen section analysis and imprint cytology are the fact that TPI is non-invasive (i.e. physical tissue disruption is not required), it does not require an on-site cytologist or histopathologist, and allows for assessing a larger tissue surface.

Results published to date on the diagnostic performance of emerging techniques for margin assessment have shown a sensitivity and specificity of 92% (95% CI 86 – 96%) and 97% (95% CI 93 – 98%) for Raman spectroscopy[12], 67 – 85% and 67 – 96% for diffuse reflectance spectroscopy[13-17], 60 – 100% and 69 – 92% for optical coherence tomography[18-20], 93 – 100% and 91.9 – 100% for mass spectroscopy[21, 22], and 87% and 76% for bioimpedance spectroscopy[23], respectively. Although the performance of the handheld probe in this study is somewhat lower than some of the other emerging techniques, TPI uses a different region of the electromagnetic spectrum and thus provides complementary information. It is possible that combinations of technologies could significantly improve the overall accuracy of identifying involved margins.

Several papers have reported on the ability of TPI to discriminate freshly excised benign from malignant breast tissue[27, 29, 34, 35]. Ashworth *et al*. performed a small pilot study using a prototype version of the TPI handheld system[34]; all other studies were conducted with systems not suited for intraoperative imaging of WLE specimens. Similar to the present results, Ashworth *et al*. found that THz impulse functions from fibrous tissue and breast cancer had strong similarities, while impulse functions from adipose tissue had clearly different features. However, none of the TPI studies in breast cancer published to date have used a dataset representative of the tissue composition found at the resection border of patients with positive margins, as all tumour samples included for analysis contained >50% tumour cells. Thus, the results in our study are the first that can be used to derive insight in the potential benefits of TPI in enabling more accurate and complete tumour resection in BCS.

The accuracy, sensitivity and specificity of the TPI probe for discriminating tumour from mixed fibrous and adipose tissue, and pure adipose tissue, was 87%, 86%, and 96% for SVM, and 88%, 87% and 96% for Bayesian, respectively. Discrimination of these tissue types is most relevant clinically, as the incidence of breast cancer is higher in older women, who are likely to have fatty or mixed fibrous and fatty breasts compared to younger women who may have more dense breasts primarily composed of fibrous tissue[36].

While the results of this feasibility study are promising, two limitations were noted. Firstly, the 0.6 mm pixel distance used for correlating TPI and histopathology was based on a linear movement of the THz pulse beam across the 15 x 2 mm scan area. However, in practice the THz beam moves faster in the centre of the scan window and slows down upon reaching the top and bottom boundary, resulting in a larger distance between pixels located in the centre compared to the edges. This introduces a degree of inaccuracy, which was not accounted for in this study. Secondly, the current dataset does not contain THz pulses from cases of pure DCIS. These samples could not be assessed, as DCIS is generally non-palpable and particularly problematic to sample in the fresh state without impairment of gold-standard histological assessment. However, since DCIS is often the cause of the clinical recommendation for re-operations in BCS, it is of key importance to assess the sensitivity of the TPI handheld probe for detecting DCIS. Based on the results of this feasibility study, a study will be performed in which TPI data will be acquired on tissue specimens with DCIS, to determine the ability of TPI to accurately detect DCIS.

In conclusion, the results of this study show that the TPI handheld probe can discriminate invasive breast cancer from benign breast tissue with a high sensitivity and an encouraging degree of accuracy. The main challenge for TPI is accurate discrimination of cancer from tissue containing a high percentage of fibrous stroma due to the similarities in the THz pulse between these two types of tissue. Larger studies are warranted to assess the performance of this technique on different tumour types including DCIS, and its impact on re-operation rate.

Disclosures

Acknowledgments

References

1.   Ferlay J., Soerjomataram I., Ervik M., Dikshit R., Eser S., Mathers C*., et al.* GLOBOCAN 2012 v1.0, Cancer Incidence and Mortality Worldwide: IARC CancerBase No. 11. In: International Agency for Research on Cancer. World Health Organisation; 2012.

2.   Jeevan R, Browne J, Van der Meulen J, Pereira J, Caddy C, Sheppard C*, et al.* First Annual Report of the National Mastectomy and Breast Reconstruction Audit 2008; 2008.

3.   McGuire KP, Santillan AA, Kaur P, Meade T, Parbhoo J, Mathias M*, et al.* Are mastectomies on the rise? A 13-year trend analysis of the selection of mastectomy versus breast conservation therapy in 5865 patients. *Ann Surg Oncol* 2009;**16**(10): 2682-90.

4.   Jeevan R, Cromwell DA, Trivella M, Lawrence G, Kearins O, Pereira J*, et al.* Reoperation rates after breast conserving surgery for breast cancer among women in England: retrospective study of hospital episode statistics. *BMJ* 2012;**345**: e4505.

5.   Houssami N, Macaskill P, Marinovich ML, Morrow M. The association of surgical margins and local recurrence in women with early-stage invasive breast cancer treated with breast-conserving therapy: a meta-analysis. *Ann Surg Oncol* 2014;**21**(3): 717-30.

6.   Dunne C, Burke JP, Morrow M, Kell MR. Effect of margin status on local recurrence after breast conservation and radiation therapy for ductal carcinoma in situ. *J Clin Oncol* 2009;**27**(10): 1615-20.

7.   Consensus on margins in breast conservation. In: Association of Breast Surgery Annual Conference; 2015; Bournemouth: Association of Breast Surgery (ABS); 2015.

8.   Xue DQ, Qian C, Yang L, Wang XF. Risk factors for surgical site infections after breast surgery: a systematic review and meta-analysis. *Eur J Surg Oncol* 2012;**38**(5): 375-81.

9.   Heil J, Breitkreuz K, Golatta M, Czink E, Dahlkamp J, Rom J*, et al.* Do reexcisions impair aesthetic outcome in breast conservation surgery? Exploratory analysis of a prospective cohort study. *Ann Surg Oncol* 2012;**19**(2): 541-7.

10.   Arora D, Hasan S, Male E, Abid R, Ord C, Dauway E*, et al.* Cost analysis of re-excisions for breast conserving surgery in Central Texas. In: ASCO Annual Meeting; 2015; 2015.

11.   St John ER, Al-Khudairi R, Ashrafian H, Athanasiou T, Takats Z, Hadjiminas DJ*, et al.* Diagnostic Accuracy of Intraoperative Techniques for Margin Assessment in Breast Cancer Surgery: A Meta-analysis. *Ann Surg* 2016.

12. Deng K, Zhu C, Ma X, Jia H, Wei Z, Xiao Y*, et al.* Rapid Discrimination of Malignant Breast Lesions from Normal Tissues Utilizing Raman Spectroscopy System: A Systematic Review and Meta-Analysis of In Vitro Studies. *PLoS One* 2016;**11**(7): e0159860.

13. Brown JQ, Bydlon TM, Kennedy SA, Caldwell ML, Gallagher JE, Junker M*, et al.* Optical spectral surveillance of breast tissue landscapes for detection of residual disease in breast tumor margins. *PLoS ONE [Electronic Resource]* 2013;**8**(7): e69906.

14. Wilke LG, Brown JQ, Bydlon TM, Kennedy SA, Richards LM, Junker MK*, et al.* Rapid noninvasive optical imaging of tissue composition in breast tumor margins. *Am J Surg* 2009;**198**(4): 566-74.

15. Keller MD, Majumder SK, Kelley MC, Meszoely IM, Boulos FI, Olivares GM*, et al.* Autofluorescence and diffuse reflectance spectroscopy and spectral imaging for breast surgical margin analysis. *Lasers Surg Med* 2010;**42**(1): 15-23.

16. Laughney AM, Krishnaswamy V, Rizzo EJ, Schwab MC, Barth RJ, Jr., Cuccia DJ*, et al.* Spectral discrimination of breast pathologies in situ using spatial frequency domain imaging. *Breast Cancer Research* 2013;**15**(4): R61.

17. Bigio IJ, Bown SG, Briggs G, Kelley C, Lakhani S, Pickard D*, et al.* Diagnosis of breast cancer using elastic-scattering spectroscopy: preliminary clinical results. *J Biomed Opt* 2000;**5**(2): 221-8.

18. Zysk AM, Chen K, Gabrielson E, Tafra L, May Gonzalez EA, Canner JK*, et al.* Intraoperative Assessment of Final Margins with a Handheld Optical Imaging Probe During Breast-Conserving Surgery May Reduce the Reoperation Rate: Results of a Multicenter Study. *Ann Surg Oncol* 2015;**22**(10): 3356-62.

19. Nguyen FT, Zysk AM, Chaney EJ, Kotynek JG, Oliphant UJ, Bellafiore FJ*, et al.* Intraoperative Evaluation of Breast Tumor Margins with Optical Coherence Tomography. *Cancer Research* 2009;**69**(22): 8790-96.

20. Erickson-Bhatt SJ, Nolan RM, Shemonski ND, Adie SG, Putney J, Darga D*, et al.* Real-time Imaging of the Resection Bed Using a Handheld Probe to Reduce Incidence of Microscopic Positive Margins in Cancer Surgery. *Cancer Res* 2015;**75**(18): 3706-12.

21. Balog J, Sasi-Szabó L, Kinross J, Lewis MR, Muirhead LJ, Veselkov K*, et al.* Intraoperative Tissue Identification Using Rapid Evaporative Ionization Mass Spectrometry. *Science Translational Medicine* 2013;**5**(194): 194ra93.

22.   St John ER, Al-Khudairi R, Balog J, Rossi M, Gildea L, Speller A*, et al.* Rapid evaporative ionisation mass spectrometry towards real time intraoperative oncological margin status determination in breast conserving surgery. In: 38th Annual San Antonio Breast Cancer Symposium. San Antonio; 2016.

23.   Dixon JM, Renshaw L, Young O, Kulkarni D, Saleem T, Sarfaty M*, et al.* Intra-operative assessment of excised breast tumour margins using ClearEdge imaging device. *European Journal of Surgical Oncology (EJSO)*.

24.   Vahrmeijer AL, Hutteman M, van der Vorst JR, van de Velde CJ, Frangioni JV. Image-guided cancer surgery using near-infrared fluorescence. *Nat Rev Clin Oncol* 2013;**10**(9): 507-18.

25.   Yu C, Fan S, Sun Y, Pickwell-Macpherson E. The potential of terahertz imaging for cancer diagnosis: A review of investigations to date. *Quant Imaging Med Surg* 2012;**2**(1): 33-45.

26.   Fan S, He Y, Ung BS, Pickwell-MacPherson E. The growth of biomedical terahertz research. *Journal of Physics D: Applied Physics* 2014;**47**(37).

27.   Fitzgerald AJ, Wallace VP, Jimenez-Linan M, Bobrow L, Pye RJ, Purushotham AD*, et al.* Terahertz pulsed imaging of human breast tumors. *Radiology* 2006;**239**(2): 533-40.

28.   Ashworth PC, Pickwell-MacPherson E, Provenzano E, Pinder SE, Purushotham AD, Pepper M*, et al.* Terahertz pulsed spectroscopy of freshly excised human breast cancer. *Opt Express* 2009;**17**(15): 12444-54.

29.   Fitzgerald AJ, Pinder S, Purushotham AD, O'Kelly P, Ashworth PC, Wallace VP. Classification of terahertz-pulsed imaging data from excised breast tissue. *J Biomed Opt* 2012;**17**(1): 016005.

30.   Park CC, Mitsumori M, Nixon A, Recht A, Connolly J, Gelman R*, et al.* Outcome at 8 years after breast-conserving surgery and radiation therapy for invasive breast cancer: influence of margin status and systemic therapy on local recurrence. *J Clin Oncol* 2000;**18**(8): 1668-75.

31.   Khan KS, Chien PF. Evaluation of a clinical test. I: assessment of reliability. *BJOG* 2001;**108**(6): 562-7.

32.   Shalabi A, Inoue M, Watkins J, De Rinaldis E, Coolen AC. Bayesian clinical classification from high-dimensional data: Signatures versus variability. *Stat Methods Med Res* 2016.

33.   Ahmed M, Rubio IT, Klaase JM, Douek M. Surgical treatment of nonpalpable primary invasive and in situ breast cancer. *Nat Rev Clin Oncol* 2015;**12**(11): 645-63.

34.   Ashworth PC, O'Kelly P, Purushotham AD, Pinder SE, Kontos M, Pepper M*, et al.* An intra-operative THz probe for use during the surgical removal of breast tumors. In: Infrared, Millimeter and Terahertz Waves, 2008 IRMMW-THz 2008 33rd International Conference on; 2008 15-19 Sept. 2008; 2008. p. 1-3.

35.   Truong BC, Tuan HD, Fitzgerald AJ, Wallace VP, Nguyen HT. A dielectric model of human breast tissue in terahertz regime. *IEEE Trans Biomed Eng* 2015;**62**(2): 699-707.

36.   Stomper PC, D'Souza DJ, DiNitto PA, Arredondo MA. Analysis of parenchymal density on mammograms in 1353 women 25-79 years old. *AJR Am J Roentgenol* 1996;**167**(5): 1261-5.
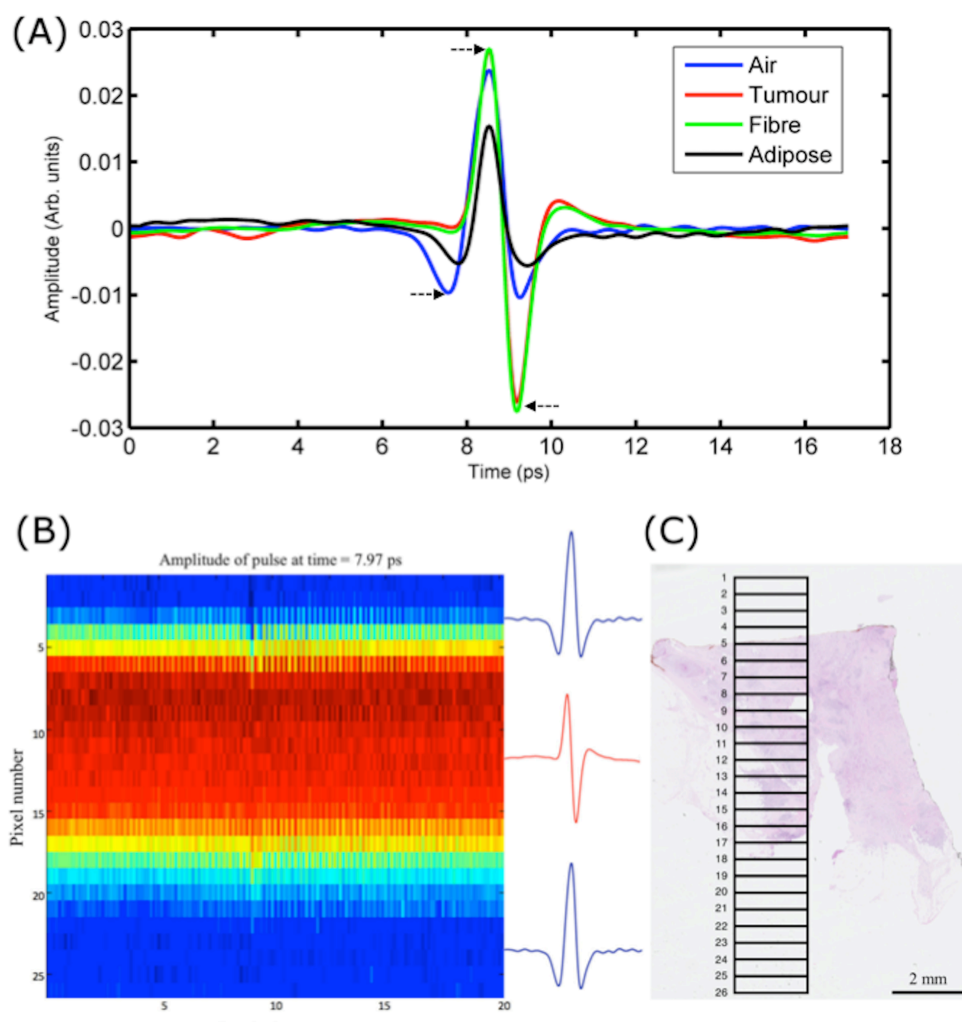
Figures with legends

Figure 1: Correlating TPI with histopathology. (A) Typical impulse function from breast tissue containing a high percentage of tumour, fibrous, and adipose cells, and air, respectively. Clear differences are seen between the impulse functions from air and from tissue, and between adipose and tumour/fibrous tissue, especially at time points t = 7.97 ps, t = 8.93 ps, and t = 9.67 ps (black arrows). (B) TPI image from sample based on the amplitude of the impulse function at t = 7.97ps. A clear contrast can be seen at the air-tissue interface at pixel 5 and pixel 17. Note an 'edge effect' at these interfaces, causing a distortion in the impulse functions of these pixels. (C) Digital histopathology slide of the same tissue sample. By using the photograph of the sample in combination with the air-tissue interface visible in the TPI image, the TPI 15 x 2 mm scan area can be accurately mapped onto the histopathology slide (black rectangle). The pixels are displayed as intermittent horizontal lines at 0.6 mm distance in the scan window. Pixel 5 – 17 contain invasive ductal/no special type (NST) carcinoma; the percentage of tumour cells in each of these pixel areas ranges between 5 – 10%. The tissue immedialtely surrounding the tumour cells (background) is composed of fibrous tissue, whilst fatty adipose tissue is seen inferiorly.
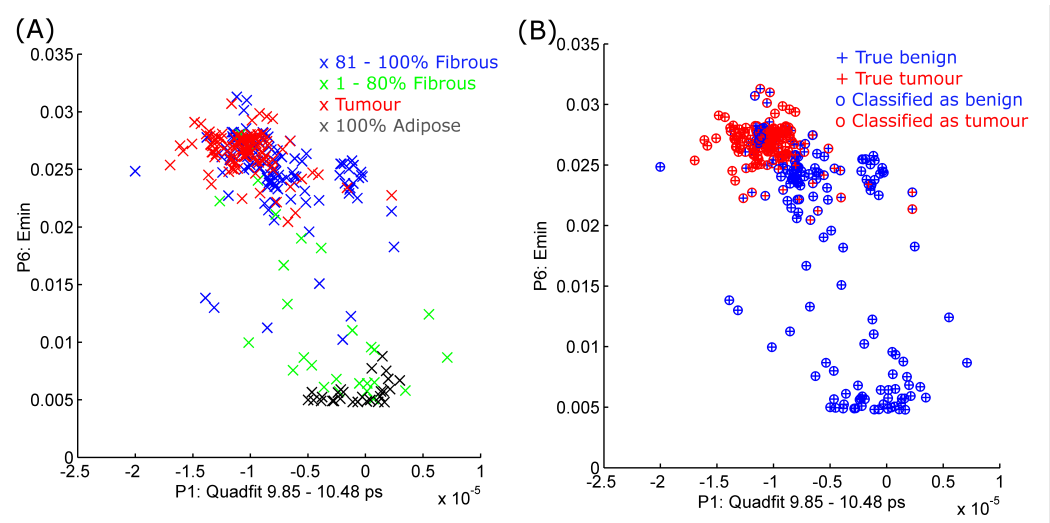
Figure 2: Two-dimensional parametric plot (A) and SVM classification results (B) for the combination of parameters P1 and P6 that performed best in terms of accuracy.

Tables with legends

Table 1: Pixel characteristics analysis dataset. A total of 257 pixels were included in the TPI dataset: 115 tumour pixels, 116 fibrous pixels and 26 pure adipose pixels. The tumour pixels predominantly consisted of invasive ductal/no special type carcinoma (N = 92) and invasive lobular carcinoma (N = 19). Most of the tumour pixels contained a low to moderate percentage of tumour cells ranging between 1 – 60% (N = 98). Almost all tumour cells had a background of pure fibrous tissue; only 5 had a background containing a mix of fibrous and adipose. Most of the fibrous pixels had a high percentage of fibrous cells ranging between 81 – 100% (N = 91). Only 26 of the 257 pixels consisted of pure adipose tissue.

Tissue percentage groups (%)	Tumour					Fibrous		Adipose
	NST	NST + DCIS	ILC	No. of pixels	BG	No. of pixels	BG	No. of pixels
81 – 100	3	1		4	F	91	A	26[1]
61 – 80	11	2		13	F	2	A	
41 – 60	22		6	28	F	7	A	
21 – 40	33	1	12	46	F: 43 F/A: 3	3	A	
1 – 20	23		1	24	F: 22 F/A: 2	13	A	
No. of pixels	92	4	19	115		116		26

NST = invasive ductal/no special type carcinoma; DCIS = ductal carcinoma *in situ*; ILC = invasive lobular carcinoma; BG = background tissue. In our dataset the background consisted of fibrous tissue (F), adipose tissue (A), or a mixture of fibrous and adipose tissue (F/A).
1.   These pixels contained 100% adipose tissue.

Table 2: Overview of selected time domain and frequency domain parameters and their AUROC values.

Parameter	Definition	AUROC value (cell density group)[1]
P1	Quadratic fit 9.85 – 10.48 ps	0.76 (All T and F)
P2	Linear fit 9.42 – 9.67 ps	0.73 (All T and F)
P3	Amplitude at t = 9.42 ps	0.72 (All T and F)
P4	Integral 9.14 – 9.65 ps	0.72 (All T and F)
P5	Peak to peak (Emax minus Emin)	0.71 (All T and F)
P6	Emin (minimum amplitude)	0.70 (All T and F)
P7	Amplitude at t = 10.05 ps	0.70 (All T and F)
P8	Quadratic fit 8.26 – 8.79 ps	0.74 (1 – 20% T, 100% F)
P9	Integral 7.47 – 9.62 ps	0.83 (41 – 60% T, 100% F)
P10	Emax (maximum amplitude)	0.73 (81 – 100% T, 100% F)
P11	Power in spectrum at frequency = 1.11 THz	0.82 (61 – 80% T, 100% F)

1. T = tumour, F = pure fibrous tissue or a mixture of fibrous and adipose tissue, 100% F = pure fibrous tissue only

Table 3: Performance of heuristic parameters with SVM classification, and wavelet deconvolution with Bayesian classification. SVM classification results are shown for individual parameters and parameter combinations that performed best in terms of accuracy. The best individual parameter and parameter combination is underlined.

| Parameters	Accuracy (%)	Sensitivity (%)	Specificity (%)	PPV[1] (%)	NPV[2] (%)
P1	73	87	62	65	85
P2	72	81	64	65	81
P3	70	77	65	64	78
P4	72	77	69	67	78
P5	72	92	56	63	90
P6	69	86	56	61	83
P7	69	87	54	61	84
P8	68	90	49	59	86
P9	56	69	46	51	64
P10	68	93	48	59	89
P11	56	56	57	51	61
P1 and P6	75	86	66	67	85
P1, P6 and P11	71	72	70	66	76
P1, P6, P9 and P11	67	56	75	65	68
Gaussian wavelets	69	87	54	60	84

1. PPV = Positive predictive value
2. NPV = Negative predictive value
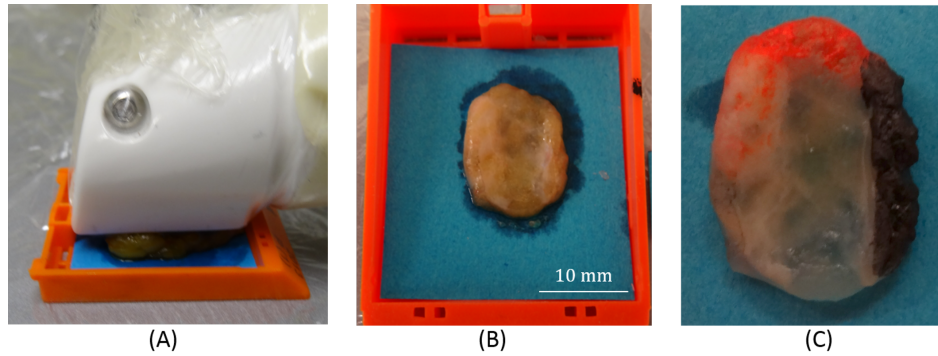
Supplementary Material

Supplementary figures with legends
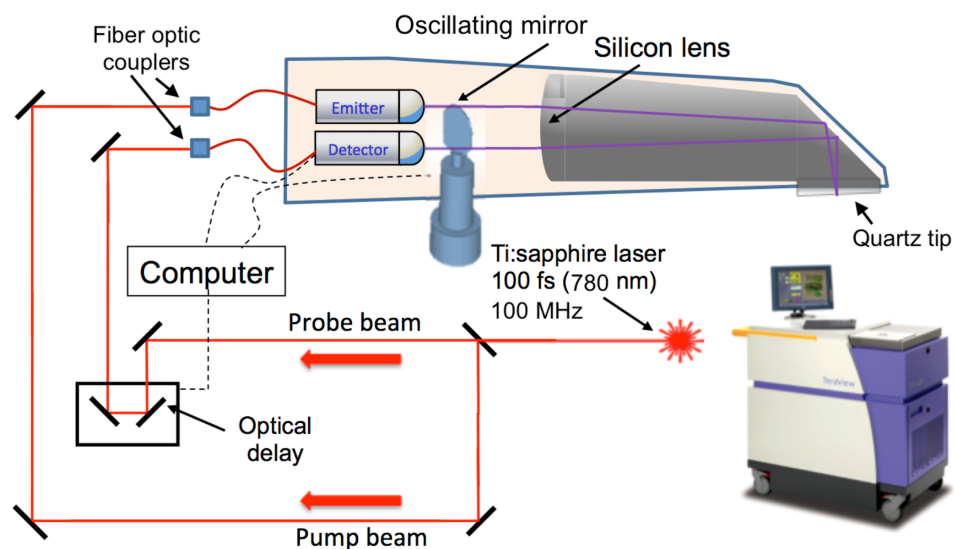
Supplementary Material Figure 1: Schematic illustration of TPI handheld probe system. The emitted laser pulses are split into a "pump beam" and a "probe beam". The pump beam is guided through the optical fibres in the umbilical cord, and subsequently incident on the photoconductive emitter to produce THz pulses. The probe beam is guided onto the photoconductive detector to detect the THz pulses reflected from the tissue sample. By altering the path length of the probe beam, the time of arrival at the detector in respect to the incident THz pulse can be changed, thus sampling the THz pulse in the time domain.
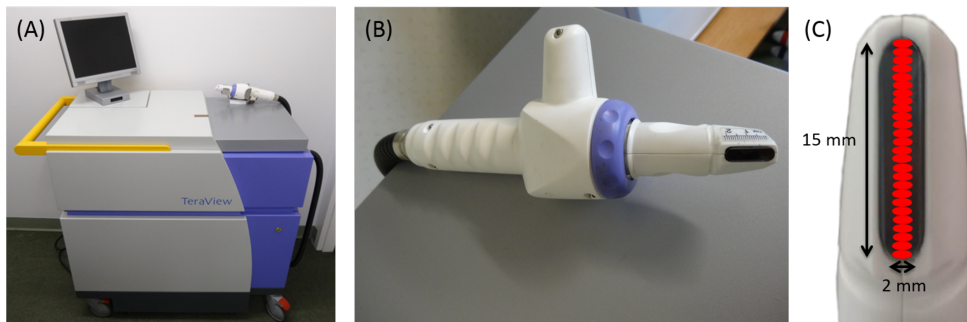
Supplementary Material Figure 2: TPI handheld probe system. (A) Main unit with computer monitor, handheld imaging probe and black umbilical cord (visible on the right). (B) Close up of the handheld imaging probe. (C) Close up of the head of the imaging probe showing the black quartz window. The probe scans an area of 15 x 2 mm, and acquires data from 26 pixels (red).

(A) (B) (C)

Supplementary Material Figure 3: TPI measurement of tissue sample. (A) TPI handheld probe measurement of tissue sample positioned in histology cassette. Note that the head of the imaging probe tightly fits in the cassette, which facilitates applying a consistent pressure throughout the measurement, while preventing displacement of the probe. (B) Photograph of the tissue sample obtained after the sample was scanned. The imprint of the scan window on the sample is clearly visible. This photograph was used to facilitate accurate correlation of TPI data with histopathology. (C) Photograph of tissue sample after it was inked. Inking was performed to enable spatial orienation of the sample when analysed microscopically by the pathologist.
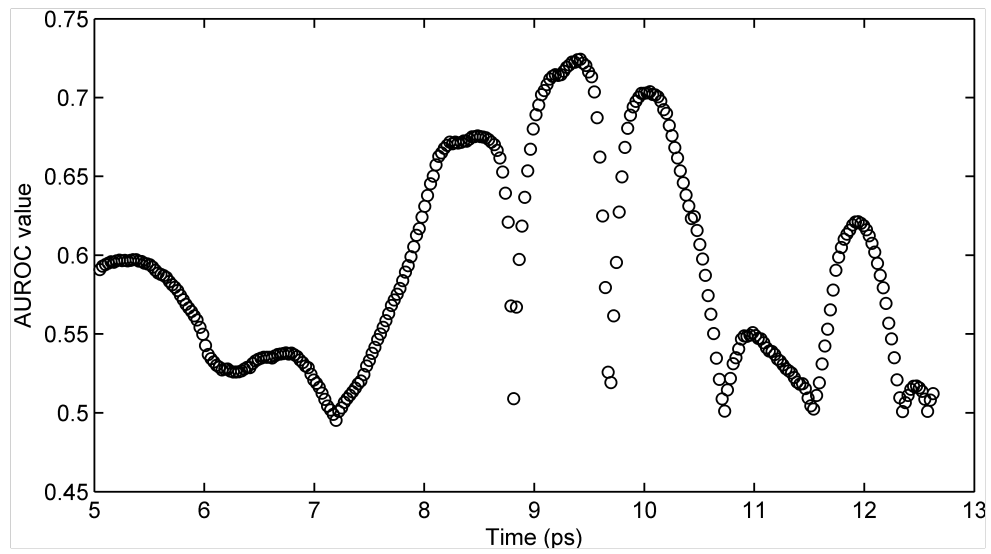
Supplementary Material Figure 4: AUROC analysis to evaluate the discriminative power of the amplitude parameter for time indices 5.0 – 12.6 ps. The highest AUROC values of 0.72 and 0.70 were found at t = 9.42 ps and t = 10.05 ps respectively, and these two parameters were therefore selected for tissue classification with SVM.

Supplementary Material Figure 5: Visualisation of the selected parameters used in SVM classification.

Each parameter is displayed in red.

P1: Quadratic fit 9.85 - 10.48 ps

P2: Linear fit 9.42 - 9.67 ps

P3: Amplitude at t = 9.42 ps

P4: Integral 9.14 - 9.65 ps

P5: Peak to peak (Emax - Emin)

P6: Emin (minimum amplitude)

P7: Amplitude at t = 10.05 ps

P8: Quadratic fit 8.26 - 8.79 ps

P9: Integral 7.47 - 9.62 ps

P10: Emax (maximum amplitude)

P11: Power frequency = 1.11 THz